Optimizing NMP-Slurry Gelation in High-Solid Content Systems for NMC622 Electrodes: Advances in Roll-to-Roll Processes and Electrochemical Efficiency

Zur Erlangung des akademischen Grades eines

Doktors der Ingenieurwissenschaften (Dr.-Ing.)

von der KIT-Fakultät für Maschinenbau
des Karlsruher Instituts für Technologie (KIT)

genehmigte

Dissertation

von

M.Sc. Francesco Colombo

Hauptreferent: Prof. Dr. Michael J. Hoffmann

Korreferent: Prof. Dr. rer. nat. Helmut Ehrenberg

Prüfungsvorsitz: Prof. Dr.-Ing. Xu Cheng

Tag der mündlichen Prüfung: 28.07.2025

Table of Contents

Declaration

I hereby declare that I completed this thesis independently by myself by only utilizing the referenced resources. All material, whether directly quoted or rephrased, from both published and unpublished works, has been duly acknowledged. By doing so I assert that this thesis represents my personal genuine effort. All sources and materials employed in the preparation of this thesis are accurately documented and cited. Additionally, I confirm that this thesis has never been submitted in the same or similar version as part of any other examination process.

The guidelines for Safeguarding Good Research Practices at the Karlsruhe Institute of Technology (KIT) have been duly fulfilled and observed.

Köln, January 7, 2025

Francesco Colombo

Acknowledgements

This work was carried out during my tenure as a research associate at the Institute for Applied Materials (IAM), Karlsruhe Institute of Technology (KIT). It represents a contribution to the ongoing research efforts at the Center for Electrochemical Energy Storage (Celest) in Karlsruhe and Ulm. The successful completion of this work would not have been possible without the incredibly supportive and stimulating atmosphere encouraged within the electrode development research group of the Institute for Applied Materials – Energy Storage Systems (IAM-ESS). My sincere gratitude goes to the colleagues, students, and collaborators whose support and collaboration have guided me through this journey. I extend my sincere thanks to Prof. Dr. Helmut Ehrenberg for sharing his expertise and providing me with invaluable input. His support, always delivered in his characteristic warm and generous manner, has been really vital when granting me the opportunity of working at his institute and pursuing my research, which culminated in this dissertation. My heartfelt appreciation also goes to Prof. Michael Hoffmann from the Institute for Applied Materials – Ceramic Materials and Technologies (IAM-KWT), who graciously agreed to oversee the evaluation of this work. Furthermore, I would like to express my deepest gratitude to Dr. Werner Bauer, who offered me the doctoral student position, shared his wealth of experience in experimental methodologies and provided insightful guidance on rheology theory. His steady mentorship and continuous support in both practical and academic matters have been invaluable, by providing me with the freedom to develop my research in my own way, while offering precious advices and steady encouragement whenever necessary. I am also thankful to Dr. Marcus Müller, whose thought-provoking discussions played a significant role in advancing this work, for his constant support in the laboratory. I am especially grateful to Dr. Fabian Jeschull for his crucial assistance in interpreting scientific findings: his support in preparing scientific publications and his constructive feedback, particularly in the area of impedance measurements, were really stunning. Last but not least a special thanks goes to my colleagues Dr. Andreas Gyulai, Alexander Vogt, Dr. Tim Mach, Andreas Weber, Noah Keim, Dr. Luca Schneider and Dr. Ulrike Kaufmann, with whom I had enriching exchanges on both experimental and scientific matters. Finally, I would like to extend my sincere thanks to all my colleagues in the IAM-ESS. The stimulating discussions and collaborative spirit made my working within this team not only productive but also immensely enjoyable. The overall support has been a constant source of motivation and I am grateful for every moment spent together with all of you.

Kurzfassung

N-Methyl-2-pyrrolidon (NMP) ist für die Verarbeitung von Elektroden auf Lösungsmittelbasis von entscheidender Bedeutung, erhöht jedoch die Herstellungskosten aufgrund seiner Verdampfung, Rückgewinnung und Behandlung erheblich. Grüne Lösungsmittel wie Wasser werden zwar erforscht, sind aber aufgrund unerwünschter Reaktionen mit aktiven Materialien für die großtechnische Produktion noch nicht geeignet. Schlicker mit sehr hohem Feststoffgehalt (SC) sind unerlässlich, um die Verwendung schädlicher, teurer und umweltschädlicher Lösungsmittel zu reduzieren. Ein hoher Feststoffgehalt in $Li(Ni_{0.6}Mn_{0.2}Co_{0.2})O_2$ (NMC622)-Slurries ist jedoch in der Regel mit einer starken Gelierung verbunden, einem wenig verstandenen Phänomen. Das Gießen von Schlickern mit hohem Feststoffgehalt kann aufgrund der hohen Viskosität und Gelierung problematisch sein und zu qualitativ schlechten Schlichten führen. In dieser Arbeit wird ein erster Ansatz vorgestellt, der versucht, die Vorteile von Schlicker- und Elektrolytzusätzen zu vereinen. Elektrolytzusätze/Salze, die in der Literatur weithin als leistungssteigernd für Batterien anerkannt sind, wenn sie im Elektrolyten gelöst sind, wurden einen Schritt früher eingesetzt, nämlich direkt beim Mischen des Schlickers, um die Rheologie günstig zu beeinflussen und so höhere SCs in NMC622-Schlickern erfolgreich zu verarbeiten. Diese Additive wurden ausgewählt, um unbekannte Wechselwirkungen innerhalb des komplexen Batteriesystems zu vermeiden. NMC622-Materialien tragen nämlich basische Oberflächenverbindungen, die die NMP-Dispersion destabilisieren und ihre Gelierung verursachen. Zum ersten Mal wird erklärt, wie diese Art von Additiven die Gelierung der Aufschlämmung verzögern kann, indem sie die Adsorption des Polyvinylidendifluorid (PVdF)-Bindemittels durch Neutralisierung und Komplexierung der NMC622-Oberfläche verändern. Zunächst wird die Verwendung von H_3PO_4 und drei Li-Elektrolytsalzen, nämlich Lithiumtrifluoracetat (LiTFA), Lithiumbis(trifluormethan)sulfonimid (LiTFSI) und Lithiumdifluor(oxalato)borat (LiODFB), als Kathodenzusätze für Slurry untersucht. Mit diesen Additiven lässt sich die Gelierung effektiv einstellen, so dass die Verarbeitung von Schlämmen mit einem hohen Feststoffgehalt von 75 Gew.% möglich ist, was über die üblichen Grenzen hinausgeht, die ohne Additiv mit 70 Gew.% SC erreicht werden können. Li-Salze sind selbst in sehr niedrigen Konzentrationen wirksamer als H_3PO_4, das für eine vergleichbare Verzögerung der Schlickergelierung höhere Beladungen erfordert. Langfristige Zyklen in NMC-Graphit-Pouchzellen mit bis zu 1000 Zyklen zeigten, dass H_3PO_4 zu einer Verschlechterung der Leistung bei hohen C-Raten und einem starken Kapazitätsabfall aufgrund von Nebenreaktionen mit der Graphitanode führte. Im Gegensatz dazu zeigten Li-Salze enthaltende Kathoden eine vergleichbare Leistungsfähigkeit wie eine Referenzelektrode ohne Zusätze. LiTFSI zeigte die beste Kapazitätserhaltung unter den Li-Salzen, die Kathoden enthalten, mit einer Langzeitkapazität, die nahe an der leistungsstärksten additivfreien probe lag. Andere Li-Salze enthaltende Elektroden zeigten im Vergleich zur Referenz eine schnellere Degradation. Ein zweiter Ansatz, der die Verarbeitung von Slurrys mit hohem Feststoffgehalt ermöglicht, wird anhand eines verbesserten Slurry-Mischschemas in Verbindung mit Formulierungen demonstriert, die sich durch einen geringeren Rußanteil (1 Gew.%) auszeichnen. Diese Strategie ermöglichte das Gießen von NMC622-NMP-Slurrys im Bereich von 80 bis 85 Gew.% Feststoffgehalt. Zusätzlich wurden die Auswirkungen eines extrem reduzierten Rußgehalts (0,5 Gew.%) auf die Rheologie bei 85 Gew.% Feststoffgehalt untersucht. Die verbesserte Deagglomeration des Rußes ermöglicht eine günstigere Konformation des PVdF-Bindemittels auf der Rußoberfläche, was zu einer verminderten brückenbildenden Verklebung und einer geringeren physikalischen Gelierung der Aufschlämmung führt. Darüber hinaus beeinträchtigte der geringere Rußgehalt in der Schlickerformulierung nicht die Zyklusleistung der Elektroden und ermöglichte die Herstellung von Beschichtungen mit höheren Aktivstoffgehalten von bis zu 98 % und geringeren Porositäten von 15 %. Die Leistungsfähigkeit der resultierenden Kathoden mit hoher Energiedichte wurde in NMC-Graphit-Vollzellen getestet, wo sie eine vergleichbare Leistung wie die Standard-Referenzelektrode zeigten. Die Standardelektrode wurde mit einer Standardmischung und höheren Additivmengen hergestellt und zeigte eine optimale Zyklusleistung bei höheren Porositäten. Industriell relevante Materialien und Zusammensetzungen werden im Rolle-zu-Rolle-Herstellungsprozess verwendet, wobei der Schwerpunkt auf kommerziellen PVdF-Bindern mit hoher Molekularmasse. Daher haben die in dieser Arbeit untersuchten Herstellungsprozesse ein inhärentes Potenzial für einen positiven wirtschaftlichen Nutzen und ein Upscaling.

Abstract

N-methyl-2-pyrrolidone (NMP) is crucial for processing solvent-borne electrodes but significantly increases manufacturing costs due to its evaporation, recovery, and treatment. While green solvents like water are being explored, they are not yet practical for large-scale production due to undesired reactions with active materials. Super high solid content (SC) slurries are essential to reduce the use of harmful, expensive, and polluting solvents. However, high SC in $Li(Ni_{0.6}Mn_{0.2}Co_{0.2})O_2$ (NMC622) slurries is typically associated with strong gelation, a poorly understood phenomenon. Casting slurries with high SC can be problematic due to high viscosity and gelation, resulting in poor-quality coatings. An initial strategy integrating the advantages of both slurry and electrolyte additives is introduced in this thesis. Electrolyte additives/salts, commonly employed to boost cell performance when dissolved in the electrolyte, were instead pre-added during slurry preparation to tune rheology and enable processing of NMC622 suspensions at high solid loadings. These additives are chosen to avoid unknown interactions within the complex battery system. Indeed, NMC622 materials bear basic surface compounds that destabilize the NMP slurry, causing its gelation. This work reveals, for the first time, that such additives delay slurry gelation by modulating PVdF adsorption via neutralization and complexation on NMC622. The application of H_3PO_4 and of three Li electrolyte salts, namely lithium trifluoroacetate (LiTFA), lithium bis(trifluoromethane)sulfonimide (LiTFSI) and lithium difluoro(oxalato)borate (LiODFB), as slurry cathode additives is at first examined[1]. These additives effectively tune gelation, enabling the processing of high 75 wt.% SC slurries, thus surpassing the regular limits attainable without additive of 70 wt.% SC. Li salts, even in very low concentrations, are more effective than H_3PO_4, which requires higher loadings for a comparable delay of slurry gelation. Long-term cycling in NMC-graphite pouch cells up to 1000 cycles showed that H_3PO_4 led to deteriorated performance at high C-rates and severe capacity fading due to side reactions with the graphite anode. In contrast, Li-salts containing cathodes demonstrated comparable rate-capability performance to a reference electrode without additives. LiTFSI exhibited the best capacity retention among Li-salts containing cathodes, with long-term capacity close to the best-performing additive-free sample. Other Li-salts containing electrodes showed faster degradation compared to the reference. A second approach to enable slurry processing at high SC is demonstrated by means of an improved slurry mixing scheme coupled with formulations characterized by reduced (1wt.%) carbon black loadings. This strategy allowed casting of NMC622-NMP slurries within the 80 wt.% to 85 wt.% SC range. Additionally, the impact of extremely reduced carbon black content (0.5wt.%) on rheology was examined at 85 wt.% SC. Enhanced carbon black deagglomeration enables a more favorable PVdF binder conformation onto the carbon black surface, thus resulting in impaired bridging flocculation and reduced physical slurry gelation. Moreover, the reduced carbon black content in the slurry formulation did not compromise the electrode cycling performance and allowed the production of coatings with higher active material loadings of up to 98% and reduced porosities of 15%. The high-power and long-term cycling performances of the resulting high energy density cathodes were tested in NMC-graphite full-cells, where they demonstrated comparable performance to the standard reference electrode. The standard electrode was produced with standard mixing and higher additive amounts and showed optimal cycling performance at higher porosities. Industrially relevant materials and compositions are used in the roll-to-roll manufacturing process, with special focus on commercial high Mw PVdF binders. Therefore, the manufacturing processes investigated in this thesis show an intrinsic potential for positive economic benefit and upscaling.

1 Introduction

A basic organic solvent-based slurry for cathodes, hereafter referred to as a solvent-borne slurry for the sake of simplicity and for distinguishing it from water-borne slurries, includes the active material (AM), carbon black (CB) as an electronic conductive agent, and polyvinylidene difluoride (PVdF) as a binder[1]. Despite its low vapor pressure and hazardousness, N-methyl-2-pyrrolidone (NMP) is the preferred dispersing medium for electrode slurries owing to its ability to dissolve PVdF. Due to its exceptional electrochemical, chemical, and thermal stability, PVdF has become the preferred fluoropolymer for a vast range of applications, spanning from medical to chemical engineering[2]. In battery technology[1], PVdF has become the standard binder for cathode coatings, playing a crucial role in electrode processing and significantly impacting cell performance[3,4]. Cathode materials such as $LiNi_{0.80}Co_{0.15}Al_{0.05}O_2$ (NCA) or various forms of $Li(Ni,Mn,Co)O_2$ (NMC) typically have mean particle sizes from 5 to 10 µm. The increased AM particle size lowers their specific surface area, enabling slurries to achieve higher solid loadings[1,5]. Since energy costs during manufacturing increase as NMP must be evaporated and recovered during the electrode drying step, innovative and greener solutions, such as super high solid content (SC) slurries, are essential to minimize solvent use[1]. Owing to higher solvent and energy use, low-SC slurries pose significantly larger economic and environmental impacts. Nevertheless, $Li(Ni_{0.6}Mn_{0.2}Co_{0.2})O_2$ (NMC622) combined with high SCs typically returns strong slurry gelation, especially beyond practical limits[6,7] of around 70 wt.% or higher, thus compromising rheology, hindering processability in the coating process, and resulting in poor quality coatings[1]. Slurry gelation is reported to occur due to the jointly interaction between the type of high-molecular weight PVdF binder used (M_w = 370’000 – 1’300’000 g/mol)[1] and the moderately high slurry SC employed (60 wt.%)[3]. Gel formation is beneficial for standard SC slurries[3] when the strength of the aggregated state prevents component segregation and AM particle sedimentation by effectively immobilizing the particles. However, coating issues can arise if the slurry's aggregated state is too strong. When the average inter-particle distance of the AM significantly exceeds the polymer's radius of gyration, the likelihood of gel formation decreases[1], which is generally true for low SCs. Generally, gelation is also more likely to take place with smaller sub-µm particles[8], thus reducing the slurry SC threshold for gelation[1]. Moreover, PVdF’s chemical instability with basic NMC surfaces likely contributes to gelation in NMP-based slurries[9]. Indeed, over and above physical gelation from bridging flocculation, chemical gelation[1] can occur in slurries with layered cathode materials due to basic impurities on their surface[9,10]. Residual lithium compounds are common on higher nickel content NMCs[9], particularly in over-lithiated NMC materials like the NMC622 adopted in this work, where excess LiOH is used in the course of the synthesis process to compensate for the lithium loss during calcination[11]. Other studies have shown that basic compounds on the NMC surface[1] can be removed by water[12,13], acidic solutions[14,15], or by directly adding $LiPF_6$ into the cathode slurry[9]. In this thesis, the use of slurry additives is the primary strategy assessed for the purposes of tuning rheology, so that to enable the processing of higher SC NMC622 slurries. H_3PO_4 is the first slurry additive tested. Subsequently, also the application of three well-known Li electrolyte salts as slurry additives is demonstrated. These additives were carefully chosen to actively manipulate gelation dynamics, facilitating the processing of high solid content (SC) slurries that exceed conventional processability limits[6,7] reported in existing literature. For comparative analysis, an additive-free reference electrode was fabricated under identical processing conditions, allowing for a comprehensive assessment of its rheological and electrochemical properties in comparison to the additive-altered counterparts. Specifically, H_3PO_4 and the selected Li electrolyte salts—namely lithium trifluoroacetate (LiTFA), lithium bis(trifluoromethane)sulfonimide (LiTFSI), and lithium difluoro(oxalato)borate (LiODFB)—were employed as additives to modify the surface chemistry of the active material (AM)[1]. This approach aimed to form complexes with NMC622 and thereby modify its interaction with PVdF, effectively fine-tuning rheological characteristics and mitigating gelation in high SC slurries. These additives were chosen based on their ability to leverage the acidic properties[16] of H_3PO_4, LiTFA[17], and LiTFSI[18], as well as the passivating capabilities of LiODFB and H_3PO_4, to chemically alter the basic surface properties of NMC622[1]. Furthermore, H_3PO_4 was selected for its demonstrated ability to reduce degradation[19] when used as an additive in waterborne slurry processing, while Li salts were chosen for their established interactions within battery cells, both as electrolytes and as additives. Subsequently, a different slurry mixing procedure is demonstrated as an alternative approach to optimally tune slurry rheology, enabling the processing of high solid contents. This mixing is performed at high SC, thus enhancing CB deagglomeration by maximizing stress transfer through the surrounding denser medium and by increasing collision frequency and friction owing to diminished interparticle spacing and reduced solvent utilization[20,21]. This alternative mixing method is combined with formulations that have reduced (1wt.%) carbon black loadings. The impact of significantly lowering carbon black content on rheology is studied down to a minimum of 0.5wt.% CB at elevated solid contents. The adjusted mixing aims to alter the degree of C65 deagglomeration, thereby modifying the PVdF binder conformations on the carbon black surface, which results in changed bridging flocculation and modified physical slurry gelation. This new mixing technique allows for the casting of NMC622-NMP slurries within a solid content range that exceeds usual practical limits[6,7]. Altered carbon black deagglomeration, coupled with reduced additive amounts in the slurry formulation, enables the production of coatings with higher active material loadings and significantly reduced porosities. These characteristics provide a potential answer to meet the challenging market demand for higher energy density batteries, which requires increasing the active material content in the electrodes while reducing the amount of additives. The high-rate capability and long-term cycling performances of the resulting high energy density coatings are tested in graphite-NMC full cells and compared to a standard reference electrode, produced with less intensive mixing and achieving optimal cycling performance at higher porosity. For comparison, processing 80 wt.% solid content NMC622-NMP slurry with 95 wt.% active material loading was previously reported[22] as challenging in extrusion-based methods. This difficulty arose from the trapping of PVDF and carbon black on the active material surface and the delamination of conductive graphite. These issues resulted in a lack of inter-particle contact points in the final electrodes, leading to poor cohesion, brittleness, increased electrical resistance, and very poor cycling performance[22] at 28% porosity.

Electrochemical impedance spectroscopy (EIS) after formation cycles is used on these high energy density cathodes to assess the impact of calendering on their electrochemical performance. This dissertation systematically investigates how slurry additives, mixing protocols, and reduced carbon black content influence rheology, processability, particle distribution, and electrochemical performance using both coin-cell based NMC half-cells and pouch-cell type graphite-NMC full cells.

2 Theoretical background

2.1 Materials

Active materials, binders, and conductive additives are the typical components used in the manufacturing of cathodes for lithium-ion batteries. The active material is the redox-active constituent, which is responsible for reversibly storing lithium-ions by incorporation into interstitial sites or by insertion/intercalation into its crystal structure. Because the active material is a fine powder to facilitate high-rate performance, the binder is a necessary component to ensure cohesion between the individual electrode components and to provide good adhesion between current collector foil and electrode coating. Since binders are dielectric polymers, the inclusion of a conductive additive is necessary in order to create a composite material with efficient electron transport across the electrodes. PVdF has become the standard binder for electrode coatings, and its incorporation during electrode processing critically determines cell performance. The mechanical integrity of the electrode has to be preserved across all processing steps in the dry state (e.g. calendering, final drying and cell assembling) and in the wet state when it´s in contact with the electrolyte, where the binder should also dampen and accommodate the AM volume changes while cycling. A suitable binder can reduce time for cell manufacturing and improve cell cycling by properly wetting the electrode with the electrolyte. In addition, it is important to mention that binders play a vital role in the interaction between electrodes and electrolytes, which has significant implications for the surface energy of the electrode and for a proper wetting with the electrolyte. Therefore, binders have also an important impact on the growth of the solid electrolyte interphase (SEI)[23], thus influencing the aging behavior of the cells. During slurry preparation, the binder should be acting as a good dispersing agent so that to improve the distribution of the solid components, particularly the conductive additive(s) in order to enhance the electronically conductive percolating network; uniformity of mechanical properties and electrical conductivity of the coating directly impact on the cycle life of the battery[3,4].

2.1.1 Polyvinylidene difluoride (PVdF)

Introduction to PVdF: Properties and Applications

Polyvinylidene difluoride[24–28] is a widely used fluorinated polymer which exhibits a distinctive set of significant properties. These features derive from the fluorine atom’s small van der Waals radius (1.32×10^{-10} m) and robust C-F bond (485 $kJ \cdot mol^{-1}$), reflective of its low polarizability and high electronegativity[29,30]. This results in enhanced oxidation resistance and hydrolytic stability. Hence, fluoroplastics combine superior thermal, chemical, and weather stability with resistance to a wide range of solvents, including hydrocarbons, acids, and bases[30]. Owing to their low surface energy, fluoroplastics exhibit oil and water repellency, low dielectric constant and refractive index, minimal flammability, and virtually no moisture uptake[30]. However, fluoroplastic homopolymers have several limitations due to their high crystallinity, which results in poor solubility in many organic solvents and complicates common processes like curing and cross-linking. To mitigate these drawbacks, a variety of fluorinated copolymers[27,28,31] incorporating bulky comonomeric side groups have been synthesized, inducing macromolecular disorder and reducing or eliminating the base homopolymer's crystallinity. The VdF-derived homopolymers[32] consist of long, semi-crystalline chains with a composition of 59.4 wt.% F and 3 wt.% H[30]. Their high inherent crystallinity (approximately 60%) imparts properties typical of thermoplastics[33], such as stiffness, toughness, and creep resistance. PVdF finds extensive applications across various fields, including chemical process equipment, electrical equipment, electronics, and specialty energy-related applications, despite its notable drawbacks[30]. These include high melting temperatures, leading to increased energy costs for polymer processing; poor solubility in many common solvents; and difficult curing processes. PVdF dissolves in only a limited set of organic solvents[34], including dimethylformamide (DMF), dimethyl sulfoxide (DMSO), dimethylacetamide (DMAc), and N-methyl pyrrolidinone (NMP) [35,36].

Synthesis of PVdF and Polymerization Kinetics

Heterogeneous reactions such as emulsion and suspension polymerization are among the most widely used industrial techniques for synthesizing polyvinylidene fluoride (PVdF) in water. These processes[30] frequently utilize fluorinated surfactants, chain transfer agents, buffering agents, or stabilizing agents, and they typically operate under pressures of 1 to 30 MPa and temperatures of 10 to 130 °C. The suspension process, in particular, generally requires higher temperatures and pressures, along with longer reaction times. Emulsion polymerization[30], as depicted in **Figure 1**, involves the polymerization of monomers in water, facilitated by the emulsifying action of surfactants. Typically, the emulsion comprises the vinylidene fluoride (VdF) monomer[37], a water-soluble initiator such as potassium persulfate (KPS) or redox systems, and surfactants that stabilize the emulsion by reducing surface tension among the emulsified phases. When the initiator generates free radicals[30] in the aqueous phase, these reactive species migrate to the surfactant-stabilized monomers, initiating the propagation process within the VdF droplets/micelles and forming growing PVdF polymer chains. These chains gradually consume the VdF monomers, producing polymer particles. The reaction usually terminates through coupling or disproportionation of free radicals, resulting in the formation of the final PVdF latex particles[30]. The polymer latex dispersion is then coagulated by adding methanol or low molecular weight electrolytes and subsequently washed to obtain a purified product. The resulting latex particles, consisting of high molecular weight PVdF, range in size of hundreds of nanometers.

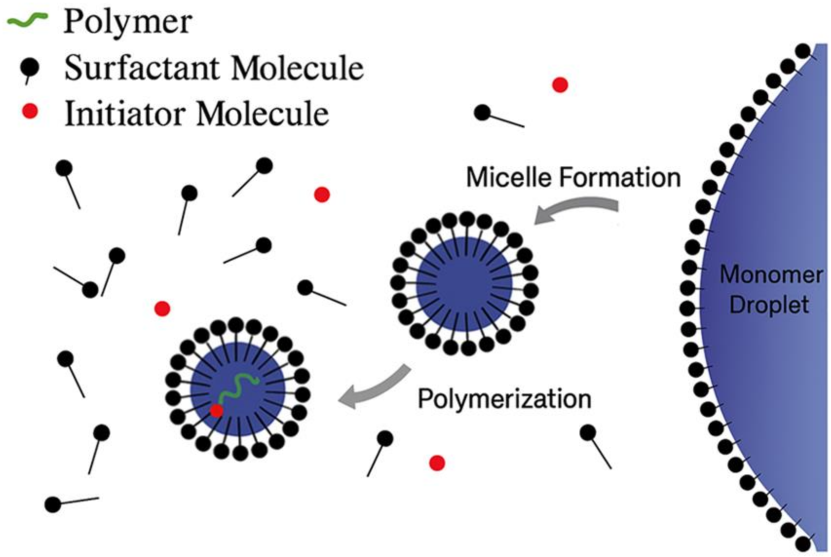

Figure 1. Emulsion polymerization mechanism. Adapted from B. Soegijono et al.[38] and licensed under CC BY 4.0.

In contrast, suspension polymerization[37] , as depicted in **Figure 2**, produces larger polymer beads, ranging from 0.5 µm to several millimeters in size. This technique distributes VdF monomers in water using suspending agents and intensive stirring, eliminating the need for surfactants and thus typically resulting in higher purity compared to emulsion PVdF. The process requires VdF monomers, a water-insoluble initiator such as organic peroxides[39–41], and a water-insoluble stabilizer such as poly(vinyl alcohol) (PVA) or cellulose, which stabilizes the suspensions. Suspending agents are essential to prevent the particles from coagulating, segregating, and settling, by providing steric stabilization through increased viscosity of the liquid medium. During the initiation step, organic peroxide dissolves into the monomer droplets, creating free radicals and triggering the polymerization process. Within each monomer droplet, the polymer chains continue to propagate, leading to the generation of polymer beads. As with the emulsion process, polymerization termination occurs through coupling or disproportionation of free radicals[42]. The resulting PVdF beads are then separated from the aqueous medium and washed to obtain the final product. PVdF polymerized through the suspension process is known to readily dissolve in various solvents, such as DMF, NMP, DMSO, and DMAc. In contrast, emulsion resins are often more challenging to dissolve, typically requiring heating to achieve solubility. The propagation rate and the formation of various diads have been studied[30] in relation to the kinetics of the radical homopolymerization of VdF. The polymerization conditions and reaction temperature determine the quantities and types of VdF-VdF diads, specifically the normal head-to-tail diad (-CH2CF2-CH2CF2-) and faulty diads such as head-to-head (-CH2CF2-CF2CH2-) and tail-to-tail (-CF2CH2-CH2CF2-) defects[43]. A higher fraction of head-to-head defects is reported[30] to occur more frequently in the emulsion process compared to suspension-polymerized PVdF, resulting in commercial PVdF grades produced by emulsion polymerization exhibiting a wider range of defects, spanning from 3-7 mol%. Pre-spin-lock radio frequency dipolar recoupling (RFDR) measurements have shown that these defect units typically localize in the amorphous polymer domains, thereby altering the overall macromolecule crystallinity.

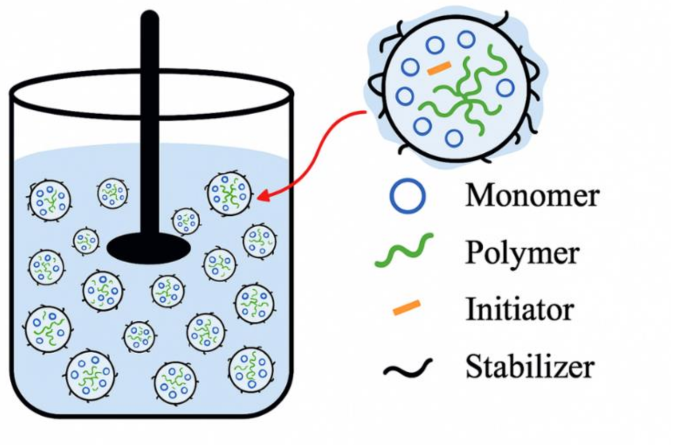

Figure 2. Schematic representation of the suspension polymerization process.

Consequently, this modification affects many crystallinity-related PVdF properties, such as toughness, mechanical strength, and impact resistance[27,35]. Indeed, PVdF produced through suspension polymerization typically exhibits higher crystallinity[30]. This is owing to the better control over the reaction conditions when compared to the emulsion process, hence typically resulting in macromolecules with more uniform chain lengths, that are more prone to crystallization[27,35]. Furthermore, unlike suspension polymerization, which results in fewer side reactions, the emulsion polymerization process, owing to its more complex reaction conditions, is more susceptible to generating branching, to retain residual surfactants, and to produce a broader molecular weight distribution[44].

Crystalline Phases and Related Physicochemical Properties of PVdF

PVdF is a highly crystalline polymer with a crystallinity ranging from 50-70%, and it exhibits multiple crystal polymorphs, including α, β, γ, δ, and ε. These polymorphs stem from the slight difference in the van der Waals radius[45] of fluorine atoms ($1.35 \cdot 10^{-10}$ m) compared to hydrogen atoms ($1.20 \cdot 10^{-10}$ m)[46–48]. Among these polymorphs, the α, β, and γ crystalline forms are the most common (**Figure 3)**. The α-phase (form II) is the kinetically favored and most prevalent form, which is characterized by a peculiar trans-gauche nonpolar conformation (TGTG'). In this configuration, hydrogen and fluorine atoms alternately position themselves on both sides of the polymer chain, thus resulting in a helix-like structure[49]. Characterized by its all-trans zigzag (TTT) chains, the polar β form (I) is the thermodynamically favored phase and is typically produced by straining, stretching, or quenching[30,50]. Owing to the perfect alignment of dipoles within the -CH2CF2- units along the polymeric chains, the β phase is extensively studied for its piezoelectric, pyroelectric, and ferroelectric properties[46]. Last but not least, the γ phase (form III), characterized by a mid-polar conformation (TTTGTTTG'), can be produced by applying moderate stress or by high-temperature annealing.

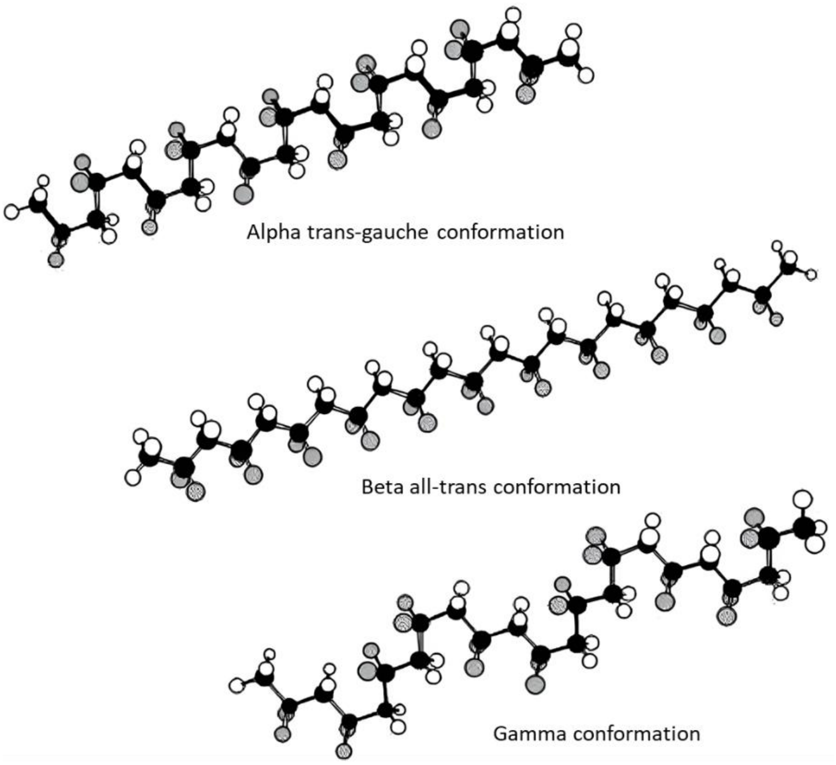

Figure 3. The main polymorphs of PVdF are illustrated with carbon, hydrogen, and fluorine atoms represented by black, white, and gray spheres, respectively. Reproduced with permission from Wiley & Sons, ref[51], copyright 2004.

The densities[30] of the α, β, and γ polymorphs are 1.92 g·cm^{-3}, 1.97 g·cm^{-3}, and 1.93 g·cm^{-3}, respectively, whereas the amorphous PVdF phase exhibits a lower density of 1.68 g·cm^{-3}. In contrast, the PVdF homopolymer, when subjected to melting conditions of 230°C and $1 \cdot 10^5$ Pa, demonstrates a further reduced density[30], ranging between 1.45 and 1.48 g·cm^{-3}. These polymorphs, especially in the α and β forms, are crucial for PVdF's well-known piezoelectric properties, thus allowing voltage generation through the application of pressure. Specifically, the crystalline α phase, characterized by antiparallel chains, exhibits no net polarization[30]. In contrast, the β phase, with its parallel chains and aligned dipoles, generates a net polarization, imparting piezoelectricity to the material. By subjecting the material to an electric field, β chains align parallelly, enhancing both net polarization and piezoelectric performance. Indeed, PVdF is a thermoplastic material with distinctive physical and electrical features[35], which are influenced by several factors, including molecular weight, molecular weight distribution, chain configurations, defects, and crystalline form[52]. Among its crystalline forms, the β-phase PVdF exhibits the highest dielectric permittivity due to the spontaneous orientation of dipoles in this crystallite, thus providing a strong polarization of the C-F bonds. Regarding the amorphous and crystalline regions of PVdF[30], the glass transition temperature (T_g) ranges from -40°C to -30°C, while the melting temperature (T_m) spans from 155°C to 192°C. These temperatures depend on various PVdF properties such as the polymer molecular weight, the number of chain defects, and the testing method employed. PVdF crystallinity, along with numerous other properties, can be systematically modified through copolymerization[30], a versatile strategy typically achieved via the radical method, that allows tailoring of polymer characteristics. Indeed, this approach allows for the modification of intramolecular and intermolecular forces by changing the symmetry of the polymer chains, thereby impacting key PVdF properties such as its melting point, glass transition temperature, crystallinity, stability, elasticity, permeability, and chemical resistance[30].

2.1.2 $LiNi_{0.6}Mn_{0.2}Co_{0.2}O_2$ (NMC622)

NMC cathodes, with the general formula $LiNi_xMn_yCo_{1-x-y}O_2$, form a versatile class of lithium-ion battery materials. By tuning the Ni, Mn, and Co ratios, compositions such as $LiNi_{0.33}Mn_{0.33}Co_{0.33}O_2$ (NMC111), $LiNi_{0.5}Mn_{0.3}Co_{0.2}O_2$ (NMC532), $LiNi_{0.6}Mn_{0.2}Co_{0.2}O_2$ (NMC622), and $LiNi_{0.8}Mn_{0.1}Co_{0.1}O_2$ (NMC811) can be engineered to balance energy density, stability, and cycle life. Among them, NMC622 offers a well-rounded compromise between performance and durability[53]. NMC622 is a widely-used layered lithium nickel manganese cobalt oxide (NMC) cathode material, characterized by the transition metal ratio of 60% nickel, 20% manganese, and 20% cobalt[54]. It strikes an optimal balance between high energy density, power, safety, and cost, making it a favored choice in the battery industry. The typical synthesis of NMC622 involves co-precipitation, followed by calcination[55]. During precursor formation, a water-based solution containing nickel, manganese, and cobalt salts (such as sulfates or nitrates) is combined with a precipitating agent like sodium hydroxide (NaOH) or ammonia (NH_4OH), resulting in a hydroxide precursor. This precursor, $Ni_{0.6}Mn_{0.2}Co_{0.2}(OH)_2$, is typically polycrystalline, and composed of smaller crystallites aggregated into larger spherical particles[56].The formation of these larger particles occurs through a controlled chemical process where uniform nucleation and growth in solution lead to spherical agglomerates. In the co-precipitation stage, supersaturation and high ion concentration promote rapid nucleation of small crystallites[56]. As these crystallites form, they aggregate to minimize surface energy, which is elevated due to their high surface-area-to-volume ratio. Driven by the reduction of surface energy, smaller crystallites may also dissolve and redeposit onto larger ones through Ostwald ripening[56]. These small crystallites are in constant motion due to Brownian motion, which can bring them close enough for van der Waals forces to foster aggregation. According to Fick's Law, ions naturally diffuse from high-concentration regions (in the bulk solution) to lower concentration areas (near the aggregate surface), thus contributing to particle growth or to new crystallite nucleation. Electrostatic interactions[57] are also crucial in particle aggregation, so that, when the surface charge is neutralized by adjusting the pH near the isoelectric point, attractive forces dominate, thus promoting aggregation and limiting repulsion between charged particles. Ultimately, these processes result in the precursor particles which are comprised of smaller crystallites and whose size typically ranges from 5 to 20 μm. While the precursor's size is often similar to that of the final NMC particles, the precise dimensions may vary depending on synthesis conditions such as temperature and calcination time, which can influence particle growth, shrinkage, or densification[57]. During the calcination process, the hydroxide precursor is combined with lithium hydroxide (LiOH) or lithium carbonate (Li_2CO_3) powders[58] and subjected to high temperatures ranging from 700°C to 900°C in an oxygen-rich atmosphere, thus facilitating the formation of the layered NMC622 structure[57]. Notably, the chemical composition of the NMC622 surface often differs from that of the bulk, and this variation can significantly impact the material's electrochemical performance by influencing factors such as lithium-ion diffusion, capacity retention, and cycling stability[59]. Specifically, the surface of NMC622 typically contains oxides of nickel, manganese, and cobalt, with a slight enrichment of nickel oxides (e.g., NiO) due to the higher reactivity of nickel. Furthermore, because of its susceptibility to react with CO_2 and H_2O, the NMC622 surface is often coated with lithium carbonate (Li_2CO_3) and lithium hydroxide (LiOH)[1]. Depending on the synthesis and post-treatment processes, the surface may also contain traces of coating materials like Al_2O_3[59] or impurities originating from the precursor materials.

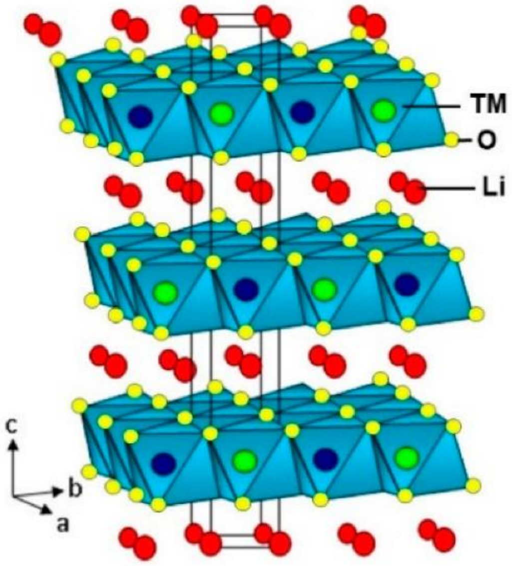

Figure 4. The layered structure of the NCM compound, with lithium depicted in red, oxygen in yellow, nickel, manganese, and cobalt represented either in green or blue. Adapted from C. M. Julien et al.[60]

The crystallographic structure of NMC622, as per **Figure 4**, is characterized by the presence of Li and transition metal ions (manganese, nickel, and cobalt), both of which occupy octahedral sites within a face-centered cubic oxygen framework[60]. NMC622 exhibits a theoretical capacity exceeding 270 mAh/g and operates at a relatively high working voltage of 3.6V versus lithium metal[60]. Despite its high theoretical capacity, the practical specific capacity[61] of NMC622 is limited by the applied cut-off voltages. While $Ni^{2+}/Ni^{3+}/Ni^{4+}$ redox reactions are active[59], transitions such as Mn^{4+}/ Mn^{3+} may remain underutilized[59]. Additional losses arise from parasitic reactions at the solid electrolyte interphase (SEI) and at the cathode electrolyte interphase (CEI), especially at or above 4.2 V, leading to electrolyte degradation and lithium consumption, which can only be partially compensated by overlithiation. Cation mixing[62] further reduces capacity through Ni^{2+} migration into Li sites, hindering Li^+ transport. As a result, typical capacities are restricted to ~175 mAh/g in both half-[63] and full-cell[1] formats under typical conditions (3.0–4.2 V, 23 °C). Its $R\bar{3}m$ layered structure, as illustrated in **Figure 4**, consists of Li layers interspersed between MO layers along the [111] direction[64], which allows enhanced mobility of Li ions along the two-dimensional interstitial space[60]. In an ideal $R\bar{3}m$ structure, transition-metal sites and lithium sites are distinctly separated. However, this ideal structure can become defective[60] as a result of the "cation mixing" mechanism[62], which implies cations exchange between transition-metal and lithium sites owing to the tendency of Ni^{2+} to occupy Li^+ sites due to their similar ionic radii[65]. Cation mixing[60] in NMC622 adversely affects electrochemical performance, leading to structural instability, diminished thermal stability and a loss of reversibly cyclable lithium. Overall this translates into lower capacity, poor rate capability, reduced cycling stability, degraded long-term performance, voltage fade, and impaired lithium-ion mobility within the bidimensional Li diffusion pathways. During the charging of NMC622, the redox reactions of the electrochemically active transition metals $Ni^{2+}/Ni^{3+}/Ni^{4+}$ and Co^{3+}/Co^{4+} contribute to approximately 67% and 33% of the total capacity, respectively[59]. Specifically, when a 4.3V cut-off voltage is applied[59], nickel undergoes oxidation from Ni^{2+} to $Ni^{3.7+}$ (without fully reaching the Ni^{4+} state), and then returns to Ni^{2+} during discharge, making it the most active transition metal. Under the same conditions, cobalt, which plays a crucial role in enhancing rate capability by minimizing Ni/Li ion mixing, is primarily active at higher voltages. It begins to oxidize at around 3.8V, contributing to approximately one-third of the total capacity as its oxidation state changes from Co^{3+} to $Co^{3.5+}$ during delithiation, and reverts to Co^{3+} upon discharge. Meanwhile, manganese remains in the Mn^{4+} state throughout the cycling process, exhibiting no electrochemical activity, but granting structural and thermal stability to the material[59]. NMC622 exhibits moderate electrical conductivity, approximately 5.9×10^{-3} S cm^{-1}, as measured by the four-probe method[66], when compared to other cathode materials. The presence of nickel within its structure enhances conductivity, making NMC622 more suitable for applications demanding higher power output and rapid charging capabilities. Its layered structure further improves electronic transport, contributing to its relatively higher conductivity compared to LFP[67] ($\sim 10^{-9}$ S cm^{-1}). However, its conductivity remains lower than that of pure nickel-rich materials or lithium cobalt oxide (LCO).

2.1.3 Carbon black

The primary carbon black particles typically exhibit a spherical shape, with diameters ranging from 30 to 50 nm. During the manufacturing process, these primary carbon black particles are invariably fused into larger secondary aggregates, measuring several hundred nanometers in size[68]. In the case of the investigated carbon black (C-NERGY Super C65, Imerys Graphite & Carbon, Bodio, Switzerland), its small primary particle size, around 30 nm, leads to the formation of secondary aggregates within the size range of 200–300 nm[69]. Aggregates formed by a small number of closely packed primary particles lead to low-structure blacks, while those comprising numerous primary particles can produce high-structure blacks with significant branching[69]. When considering a specific mass of carbon black aggregates, high-structure blacks generally provide a larger surface area for electron conduction in comparison to low-structure blacks[69]. It's important to note that once the aggregate structure is established, conventional hydrodynamic shear forces cannot alter it[69]. For the sake of clarity, these carbon black secondary aggregates will be referred to as carbon black particles henceforth. The existing literature has unequivocally shown that colloidal interactions can induce the agglomeration of carbon black particles, giving rise to highly branched agglomerates that exhibit a fractal nature[70–72]. When carbon black is mixed with PVdF and NMP, the binder becomes physically absorbed onto the surface of the carbon black particles, thus effectively mitigating the considerable surface tension between the carbon black particles and NMP[73]. The key forces governing carbon black agglomeration involve van der Waals attraction among minute colloidal particles, steric repulsion arising from the adsorbed polymer coating, and electrostatic (double layer) repulsion originating from the surface charge of carbon black[74]. According to research findings[68], C45 carbon black particles (C-Nergy Super C45, Imerys Graphite & Carbon, Bodio, Switzerland) dispersed in NMP exhibited a zeta potential of around 10mV, as measured by a zeta potential meter. This would imply that the electrostatic repulsion can be considered negligible and inconsequential. In contrast, another study[75] suggests that L6 carbon black (Printex L6, Degussa, Frankfurt, Germany) achieves electrostatic stabilization in NMP without the need for additional dispersants. This is evidenced by a zeta potential of approximately -50 mV and the presence of charged particles resulting from the dissociation of counterions from surface groups. Nonetheless, the stability of the slurry predominantly depends on the strong steric repulsion between particles due to the presence of the absorbed PVdF layer[5,68]. The formation of the absorbed PVdF layer is intricately influenced by factors such as the choice of solvent, particle surface morphology, particle-to-polymer ratio, and the binder molecular weight[76]. Additionally, under the influence of Van der Waals forces, these aggregates can coalesce into larger entities known as agglomerates, typically measuring 10–100 µm, which can be disrupted by hydrodynamic forces[77]. Notably, the particle suspension consists of fractal agglomerates that readily create an interconnected, space-filling network. Moreover, considering that the maximum attraction between carbon black particles is less than 20k_BT, the agglomeration process of these particles is reversible[78]. Reference[68] demonstrated that carbon black-polymer suspensions exhibit shear-thinning, with viscosity decreasing as shear rate increases. At low shear rates, an interconnected gel network of fractal agglomerates, previously formed through interparticle colloidal interactions, extends throughout the entire slurry. In this regime the relative viscosity remains high, owing to the robust interparticle bonding energy and the high-volume fraction of aggregates. As shear rates increase, hydrodynamic interactions become increasingly significant. At intermediate shear rates, where hydrodynamic forces slightly surpass or match the maximum bonding energy between carbon black particles, the intricate network and sizable flocs of carbon black particles break down into smaller fractal agglomerates. As the shear rate continues to rise, hydrodynamic interactions grow stronger, surpassing the bonding energy between carbon black particles. As a result, larger agglomerates fragment into smaller ones and eventually disintegrate into individual carbon black particles. In this condition, the viscosity of the carbon black suspension remains low, primarily due to the hydrodynamic interactions among particles. The breaking and reforming of this space filling network constitute a reversible process for carbon black particles owing to their limited inter-particle bonding energy[68]. Hence, the mixing of sizable 5–10 µm NMC particles with NMP, PVdF, and CB to create a slurry may induce the formation of a strengthened gel due to the interaction of the active material particles with the intricately entwined polymer chains ensnared within the CB-PVdF space-filling network[1]. Therefore, elongated polymer layers have the capacity to interact with each other, and when segments of a single polymer chain adsorb to different particles, aggregation occurs through bridging flocculation[1].

2.1.4 Slurry additives

In this thesis, H_3PO_4 and three lithium salts, specifically LiTFSI, LiODFB, and LiTFA, have been utilized as cathode additives in NMP-based slurries to chemically alter the composition of the NMC622 surface.

Phosphoric Acid (H_3PO_4)

H_3PO_4 is a widely used additive in water-based processing of cathode materials[19,79,80] slurries, where it actively reduces electrode degradation[19] and protects the Al current collector from corrosion by reducing the slurry pH to the range 4.5 to 8.5, which is the stable passivation regime for Al_2O_3. In water-based NMC111 suspensions, H^+ exchange with water has been shown[19,81–83] to rapidly leach lithium from the particle surface and, as proton concentration increases, shifts the equilibrium to expedite Li^+ removal. Although at elevated pH (≥9) only lithium is significantly released, near-neutral pH (≈7) also dissolves nickel, manganese, and cobalt[19]. Acidifying the slurry with acetic acid[19], for instance, lowers the pH and initially enhances capacity, but residual acid that survives drying corrodes NMC particles during prolonged cycling, thereby inducing internal cracks and severe capacity fade compared to acid-free samples over 900 cycles. By analogy[19,81–83], incorporating H_3PO_4 is likewise anticipated to increase acid-mediated metal dissolution from NMC-based materials; however, as detailed below, its scavenging action may offset this effect. In particular, H_3PO_4 is claimed to be a scavenger[80] for dissolved transition metal ions in the aqueous medium because of its potential of forming hardly soluble metal phosphates that, by precipitation on the particle surface, could block detrimental side reactions. Dissolved transition metal ions are, indeed, known for triggering severe irreversible side reactions into the battery system, even in very low concentrations[84]. Additionally, H_3PO_4 has also been used as additive for water-processed $Li_4Ti_5O_{12}$ anodes[85] where its usage in a ball-milling mixing process produces a protective phosphate sheet around the LTO particles, therefore leading to enhanced cycling stability and improved capacity retention upon long-term cycling in NMC532-LTO full-cells.

Lithium bis(trifluoromethane)sulfonimide (LiTFSI)

LiTFSI is notable for its thermal stability[16], boasting a melting point of 236°C and remaining stable up to 360 °C. It exhibits robust electrochemical properties, with an oxidation potential of 4.3 V vs. Li/Li^+ in a 1:1 (v/v) binary solution[86] of EC/DEC at 25°C. This electrolyte salt has a high dissociation constant, ensuring effective performance even in low dielectric constant solvents[1]. Additionally, its bulky anion, that facilitates enhanced electron delocalization[87], promotes excellent ionic conductivity in solution. Since its introduction to rechargeable lithium-ion batteries in 1984[88], its commercial application has been limited by corrosion issues with aluminum current collectors[16].

Lithium difluoro(oxalato)borate (LiODFB)

LiODFB represents a new generation of electrolyte lithium salts, demonstrating exceptional thermal stability up to 240 °C[16]. It features extended electrochemical stability, with an oxidation potential of 5.57 V vs. Li/Li^+ in 1:1:1 wt% EC/DMC/EMC electrolytes at 25°C[89]. When dissolved, LiODFB exhibits ionic conductivity comparable to that of $LiPF_6$ at room temperature and promotes stable aluminum passivation[16]. Its solubility in alkyl carbonate solvents is significantly enhanced compared to its predecessor, LiBOB[90–92], and it aids in the formation of solid-electrolyte interfaces[16] on both negative[89,93] and positive[94,95] electrodes. Due to its strong passivation capabilities, LiODFB functions not only as an electrolyte salt but also as an additive[1] that improves stability at high temperatures[90] and voltages[95], ultimately leading to enhanced battery cycle life[96].

Lithium trifluoroacetate (LiTFA)

LiTFA is an additive utilized in lithium metal batteries[97] to regulate the composition of the Li^+ solvation sheath within the electrolyte, thereby promoting stable and uniform solid-electrolyte interphase (SEI) formation[1]. This role significantly reduces lithium dendrite formation, resulting in improved full-cell Coulombic efficiencies[1]. Importantly, the preferential reduction of LiTFA, compared to other electrolyte components, generates a stable lithium metal passivation layer characterized by a uniform distribution of LiF and Li_2O[97].

2.2 State-of-the-art electrode manufacturing

2.2.1 Mixing

Slurry mixing is performed in order to disperse agglomerates and to achieve a uniform consistency in the slurry. Several mixer technologies have been employed as efficient options for lab-scale or pilot plant blending of electrode slurries, like hydrodynamic shear mixers, ball-mill mixers, ultrasonic mixers, planetary centrifugal mixers, and extruders. The predominant methods for slurry mixing in industrial settings are extruders or large planetary mixers[23]. Planetary centrifugal mixers, such as the Thinky Mixer used in this thesis, are highly versatile tools widely utilized in research settings for battery slurry production. While their primary application is in research and prototype development, they also play a role in small-scale industrial processes, including quality control and specialized battery applications. The Thinky Mixer disperses materials through the combined forces of revolution and rotation[98]. The material container undergoes a high-velocity spinning motion (anticlockwise rotation), generating centrifugal force that drives the slurry outward, thus also guaranteeing effective defoaming. Simultaneously, the container revolves in a planetary motion around a central axis (clockwise revolution), which is typically tilted at a 45° angle from the spinning axis[98], as depicted on the left side of **Figure 5**.

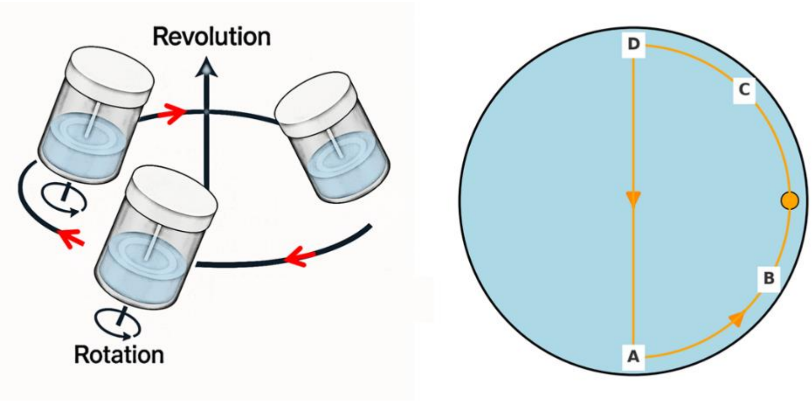

Figure 5. Schematic of the Thinky planetary mixer's working principle. On the left side, the material vessel spins at high speed around its own axis (rotation). Simultaneously, the container revolves in a tilted (~45°) planetary orbit around a central axis (revolution), exposing the slurry to intense shear. On the right side, a schematic illustration of the planetary centrifugal comminution mechanism: zirconia balls are accelerated by the rapid rotation–revolution motion to collide with the material against the beaker wall, promoting particle size reduction through collision energy transfer.

Moreover, according to the manufacturer's website, when the mixing chamber is filled with highly wear-resistant zirconia balls, the rapid rotation–revolution motion causes the balls to collide vigorously with the feed material against the beaker wall, utilizing collision energy to progressively reduce particle size, as illustrated on the right side of **Figure 5**. A similar mechanism is expected to govern the motion of NMC622 particles during mixing, thereby enabling efficient particle comminution within the NMP-based slurry system (NMP + NMC622 + PVdF + CB). This configuration subjects the material to high shear forces without the need for stirring blades, minimizing contamination and enabling homogeneous mixing of slurries, even at elevated solid contents[1]. Mixing a slurry of NMC622, carbon black (CB), and PVdF binder at high solid content using a Thinky planetary centrifugal mixer is anticipated to improve CB deagglomeration compared to slurries with lower solid content and higher solvent levels. High solid content increases the slurry's viscosity, which maximizes the stress imparted by the surrounding medium, as noted by Grießl[21]. In dense systems, the surrounding medium more efficiently transfers stress, facilitating better dispersion of components like carbon black. Additionally, reducing solvent in the slurry decreases interparticle spacing, lowering the mean free path between particle collisions events[20], and enhancing the likelihood of impacts and friction. These increased interactions improve mixing and deagglomeration efficiency. Such stresses enable effective particle comminution through impact and friction, without damaging the active material. The high energy input in this system fosters CB dispersion through particle collisions, a result less achievable in low-viscosity, solvent-rich slurries, where impact stresses are weaker, thus optimizing CB dispersion while maintaining material integrity. The duration of the mixing process can vary considerably based on the specific chemistry and on batch size. Typically, mixing times range from 1 to 6 hours for planetary mixers and 5 to 30 minutes for extruders, followed by an additional degassing step that may last from 5 minutes to 1 hour[23]. Since many active materials are highly moisture-sensitive, it is advisable to carry out slurry preparation in a dry environment with a dew point ranging from -40 to -60 °C. After the completion of the mixing process, the rheology of the slurry is carefully checked for suitability with the in-use coating device. It is also common practice to filter slurries to eliminate any sizable agglomerates before transfer to the coater.

2.2.2 Slurry microstructure of NMP based cathodes

After completing the mixing process, the rheological properties of the slurry provide valuable insights into various aspects such as its stability, resistance to sedimentation, suitability for coating applications, anticipated dry thickness, and the sharpness of dried electrode edges. Indeed, slurry optimization is a crucial step in electrode manufacturing and must be tailored to meet the specific requirements of each coating line. To prevent issues like segregation, flocculation, and precipitation of the slurry's solid components, it is essential to control viscosity during storage tank dwell times, so that to avoid clogging in tubing, filters, and feeds along the coating line. The elastic, gel-like behavior of the slurry often plays a more critical role than a simple viscous response to shear[99], enabling optimal processability in various applications such as coating, spraying, or extrusion. The rheology of the slurry can change significantly depending on the applied solid content. Factors such as the PVdF's long-chain molecular architecture and the solid content can dramatically influence the binder conformation adsorbed on the surface of solid active material particles[1]. Macroscopically, this can lead to particle sedimentation below the optimal solid content or inhomogeneous component distribution and slurry gelation above the optimal solid content. The appropriate selection of the PVdF binder is essential to impart the desired flow behavior, aligning with the specific requirements of each coating process. Nevertheless, despite its extensive industrial use, the full potential of PVdF remains underexplored due to an insufficient understanding of its interactions with other electrode components. A deeper comprehension of these interactions is crucial to develop new and more suitable polymer functionalizations, ensuring PVdF maintains its role as a standard additive for current and future generations of batteries. Carbon black (CB) tends to aggregate into networks when mixed with PVdF in NMP due to its high surface area and sub-micron primary particle size, which allows van der Waals forces to become significant[1]. To mitigate the high surface tension between CB and the solvent, the PVdF binder readily adsorbs onto the CB surface, thereby stabilizing the colloidal system and immobilizing the CB particles[71,100,3]. When large 5–10 µm NMC particles are combined with these CB-PVdF colloidal domains and mixed with NMP, gel formation typically occurs due to the interaction between the active material (AM) particles and the entangled polymer chains[1]. The adsorption of polymer onto a ceramic surface can be influenced by kinetic factors, such as the potential barriers arising from the repulsion of pre-adsorbed solvent molecules[1]. Adsorption proceeds once polymer chains reach the solvated solid interface by diffusion or convection; the overall rate is governed chiefly by the conformational rearrangement kinetics and the flexibility of the nascent adsorbed layer[1,101]. The conformation of these adsorbed polymer layers is characterized by surface-adherent trains and solution-protruding loops or tails[102,103]. A dense polymer layer in train conformation, indicating high monomer density, is typically found in close contact with the ceramic particle surface[1]. Conversely, as the polymer extends into the solution, the density decreases, and the structure becomes more diffuse, with protruding loops or tails[1]. The molecular weight of the polymer generally dictates the extent of these polymer tails from the AM surface into the bulk solution[1]. Polymers with high adsorption energy tend to form a higher percentage of trains in direct contact with the ceramic, while those with lower adsorption energy are more likely to form loops or tails[104]. In good solvents, ceramic surfaces fully covered with polymer layers experience steric stabilization, causing mutual repulsion and preventing agglomeration[1]. However, if the polymer layers are not saturated, they may cause bridging flocculation when the bridging process is faster than the flattening and compaction of the polymer film on the ceramic surface[1,105]. Under these conditions, protruding polymer segments on the AM surface may interact, and when distinct regions of a single chain adhere to separate particles, bridging flocculation can provoke aggregation[1]. The probability of interparticle interactions is anticipated to increase with rising solid content[106]. At low solids loading, increased interparticle spacing hinders network formation, whereas at high solids loading, decreased spacing enhances both the frequency and strength of particle interactions[1], as illustrated in **Figure 6**.

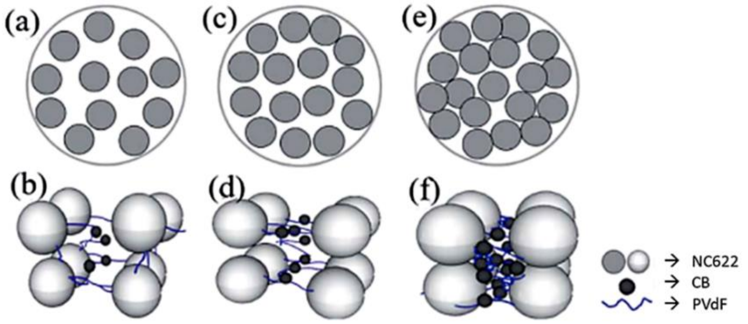

Figure 6. Schematic illustration of NMC622-CB-PVdF slurry structures and interparticle interaction mechanisms at three solid-content levels. Panels (a), (c), and (e) depict the top-view dispersion of NMC622 particles (grey) at low, intermediate, and high solid contents, respectively. The corresponding slurry microstructures and binder-particle interactions involving NMC622 particles (light grey), carbon black (dark grey), and PVdF binder (wavy lines) are shown in panels (b), (d), and (f). Adapted from L. Ouyang, Z. Wu, J. Wang et al[6] with permission from the Royal Society of Chemistry.

Besides physical slurry gelation due to bridging flocculation, residual lithium compounds such as Li_2O, LiOH and Li_2CO_3[9,10] on the surface of layered cathode materials can initiate chemical slurry gelation[1]. If the NMC surface is exposed to air, Li_2O may react with H_2O and CO_2, forming additional surface contaminants like LiOH[1] or Li_2CO_3[107]. These basic lithium compounds are undesirable because they produce gas during full-cell cycling due to their reaction with carbonate solvents[108]. Furthermore, they are believed to catalyze PVdF binder dehydrofluorination[109,37,110,111,112] in the cathode slurry, which can degrade the polymer by creating unsaturated C=C bonds in its backbone[1]. The dehydrofluorination of the PVdF binder releases HF, which reacts with basic Li compounds on the AM surface to generate H_2O. Since water is a non-solvent for PVdF and the presence of C=C double bonds can trigger crosslinking of the polymer chains, dehydrofluorination ultimately leads to chemical slurry gelation[1].

2.2.3 Coating and drying

Slot-die coater, reverse comma bar coater, and doctor blade are the most commonly used devices for the application of slurry onto a substrate. The slot-die coater is deemed to be the main device for commercial applications owing to its superior precision and tight tolerances[23]. The slurry is usually pumped through the slot-die head, in which a shim is used to set the gap for a controlled flow. The slurry is then deposited to the substrate from the slot-die head, which can be positioned either directly above, below, or horizontally with respect to the moving Al or Cu foil (**Figure 7A**).

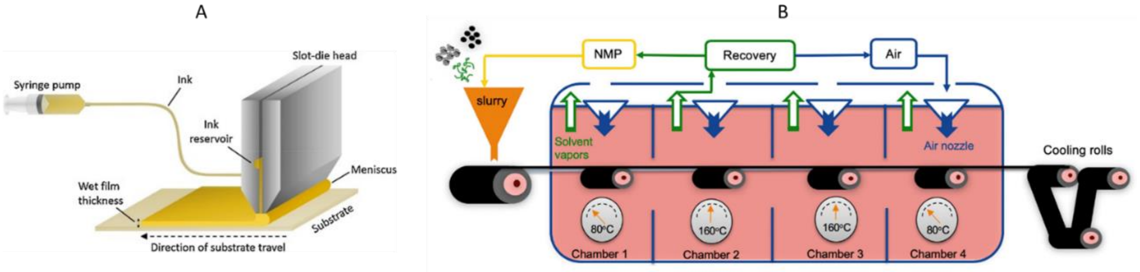

Figure 7. A: Scheme of a slot-die coater. Reprinted with permission from ref[113]. Copyright 2020 Elsevier. B: scheme of the typical process for drying of a solvent-borne slurry and solvent recovery. Reprinted with permission from ref[114]. Copyright 2021 MDPI.

The desired coating thickness is achieved depending on the balance between the pumping speed and the substrate line speed. Electrode casting is carried out in a roll-to-roll coater, with speeds typically ranging from 10 to 80 meters per minute in high throughput processes. The quality of the coating depends on the coating conditions and on the careful balancing of slurry stability and rheology. It is a common practice to prepare large batches of mixed slurries at first and which are then cast in a subsequent process, so that at least 8 hours of slurry stability is usually required. Albeit deemed to be stable, the slurry rheology has a small but inevitable evolution in time, that may introduce some level of variability into the final product. After the coating process, the wet electrode goes through a drying zone to eliminate the solvent(s), typically for 1 or 2 minutes[115], as in **Figure 7B**. In general, water-borne anodes tend to dry more rapidly and consume less energy[114] than solvent-borne cathodes. In fact, water is a well-established solvent for graphite anodes and it is currently under investigation for moisture-sensitive cathodes, albeit not being extensively employed in large scale production due to undesirable side reactions with the active materials[19]. When NMP is used, it is essential to capture and recycle the vaporized solvent due to safety and environmental concerns. Special attention should be paid to the amount of residual solvent in the coating as it exits the dryer, since excessive residues can lead to defects like blistering or mud-cracking[23]. Nevertheless, research highlights[116] the importance of achieving an optimal drying rate to prevent the electrodes from becoming either excessively dry or overly moist. This balance is crucial to avoid issues such as brittleness, poor adhesion to the current collector, or the development of microstructural defects[116]. Electrode drying is a crucial process that should eliminate solvents effectively and produce an electrode with consistent morphology, structure, and properties. In high-speed coating operations, rapid drying is particularly advantageous in order to minimize plant space requirements and reduce capital costs associated with longer drying lines. Among the different stages in lithium-ion battery production, the drying zone has a pivotal role, especially with high coating speeds, due to the occurrence of phenomena like binder migration[117–121]. During drying, the solvent molecules located near to the surface are at first vaporized. The remaining solvent has to diffuse through the entire thickness of the coating to maintain a continuous evaporation rate. Depending on the drying conditions, the evaporating solvent can actively drag with itself binders and conductive additives through the coating, thus leading to the so-called binder migration. This phenomenon can produce reduced adhesion at the electrode-current collector interface, thus leading to higher electrode resistance and to a weaker electronic conductivity in the proximity of the current collector. Weaker adhesion can cause significantly faster capacity degradation while cell cycling, also due to the electrode volumetric changes that arise from the reversible intercalation process inside the active material. Additionally, poor adhesion between the electrode and the current collector[122] may also have a negative impact on the rate capability of the cell[23]. To mitigate the migration of binders and conductive additives, an ideal drying protocol would involve a slow movement of each solvent molecule to the surface, resulting in minimal reconfiguration of the microstructure. A three-stage drying process has been proposed[123] as a strategy that may offer a compromise between reduced binder migration and accelerated drying speeds.

2.2.4 Calendering

Post-drying the electrode is subjected to the calendering process in order to achieve a desired reduced thickness. This process helps reducing the pores volume, enhancing the energy density, improving the electron conductivity, but it may reduce ion transport through the network of electrolyte-infiltrated pores. Calendering is typically performed at temperatures well above the glass-transition temperature of the binder, so that to help the distribution of materials and to reduce the stresses generated during the process. However, denser electrodes exhibit an increased electrode tortuosity owing to the reduced space between neighboring particles, thus diminishing the number of electrolyte-filled pores through which ions can travel[124]. In thin high power electrodes, the diffusion coefficient of lithium ions in the solid active material phase is significantly smaller compared to that within the liquid electrolyte[125]. Nevertheless, as the electrode thickness increases, the diffusion of lithium ions in the liquid electrolyte can be dumped to such a point, to become the main performance-limiting factor[125]. For every specific electrode, depending on its formulation and areal loading, the ideal porosity should set an optimum balance between the electrode conductivity and the diffusion length of lithium ions in the liquid electrolyte[126]. Research-grade cathodes[19,96,120,127–130] with moderate areal capacities (e.g. 2 to 4 mAh/cm²) typically exhibit a porosity ranging from 30% to 35%, thus enabling high-power and high-rate performance (≥5C). However, for commercial battery electrodes and particularly for the electric vehicle (EV) market, lower porosities should be favored in order to achieve higher volumetric energy density at the cell-level and lower costs due to reduced requirement of electrolyte[124]. Indeed, reduced electrode porosity can be a more effective strategy to get to high volumetric energy density compared to minimized separator thickness, since thin separators can compromise safety, owing to their decreased mechanical strength[23]. Nevertheless, low porosity cathodes (e.g. 25% or 15%) are reported as challenging to cycle in real cells, owing to their very low electrochemical performances[124,130]. Also, electrolyte wetting of cathodes with bulk porosity of less than 20% is reported being problematic due to the lower apparent surface energy of heavily compressed electrodes[23,131]. Due to a significant difference in elastic modulus between the coating and the current collector, uncalendered electrodes usually exhibit better adhesion compared to electrodes calendered to low 20-27% porosity. Indeed, calendering to these moderately low porosities can causes the coating to be stretched to a much greater extent than the substrate, thus leading to the contacts loss[132] between the binder and the current collector[133]. Interestingly, when the electrodes are calendered to lower porosities (<30%), a slight increase in adhesion strength compared to the value attained at intermediate porosities is reported, owing to the mechanical interlocking binding mechanism[133].

3 Experimental

3.1 Electrode materials

Cathode slurries were prepared by blending NMC622 (HED NMC622, BASF, Germany) as the active material, carbon black (C-NERGY Super C65, Imerys Graphite & Carbon, Bodio, Switzerland) and graphite (C-NERGY KS6L, Imerys Graphite & Carbon, Bodio, Switzerland) as conductive additives, high molecular weight PVdF binders, and NMP (1-Methyl-2-pyrrolidone, Emplura, Sigma-Aldrich, USA) as organic solvent[1]. Two different binders were utilized:

- PVdF Type A as an example of high Mw homopolymer (Kynar® HSV 900, PVdF produced by emulsion polymerization[134] with Mw=900.000–1.300.000 g/mol, Arkema Inc., France)[1].
- PVdF Type B as an example of high Mw functionalized polymer (Solef® 5130, PVdF produced by suspension polymerization[134] with ultra-high molecular weight and modified with polar functional groups distributed in the polymer chain, Mw=1.000.000–1.100.000 g/mol, Solvay Inc., Belgium). This suspension-type homopolymer exhibits a low number of head-to-head defects, no long-chain branches, and virtually no microgels when dissolved[135].

The particle size distribution of NMC622 was determined using a laser scattering particle size analyzer (LA-950V2, Horiba, Japan), yielding values of D_{10} = 6.12 µm, D_{50}= 9.46 µm, and D_{90} = 14.17 µm[1]. The specific surface area was measured via BET analysis, with results of 0.33 m^2/g for NMC622 and 58.7 m^2/g for C65, using a surface area analyzer (Gemini VII, Micromeritics, USA)[1]. The density of NMC622 powder was found to be 4.63 g/cm^3, determined by a helium pycnometer[1] (Pycnomatic ATC, Porotec, Germany). Additionally, the following slurry additives are employed: H_3PO_4 (crystalline, ≥99.999%, Sigma-Aldrich, USA), LiTFSI (99.95% trace metals basis, Sigma-Aldrich, USA), LiTFA (97%, Alfa Aesar, USA), and LiODFB (99.5%, Sigma-Aldrich, USA)[1].

3.2 Mixing

Stock solutions of PVdF (9 wt.% and 15 wt.%) were prepared by dissolving the binder in NMP with a Dispermat dissolver (VMA Getzmann GmbH, Germany) run for 1 hour at 700 rpm and 2000 rpm, respectively[1]. Following this, the stock solutions were degassed by mixing for 15 minutes at 700 rpm under vacuum[1]. Additives were initially dissolved in NMP to the required concentration[1] prior to slurry mixing as shown in **Table 1**. The additive concentration for each NMP-PVdF stock solution is related to the amount of PVdF and the corresponding slurry concentrations[1] can be found in **Table 1**. For the preparation of cathode slurries, an ARV 310 Thinky Planetary Mixer (Thinky Corporation, Japan) was used[1]. Two distinct mixing processes were employed for slurry production, as illustrated in **Figure 8**. In the Mixing 1ST protocol, the slurry is initially prepared at 86.4 wt.% solid content (SC) upon active-material addition and then stepwise diluted across successive mixing stages to reach the target SC. By contrast, Mixing 2ND uses the same number of mixing steps but keeps the slurry at a constant 87.7 wt.% SC until just before the final four dispersion stages, at which point it is diluted to the target SC. Maintaining this higher viscosity throughout most of the process is envisaged to sustains stronger stress transfer and more frequent particle collisions, thereby maximizing carbon-black deagglomeration by impact and friction compared to mixing-first.

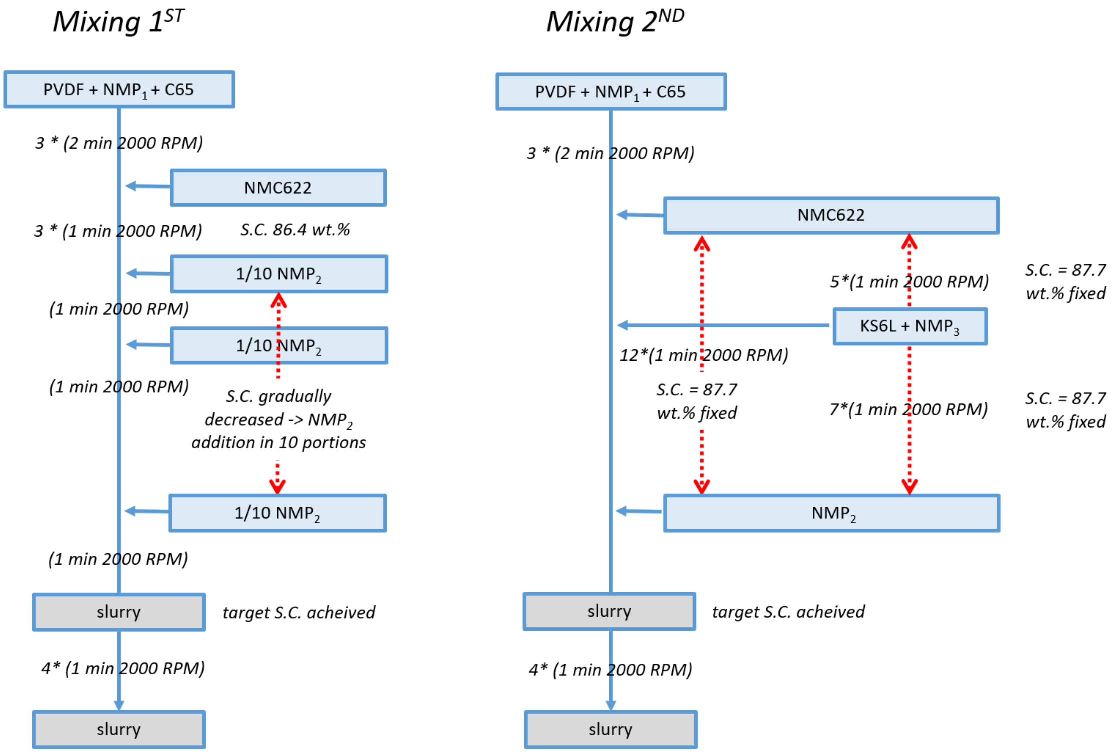

Figure 8. Flow diagrams envisioning Mixing 1ST and Mixing 2ND.

- Mixing 1ST. In the first step C65, PVDF stock solution and an initial amount of NMP are mixed 3 times, each time for 2' at 2000 rpm. The initial NMP required is calculated in order to get a target solid content of 86.4 % in mass after that all the AM is added in the next step. The NMC622 is then added and mixed 3 times for 1 min at 2000 rpm[1]. The remaining NMP is subsequently added in 10 mixing steps (1/10 of NMP for each mixing step), each one of 1 min at 2000 rpm till the final target SC is reached. Finally, four mixing steps of 1 min at 2000 rpm are carried out.

The general composition of the slurries produced with Mixing 1ST and the SCs employed are shown in **Table 1**.

Table 1. Slurry & cathode composition for pouch assembling using Mixing 1ST.

Sample name - additive type	SC in wt.%	ADDITIVE in wt.%	NMC622 in wt.%	Carbon black C65 in wt.%	PVdF in wt.% & (Type)
additive-free A	70.0		97.0	1.5	1.5 (Type A)
additive-free A T	70.0		97.0	1.5	1.5 (Type A)
additive-free B	70.0		97.0	1.5	1.5 (Type B)
additive-free B II	75.5		97.0	1.5	1.5 (Type B)
H_3PO_4 4.3wt.%$_{PVdF}$	75.5	0.064	96.936	1.500	1.500 (Type A)
H_3PO_4 6.1wt.%$_{PVdF}$	75.5	0.091	96.909	1.500	1.500 (Type A)
H_3PO_4 8wt.%$_{PVdF}$	75.5	0.120	96.880	1.500	1.500 (Type A)
LiTFA 0.5wt.%$_{PVdF}$	75.5	0.007	96.993	1.500	1.500 (Type A)
LiTFA 1wt.%$_{PVdF}$	75.5	0.015	96.985	1.500	1.500 (Type A)
LiTFA 2wt.%$_{PVdF}$	75.5	0.030	96.970	1.500	1.500 (Type A)
LiODFB 2wt.%$_{PVdF}$	75.5	0.030	96.970	1.500	1.500 (Type A)
LiTFSI 2wt.%$_{PVdF}$	75.5	0.030	96.970	1.500	1.500 (Type A)
LiTFA 8wt.%$_{PVdF}$	75.5	0.120	96.880	1.500	1.500 (Type A)

- Mixing 2ND. In the first step C65, PVDF stock solution and an initial amount of NMP are mixed 3 times, each time for 2’ at 2000 rpm. The initial amount of NMP is calculated in order to get a target SC of 87.7 % in mass after that all the AM is added in the next step. The NMC622 is added and mixed 12 times for 1 min at 2000 rpm[1]. A second NMP amount, calculated in order to reach the final target slurry SC, is subsequently added to the formulation, which is mixed 4 times, each one for 1 min at 2000 rpm. When the KS6L graphite is employed, the mixing is carried out as follows. In the first step C65, PVDF stock solution and an initial amount of NMP are mixed 3 times, each time for 2’ at 2000 rpm. The initial amount of NMP is calculated in order to get a target SC of 87.7 % in mass after that all the AM is added in the next step. The NMC622 is added and mixed 5 times for 1 min at 2000 rpm. The KS6L graphite is added together with a second NMP amount and mixed 7 times for 1 min at 2000 rpm. The second amount of NMP is calculated in order to keep a constant SC of 87.7 % in mass after that all the KS6L graphite is added to the formulation. A third NMP amount, calculated in order to reach the final target slurry SC, is subsequently added to the formulation, which is mixed 4 times, each one for 1 min at 2000 rpm.

The general composition of the slurries produced with Mixing 2^{ND} and the SCs employed are shown in **Table 2**.

Table 2. Slurry & cathode composition for pouch assembling using Mixing 2^{ND}.

Sample name	SC in wt.%	NMC622 in wt.%	Graphite KS6L in wt.%	Carbon black C65 in wt.%	PVdF in wt.% & (Type)
0.5wt.%$_{C65}$B	85.0	98.8		0.5	0.7 (Type B)
1wt.%$_{C65}$B	80.0	98.0		1.0	1.0 (Type B)
1wt.%$_{C65}$B II	82.5	98.0		1.0	1.0 (Type B)
1wt.%$_{C65}$B III	85.0	98.0		1.0	1.0 (Type B)
1wt.%$_{C65}$A	80.0	98.0		1.0	1.0 (Type A)
1wt.%$_{C65}$1wt.%$_{KS6L}$B	85.0	97.0	1.0	1.0	1.0 (Type B)

3.3 Rheology

Since segregation in non-transparent slurries is difficult to detect by visual methods, rheology becomes the preferred technique for assessing both the flowability and stability of a dispersion[1]. A comprehensive characterization of a viscoelastic sample, such as an NMP-based slurry (NMP + NMC + PVdF + CB), begins with a steady-state flow test (shear stress versus shear rate) to determine the system's viscosity[1]. This is followed by dynamic oscillatory shear and frequency sweep measurements, which respectively evaluate the strength of the slurry's aggregated state[1] and its time-dependent structural stability[99]. Rheological characterization of these viscoelastic samples is performed using a rheometer (MCR 302, Paar Physica, Austria) in stress-controlled mode, employing a PP50 plate-plate geometry, with a 500 µm gap, and at a constant temperature of 25 °C[1]. Steady-state flow, amplitude, and frequency sweep tests are conducted sequentially, immediately after the mixing process[1]. A resting period of five minutes is allowed to stabilize the residual normal force at 25 °C, ensuring thermal equilibrium before the rheological measurements commence[1]. Steady-state flow viscosities are evaluated by applying shear stresses ranging from 0 Pa to 1000 Pa, allowing for the determination of viscosity and shear-thinning behavior[1]. For the 1wt.%$_{C65}$B II (82.5 wt.% S.C.) and the 0.5wt.%$_{C65}$B (85.0 wt.% S.C.) slurry samples, the maximum shear stress is increased to 1500 Pa due to their medium-to-high viscosities. In contrast, for the 1wt.%$_{C65}$B III (85.0 wt.% S.C.) and the 1wt.%$_{C65}$1wt.%$_{KS6L}$B (85.0 wt.% S.C.) slurry samples, which exhibit exceedingly high viscosities, the maximum shear stress is raised to 2100 Pa. Amplitude sweeps are conducted at a fixed frequency of ω = 10 Hz within the strain range γ = 0.01% to 10000%[1]. Frequency sweeps are measured within the linear viscoelastic region (LVR), if present, at a fixed strain γ = 0.1% over a frequency window of ω = 0.01 Hz to 1000 Hz[1]. The critical strain value γ_{crit} defines the boundary of the linear viscoelastic region (LVR), beyond which the material's behavior becomes progressively non-linear[1]. Determination of the LVR is done using the Anton Paar RheoCompass™ software with curve smoothing of 19% to reduce low-end outliers and with the calculation mode “leaving a tolerance band” set with a tolerance of ±3% to determine the LVR limit. From this critical strain value (γ_{crit}) and the modulus G' within the LVR, wherein the equation $\sigma = G'_{LVR}\,\gamma^2_{crit}$ applies[1], it is possible to calculate the cohesive energy (E_{coh}) of the sample[136].

$$E_{coh} = \int_0^{\gamma crit} \sigma(\gamma) d\gamma = \frac{1}{2} G'_{LVR} \gamma^2_{crit} \quad (1)$$

E_{coh} is defined as the energy per unit volume that upholds particle cohesion in the slurry’s aggregated form[1].

3.4 Electrode manufacturing

The electrodes were fabricated by casting NMP-based slurries onto 20 µm Al foil using a roll-to-roll coater (KTFS, Mathis AG) with a doctor blade, drying sequentially at 80 °C and 120 °C at 0.2 m/min, and then calendering at 50 °C on a Saueressig GLK 200 to reduce porosity[1]. Adhesion strength was evaluated before and after calendering via 90° peel tests (DIN EN 28510-1) on a zwikiLine Z2.5/TN (Zwick-Roell) with a 10 N load cell: 80 × 17 mm electrode strips, coating side down, were pressed under 200 kg for 2 s, then peeled at 600 mm/min over 30 mm to determine adhesion in N/m[1]. A post-coating heat treatment at 167 °C for 15 minutes was performed to optimize adhesion when LiTFA and LiTFSI were used as slurry additives or for electrodes with reduced binder content. Subsequently, electrode mass and thickness were determined, and through-plane resistance was measured in DC mode with an RM3544 milliohm meter (Hioki E.E. Corp., Japan) on 12 mm disks sandwiched between 14 mm copper cylinders at 6.5 kPa[1]. All data regarding cathode manufacturing, including composition, mass loading, adhesion, porosity, and electrical resistance, were thoroughly documented and can be found in **Table 1**, **Table 2**, **Table 6**, **Table 10**, **Table 14**, **Table 18**, **Table 22** and **Table 25.**

3.5 Cell assembly and electrochemical characterization

3.5.1 Cell assembly

Prior to assembly, all cell components (electrodes and separator) are dried overnight at 130 °C under vacuum to minimize water uptake, resulting especially from the hygroscopic LiOH compounds[137,138] on the surface of NMC622[1]. Although Li-salts exhibit hygroscopicity, their mere 0.03 wt.% presence in the dry electrode renders their effect on water uptake negligible compared with the 96.97 wt.% NMC622[1]. Pouch cells (45 mAh) were assembled in a dry room held at a dew point lower than –50 °C. The positive electrode measures 50 × 50 mm^2, while the negative electrode is slightly larger at 54 × 54 mm^2. A ceramic-coated separator (Separion, Litarion, Germany) is used, along with 450 µL of LP30 electrolyte (1:1 EC/DMC, 1 M $LiPF_6$, BASF, Germany)[1].

Table 3. Anodic balancing for pouch-cell assembly: graphite anodes (SMGA3/C65/CMC/SBR, 96/1.5/1.25/1.25 wt.%) matched to the cathode by their storage-capacity ratio (anode/cathode)[1].

Electrode sample	Porosity in %	Anode Balancing in %
additive-free A	33	117
additive-free A T	32	*
	28	*
	20	*
H_3PO_4 8wt.%$_{PVdF}$	33	131
LiTFA 2wt.%$_{PVdF}$	33	113
LiODFB 2wt.%$_{PVdF}$	33	113
LiTFSI 2wt.%$_{PVdF}$	33	117
0.5wt.%$_{C65}$B	15	120
1wt.%$_{C65}$B	27	118
	21	113
	15	134
1wt.%$_{C65}$A	15	117
1wt.%$_{C65}$1wt.%$_{KS6L}$B	21	132
	15	114

*Half cells with Li-metal anode.

Details regarding the anode composition and its balancing with respect to the cathode are provided in **Table 3**. For each coating type, at least two pouch cells are assembled and tested[1]. In the case of half-cells, CR2032 stainless steel coin cells from Hohsen (Japan) are used. All coin cell components undergo ultrasonic cleaning with isopropanol, followed by drying in a vacuum oven at 120 °C for 24 hours[1]. Cathode disks (12 mm) were dried overnight at 110 °C under vacuum (VDL 23, Binder GmbH). In an argon glove box (MB 200B, MBraun), cells were assembled by stacking a 16 mm × 1.5 mm Li-metal disk (MTI Corp.), an 18 mm GF/C separator (Whatman), and the 12 mm cathode[1]. After adding 150 µL of LP30 electrolyte, the stack was crimped at 5.17 MPa using a hydraulic press (MSK-110, MTI Corp.) and then rinsed with isopropanol[1].

3.5.2 Galvanostatic cycling and rate-capability

Pouch cells are allowed to rest for 20 h at 40 °C (half-cells for 24 h at room temperature) to ensure complete electrolyte wetting[1]. Rate-capability measurements are then carried out at 23°C, using 175 mAh/g NCM622 with 3.0–4.2 V cut-offs for both half[63] and full cells[1]. After two formation cycles at 0.05 C (charge/discharge), ten cycles are run at each C-rate in the sequence 0.5C/0.5C, 1C/1C, 1C/2C, 1C/3C, 1C/5C, and back to 1C/1C[1]. Charging follows a CCCV protocol—constant current to 4.2 V, then constant voltage at 4.2 V with a C/20 current limit—to fully extract capacity[1]. Finally, long-term cycling continues under CCCV 1C charge/3C discharge conditions until 1000 cycles are reached[1]. When studied throughout long-term cycling, differential capacity (dQ/dV) curves[139] are recorded, corresponding to the plateaus observed in the precursor Q-V curves[1].

3.5.3 Electrochemical impedance spectroscopy (EIS)

Electrochemical impedance spectroscopy (EIS) was carried out on pristine cathodes in a three-electrode cell with Li metal as both counter and pseudo-reference[1]. After one formation cycle, impedance spectra were collected at ΔSOC = 0.1 during OCV holds inserted within a full C/10 charge–discharge cycle[1]. Impedance spectra acquired at various SOCs were interpreted using the simplified contact–Randles–film (SCRF) equivalent circuit of by Atebamba et al.[140]. Cathodes were punched into 16 mm disks and dried overnight at 110 °C under vacuum[1]. In an argon glove box, EC-Ref cells (EL-CELL) were assembled with an 18 mm Li disk, three 18 mm GF/B separators, a 16 mm cathode, and 800 µL LP30 electrolyte, using Li metal as reference[1]. EIS was recorded from 50 mHz to 100 kHz with a 10 mV AC perturbation on a MPG2 potentiostat at room temperature[1]. Following a 0.1 C formation cycle (1 C = 175 mAh g^{-1}), spectra were acquired every 10 % SOC during a subsequent C/10 cycle between 2.5 V and 4.2 V, with both forward and reverse frequency sweeps (two spectra per SOC) [1]. Two cells per sample were analyzed. The same protocol was applied to fatigued 16 mm cathodes retrieved after 1000 cycles, which were washed in DMC prior to EC-Ref assembly[1].

3.5.4 SEM and EDS Analysis

Field-emission SEM (Supra 55, Zeiss) was used to image the samples, and EDS was carried out with an Ultim Extreme silicon-drift detector (Oxford Instruments) at 4 kV[1]. Cross-sectional specimens were prepared by argon-ion milling (EM TIC3X, Leica) at 6.5 kV and 3 mA[1]. Post-mortem EDS analyses on anode and cathode surfaces were performed under the same conditions using AZtec v6.0 to maximize spatial resolution while limiting beam damage[1]. Although surface roughness renders the data semi-quantitative, the uniform acquisition parameters ensure that relative elemental differences faithfully represent true surface composition[1]. Prior to post-mortem EDS on fatigued anodes from cycled pouch cells, residual electrolyte is removed by immersion in excess DMC[1]. Aside from graphite's dominant carbon signal, oxygen quantification provides insights into SEI formation[1]. Al_2O_3 and SiO_2 separator fragments adhering to the anode even after DMC wash contribute to the oxygen signal and are subtracted to yield the true SEI oxygen content[1]. Fluorine and phosphorus derive from the $LiPF_6$ salt, and sodium originates from the CMC binder in the aqueous-processed anode[1]. If Ni, Mn, and Co are undetected on the anode, should any cathode-derived transition metals be present at all, then the actual amount present must be below the EDS detection threshold (<0.1 At.%)[1].

4 Results and Discussion

4.1 Slurry gelation in additive-free samples

This chapter investigates gelation in additive-free slurries using different binders, contrasting the rheology of a PVdF homopolymer slurry with that of a PVdF homopolymer modified with polar backbone functionalities. This investigation focuses on the influence of these ultra-high molecular weight binders on defining the upper boundary of the solid content (SC) processability window. Here, the upper limit of processability is understood as the maximum SC suitable for electrode casting without compromising the roll-to-roll process efficiency due to premature onset of gelation. Subsequently, thick electrodes produced with homopolymer PVdF-based slurries are assessed by examining cycling performance across varying porosities. This approach identifies a reference porosity of 33%, which is subsequently maintained when fabricating thinner electrodes of the same composition and mixing method (Mixing 1^{ST}). This consistent porosity allows for accurate performance comparisons by avoiding ion diffusion limitations that could arise from excessive calendering.

4.1.1 Gelation behavior with PVdF type A and B

When PVdF Type A is employed to create an additive-free A slurry (as shown in **Table 1**) with 70 wt.% SC using Mixing 1^{ST}, gelation occurs rapidly, with a gel forming within minutes after mixing. To enable the coating process, a dissolver mixing step is necessary to re-fluidize the slurry just before casting. However, during the casting process, after approximately manufacturing one meter of electrode length, the slurry reverts to a gel-like state. This swift gelation impedes continuous electrode processing, as depicted in the **Figure 9.**

Figure 9. Image of a coated NMC622 cathode on an aluminum current collector, taken immediately after casting and drying, illustrating variations in coating quality along the coating direction. On the left side, corresponding to the initial stages of coating, a uniform and defect-free layer is observed, attributed to favorable slurry rheology. In contrast, on the right side, significant coating defects become evident, resulting from rapid slurry gelation that hindered continuous processability during the coating of the additive-free A 70 wt.% SC cathode slurry.

Table 4. Rheological profiles of additive-free NMP slurries (70.0 wt.% SC) containing NMC622, carbon black, and either PVdF Type A (additive-free A) or PVdF Type B (additive-free B sample), recorded immediately after mixing and after three days' storage.

Slurry sample	η in Pa*s at $50s^{-1}$ - 0h	η in Pa*s at $50s^{-1}$ - 3days	E_{coh} in mJ/m^3 - 0h	E_{coh} in mJ/m^3 - 3days	Yield stress in Pa - 0h	Yield stress in Pa - 3days
additive-free A	0.5	4.1	40.6	97.6	4	156
additive-free B	0.8	0.2	-	-	-	-

Under identical manufacturing conditions, PVdF Type B presents an opposite downside, leading to an unstable formulation prone to AM sedimentation, as demonstrated in the rheology study henceforth. Despite initially having a low viscosity value of 0.5 Pa*s after mixing, there is a notable surge in viscosity related to gelation of +688% observed in the flow curves measured after 3 days of slurry resting time (refer to **Figure 10B**). Amplitude sweeps conducted immediately after slurry mixing for the additive-free A sample (depicted in **Figure 11A**) already reveal a predominant gel-like consistency. Indeed, the gel network, which is corresponding to G´ > G'' in the LVR region[1], has a non-negligible cohesion energy of E_{coh} =40.6 mJ/m^3 already upon mixing (calculated with eq. (1)). Upon storage for 3 days, the gel strength notably increases to E_{coh} =97.6 mJ/m^3 for the additive-free A sample (**Figure 11B**). Conversely, when PVdF Type B is utilized to produce the additive-free B slurry with the same composition and Mixing 1^{ST} (as listed in **Table 1**), and with an identical 70.0 wt.% SC, sedimentation effects become apparent after 3 days of slurry storage.

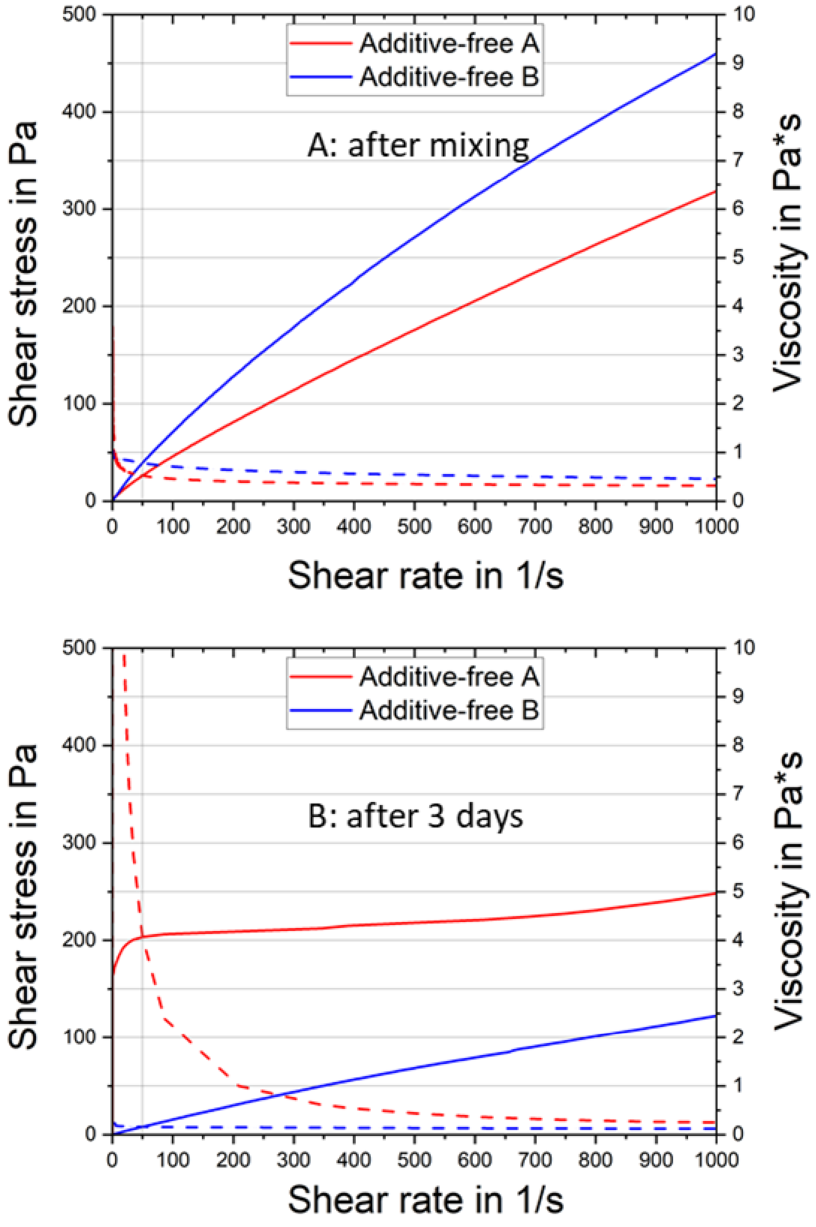

Figure 10. A: Flow (solid) and viscosity (dashed) profiles immediately after mixing NMP slurries (70 wt.% SC) of NMC622, high-Mw PVdF Type A (red) or Type B (blue), and carbon black. B: The same flow and viscosity measurements after three days' storage[1].

Although the additive-free B sample initially exhibits a higher viscosity of 0.8 Pa*s compared to the additive-free A sample, it exhibits a notable viscosity drop of -79%, as observable in the flow curves measured after 3 days of storage. This contrasts with the viscosity surge observed for the additive-free A sample after storage, as depicted in **Figure 10B** and outlined in **Table 4**.

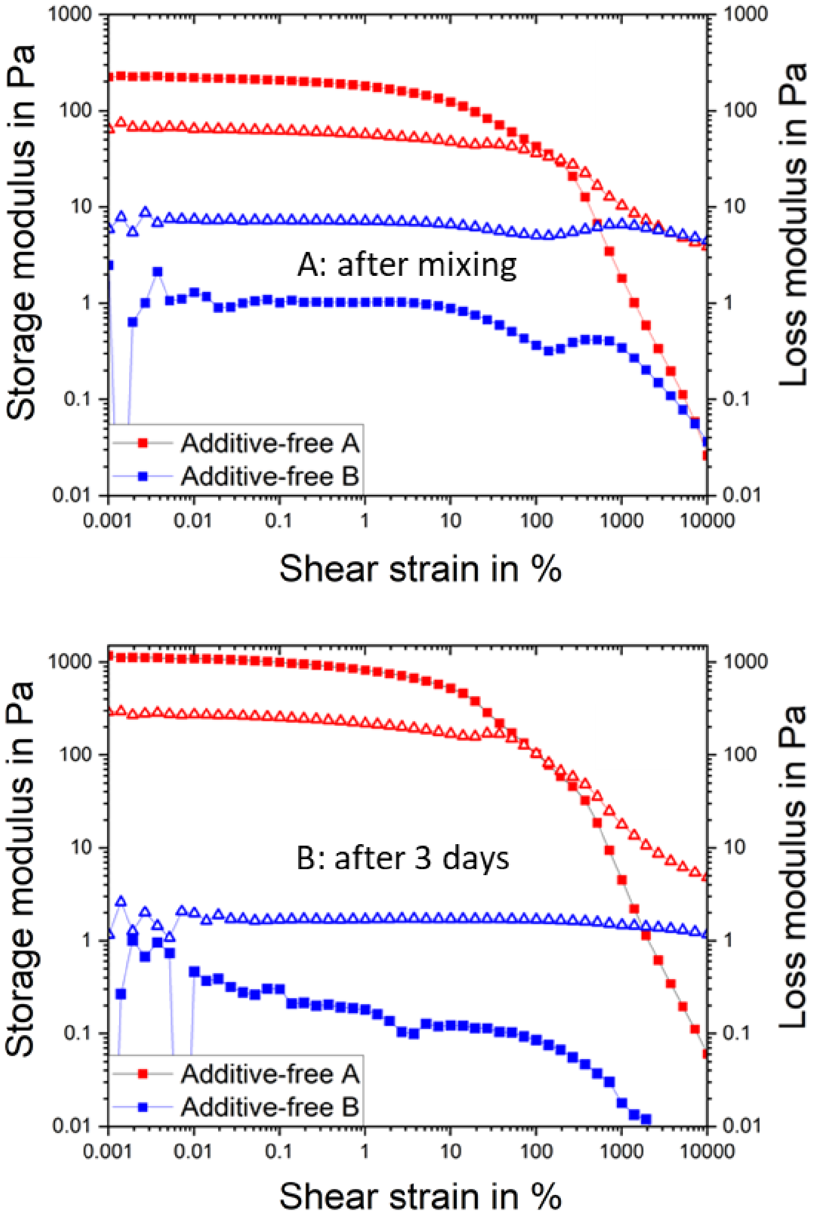

Figure 11. A: Amplitude sweeps (G’ ■, G’’ ▲) at ω=10s^{-1} immediately after mixing NMP-based slurries encompassing NMC622 powder, high Mw PVdF, carbon black for the additive-free A sample with PVdF Type A at 70 wt.% SC (red) and for the additive-free B sample with PVdF Type B at 70 wt.% SC (blue). B: The same amplitude sweeps recorded after three days of storage[1].

In the amplitude sweeps conducted for the additive-free B sample immediately after slurry mixing (**Figure 11A**), the dominance of the loss modulus (G”) over the storage modulus (G’) throughout the shear strain spectrum indicates predominantly viscous (liquid) behavior[1]. Even after 3 days of slurry storage, the absence of a robust gel network in the additive-free B sample is evident, with a predominantly liquid-like character still observable in the corresponding amplitude sweeps measurements (**Figure 11B**).

This lack of a strong gel network allows for the sedimentation process of the AM particles to occur, which correlates with the aforementioned viscosity drop observed in the corresponding flow curves.

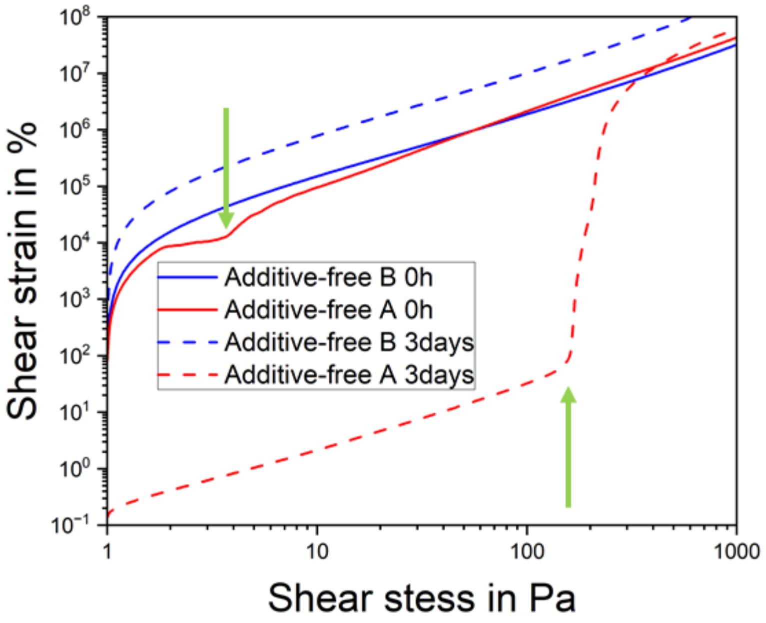

Figure 12. Deformation curves of NMP slurries with NMC622 powder, high Mw PVdF, carbon black for the additive-free A sample with PVdF Type A at 70 wt.% SC (red) and for the additive-free B sample with PVdF Type B at 70 wt.% SC (blue). Measurements taken immediately after mixing and after three days of slurry storage are shown as solid and dashed lines, respectively. Arrows indicate the yield point of the slurries, where applicable.

The flow curve-derived yield point, albeit not being quantitatively correlated with the dynamic yield point detected in the amplitude sweep measurements[3], can deliver an additional evaluation of the viscoelastic slurry system's response to a mechanical input. The yield point is more accurately identified in deformation curves[3], where it typically appears as a broad transition kink separating the elastically deformed region from plastic flow. By defining the onset of this transition as the yield point, the corresponding stress can be termed the yield stress, which is the minimum stress required for the slurry to flow[141]. Consistent with the predominantly liquid-like behavior observed in amplitude sweep measurements, the additive-free B sample does not exhibit a yield point, either immediately after mixing or after three days of storage, as depicted in **Figure 12**. Conversely, as detailed in **Table 4** and shown in **Figure 12**, the additive-free A formulation demonstrates a yield stress of around 4 Pa immediately after mixing, which increases significantly to 156 Pa after three days of storage, reflecting the slurry's predominant gel-like consistency.

In order to achieve a stable formulation and prevent sedimentation of active material with PVdF Type B, an additive-free B II slurry is produced with the same composition and Mixing 1^{ST} (as outlined in **Table 1**), but with a higher 75.5wt.% SC. Under these conditions, where gelation consequences are anticipated to be more severe, the slurry with binder A results in a strong gel immediately after mixing, whose extremely high viscosity impedes any processing or any rheological characterization. Consequently, a direct comparison between PVdF Type B and PVdF Type A is omitted, and only the additive-free B II slurry is examined at the elevated 75.5wt.% SC. The additive-free B II slurry exhibits a moderate viscosity of 1.6 Pa*s soon after mixing and demonstrates a notable viscosity increase of +40% in the flow curves measured after 3 days of storage (as depicted in Figure 13A and detailed in Table 5).

Table 5. Rheological profiles of NMP slurries containing NMC622, carbon black, and PVdF binder for the additive-free B II sample with PVdF Type B at 75.5 wt.% SC, recorded immediately after mixing and after three days' storage.

Slurry sample	η in Pa*s at $50s^{-1}$ - 0h	η in Pa*s at $50s^{-1}$ - 3days	E_{coh} in mJ/m³ - 0h	E_{coh} in mJ/m³ - 3days	Yield stress in Pa - 0h	Yield stress in Pa - 3days
additive-free B II	1.6	2.2	-	6.5	-	8

Immediately after mixing, amplitude sweeps of the additive-free B II slurry (light green curve in **Figure 13B**) exhibit liquid-like behaviour, with G″ remaining higher than G′ throughout the entire shear-strain range. However, after 72 h of storage, gelation-induced phenomena develop, with the additive-free B II sample forming a strong gel network, as indicated by G´ > G'' in the LVR region of the amplitude sweeps measurements (green curve in **Figure 13B**). By calculating the energy of the aggregated state using eq. (1), a notable cohesion energy of E_{coh} =6.5 mJ/m³ vividly illustrates slurry gelation with PVdF Type B at the elevated 75.5wt.% SC.

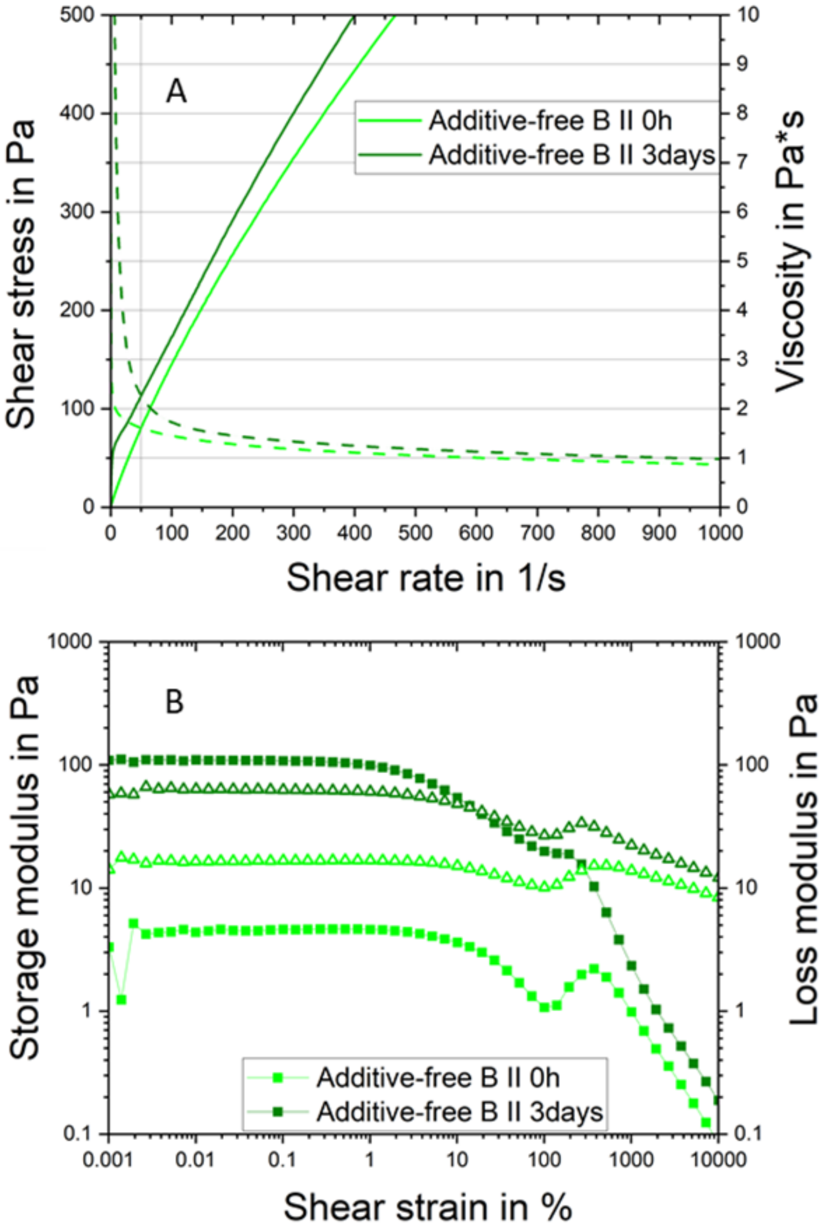

Figure 13. A: Flow (solid) and viscosity (dashed) profiles of the additive-free B II slurry encompassing NMC622 powder, high-Mw PVdF Type B, carbon black at 75.5 wt.% SC immediately after mixing (light green) and after three days' storage (green)[1]. B: Corresponding amplitude sweeps (G' ■, G'' ▲) at $\omega=10s^{-1}$ for the same slurry at the two time points, e.g. after mixing (light green) and after storage (green) [1].

Comparison between PVdF Type B and PVdF Type A at the same SC reveals that emulsion polymerized PVdF Type A triggers rapid slurry gelation, whereas suspension polymerized PVdF Type B binder does not induce sufficient gelation, leading to sedimentation of the active material particles. This difference in rheological behavior at the same composition and SC for emulsion polymerized PVdF-based slurries (additive-free A) compared to slurries based on suspension polymerized binders (additive-free B) aligns with findings from previous literature[142].

Furthermore, the study conducted at the higher 75.5wt.% SC demonstrates that also suspension polymerized binders (PVdF Type B) may trigger slurry gelation after storage, albeit having a different edge of the processability window, when compared to emulsion polymerized PVdF binders. In conclusion, when investigating the SC boundaries of the processability window with both binders, issues with handling and compromised processability due to slurry gelation emerge, either sooner or later, for both types of PVdF. While direct comparisons across different solid contents provide only qualitative insights, an analysis between PVdF Type A at 70.0 wt.% SC and PVdF Type B at 75.5wt.% SC shows that PVdF Type B stores less elastic energy, thus providing a less robust gel network, which may allow for easier processing at higher solid contents but possibly compromising the segregation resistance potential of the formulation. Research suggests[143,144,145] that the amorphous phase largely determines a slurry's storage modulus owing to the combined effects of macromolecular chain mobility and polymer entanglements, thus creating a polymer network that stores and releases elastic energy, wherein the crystalline regions are functioning as anchoring points that limit the overall elastic extension of the deformable amorphous regions. Consequently, the origin of the robust gel-forming ability of PVdF Type A is not trivial, and it may stem from a complex interplay of many macromolecular characteristics, that may include, greater chain branching, reduced or imperfect crystallinity, a higher proportion of amorphous regions, broader molecular weight distributions, or presence of higher molecular weight polymeric fractions, when compared to PVdF Type B. Together, these characteristics enhance its structural strength and energy-storing capacity, key for formulating stable and resilient colloidal gels, but they may lower the maximum SC applicable for convenient slurry processability (**Figure 9**).

4.1.2 Electrochemical analysis on compaction effects in additive-free samples

A cathode of more than 100 µm thickness was produced in order to assess the feasibility of thick electrodes using a low additives amount. Mixing 1^{ST} is used to produce a slurry at 70 wt.% SC following the composition of the additive-free A T formulation (**Table 1**), wherein “A” refers to the binder type, while “T” designates the thick electrode configuration. Cell manufacturing data and specifications for the resulting additive-free A T coating are reported in **Table 3** and **Table 6,** respectively.

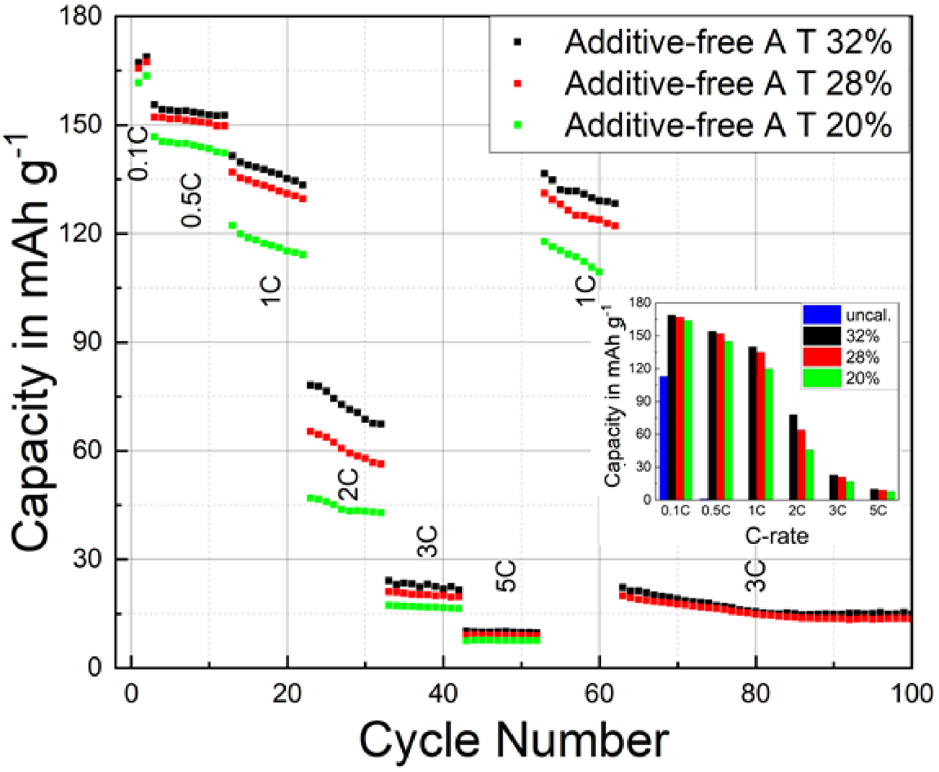

Figure 14. Rate capability of Li-NMC half-cells with the additive-free A T cathode at different porosities. A bar chart of the discharge capacity at the second cycle for each C-rate is reported as insert. The final green cycling points are missing due to cell failure. The control experiment, i.e. a repetition experiment demonstrating the reproducibility of the C-rate performance in Li-NMC half cells, is reported in **Figure S-1**.

Thick electrodes face significant ion diffusion limitations, especially at high current densities, due to the longer distance ions must travel to reach active sites near the current collector. This creates an "active layer" close to the separator that effectively participates in the electrochemical reactions, while inner layers contribute minimally, a phenomenon that limits the effective capacity at high C-rates in thick electrodes[146,147]. The reduced capacity at high C-rates, which worsens as electrode porosity decreases, results from this superficial electrochemical active layer constraining the total available capacity, as illustrated in **Figure 14**. Specifically, C-rate testing in **Figure 14** shows a neat capacity decline above 1C for all the different calendering states with 20% porosity being the worse at every C rate. The uncalendered cathode, with a porosity of 43%, failed to function properly due to the exceedingly low concentration of carbon black per unit volume. The negative slope of the capacity observed across all C-rates can be therefore attributed to anisotropic effects associated with the substantial electrode thickness. Over time, this layer near the separator interface experiences accelerated degradation and drives long-term capacity fading. This nonisotropic effect, where the uppermost layers closest to the separator are the most active at high C-rates, is also linked to uneven wear during extended cycling. Specifically, the electrochemically active regions near the separator undergo intense wear, leading to structural deterioration such as ion rearrangement and cation mixing, further impairing long-term performance[146,147]. Hence, although not evident in the here presented C-rate results, prolonged cycling of the evaluated cells is expected to lead to accelerated degradation of the electrode layers in closer proximity to the separator, as described by previous studies[148,149]. Interestingly, sluggish ion diffusion within thick electrodes is the main factor underlying the observed low capacity retention at high C-rates and the accelerated degradation over extended cycling, as documented in the literature[146–149]. Due to the restricted mass transport within thick electrodes, the potential for preferential reactions in specific cathode regions has been identified as of crucial concern. Electrode regions in proximity to the separator tend to reach higher "states of charge/discharge" faster than less accessible areas in the bulk or bottom of the electrode, where a higher diffusion hindrance slows down the electrochemical process (e.g. longer diffusion pathways for charge transfer to happen)[150]. As a result, sluggish diffusion within thick electrodes restricts the electrochemical activity of otherwise available active material.

Table 6. Summary of mass loading, thickness, porosity, resistance, and adhesion for tested cathodes, evaluated before and after calendering and, if applicable, after heating treatment[1].

Electrode sample	Mass loading in mg/cm^2	Thickness in µm	Porosity in %	Resistance in Ω - cal	Adhesion in N/m - uncal	Adhesion in N/m - cal
additive-free A T	27.7	94.8	32	96	34	33
	27.7	89.6	28	96	34	28.5
	27.7	80.3	20	42	34	28.8

Actually, the non-uniform degradation of nickel-rich materials within the electrode owing to the excessive utilization of active materials on the surface side is also correlated to a significant non-uniform potential distribution during the cycling process[149]. In fact, an investigation[149] have proposed that the heterogeneous degradation in thick NCM electrodes may involve severe structural deterioration, marked by significant rearrangement of Li^+ and Ni^{2+} ions, that can induce both intergranular and intragranular cracking, predominantly in the upper regions of the electrode facing the separator. In contrast, degradation in the lower part of the electrode (facing the current collector) is less severe and involves fewer Li^+/Ni^{2+} interactions. Ni^{2+} ions play a significant role in electrode failure by inducing a high degree of cationic disordering with an increased presence of oxygen vacancies at the atomic level. This process ultimately results in severe phase transitions at the NMC particle level, generating numerous cracks at the electrode level, and accompanied by the release of gas at the full-cell level. Additionally, Ni^{2+} ions are known for adversely affecting both the CEI and SEI structures[149].

With the failure mechanisms of thick NCM electrodes elucidated, the focus is now shifted to the pristine electrode morphology by examining SEM images of fresh (non-cycled) electrodes.

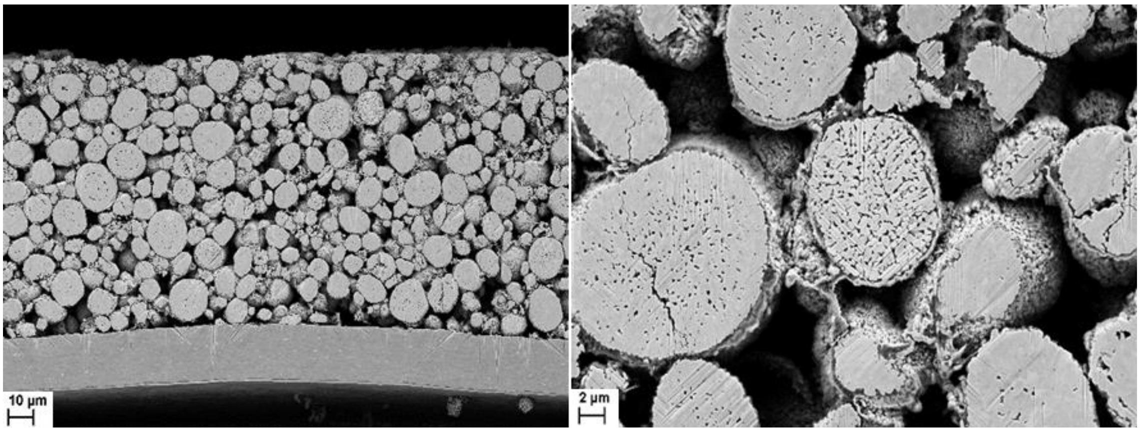

Figure 15. SEM cross section of the additive-free A T electrode compressed to 32% porosity.

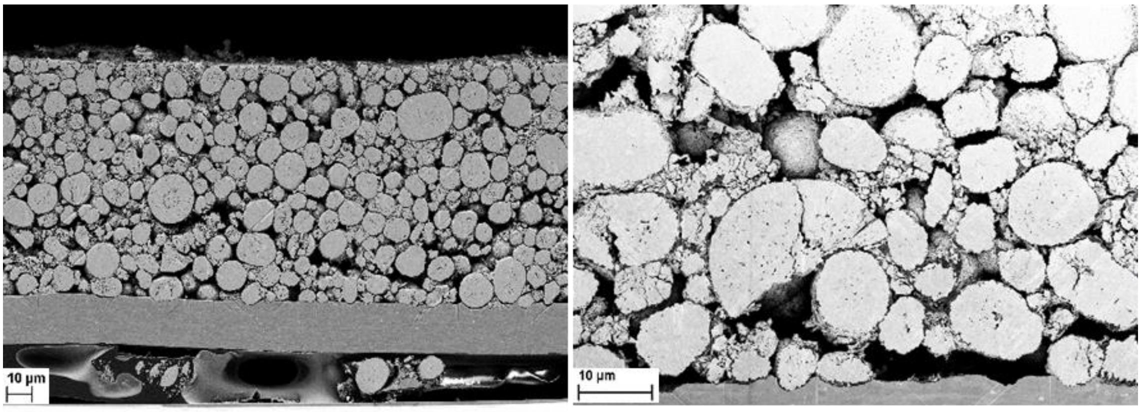

Figure 16. SEM cross section of the additive-free A T electrode compressed to 20% porosity.

From SEM images in **Figure 15**, we see CB-PVdF domains providing interparticle bridging and adhesion to the current collector with only a tiny fraction of particles displaying cracking due to compression to 32% porosity. In **Figure 16**, we see the effect of extreme densification to 20% porosity, where a non-negligible high number of completely cracked particles is apparent. Specifically, calendering to 20% porosity induces severe cracking and completely wrecked particles in the electrode’s upper regions, whereas interparticle friction in the lower regions dissipates stress and mitigates crack formation. Moreover, clearly detectable is indentation of the Al current collector by AM particles and an uneven distribution of the residual porosity.

4.2 Modification of gelation by slurry additives

The second chapter focuses on a chemical approach to tune rheology when processing high SC in NMC662 slurries employing an homopolymer PVdF-binder (PVdF Type A). H_3PO_4 and three well established Li-salts have been investigated as different slurry additives in order to shift the processability window to the higher SCs. For the first time the mechanism through which slurry additives can actively control slurry gelation is elucidated. The electrochemical performance of electrodes containing these slurry additives are scrutinized, by focusing on the high C-rate and long-term cycling behavior. To delve deeper into the electrochemical outcomes when employing lithium salts, differential capacity dQ/dV curves are analyzed and recorded throughout high C-rate and long-cycling tests. Furthermore, to elucidate variations in electrode processes, electrochemical impedance spectroscopy (EIS) was employed to assess how slurry additives influence electrochemical performance and the electrode-electrolyte interface unique to each varied cathode formulation[1]. For the best class of slurry additives EIS measurements are conducted in an initial set of experiments, involving fresh cathodes. Subsequently, measurements were replicated on fatigued cathodes extracted from pouch cells after 1000 cycles to investigate capacity-fading mechanisms[1].

4.2.1 Role of H_3PO_4 in slurry gelation

A breakthrough in mitigating gelation in high solid content (SC) slurries was achieved by incorporating H_3PO_4 as an additive. This method enabled the preparation of a PVdF Type A-based slurry with 75.5 wt.% SC, completely preventing gelation immediately after initial mixing (Mixing 1^{ST}). Attempts to create a similar slurry without additives at 75.5 wt.% SC resulted in a strongly gelled slurry with extremely high viscosity, rendering rheological analysis unfeasible. Consequently, additive-free A slurry with a reduced SC of 70 wt.% was used as the reference sample. This SC represents the maximum achievable with PVdF Type A and Mixing 1^{ST} without additives. While the reference sample exhibited a low viscosity of 0.5 Pa*s soon after mixing, its rapid gelation led to artifacts during electrode casting, as depicted in **Figure 9**. A rheological study was conducted to determine the minimum effective concentration of H_3PO_4 needed to suppress gelation, with additive concentrations ranging from 8.0 $wt.\%_{PVdF}$ to 4.3 $wt.\%_{PVdF}$ (where $wt.\%_{PVdF}$ indicates the weight percentage of H_3PO_4 relative to the PVdF in the formulation). **Table 1** summarizes the composition of all samples, while **Table 7** includes detailed rheological data.

Viscosity measurements were reported at a shear rate of 50 s^{-1}, which aligns with the operating range of the coating equipment (represented by a grey vertical reference line in the flow curve plots). **Figure 17A** compares initial viscosity values (immediately after mixing) for H_3PO_4-containing samples and the additive-free A sample. Minimal differences were observed in viscosity for the 8.0 wt.%$_{PVdF}$ and 6.1 wt.%$_{PVdF}$ samples, while the 4.3 wt.%$_{PVdF}$ sample showed a marginally elevated viscosity of 2.6 Pa*s due to rapid gelation. The additive-free A slurry exhibited the lowest viscosity due to its lower SC. **Figure 17B** displays the flow curves of all samples after 3 days of storage, revealing significant viscosity increases across all shear rates compared to initial measurements. The development of yield points with extended vertical branches at low shear rates indicated the formation of a gel-like structure.

Table 7. Rheological profiles for NMP slurries containing NMC622 powder, PVdF Type A binder, and carbon black, measured both shortly after preparation and following a storage period of 3 days.

Slurry sample	η in Pa*s at 50s^{-1} - 0h	η in Pa*s at 50s^{-1} - 3days	E_{coh} in mJ/m^3 - 0h	E_{coh} in mJ/m^3 - 3days	Yield stress in Pa - 0h	Yield stress in Pa - 3days
additive-free A	0.5	4.1	40.6	97.6	4	156
H_3PO_4 4.3wt.%$_{PVdF}$	2.6	gel*	4.8	gel*	24	gel*
H_3PO_4 6.1wt.%$_{PVdF}$	2.2	6.8	-	54.9	-	156
H_3PO_4 8wt.%$_{PVdF}$	2.3	5.8	-	14.5	-	119

*Viscosity exceeded the rheometer's measurement range due to extensive gelation, precluding any rheological analysis.

After 3 days, viscosity increased substantially for the 8.0 wt.%$_{PVdF}$ and 6.1 wt.%$_{PVdF}$ samples, by +152% and +209%, respectively. In contrast, the 4.3 wt.%$_{PVdF}$ sample formed a highly viscous gel that could not be analyzed rheologically. The additive-free A slurry experienced the most extreme gelation, with a +688% viscosity surge, despite its moderate SC.

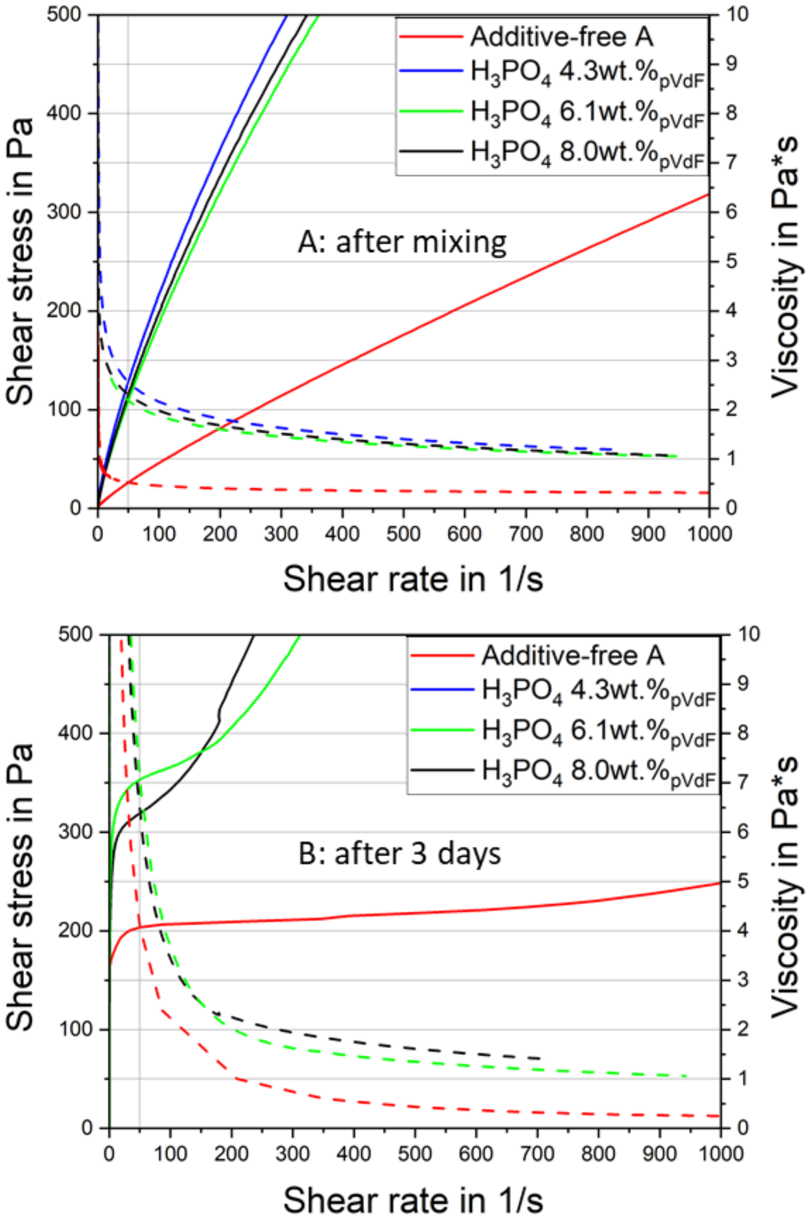

Figure 17. A: Flow (solid) and viscosity (dashed) profiles immediately after mixing NMP slurries encompassing NMC622 powder, high-Mw PVdF, carbon black at SC 75.5 wt.% for the H_3PO_4 4.3 wt.%$_{PVdF}$ (blue), H_3PO_4 6.1 wt.%$_{PVdF}$ (green), H_3PO_4 8.0 wt.%$_{PVdF}$ (black) samples and at SC 70.0 wt.% for the additive-free A sample (red). B: The same flow and viscosity measurements after three days' storage; the H_3PO_4 4.3 wt.%$_{PVdF}$ sample (absent blue curve) underwent severe gelation and viscosity exceeded the rheometer's measurement range, preventing characterization[1].

Amplitude sweeps were performed immediately after mixing for all H_3PO_4-containing samples and the additive-free reference (**Figure 18A**).

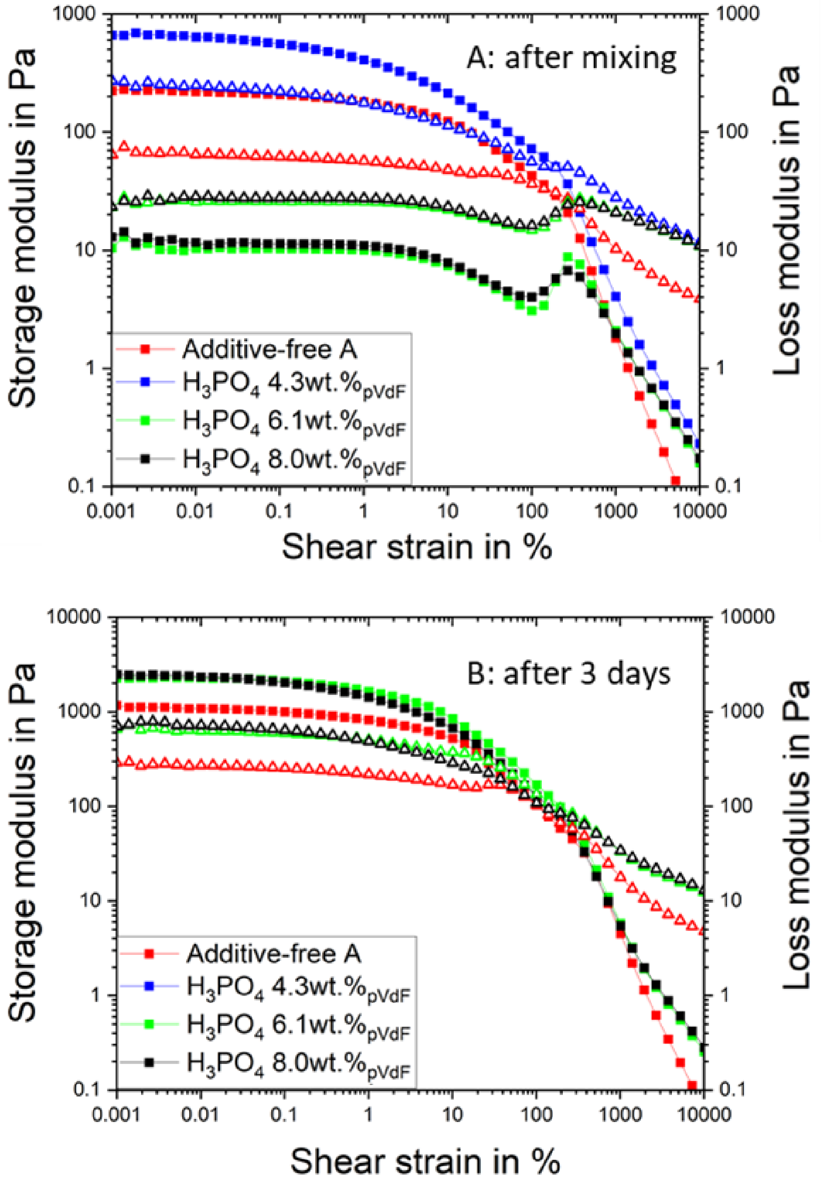

Figure 18. A: Amplitude sweeps (G′ ■, G′′ ▲) at $\omega=10s^{-1}$ immediately after mixing NMP-based slurries encompassing NMC622 powder, high Mw PVdF Type A, carbon black at SC 75.5 wt.% for the H_3PO_4 4.3 wt.%$_{PVdF}$ (blue), H_3PO_4 6.1 wt.%$_{PVdF}$ (green), H_3PO_4 8.0 wt.%$_{PVdF}$ (black) samples and at SC 70.0 for the additive-free A sample (red). B: The same amplitude sweeps recorded after three days of storage; the H_3PO_4 4.3 wt.%$_{PVdF}$ sample (absent blue curve) underwent severe gelation and viscosity exceeded the rheometer's measurement range, preventing characterization[1].

When the additive concentration was 6.1 wt.%$_{PVdF}$ or higher, the slurries exhibited predominantly liquid-like behavior, with the loss modulus (G″) exceeding the storage modulus (G′) across the shear strain range. Conversely, the 4.3 wt.%$_{PVdF}$ and additive-free A samples demonstrated gel-like behavior, characterized by G′ dominating over G″ at low shear strains.

The gel network in these two samples showed high cohesion energy (E_{coh}), calculated using Equation (1), with values of 4.8 mJ/m^3 and 40.6 mJ/m^3 for the 4.3 wt.%$_{PVdF}$ and additive-free A samples, respectively. Despite its lower G′, the additive-free A slurry displayed higher E_{coh} due to its broader linear viscoelastic region (LVR), which suggests a less rigid but more elastic gel. Amplitude sweeps conducted after 3 days of storage (**Figure 18B**) confirmed the formation of gel networks in all samples, as indicated by G′ exceeding G″ in the low shear strain region. Notably, the curve for the 4.3 wt.%$_{PVdF}$ sample is absent due to its extreme gelation and excessively high viscosity. Analysis of cohesive energy revealed a descending trend with storage: additive-free A > H_3PO_4 6.1 wt.%$_{PVdF}$ > H_3PO_4 8.0 wt.%$_{PVdF}$ (**Table 7**). The highest cohesive energy in the additive-free A and H_3PO_4 6.1 wt.%$_{PVdF}$ samples was associated with their extended LVR regions[1]. Interestingly, the 8.0 wt.%$_{PVdF}$ sample, despite similar G′ and G″ magnitudes to the 6.1 wt.%$_{PVdF}$ sample, exhibited a narrower LVR region.

4.2.2 Effect of Li salts on slurry rheology

An additional advance in addressing high solid content (SC) slurries gelation challenges in high SC slurries has been the strategic introduction of a second category of additive: organic fluorinated lithium salts. These compounds, owing to their unique rheological effects, have shown significant potential in modifying slurry properties to delay gelation onset while maintaining desirable flow characteristics during processing of a PVdF Type A-based slurry at 75.5 wt.% SC. This dual functionality of enhanced processability and stability positions fluorinated Li-salts as a promising solution in the optimization of high SC slurry formulations produced with Mixing 1ST, further contributing to the development of advanced electrode manufacturing techniques. Because the additive-free 75.5 wt.% SC slurry exhibited excessively high viscosity, coating was unachievable and rheological characterization was impossible with the available equipment. However, a coating was achieved with an additive-free A cathode sample using a less viscous 70.0 wt.% SC slurry, though only the initial portion of the coating yielded high-quality electrodes[1]. The feasibility of continuous casting with the 70.0 wt.% SC slurry was compromised by its swift gelation (**Figure 9**). Li-salts were incorporated in minimal amounts, expressed in wt.%$_{PVdF}$, representing the additive's weight relative to PVdF in the slurry composition. The rheological properties of the additive-free A 70.0 wt.% SC slurry are presented in **Table 8** for comparison[1].

Initially, LiODFB, LiTFSI, and LiTFA were evaluated as cathode slurry stabilizers at 2 wt.%$_{PVdF}$. Flow curves provide insights into slurry stability by indicating the yield point and reflecting changes in viscosity during storage, which reveal tendencies like sedimentation[1]. Steady-state viscosity measurements were conducted at a shear rate of 50 s^{-1}, a reference point well-suited for the coating device, marked by the gray vertical line in flow curve graphs[1]. Flow curves measured immediately post-mixing (**Figure 19A**) for 2 wt.%$_{PVdF}$ Li-salt slurries showed minimal viscosity variations within measurement uncertainty. In **Figure 19B**, post-storage flow curves for the same slurries reveal viscosity increases across all shear rates and more pronounced yield points with extended vertical slopes at low shear rates, signifying gel formation. After 3 days, LiTFA exhibited the lowest viscosity increase (+55%, green curve), whereas LiODFB and LiTFSI showed significant rises of +125% and +155%, respectively (**Table 8**). LiTFA at 2 wt.%$_{PVdF}$ demonstrated superior gelation delay, although also LiODFB and LiTFSI facilitated a smooth coating process due to the slurry's flowable nature post-mixing[1]. Oscillatory shear measurements in the linear viscoelastic range (LVR) provided more precise slurry characterization.

Table 8. Rheological behavior of NMP slurries containing NMC622, PVdF Type A, and carbon black, measured immediately after mixing and after 72 h of storage.[1]

Slurry sample	η in Pa*s at 50s^{-1} - 0h	η in Pa*s at 50s^{-1} - 3days	E_{coh} in mJ/m^3 - 0h	E_{coh} in mJ/m^3 - 3days	Yield stress in Pa - 0h	Yield stress in Pa - 3days
additive-free A	0.52	4.1	40.6	97.6	4	156
LiTFA 0.5wt.%$_{PVdF}$	3.5	12.4	25.0	104.7	-	237
LiTFA 1wt.%$_{PVdF}$	2.9	6.9	-	35.1	-	103
LiTFA 2wt.%$_{PVdF}$	2.5	3.9	-	27.4	-	45
LiODFB 2wt.%$_{PVdF}$	2.7	6.0	-	39.0	-	90
LiTFSI 2wt.%$_{PVdF}$	2.7	7.0	-	42.2	-	127
LiTFA 8wt.%$_{PVdF}$	2.1	2.7	-	15.8	-	11

* The gel's exceedingly high viscosity prevented any rheological characterization with the employed instrument.

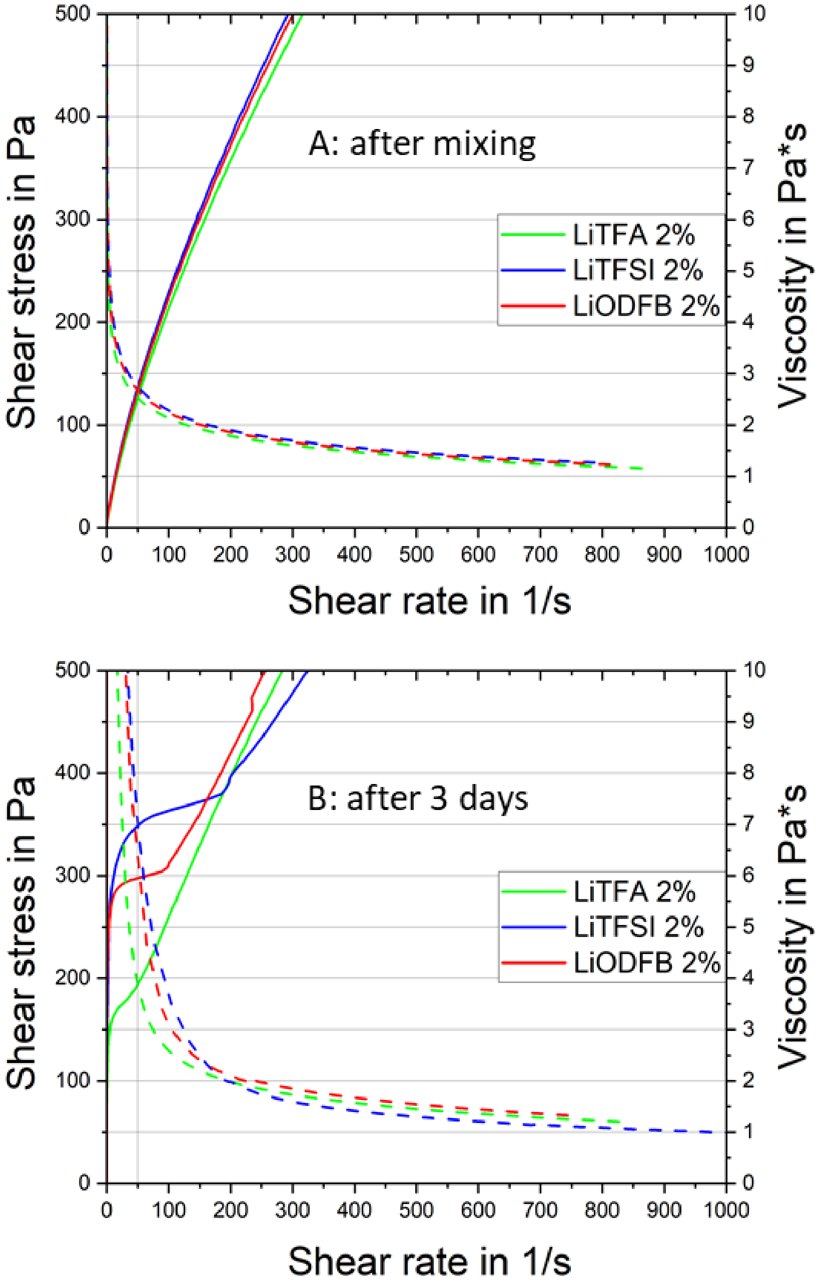

Figure 19. A: Flow (solid) and viscosity (dashed) profiles immediately after mixing NMP slurries encompassing NMC622 powder, high-Mw PVdF Type A, carbon black at SC 75.5 wt.% for 2 wt.%$_{\mathrm{PVdF}}$ LiTFA (green), 2 wt.%$_{\mathrm{PVdF}}$ LiODFB (red) and 2 wt.%$_{\mathrm{PVdF}}$ LiTFSI (blue). B: The same flow and viscosity measurements after three days' storage. Adapted from F. Colombo et al.[1] with permission from the Royal Society of Chemistry.

Amplitude sweeps revealed a notable increase in cohesive energy when gelation occurred (e.g., in high SC slurries). Immediately post-mixing (**Figure 20A**), all slurries exhibited a predominantly liquid-like behavior, with LiTFA being the most flowable (green curve).

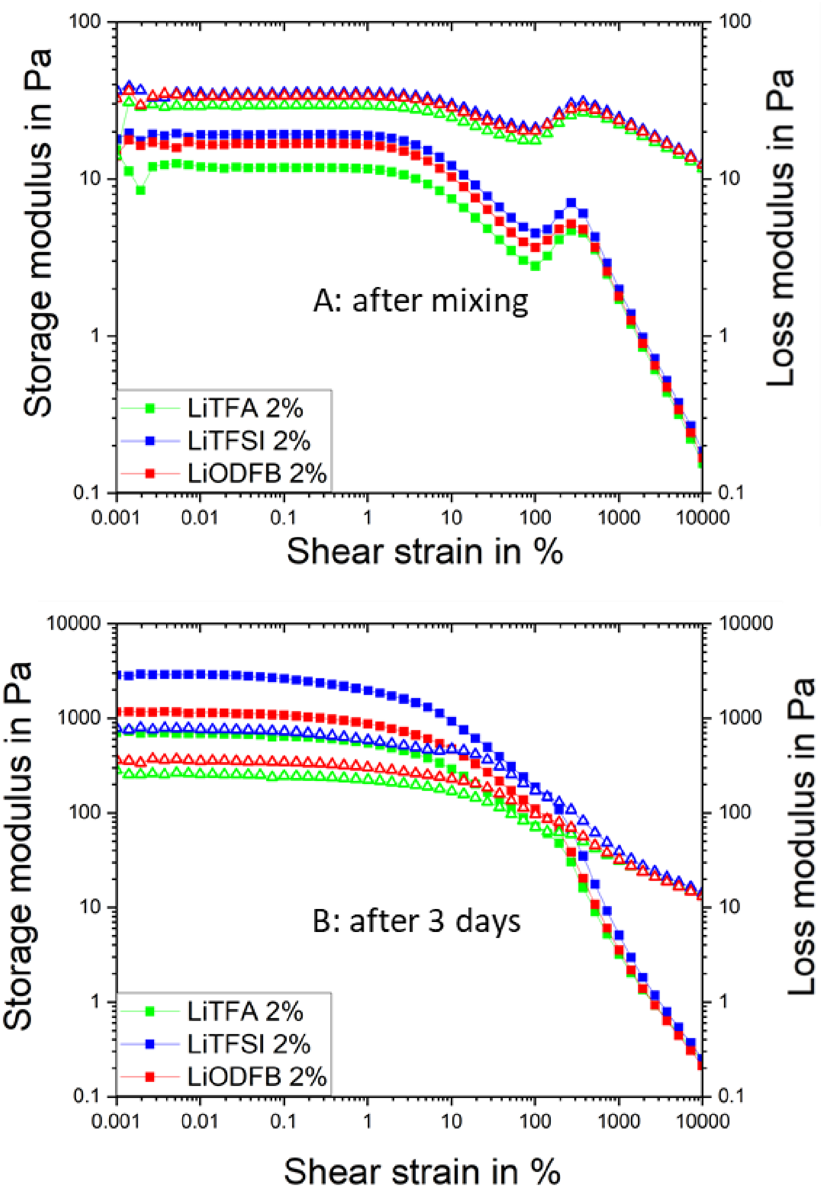

Figure 20. A: Amplitude sweeps (G' ■, G'' ▲) at ω=10s^{-1} immediately after mixing NMP-based slurries at SC 75.5 wt.% with NMC622 powder, high Mw PVdF Type A, carbon black and 2 wt.%$_{PVdF}$ LiTFA (green), 2 wt.%$_{PVdF}$ LiODFB (red) and 2 wt.%$_{PVdF}$ LiTFSI (blue). B: The same amplitude sweeps recorded after three days of storage. Adapted from F. Colombo et al.[1] with permission from the Royal Society of Chemistry.

Post-storage amplitude sweeps (**Figure 20B**) displayed G' > G'' in the LVR region for all samples, confirming dominant gelation. The highest gel strength (E_{coh} = 42.2 mJ/m^3) was observed for LiTFSI (blue curve), while LiODFB (E_{coh} = 39.0 mJ/m^3, red curve) and LiTFA (E_{coh} = 27.4 mJ/m^3, green curve) exhibited weaker gel states[1]. All slurries maintained a liquid-like character post-mixing, with gelation delayed until after storage, highlighting LiTFA as the most effective and LiTFSI as the least effective additive in controlling gelation.

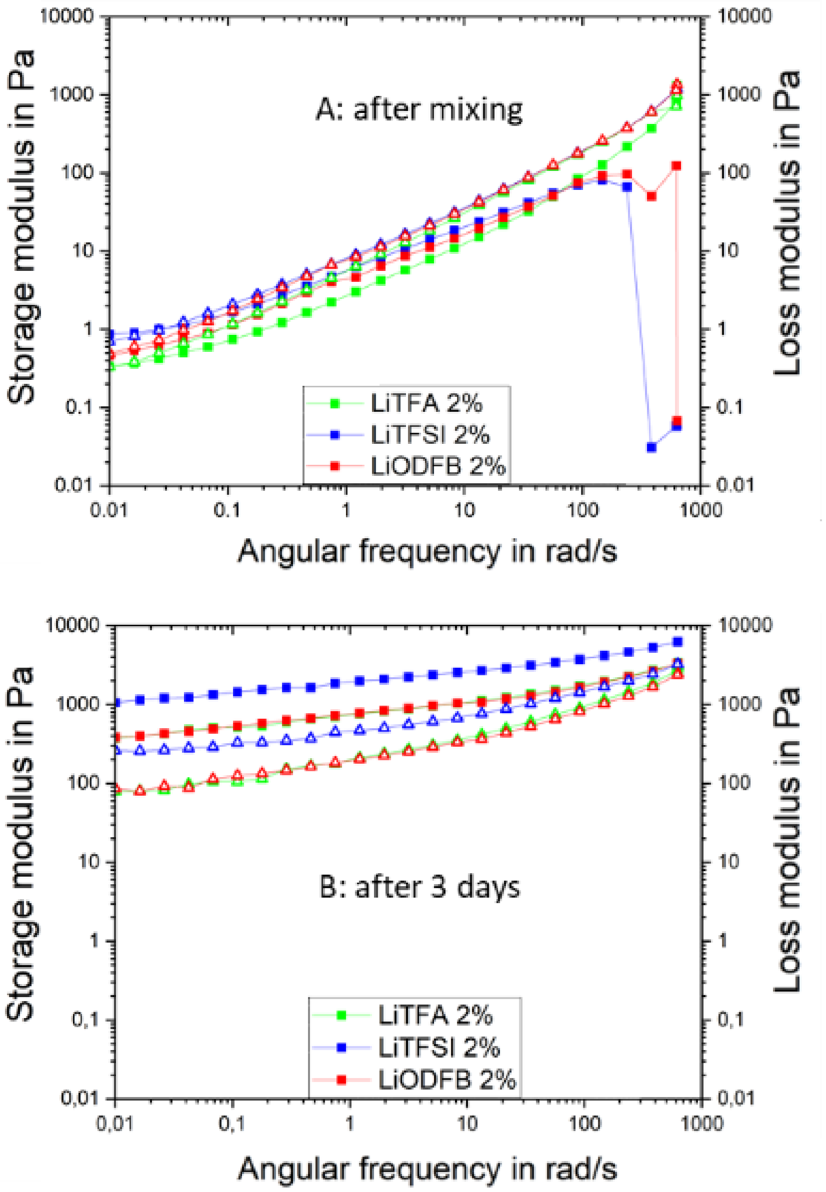

Figure 21. A: Frequency-dependent rheological moduli - storage (G’, ■) and loss (G’’, ▲) at strain γ = 0,1% -immediately after mixing NMC622 slurries (75.5 wt.% solids; high-Mw PVdF, carbon black) containing 2 wt.%$_{PVdF}$ LiTFA (green), 2 wt.%$_{PVdF}$ LiODFB (red) and 2 wt.%$_{PVdF}$ LiTFSI (blue). B: The same frequency sweeps recorded after three days of slurry storage. Adapted from F. Colombo et al.[1] with permission from the Royal Society of Chemistry.

This observation was further corroborated by frequency sweeps measurements **Figure 21A**, confirming that the flowable nature of all samples remains preserved even few hours after slurry mixing[1]. This will be clarified in the subsequent analysis of frequency sweeps across varying LiTFA concentrations, with the result that, the same considerations drawn for LiTFA at 2 wt.%$_{PVdF}$ are applicable systematically here to the other two additives utilized at the same concentration. In **Figure 21B**, the 3-day-old slurry frequency sweeps reproduce the amplitude-sweep findings: all three additives exhibit solid-like behavior across the whole frequency range, with LiTFSI (blue curve) showing the highest gel strength (G′) of the group after storage. Because frequency sweeps after slurry storage merely confirm the amplitude-sweep results, they will not be discussed further.

An extended investigation into LiTFA, the most effective gelation control additive, revealed its impact at concentrations below 2 wt.%$_{\mathrm{PVdF}}$. The study examined varying LiTFA amounts (0.5–8 wt.%$_{\mathrm{PVdF}}$). Flow curves (**Figure 22A**) showed that increasing LiTFA reduced gelation-related viscosity. Freshly prepared slurries displayed pseudo-plastic behavior, with viscosity decreasing as shear rate increased and steep vertical slopes near low shear rates indicating a yield point. Post-storage flow curves (**Figure 22B**) indicated notable viscosity increases for lower concentrations (+139% for 1 wt.%$_{\mathrm{PVdF}}$, +250% for 0.5 wt.%$_{\mathrm{PVdF}}$, **Table 8**)[1]. Amplitude sweeps measured post-mixing (**Figure 23A**) revealed liquid-like behavior (G″ > G′) for concentrations above 0.5 wt.%$_{\mathrm{PVdF}}$. Conversely, 0.5 wt.%$_{\mathrm{PVdF}}$ showed gel-like behavior (G′ > G″). Post-storage amplitude sweeps (**Figure 23B**) indicated gel network formation for all samples, with decreasing gel strength from 0.5 wt.%$_{\mathrm{PVdF}}$ (E_{coh} = 25.0 mJ/m³) to 8 wt.%$_{\mathrm{PVdF}}$. Finally, the time-dependent behaviors of the viscoelastic system can be evaluated within the LVR by imposing a constant deformation across varying frequencies during a frequency sweep analysis[1]. This technique acts as a distinctive fingerprint of the slurry's structure, offering high sensitivity to formulation alterations and shedding light on its temporal characteristics, such as shelf-life stability (extended storage), idle consistency, or sedimentation tendencies[3]. In the long-time scale limit ($\omega \approx 0$), when the loss modulus G″ surpasses the storage modulus G′, the system exhibits a predominantly liquid-like nature[1]. Under these conditions, extended shelf-life stability may not be achievable if gelation occurs too slowly to counterbalance the sedimentation of active material (AM).

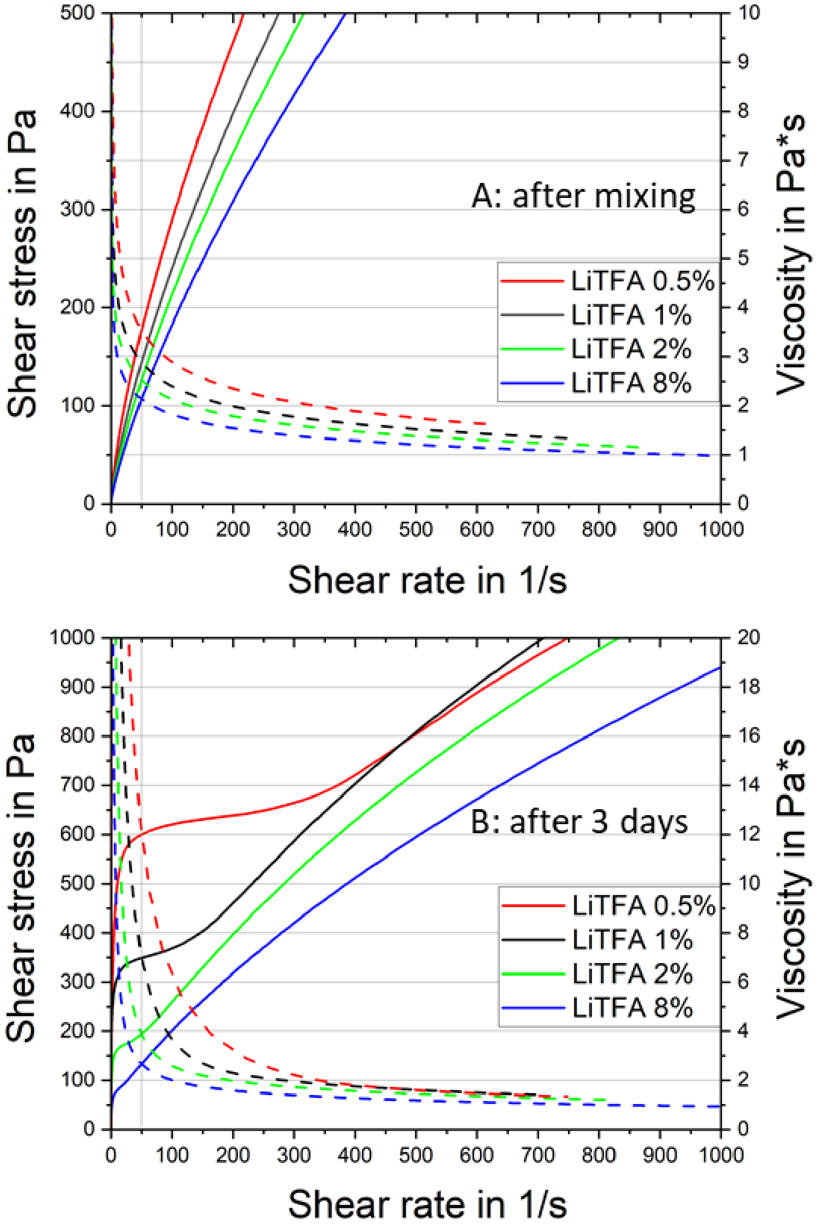

Figure 22. A: Flow (solid) and viscosity (dashed) profiles immediately after mixing NMP slurries encompassing NMC622 powder, high-Mw PVdF Type A, carbon black at SC 75.5 wt.% for LiTFA at 8 wt.%$_{\mathrm{PVdF}}$ (blue), 2 wt.%$_{\mathrm{PVdF}}$ (green), 1 wt.%$_{\mathrm{PVdF}}$ (black), 0.5 wt.%$_{\mathrm{PVdF}}$ (red). B: The same flow and viscosity measurements after three days' storage. Adapted from F. Colombo et al.[1] with permission from the Royal Society of Chemistry.

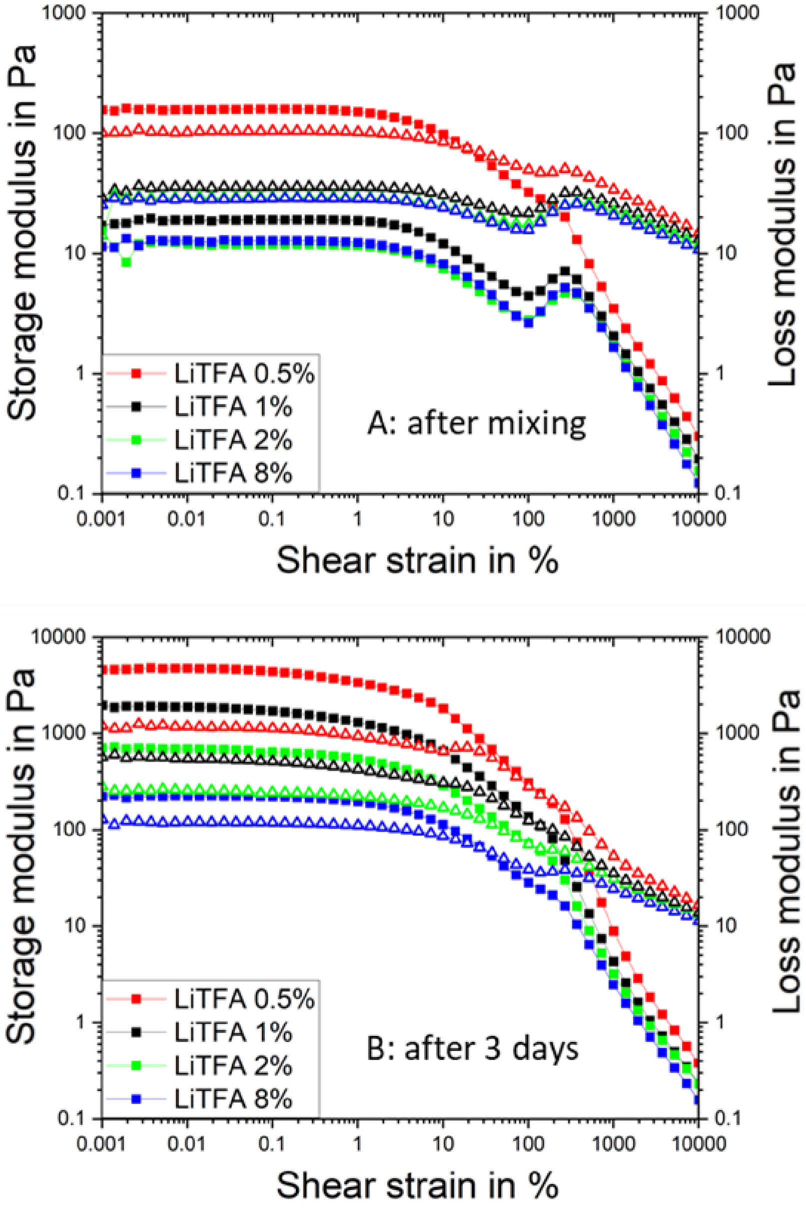

Figure 23. A: Amplitude sweeps (G′ ■, G′′ ▲) at $\omega=10s^{-1}$ immediately after mixing NMP-based slurries at SC 75.5 wt.% encompassing NMC622 powder, high Mw PVdF Type A, carbon black for LiTFA at 8 wt.%$_{\text{PVdF}}$ (blue), 2 wt.%$_{\text{PVdF}}$ (green), 1 wt.%$_{\text{PVdF}}$ (black), 0.5 wt.%$_{\text{PVdF}}$ (red). B: The same amplitude sweeps recorded after three days of storage. Adapted from F. Colombo et al.[1] with permission from the Royal Society of Chemistry.

Frequency sweeps performed immediately after mixing (**Figure 24**) for each LiTFA loading were used to characterize the slurry's viscoelastic time response[1]. To assess whether the slurry will retain good processability after few hours, viscoelastic measurements, specifically frequency sweep data, are analyzed with a focus on the behavior of the storage modulus G′ and the loss modulus G″ over time[1]. At the low-frequency limit (ω→0), the rheological response characterizes the slurry's long-term behavior, delineating the predominance of liquid-like versus solid-like regimes[1]. If G”>G’ at low frequencies (ω→0), the slurry demonstrates a liquid-like character, dissipating more energy than it stores elastically, suggesting it will likely remain processable over extended periods. Conversely, if G’>G”, the slurry exhibits a prevailing solid-like character, indicating it stores more energy than it dissipates, which may hinder processability after a few hours. For instance, LiTFA at 2 wt.%$_{\mathrm{PVdF}}$ (green) and 1 wt.%$_{\mathrm{PVdF}}$ (black) shows G”>G’ at low frequencies (close to ω→0), suggesting a liquid-like behavior conducive to maintaining processability over time. In contrast, LiTFA at 8 wt.%$_{\mathrm{PVdF}}$ (blue) exhibits G’>G” (close to ω→0), indicating a solid-like behavior[1]. However, the low storage modulus (G’ ≈ 1 Pa), nearly matching the loss modulus, indicates a soft-gel state that remains practicable for coating[1]. Meanwhile, LiTFA at 0.5 wt.%$_{\mathrm{PVdF}}$ displays G”>G’ across the entire frequency range, with G’>>G” at ω→0 and a magnitude of G’ around 70 Pa, identifying strong gelation that may impede processability within few hours after mixing. Notably, the LiTFA 0.5 wt.%$_{\mathrm{PVdF}}$ slurry’s gel-like consistency likely enhances storage stability by suppressing active-material sedimentation[1]. However, excessive strength in its aggregated state could cause challenges during coating[1].

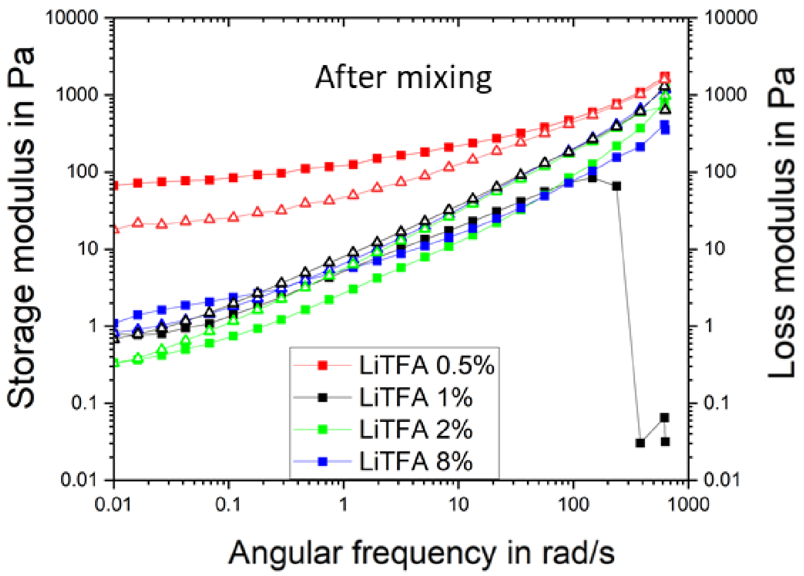

Figure 24. Frequency-dependent rheological moduli - storage (G’, ■) and loss (G’’, ▲) at strain γ = 0,1% -immediately after mixing NMC622 slurries (75.5 wt.% solids; high-Mw PVdF, carbon black) containing LiTFA at 8 wt.%$_{\mathrm{PVdF}}$ (blue), 2 wt.%$_{\mathrm{PVdF}}$ (green), 1 wt.%$_{\mathrm{PVdF}}$ (black), 0.5 wt.%$_{\mathrm{PVdF}}$ (red). (B) The same frequency sweeps recorded after three days of slurry storage. Adapted from F. Colombo et al.[1] with permission from the Royal Society of Chemistry.

Hence, in summary, incorporating LiTFA, LiTFSI, and LiODFB as slurry additives at 2 wt.%$_{\mathrm{PVdF}}$ optimally adjusted the rheology at the challenging 75.5 wt.% SC during electrode casting in the laboratory in a continuous roll-to-roll process, thus facilitating manufacturing of uniform coatings without gelation artifacts, as opposed to the additive-free A electrode, as shown in **Figure 9**.

4.2.3 Discussion and comparative analysis

It has been demonstrated that both H_3PO_4 and lithium salts play an active role in delaying gelation and reducing the viscosity of PVdF-based slurries, enabling the formulation of slurries with higher solid content (SC). Drawing on molecular adsorption studies reported by others[151], the modifications in slurry rheology associated with these additives are primarily linked to their chemical coordination interactions with the NMC622 surface. Specifically, H_3PO_4 introduces H^+ ions, which interact with the basic oxygen sites on the NMC622 surface[9,10]. Through electrostatic acid-base interactions[1], the electron-accepting H^+ ions neutralize the electron-donating Lewis-basic oxygen sites. Similarly, lithium salts contribute to the reduction of slurry viscosity by supplying Li^+ ions, which also interact with the basic oxygen sites on the NMC622 surface via acid-base interactions. Acting as Lewis-acidic electron acceptors, Li^+ or H^+ ions neutralize the NMC622 electron-donating oxygen sites. PVdF, a polymer with Lewis-acidic character[152] attributed to the dipole moment between its CF_2 and CH_2 units, typically binds to Lewis-basic oxide surfaces[153] through strong dipole interactions[153]. The addition of either H^+ or Li^+ ions into the slurry significantly modifies the net surface charge of the active material (AM), impacting these interactions[152]. H^+ ions introduced by additives such as H_3PO_4 convert negatively charged Lewis-basic oxygen sites on the AM surface into positively charged Lewis-acidic sites[1]. This transformation inhibits the adsorption and bonding of PVdF onto the AM surface[152]. Similarly, Li^+ ions from lithium salts induce comparable modifications, converting Lewis-basic sites into electron-accepting Lewis-acidic sites[1], further restricting PVdF adhesion. Additionally, Li^+ or H^+ ions adsorbed on the AM surface may interact with their associated anions, introducing additive-dependent variations in PVdF-surface interactions according to the specific properties of the anion, such as its electron-donating (basic) nature or polarizability[1]. In particular, it is worth noting that surface-adsorbed H^+ ions on NMC622 may coordinate with corresponding PO_4^{3-} anions. Prior studies have shown that introducing H_3PO_4 into waterborne cathode[79] and anode ($Li_4Ti_5O_{12}$)[85] slurries results in localized phosphate precipitation around AM particles, altering the electrode/electrolyte interface. The PO_4^{3-} group, known for its strong anchoring properties on acidic surfaces like silica[154], is expected to behave similarly, binding to the protonated (acidic) NMC622 surface in NMP. Additionally, it is hypothesized that the employment of additive may enhance the deagglomeration of carbon black (CB) compared to the additive-free A slurry, potentially leading to a more efficient binder adsorption onto the CB surface. Therefore, this effect should not be ruled out, since it may reduce bridging flocculation within the colloidal slurry system, a concept explored in subsequent chapters, where the role of CB deagglomeration in slurry gelation is comprehensively discussed.

As an initial approximation, the adsorption of both H_3PO_4 and lithium salts onto the carbon black (CB) surface can be disregarded due to the prevailing nonpolar nature of CB, which does not favor interaction with polar additives. The predominantly nonpolar nature of carbon black (CB) arises primarily to its extended sp^2-hybridized carbon network, which is inherently hydrophobic and apolar[155,156]. This is despite the possible presence of oxygen-containing surface functional groups, such as hydroxyls, carboxyls, lactones, and phenols groups, which are typically concentrated at the edges of the graphitic domains or at defective sites within the graphite planes[157,158]. These polar moieties are generally present in lower densities relative to the bulk sp^2 network, meaning that their contribution to the overall surface chemistry of CB can only be modest[159,160]. While these functional groups can introduce some degree of polarity to localized regions on the CB surface[161,162], the overall surface polarity remains significantly lower than that of metal oxide surfaces like NMC622. The latter, with their higher density of strongly Lewis-basic sites (e.g., oxygen atoms coordinated to transition metals), exhibit much greater polarity. Like several studies have indicated[161,162], the surface polarity of CB is minimal in comparison to that of metal oxides, leading to interactions that are primarily governed by van der Waals forces. In contrast, the highly polar surfaces of NMC622 are mainly influenced by electrostatic acid-base interactions due to their metal-oxygen surface groups. Consequently, although CB may acquire some polar functionalities during synthesis or post-synthesis oxidation treatments, its inherent sp^2 carbonaceous network predominates[163], imparting an overall apolar character when compared to the highly polar metal oxide surfaces. Additionally, the adsorption of these additives onto Al_2O_3, which refers to the native oxide layer that forms on the surface of the aluminum current collector, is considered negligible, owing to the minimal surface area of Al_2O_3 that limits its interaction capacity. Therefore, it is reasonable to conclude that the adsorption of both H_3PO_4 and lithium salts predominantly occurs on the active material (AM) surface. This selective adsorption on the AM surface emphasizes the critical role of these additives in modifying the surface chemistry of the AM, which in turn influences the overall properties of the PVdF-based slurry system.

Remarkably, all the H_3PO_4 concentrations employed are sufficient to form more than a single molecular layer on the AM surface, as deduced from a straightforward footprint estimation of the additive molecule detailed below. To approximate the molecular footprint (F_p) in nm^2, the volume of an additive molecule is first calculated using its molecular weight Mw, solid density ρ, and Avogadro's number Na, as follows:

$$V_{mole} = \frac{Mw}{\rho} \quad (2)$$

$$V_{molecule} = \frac{V_{mole}}{N_A} \quad (3)$$

Assuming a spherical shape, the approximated molecular radius is and derived from the sphere volume V, and the footprint F_p corresponds to the cross-sectional area of the sphere, i.e., the area of a circle with the molecular radius r:

$$r_{molecule} = \left(\frac{3V_{molecule}}{4\pi}\right)^{1/3} \quad (4)$$

$$Footprint\ F_p = \pi(r_{molecule})^2 \quad (5)$$

Using the number of moles of additive, the total additive surface area in the slurry (nm^2) is determined and divided by the BET surface area of NMC622 in the slurry to estimate the number M_L of monomolecular layers formed on the NMC622 surface, as shown in **Table 9** and calculated with the following equation:

$$Monolayers\ M_L = \left(\frac{F_p * moles * N_A}{NMC622\ BET\ surface}\right) \quad (6)$$

Under these approximations, the amount of additive used is adequate to form multiple monomolecular layers on the NMC622 surface for most of the concentrations employed, as illustrated in **Table 9**. Interestingly, even at the lowest additive concentration of 4.3 $wt.\%_{PVdF}$ H_3PO_4, the amount is sufficient to form three layers on the NMC622 surface. However, the inability of this concentration to control slurry gelation hints that a significant portion of the additive may be distributed within CB-PVdF domains rather than being concentrated on the NMC622 surface. Alternatively, incomplete solvation of H_3PO_4 in the NMP solvent may also reduce its effectiveness in complexing with the NMC622 surface. In contrast, for Li-salt additives at a 2 $wt.\%_{PVdF}$ concentration, the quantity is sufficient to form a complete monolayer on the NMC622 surface, as evidenced in **Table 9**.

Table 9. Estimation of the number of mono-molecular additive layers on the AM surface. For H_3PO_4, the solid density is 1.834 g/cm³, and the molar mass is 97.994 g/mol. Comparable values for Li-salts are 119.96 g/mol and 1.743 g/cm³ for LiTFA, 143.77 g/mol and 2.04 g/cm³ for LiODFB, and 287.09 g/mol and 1.33 g/cm³ for LiTFSI. The measured BET surface area of NMC622 is 0.33 m²/g.

Slurry sample	Footprint F_p of a single additive molecule in nm²	Moles of additive in slurry*	Additive surface in slurry* in nm²	NMC622 surface in slurry* in nm²	Number M_L of monomolecular additive layers
H_3PO_4 4.3wt.%$_{PVdF}$	0.24	6.5E-04	9.5E+19	3.2E+19	2.9
H_3PO_4 6.1wt.%$_{PVdF}$	0.24	9.3E-04	1.3E+20	3.2E+19	4.2
H_3PO_4 8wt.%$_{PVdF}$	0.24	1.2E-03	1.8E+20	3.2E+19	5.5
LiTFA 0.5wt.%$_{PVdF}$	0.28	5.8E-05	1.0E+19	3.2E+19	0.3
LiTFA 1wt.%$_{PVdF}$	0.28	1.3E-04	2.1E+19	3.2E+19	0.7
LiTFA 2wt.%$_{PVdF}$	0.28	2.5E-04	4.3E+19	3.2E+19	1.3
LiODFB 2wt.%$_{PVdF}$	0.29	2.1E-04	3.6E+19	3.2E+19	1.1
LiTFSI 2wt.%$_{PVdF}$	0.61	1.0E-04	3.8E+19	3.2E+19	1.2
LiTFA 8wt.%$_{PVdF}$	0.28	1.0E-03	1.7E+20	3.2E+19	5.3

* For each slurry sample the calculation is based on the corresponding composition in **Table 1**, by considering 100g as a fix amount representing the total dry components of the slurry.

This finding indicates a preferential activity of these additives on the AM surface, as this concentration effectively impairs bridging flocculation. However, at lower concentrations of LiTFA (0.5 wt.%$_{PVdF}$ and 1 wt.%$_{PVdF}$), the coverage is insufficient to fully coat the AM surface, whereas at 8 wt.%$_{PVdF}$, LiTFA could theoretically form five monolayers. The extent of surface coverage and the binding strength of the additives are influenced by the properties of the PO_4^{3-} or by the various lithium salt anions, including their peculiar attributes, such as electron-donating (basic) nature or polarizability. Each slurry additive, therefore, imparts a unique surface chemistry, as outlined in **Figure 25**. Consequently, lithium salts and H_3PO_4 play a crucial role in impeding rapid chemical slurry gelation by neutralizing the basic groups on the NMC622 surface, while also reducing physical gelation by partially inhibiting PVdF binder adsorption[1]. These interactions between the additives and the surface groups influence both the chemical and physical behavior of the slurry, highlighting the complex role that additives play in the formulation process[1].

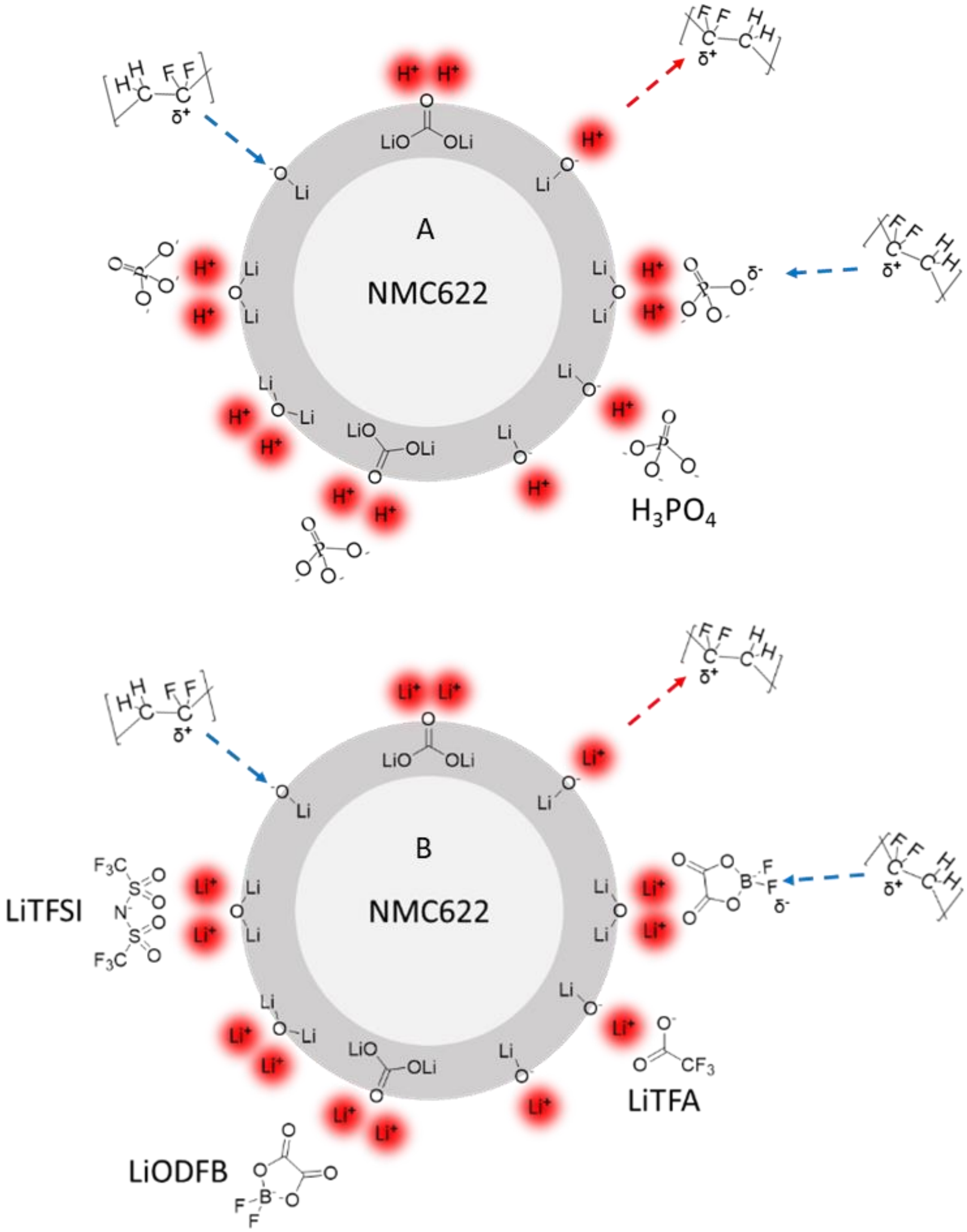

Figure 25. Schematic illustration showing H^+ (A) and Li^+ (B) ions neutralizing basic surface sites (dark gray regions - not to scale) on the NMC622 surface within the slurry. Adsorbed H^+ and Li^+ ions are partially complexed by their corresponding anions. PVdF interactions with surface species are represented by blue (attractive) and red (repulsive) dotted arrows, reflecting acid-base interactions. Adapted from F. Colombo et al.[1] with permission from the Royal Society of Chemistry.

4.2.4 Electrochemical study of electrodes encompassing H_3PO_4

Electrochemical cycling was carried out on NMC-graphite full cells in a pouch-cell format[1], as described in the experimental section. The electrochemical behavior of cathodes containing H_3PO_4 8.0 wt.%$_{PVdF}$ was compared to an additive-free A reference sample (details on cathode and cell fabrication are provided in in **Table 1, Table 3** and **Table 10**.

Table 10. Summary of mass loading, thickness, porosity, resistance, and adhesion for tested cathodes, evaluated before and after calendering and, where performed, and, if applicable, following heating treatment[1]. All the electrodes are calendered to 33% porosity.

Electrode sample	Mass loading in mg/cm^2	Thickness in µm	Resistance in Ω - cal	Adhesion in N/m - uncal	Adhesion in N/m - cal
additive-free A	11.3	38.8	108	56.1	44.3
H_3PO_4 8wt.%$_{PVdF}$	10.2	36.0	171	34.2	45.5

During the formation cycles at a low C-rate of C/20 (**Figure 26**), the cells exhibited an average discharge capacity of 168 ± 2 mAh/g, with limited variation between samples. A subsequent rate-capability test conducted between C/2 and 5C (after two C/20 formation cycles) revealed comparable rate stability for all coatings at the lowest rates of C/2, C and 2C. Significant differences in capacity retention emerged at higher rates, ranging from 3C to 5C. As the C-rate increased, the performance gap widened, with the additive-containing cathodes underperforming compared to the superior additive-free A sample. In the long-term cycling study (**Figure 26B**), the H_3PO_4-containing cells exhibited significantly faster degradation than the additive-free A cells.

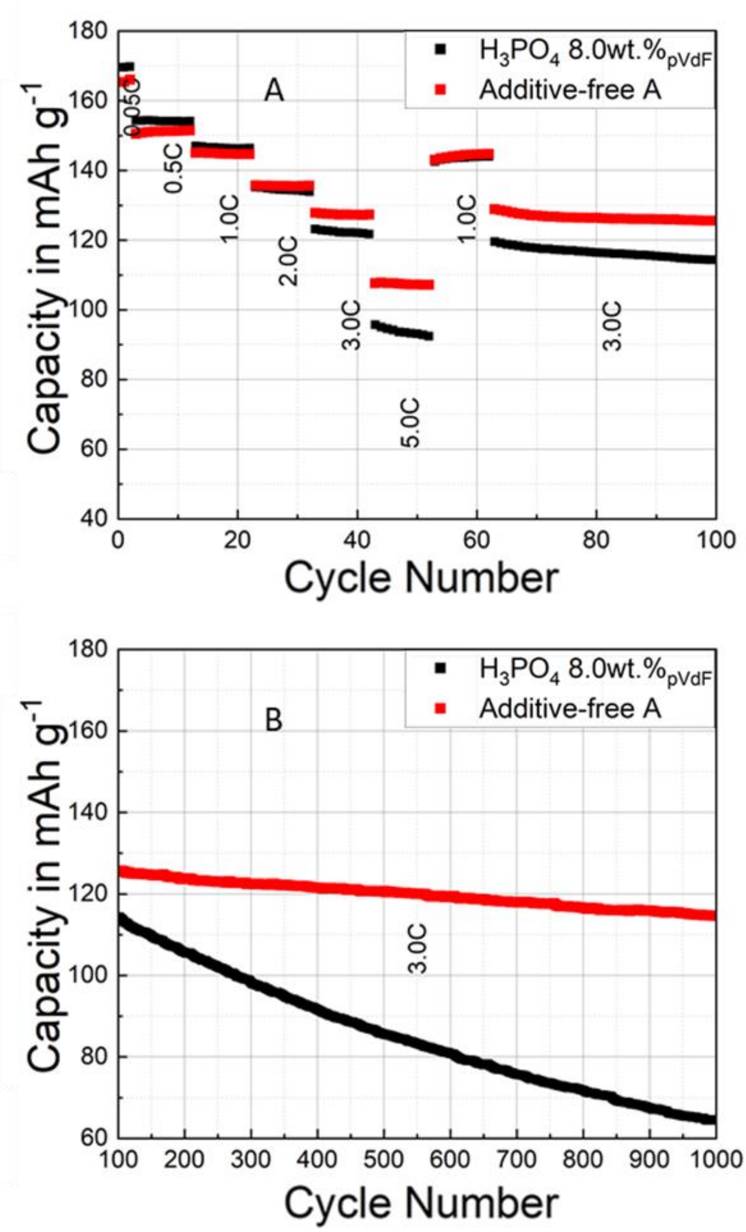

Figure 26. Rate capability (panel A) and prolonged cycling (panel B) metrics of graphite-NMC full cells for H_3PO_4 8.0 wt.%$_{PVdF}$ (black) and additive-free A (red) cathodes. The control experiment, repeating the same test under identical conditions to assess reproducibility, is shown in **Figure S-2**.

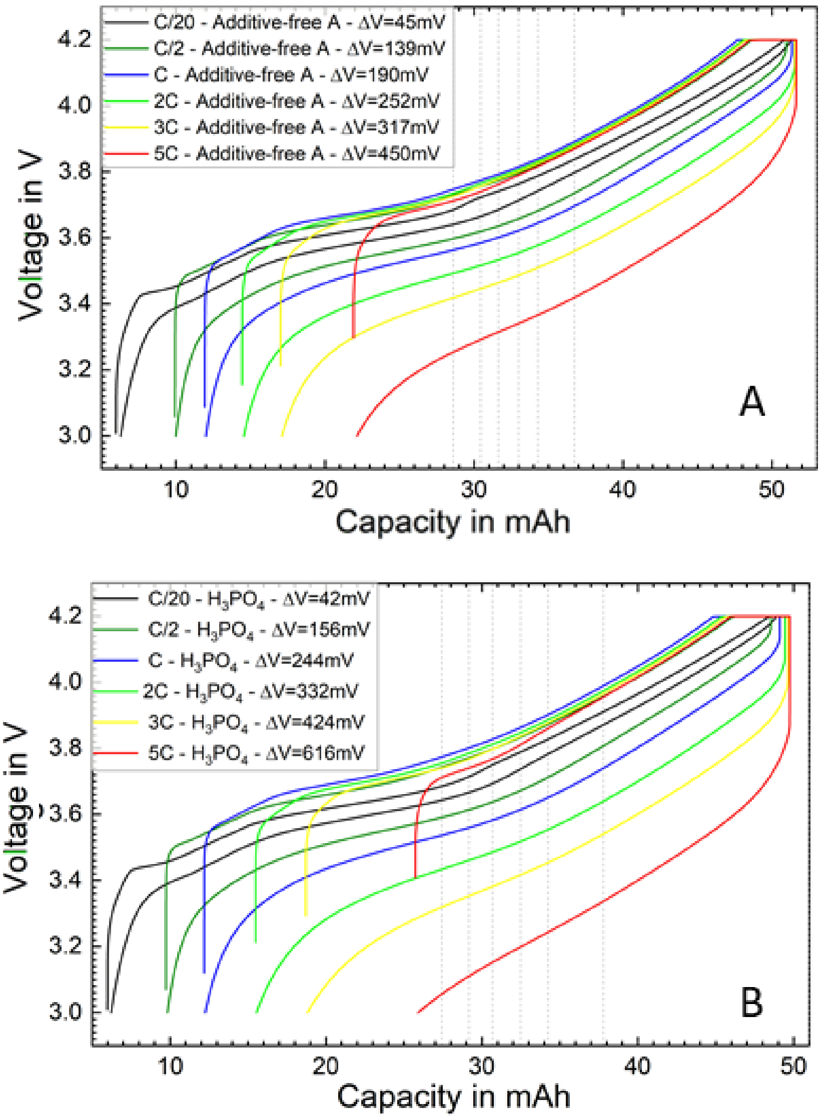

Figure 27. Voltage versus capacity charge discharge curves at the 2nd cycle for each C-rate for the additive-free A (A) and the H_3PO_4 8.0 wt.%$_{PVdF}$ (B) cathodes with values of cell polarization at half depth of charge/discharge (x=0,5 is marked by vertical dashed reference lines for every C-rate)[1].

Higher overpotentials were observed for the H_3PO_4 electrode at all C-rates exceeding C/20, as shown in **Figure 27**. These elevated overpotentials are likely attributable to the localization of H_3PO_4 on the NMC622 surface and the native Al_2O_3 layer at the current collector in the dry cathode, forming additional surface layers that reduce the overall electrical conductivity[1]. This is supported by elemental EDS analysis (**Table 11**), which confirms significant phosphorus presence on the surface of the H_3PO_4-containing sample.

Table 11. Post-mortem elemental EDS analysis of electrode surfaces for H_3PO_4 8.0 wt.%$_{PVdF}$ and additive-free A cathodes[1].

Element	Line	Mass in % - H_3PO_4 8wt.%$_{PVdF}$	Mass in % - additive-free A	Atom in % - H_3PO_4 8wt.%$_{PVdF}$	Atom in % - additive-free A	Standard name
O	K-Serie	33.18	32.02	62.24	60.30	SiO2
F	K-Serie	1.82	3.46	2.87	5.49	CaF2
Al	K-Serie	0.56	0.65	0.62	0.72	Al2O3
P	K-Serie	0.88	0.00	0.85	0.00	GaP
S	K-Serie	1.06	0.39	1.00	0.36	FeS2
Mn	L-Serie	13.98	16.63	7.63	9.12	Pure Element
Co	L-Serie	13.48	14.57	6.87	7.45	Pure Element
Ni	L-Serie	35.04	32.28	17.91	16.56	Pure Element
Total:		100	100	100	100	

The higher resistance recorded for the H_3PO_4 8.0 wt.%$_{PVdF}$ cathode versus the additive-free A sample (**Table 10**) corroborates the hypothesis that supplementary surface layers obstruct electrical conduction. The rapid capacity fading during extended cycling of H_3PO_4-treated cells may also result from increased SEI formation caused by proton diffusion to the anode, which is known to induce graphite exfoliation and SEI interface degradation[16]. Post-mortem elemental EDS analysis of the anodes (**Table 12**) revealed a higher oxygen content for the H_3PO_4-containing cells, consistent with increased SEI formation, supporting this hypothesis.

Table 12. Post-mortem elemental EDS analysis of the anodes surface for the H_3PO_4 8.0 wt.%$_{PVdF}$ and the additive-free A samples after retrieval from cycled pouch cells after cycle 1000th.

Element	Line	Mass in % - H_3PO_4 8wt.%$_{PVdF}$	Mass in % - additive-free A	Atom in % - H_3PO_4 8wt.%$_{PVdF}$	Atom in % - additive-free A	Standard name
C	K-Serie	67.60	74.20	74.43	79.03	Pure Element
O	K-Serie	28.26	22.36	23.36	17.88	SiO2
F	K-Serie	1.97	1.88	1.37	1.27	CaF2
Na	K-Serie	0.19	0.01	0.11	0.15	Albite
P	K-Serie	1.34	0.03	0.57	0.53	GaP
Mn	L-Serie	0.46	0.10	0.11	0.00	Pure Element
Co	L-Serie	0.17	0.05	0.04	0.00	Pure Element
Ni	L-Serie	0.00	0.03	0.00	0.00	Pure Element
Total:		100.00		100.00		

Furthermore, it should not be excluded that the H_3PO_4 additive may promote a superior deagglomeration of carbon black in additive-containing electrodes when compared to the additive-free A sample. Consequently, unlike the additive-free A sample, these electrodes may require a more intensive calendering to achieve optimal electrical conductivity. This will be demonstrated in the following dedicated chapters, where the effects of modified carbon black deagglomeration and the optimal calendering degree are thoroughly explored. SEM images of ion-milled cross-sections of non-cycled calendered cathodes (**Figure 28**) indicate that the inclusion of additives does not alter the electrode morphology in the dry state.

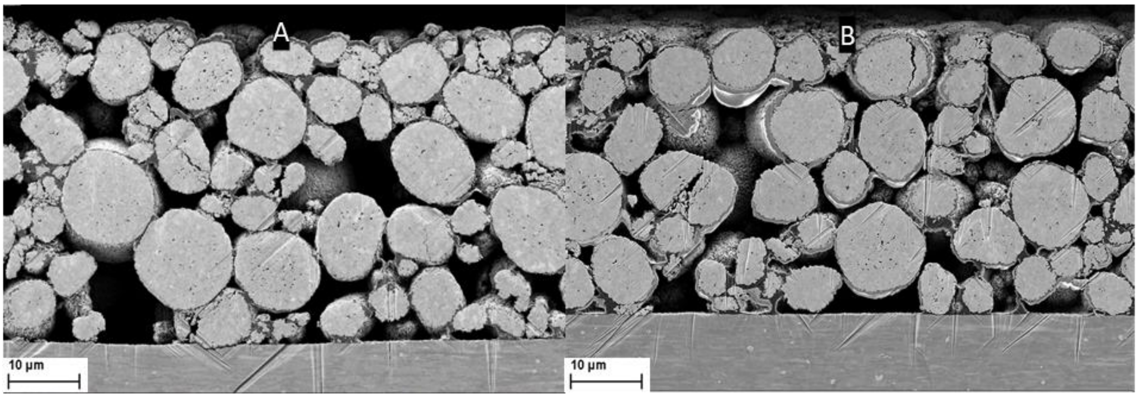

Figure 28. SEM images of ion-milled cross-sections of pristine calendered electrodes for additive-free A (A) and H_3PO_4 8.0 wt.%$_{PVdF}$ (B) samples.

To elucidate the slurry additive's role at the electrode-electrolyte boundary, EIS responses were modelled with the SCRF[140] equivalent circuit (inset of **Figure 29**)[1]. In this scheme, R_{el} is the uncompensated resistance; R_0 and Q_{CPE0} account for contact impedance at the Al foil/composite interface, R_0 measuring electron-transfer resistance into the electrode conductive network and Q_{CPE0} representing the interfacial constant phase element (CPE) from Al_2O_3 or other passivation layers. R_f and Q_{CPEf} describe the high-voltage surface-film impedance on carbon black and active particles, indicative of CEI formation or oxygen-evolution-driven interface modifications[1].

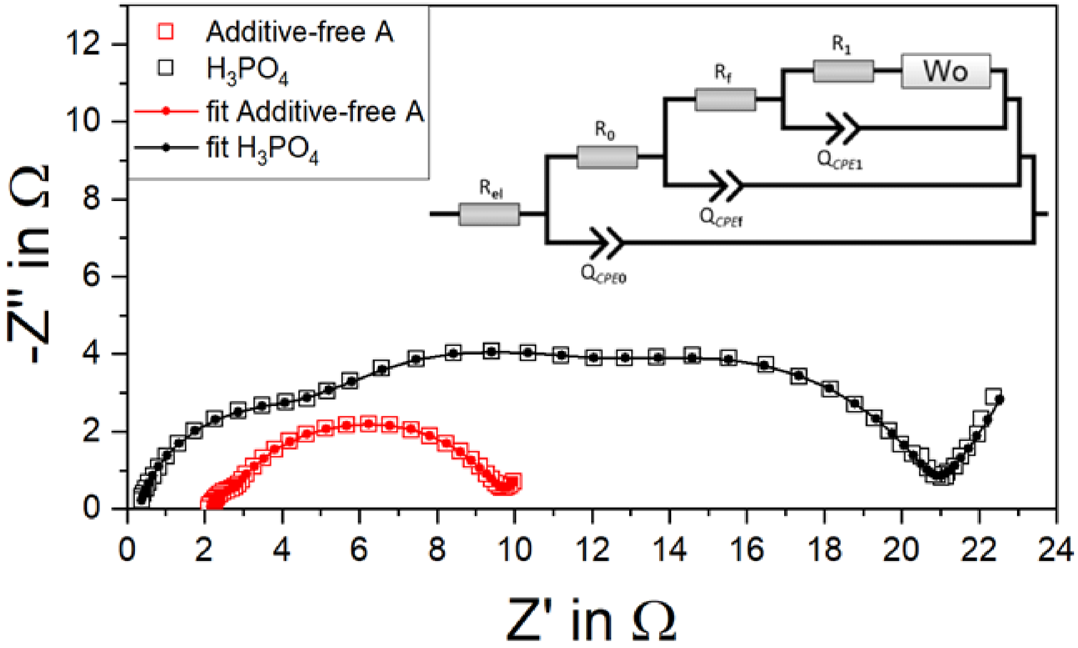

Figure 29. Nyquist plots (open squares) and fitted spectra (solid lines with markers) for fresh NMC622 electrodes at 0.8 SOC during the first cycle post-formation: additive-free A (red) and H_3PO_4 8.0 wt.%$_{PVdF}$ (black). Data span 20 kHz to 50 mHz; the equivalent-circuit model is shown in the insert[1]. The matching Bode plots are presented in **Figure S-6**.

Recognizing NMC622's air and moisture sensitivity[10], the SCRF model was adopted, which includes surface/passivation layers, to analyze the coatings. Here, R_1 and Q_{CPE1} capture Li-ion charge-transfer resistance and its double-layer CPE owing to lithium-ion intercalation, while an open Warburg (W_o) in series reflects electrolyte diffusion resistance[1].

In fitting, α was constrained to ≤ 0.75 (with $\alpha = 1$ being ideal); values near 0.75 indicate marked non-idealities from heterogeneous surfaces and film-thickness fluctuations[1,7]. It should be noted that fitting with eight parameters risks over-parameterization if mid-to-low-frequency relaxation peaks overlap[1]. For instance, the Nyquist plot of the additive-free A cathode (red curve, **Figure 29**) reveals a minor high-frequency semicircle, linked to contact resistance, followed by a broadened arc stretching across the mid-to-low frequencies[1]. In contrast, the mid-to-low frequency arc is amplified in the H_3PO_4-treated sample. While the additive-free A sample struggles to differentiate individual RQ element contributions within this frequency range, the H_3PO_4 sample achieves clearer separation due to the expanded arc[1]. Nonetheless, uncertainties persist in both cases, especially when interpreting relaxation frequencies based on parameters tied to non-ideal capacitors (CPEs) [1]. For $\alpha > 0.75$, the product of R and Q approximates [164] the relaxation frequency using Equation[1] (7):

$$R \cdot Q = \tau^{\alpha} = (RC)^{\alpha} \quad (7)$$

As outlined in **Table 13**, the relaxation frequencies for specific RQ circuit components vary by about one order of magnitude. For the additive-free A cathode, R_fQ_{CPEf} and R_1Q_{CPE1} differ by half an order of magnitude, while R_0Q_{CPE0} and R_fQ_{CPEf} are separated by two orders of magnitude[1]. The values of R_f and R_1 for both samples lie between 2 and 10 Ω, making trends less apparent. However, the total of $R_f + R_1$ shows good correlation with long-term capacity retention[1]. For the additive-free A sample (red curve, **Figure 29**), the Nyquist plot illustrates a small high-frequency semicircle linked to contact resistance and a widened semicircle at mid-to-low frequencies, encompassing both surface-film and charge-transfer resistances. The H_3PO_4-containing cathode demonstrates increased impedance, with significant broadening of both high-frequency and mid-to-low frequency arcs. Interestingly, the EIS data reveal significant differences in electrode impedance in the low-frequency range at SOC = 0.1 and SOC = 0.2, attributed to diffusion processes[1], whereas at higher SOC values (≥ 0.2), a well-defined charge-transfer arc is observed, as depicted in **Figure S-4** and **Figure S-5**, with its impedance decreasing as SOC increases, consistent with prior studies [165–168].

Table 13. Average EIS fitting variables, each based on two separate impedance runs, at 0.8 SOC for the additive-free A and the H_3PO_4 8.0 wt.%$_{PVdF}$ cathodes at 33% porosity.

Sample	R_{el} in Ω	R_0 in Ω	Q_{CPE0} in $S*s^{\alpha}$	α_{CPE0}	R_0Q_{CPE0} in s^{α}	R_f in Ω	Q_{CPEf} in $S*s^{\alpha}$	α_{CPEf}	R_fQ_{CPEf} in s^{α}	R_1 in Ω	Q_{CPE1} in $S*s^{\alpha}$	α_{CPE1}	R_1Q_{CPE1} in s^{α}
additive-free A	1.3	0.5	9.8E-05	1	4.9E-05	3.9	2.4E-03	0.84	9.4E-03	2.1	2.7E-02	0.75	5.7E-02
H_3PO_4 8wt.%$_{PVdF}$	0.5	5.5	3.0E-05	0.84	1.7E-04	5.0	7.5E-04	0.82	3.7E-03	6.9	6.6E-03	0.75	4.5E-02

The equivalent circuit model parameters (**Table 13**) highlight that the largest impedance increases for H_3PO_4 samples pertain to contact resistance R_0. The lowest R_0 values were recorded for the additive-free A cathodes, while R_0 increased significantly for H_3PO_4-containing samples. The native Al_2O_3 layer on the Al current collector, with unsaturated Lewis oxygen sites similar to those on the NMC surface (**Figure 25**), may undergo enhanced passivation due to H_3PO_4 adsorption, accounting for the elevated R_0 values. Surface-adsorbed H^+ ions on the alumina layer are hypothesized to interact extensively with PO_4^{3-} anions, restoring partial negative surface charge and enabling PVdF adsorption. This mechanism is consistent with the uncalendered-state adhesion values of H_3PO_4 coatings, which almost approach those of the best performing additive-free A samples (**Table 10**). EIS data reveal a general increase in charge-transfer R_1 and interfacial impedance R_f for additive-containing cathodes compared to the reference. The charge-transfer resistance R_1, in particular, was substantially higher for H_3PO_4-containing electrodes. **Table 13** also shows that the surface-film resistance (R_f) for the additive-free A sample was slightly lower than for H_3PO_4-treated cathodes. This increased R_f may arise from H_3PO_4 adsorption on the NMC622 surface. In contrast, uncompensated resistance R_{el} was lower for additive-containing cathodes, likely attributable to enhanced local ionic conductivity from H_3PO_4 salts in the electrode pores[1].

4.2.5 Electrochemical study of electrodes encompassing Li salts

Cycling experiments utilized pouch-format NMC-graphite full cells, as detailed in the experimental methodology. Electrochemical performance of cathodes incorporating 2 wt.%$_{\text{PVdF}}$ Li-salts was benchmarked against an additive-free A cathode reference (fabrication details in in **Table 1** and **Table 14**). During initial low C-rate formation cycles at C/20, all cells reached a mean discharge capacity of 165.6 ± 1.9 mAh/g, exhibiting minimal variation across samples[1]. Rate-capability analysis (**Figure 30A**) spanning C/2 to 5C, after two C/20 formation cycles, revealed invariable performance across all formulations, including the reference (black). Minor capacity retention differences at 3C and 5C fell within the experimental error, corroborated by control data in **Figure S-3**. Long-term cycling (**Figure 30B**) indicated earlier degradation for additive-containing cells relative to the reference, though the LiTFSI-containing cathode exhibited capacity retention comparable to additive-free A[1].

Table 14. Summary of mass loading, thickness, porosity, resistance, and adhesion for tested cathodes, both before and after calendering, and, if applicable, following heating treatment (FHT) [1]. All the electrodes are calendered to 33% porosity.

Electrode sample	Mass loading in mg/cm^2	Thickness in µm	Resistance in Ω - cal	Adhesion in N/m - uncal	Adhesion in N/m - cal	Adhesion in N/m - FHT
additive-free A	11.3	38.8	108	56.1	44.3	-
LiTFA 2wt.%$_{\text{PVdF}}$	11.6	39.8	76	7.0	14.1	28.7
LiODFB 2wt.%$_{\text{PVdF}}$	11.7	41.1	88	45.4	63.4	-
LiTFSI 2wt.%$_{\text{PVdF}}$	11.2	38.4	73	13.1	10.3	32.4

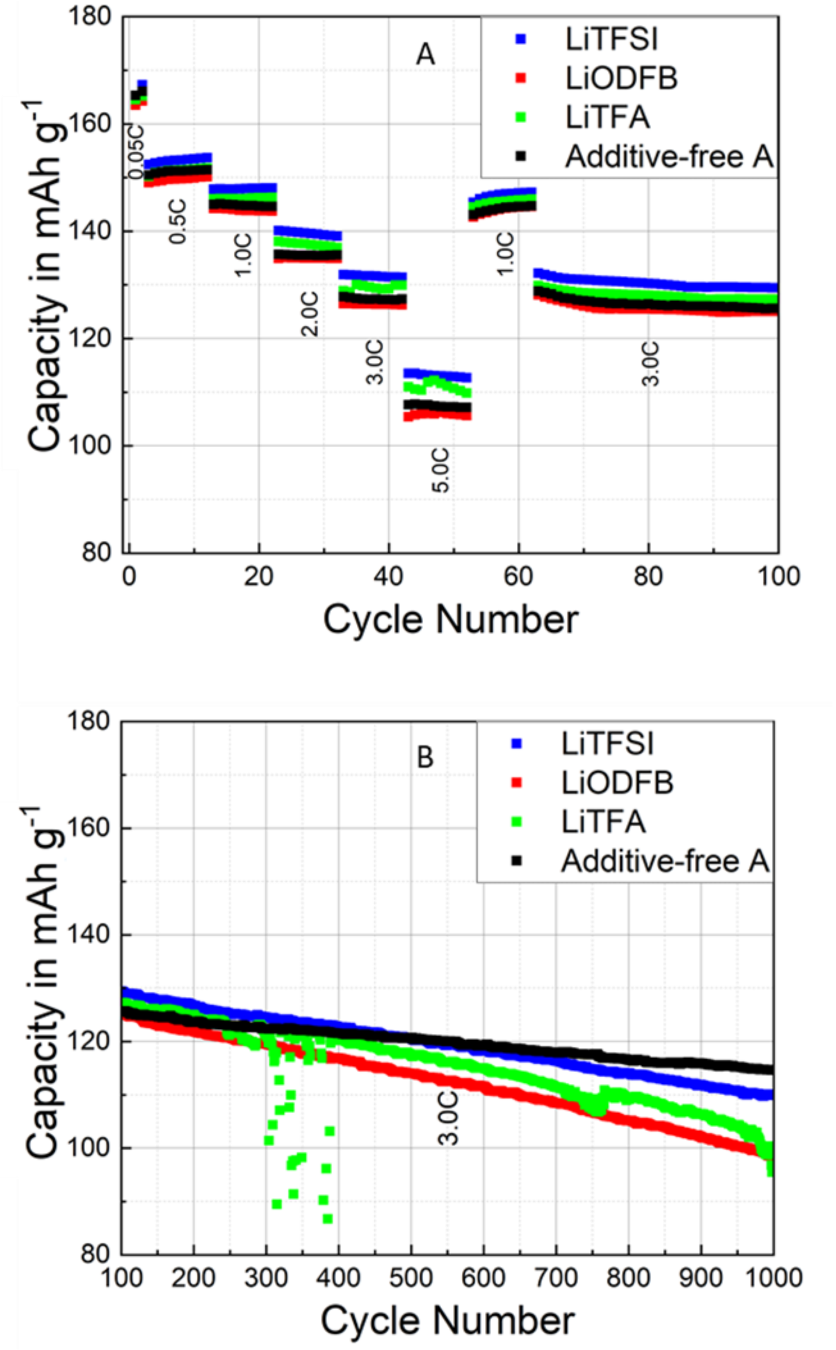

Figure 30. Rate capability (panel A) and prolonged cycling (panel B) metrics of graphite-NMC full cells for additive-free A (black), 2 wt.%$_{\mathrm{PVdF}}$ LiTFA (green), 2 wt.%$_{\mathrm{PVdF}}$ LiODFB (red), and 2 wt.%$_{\mathrm{PVdF}}$ LiTFSI (blue) cathodes. The green isolated aberrations stem from momentary potentiostat malfunctions. A control test, verifying the reproducibility of the cycling performance, is shown in **Figure S-3**. Reproduced from F. Colombo et al.[1] with permission from the Royal Society of Chemistry.

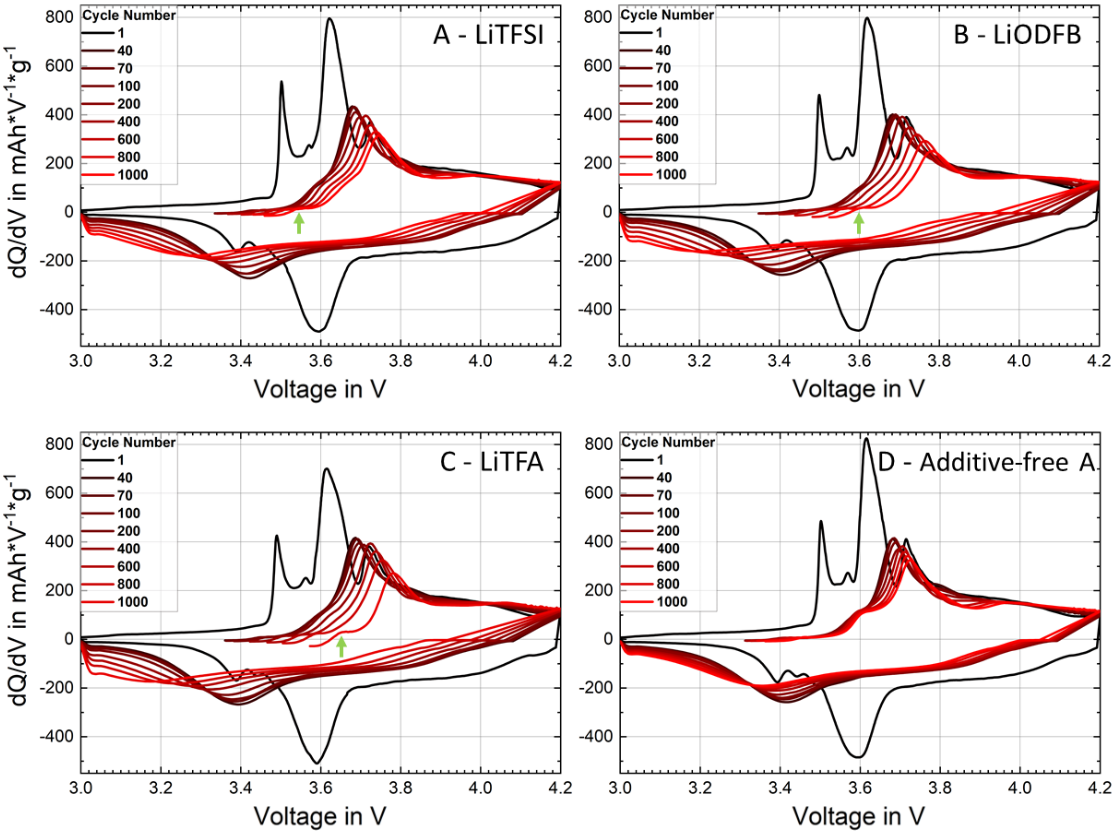

Figure 31. Differential-capacity (dQ/dV) profiles at formation (0.05 C, black) and during cycling (1C/3C, red) for cells with (A) LiTFSI, (B) LiODFB, (C) LiTFA, and (D) additive-free A cathodes, shown for cycle 1 (black) and cycles 40, 70, 100, 200, 400, 600, 800 and 1000 (light red). Anodic peaks (green pointers), absent during formation, emerge upon extended cycling in the LiTFA and LiODFB cells, with a subtler manifestation in LiTFSI[1]. Reproduced from F. Colombo et al.[1] with permission from the Royal Society of Chemistry.

Differential capacity (dQ/dV) profiles (**Figure 31**) were examined to clarify behaviours under high C-rates and extended cycling[1]. The symmetric formation cycle at C/20 is shown in black, while asymmetric 1C/3C profiles from cycle 40 (dark red) through cycle 1000 (light red) highlight selected stages[1]. Notably, 3C discharge rates induce broadening of the voltage-domain signals[1]. In NMC622 half-cells, two dominant oxidation features at 3.64 V and 3.74 V vs. Li^+/Li arise from the $Ni^{2+/3+}$ and $Ni^{3+/4+}$ redox couples[54], respectively, with a single reduction feature at 3.66 V[1]. In fully assembled cells, the stepwise intercalation processes of graphite result in these oxidation peaks being multiplied[1] into several distinct anodic peaks[169,170,171]. The area under each peak correlates with the capacity from each process[139]. Alterations in the onset of the upper oxidation peak at 3.5 V (black curve) primarily stem from graphite anode reactions[139,172,173]. Meanwhile, the second major peak near 3.6V (black), along with its left (3.57V) and right (3.71V) satellite peaks, reflects sequential Ni redox processes in NMC622[1]. Peak intensities and areas diminish over cycles, signaling active material losses due to structural evolution, transition metal dissolution, or surface layer alterations[139]. Notably, peak attenuation at 3.71 V during cycling reflects lithium inventory depletion driven by SEI growth and electrolyte decomposition[172,169]. In the high-potential anodic region, dQ/dV peaks broaden and shift anodically (to more positive potentials) from the formation cycle (black) to 1 C cycling (red), reflecting aging phenomena[1]. While cycling, the primary peak near 3.6 V (black curve) persists alongside the peaks at 3.5 V and 3.71 V, manifesting as shoulder features on both flanks of the primary peak[1]. Among the three Li-salt additive-containing cells, two exhibit a significant reduction in main peak area, indicating a greater loss of active material during cycling compared to the reference[1]. Notably, the 2 wt.%$_{PVdF}$ LiTFSI sample demonstrates behavior closely resembling the reference, with substantially lower degradation compared to the 2 wt.%$_{PVdF}$ LiODFB and 2 wt.%$_{PVdF}$ LiTFA samples. A small anodic feature (green pointer), absent in the formation curve (black), appears after extended cycling in LiTFA and LiODFB cells, and to a lesser extent in LiTFSI, while remaining nearly undetectable in the reference cell[1]; this peak likely corresponds to anodic lithium plating[107]. The separation ΔV between the anodic and cathodic peaks at ≈3.6 V (**Table S-1**) serves as a polarization metric, with an increased ΔV reflects higher cell impedance and lower cycling efficiency[1]. As **Table S-1** shows, all cells exhibit comparable ΔV through cycle 100, but from cycle 200 onward the additive-containing cells develop significantly larger overpotentials[1]. In this regard, the 2 wt.%$_{PVdF}$ LiTFSI sample again aligns most closely with the reference, while the 2 wt.%$_{PVdF}$ LiODFB and 2 wt.%$_{PVdF}$ LiTFA samples show notably higher polarization, consistent with their accelerated capacity degradation[1].

SEM analysis of ion-milled cross-sections of pristine, calendered electrodes (**Figure 32**, **Figure 33** and **Figure 34**) reveals no significant changes in electrode morphology in the dry state due to additive use. However, as illustrated in **Figure 33**, the 2 wt.%$_{PVdF}$ LiTFA sample exhibits both regions of partial adhesion failure (A) and areas maintaining full adhesion (B).

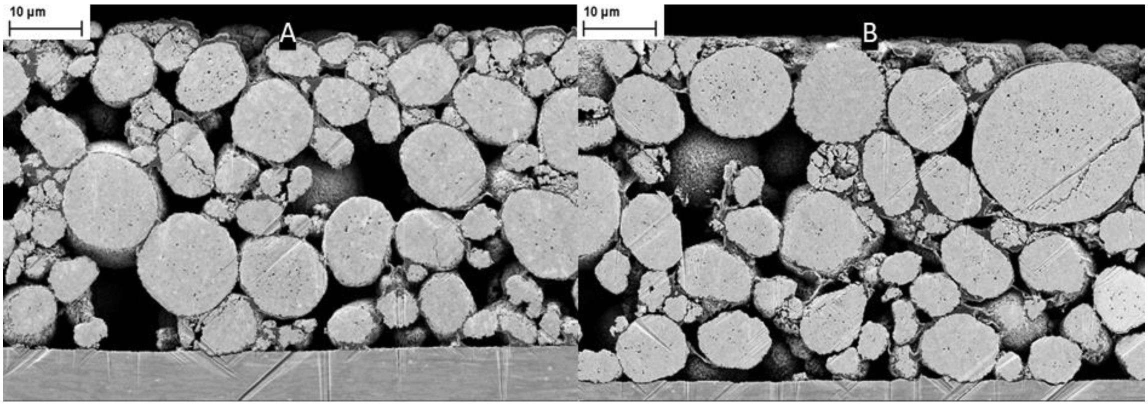

Figure 32. SEM micrographs of ion-milled cross-sections of pristine, calendered electrodes: (A) additive-free A and (B) 2 wt.%$_{PVdF}$ LiODFB[1]. Reproduced from F. Colombo et al.[1] with permission from the Royal Society of Chemistry.

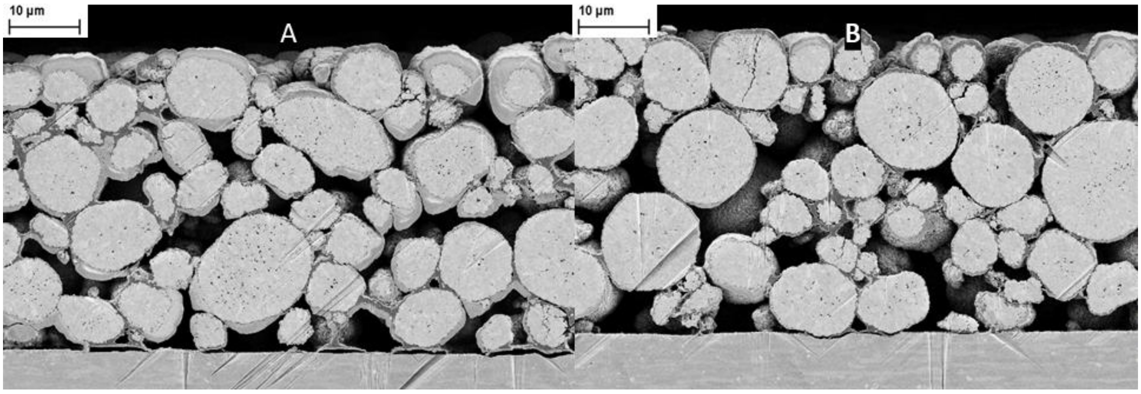

Figure 33. Ion-milled SEM cross-sections of pristine calendered electrodes with 2 wt.%$_{\mathrm{PVdF}}$ LiTFA, illustrating regions of partial delamination (A) alongside areas of intact adhesion (B). Reproduced from F. Colombo et al.[1] with permission from the Royal Society of Chemistry.

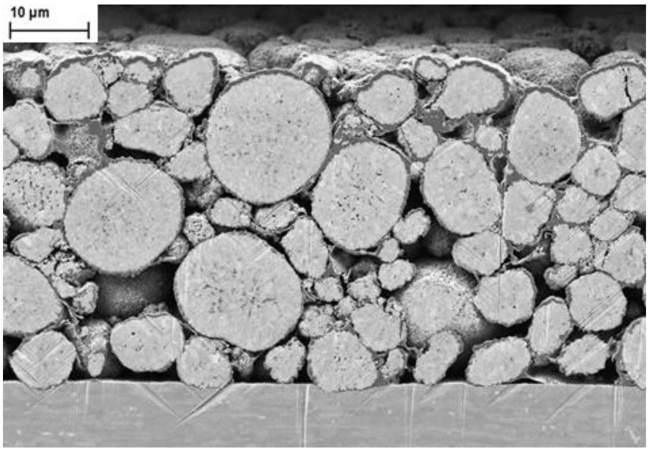

Figure 34. SEM micrographs of ion-milled cross-sections of pristine, calendered 2 wt.%$_{\mathrm{PVdF}}$ LiTFSI electrodes[1]. Reproduced from F. Colombo et al.[1] with permission from the Royal Society of Chemistry.

To elucidate the impact of slurry additives on cathode electrochemistry and interfacial properties, EIS was performed on fresh electrodes and on those retrieved after 1000 cycles[1]. The impedance data for fresh cathodes at 0.8 SOC, shown in **Figure 35,** depict the behavior for SOC values above 0.5.

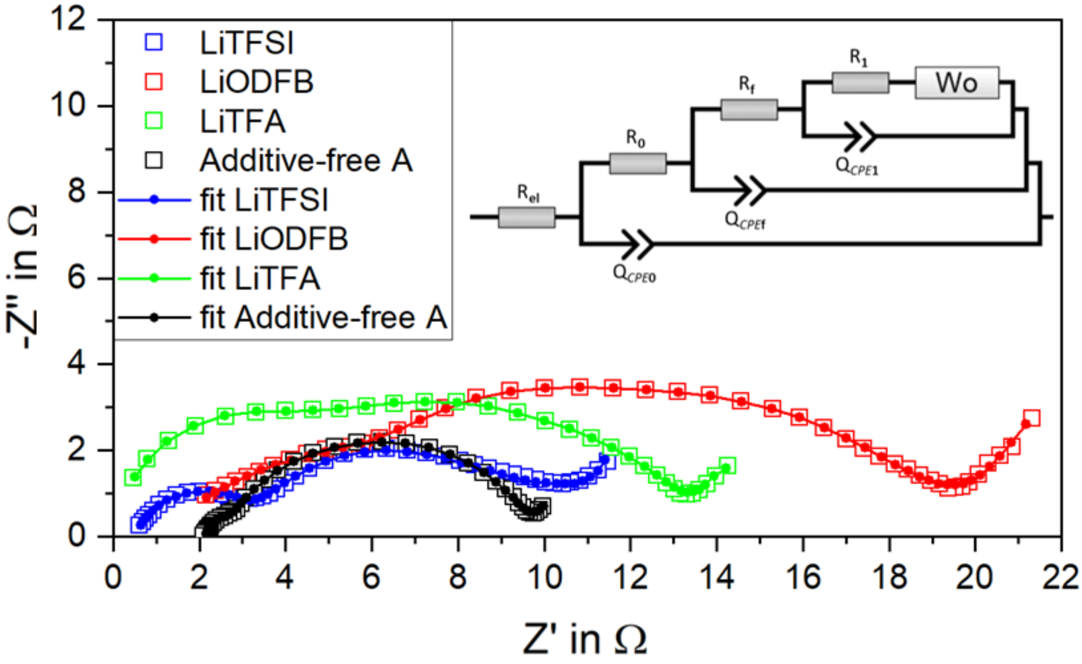

Figure 35. Nyquist plots (open squares) and fitted spectra (solid lines with markers) for fresh NMC622 electrodes at 0.8 SOC during the first cycle post-formation: additive-free A (black), 2 wt.%$_{\mathrm{PVdF}}$ LiTFA (green), 2 wt.%$_{\mathrm{PVdF}}$ LiODFB (red) and 2 wt.%$_{\mathrm{PVdF}}$ LiTFSI (blue). Data span 20 kHz to 50 mHz; the equivalent-circuit model is shown in the insert. The matching Bode plots are presented in **Figure S-6**, **Figure S-10**, **Figure S-11** and **Figure S-12**. Reproduced from F. Colombo et al.[1] with permission from the Royal Society of Chemistry.

At high SOC, the Nyquist plots undergo only minor alterations compared to the significant variations seen during initial charge (SOC < 0.5)[1]. The full impedance dataset covering for SOC=0.1 to SOC=1 can be found in **Figure S-5**, **Figure S-7**, **Figure S-8** and **Figure S-9**. Marked low-frequency variances at SOC = 0.1 and 0.2 highlight diffusion processes. For SOC ≥ 0.2, the charge-transfer arc at lower frequencies appears, and, as noted in studies[165–168], impedance falls steeply with increasing SOC[1]. The curves are fitted utilizing the SCRF[140] model (inset in **Figure 35**), and the comprehensive physical foundations of all components involved in simulating the equivalent circuit have been extensively covered beforehand. Using eight parameters often over-parameterizes the model when mid-to-low-frequency processes overlap[1]. As seen in **Figure 35,** the additive-free A sample (black curve) exhibits a small high-frequency arc due to contact impedance and a broad mid-to-low-frequency semicircle; this semicircle expands considerably in slurry-additive samples[1]. Except for the LiODFB sample, which exhibits two distinct RQ elements in this frequency range, the overlapping features in the other formulations introduce significant ambiguity in parameter fitting[1]. While formally defined for ideal capacitors rather than CPEs, relaxation frequencies can still be estimated: for $\alpha > 0.75$, the R·Q product approximates the relaxation frequency according to equation (7)[1].

Table 15. Average EIS fitting variables, each based on two separate impedance runs, at 0.8 SOC for 2 wt.$\%_{PVdF}$ LiTFA, 2 wt.$\%_{PVdF}$ LiODFB and 2 wt.$\%_{PVdF}$ LiTFSI cathodes at 33% porosity.

Sample	**R_{el} in Ω**	**R_0 in Ω**	**Q_{CPE0} in $S*s^{\alpha}$**	**α_{CPE0}**	**R_0Q_{CPE0} in s^{α}**	**R_f in Ω**	**Q_{CPEf} in $S*s^{\alpha}$**	**α_{CPEf}**	**R_fQ_{CPEf} in s^{α}**	**R_1 in Ω**	**Q_{CPE1} in $S*s^{\alpha}$**	**α_{CPE1}**	**R_1Q_{CPE1} in s^{α}**
additive-free A	1.3	0.5	9.8E-05	1	4.9E-05	3.9	2.4E-03	0.84	9.4E-03	2.1	2.7E-02	0.75	5.7E-02
LiTFA	0.3	5.7	2.2E-04	0.89	1.3E-03	6.2	4.3E-03	0.78	2.7E-02	3.3	4.9E-02	0.86	1.6E-01
LiODFB	0.4	3.2	3.9E-04	0.75	1.2E-03	10.0	2.6E-03	0.75	2.6E-02	4.7	4.2E-02	0.75	2.0E-01
LiTFSI	0.5	2.0	4.5E-04	0.78	9.0E-04	4.6	8.0E-03	0.75	3.7E-02	3.6	1.2E-01	0.75	4.2E-01

As **Table 15** indicates, the relaxation frequencies for RQ circuit pairs in the equivalent circuit differ by approximately an order of magnitude (R_0 to R_f, and R_f to R_1). In the additive-free A sample, R_fQ_{CPEf} and R_1Q_{CPE1} are separated by about half an order of magnitude, whereas R_0Q_{CPE0} and R_fQ_{CPEf} differ by two orders of magnitude. Notably, R_f and R_1 values remain within 2–10 Ω, complicating trend derivation[1]. More generally, the combined resistance R_f + R_1 reasonably correlates with long-term capacity retention. During equivalent circuit fitting, the CPE exponent α was restricted to 0.75 (ideal capacitors have $\alpha = 1$). The proximity of α to this limit indicates deviations attributed to factors like surface roughness, uneven reaction rates, and variable surface layer thickness[7]. In the additive-free A sample (**Figure 35**, black trace), the Nyquist plot exhibits a tiny high-frequency arc attributable to contact resistance and a broad mid-low-frequency semicircle all-encompassing surface-film and charge-transfer impedances. Incorporating additives conspicuously elevates both charge-transfer and interfacial resistances relative to the A reference. For the LiODFB (red), LiTFSI (blue), and LiTFA (green) samples (**Figure 35**), additives cause a visible high-frequency arc increase, with notable medium-low frequency arc expansion observed in LiODFB and LiTFA but, to a much lesser extent, in LiTFSI, which remains similar to the reference[1]. From an overall perspective, impedance and capacity retention rank as follows: LiODFB < LiTFA < LiTFSI < additive-free A.

Equivalent-circuit analysis in **Table 15** shows that R_0 (contact resistance) contributes most significantly to the impedance increase versus the additive-free A sample. The lowest R_0 occurs in the additive-free A formulation, with R_0 values increase in the sequence additive-free A < LiTFSI < LiODFB < LiTFA, while the uncompensated resistance (R_{el}) decreases in additive-containing samples, potentially due to enhanced ionic conductivity from Li-salts in electrode pores[1]. Although LiTFA has the largest contact resistance (R_0), both LiTFSI and LiTFA samples outperform the additive-free A and LiODFB variants in rate capability (**Figure 30A**).

EIS data highlight increased charge-transfer resistance (R_1) and surface film impedance (R_f) with additives compared to the reference. R_f significantly rises with LiODFB, while LiTFA and LiTFSI exhibit smaller increases, remaining higher than in additive-free A. Additive-bearing electrodes exhibit marginally higher R_1 values. As display in **Table 15**, R_f more than doubles with LiODFB and rises substantially with LiTFA, whereas LiTFSI shows R_f values close to the additive-free A sample. Differences in R_f likely result from varying NMC622 surface adsorption behaviors of Li-salt anions. Stronger adsorption of $ODFB^-$ correlates with the highest R_f for LiODFB, given its lower likelihood of forming passivating CEI layers due to high electrochemical stability[1]. Similarly, the Al current collector, with its naturally basic[19] Al_2O_3 surface, facilitates Li-salt adsorption through unsaturated oxygen sites. Higher R_0 values in LiODFB and LiTFA samples may stem from $Li^+/ODFB^-$ interactions on Al_2O_3, promoting PVdF adsorption and generating a negatively charged surface[1]. Conversely, reduced PVdF adsorption for LiTFSI and LiTFA likely results from positively charged surfaces with weaker anion adsorption, leading to lower adhesion values (**Table 14**).

SEM images of fatigued cathodes (**Figure 36**) reveal that, despite good dry-state adhesion in LiODFB, delamination occurs in all 2 $wt.\%_{PVdF}$ additive samples after 1000 cycles, whereas the additive-free A electrode retains intact Al/composite contact[1]. Significant cracking of the active material (AM) after extended cycling is evident primarily in the additive-free A sample (**Figure 36D**). The tendency for delamination observed in the post-mortem SEM cross-sections of Li-salt-containing electrodes (**Figure 36**) is likely linked to the exchange of Li-salt anions adsorbed at the Al current collector interface (Al/composite electrode) with electrolyte species (carbonate solvents/$LiPF_6$) during cycling[1]. Uniquely, the SEM cross-section of the 2 $wt.\%_{PVdF}$ LiTFA cathode shows distinct Al foil corrosion (**Figure S-23**), likely due to the acidic nature of this additive. EIS analysis of fatigued cathodes, performed after 1000 cycles (**Figure 36**), sheds light on cathodic capacity fade mechanisms. Two electrode samples per formulation were tested in a 3-electrode setup. Unlike initial measurements, mid- to low-frequency variances between electrodes of the same type have significantly increased, particularly in the LiODFB-containing samples, warranting a qualitative discussion[1]. EIS spectra exhibit consistent alterations in the high- and mid-frequency domains attributed to contact impedance, which is markedly elevated in fatigued, Li-salt-doped electrodes. Notably, the fatigued additive-free A cathode presents the smallest high-frequency semicircle, reflecting the lowest contact resistance, relative to its additive-bearing analogues[1]. Among these, the 2 $wt.\%_{PVdF}$ LiTFSI cathode shows the lowest contact resistance, consistent with single-cycle measurements (**Figure 35**), followed by 2 $wt.\%_{PVdF}$ LiTFA, and the 2 $wt.\%_{PVdF}$ LiODFB, which exhibits the largest impedance increase[1].

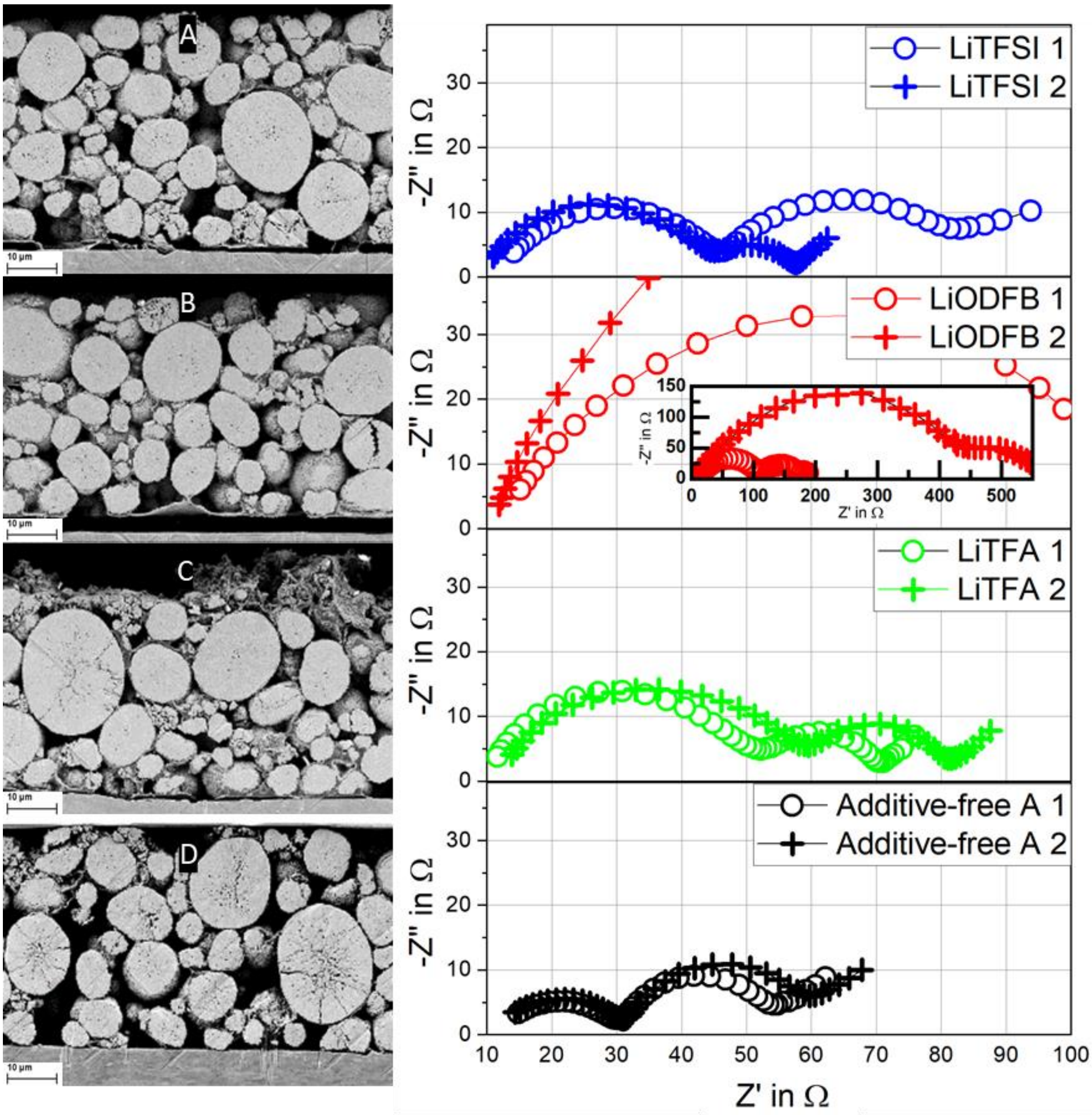

Figure 36. Left: post-mortem SEM of ion-milled cross-sections of electrodes fatigued for 1000 cycles: 2 wt.%$_{PVdF}$ LiTFSI (A), 2 wt.%$_{PVdF}$ LiODFB (B), 2 wt.%$_{PVdF}$ LiTFA (C) and additive-free A (D). Right: corresponding Nyquist spectra (two cells each) acquired at 0.8 SOC after 1000 cycles, over 20 kHz -50 mHz, for NMC622 cathodes with the above additives and additive-free A. Bode plots are given in **Figure S-18**, **Figure S-19**, **Figure S-20**, **Figure S-21**. Reproduced from F. Colombo et al.[1] with permission from the Royal Society of Chemistry.

SEM cross-sectional micrographs of post-mortem electrodes samples (**Figure 36** and **Figure S-23**) show that elevated contact resistance in Li-salt-doped samples corresponds to weakened Al/composite adhesion. In the mid–low frequency region, dominated by surface-film and charge-transfer processes, the semicircle diameters for 2 wt.%$_{\text{PVdF}}$ LiTFSI, 2 wt.%$_{\text{PVdF}}$ LiTFA, and the additive-free A cathode are statistically indistinguishable. Nevertheless, EIS confirms that the increase in contact resistance at the Al current collector is the principal factor in impedance growth during prolonged cycling of Li-salt-containing electrodes[1]. Poor adhesion between PVdF and the Lewis-basic oxide surface of the Al collector likely contributes to these trends. Interestingly, while LiODFB achieves superior dry-state adhesion, its fatigued samples exhibit the highest contact resistance, indicating adhesion failure over time. These findings indicate that anion exchange between the coating and the electrolyte governs adhesion. Enhanced ODFB$^-$ adsorption during casting accounts for LiODFB's strong initial adhesion, but its accelerated exchange with electrolyte anions drives rapid contact loss upon cycling[1]. This hastened delamination elevates contact resistance by promoting Al passivation through $LiPF_6$ decomposition[1].

Table 16. EDS of anodes retrieved from their respective pouch cells and matching with 2 wt.%$_{\text{PVdF}}$ LiTFA, 2 wt.%$_{\text{PVdF}}$ LiODFB, 2 wt.%$_{\text{PVdF}}$ LiTFSI and additive-free A cathodes, respectively. The elemental composition of the fatigued anode surface (**Figure S-22**) after cycling for more than 1000 cycles is summarized.

Element	Atom in % - anode of LiTFA	Atom in % - anode of LiODFB	Atom in % - anode of LiTFSI	Atom in % - anode of additive-free A
C	80,4	84,1	82,4	82,0
O (SEI)	17,6	13,3	14,3	12,9
O (Sep. Particle)	0,2	0,8	1,1	2,0
F	1,1	0,9	0,9	1,1
P	0,5	0,3	0,4	0,4
Na	0,1	0,1	0,1	0,1
Al	0,1	0,5	0,6	1,1
Si	-	-	0,2	0,3
Ni, Mn, Co	-	-	-	-

SEM cross-sections of fatigued electrodes (**Figure 36**) show minimal NMC622 particle cracking in Li-salt-modified samples, in contrast to the pronounced fractures observed in the additive-free A cathode. **Figure 31**'s dQ/dV analysis suggests that active material loss, lowered overpotentials, and a smaller R_0 combine to suppress impedance growth in additive-free A sample. Conversely, the increased insulating layers at the Al/composite interface, attributed to additives, promote active material loss and capacity fading[1]. Post-mortem EDS analysis of anodes, which are previously retrieved from their respective pouch cells and immersed in excess DMC to remove residual electrolyte (**Table 16**) shows elevated oxygen levels in additive-containing cells, particularly LiTFA. This higher oxygen content indicates increased SEI formation during cycling. Although transition metal migration (Ni, Mn, Co) from cathode to anode remains below EDS detection limits, even trace dissolution could accelerate SEI growth. Transition metals chemically react with SEI components, degrading its structural integrity, leading to crack formation, consuming lithium ions, and forming inorganic passivation debris [174–177] . Mn^{2+} ions, for instance, can deplete ~100 additional lithium ions per ion [178], accelerating cyclable lithium loss. In dQ/dV curves, small anodic peaks absent during initial cycles (green arrows, **Figure 31**) develop with cycling in LiTFA and LiODFB samples, and to a lesser extent in LiTFSI. These peaks, correlated with SEI formation, suggest Li plating[107] at the graphite anode. LiTFA's pronounced oxygen levels and anodic peaks reinforce this link. Additionally, co-intercalation[1] of TFA^- or similar anions into graphite layers may lead to structural exfoliation or disintegration due to gas evolution, further damaging the negative electrode [179].

4.3 Impact of mixing

In the preceding chapters it was envisaged how the use of the additive may promote improved deagglomeration of carbon black compared to the additive-free A sample, potentially promoting a more favorable binder adsorption onto the carbon black surface. This is hypothesized to reduce bridging flocculation in the colloidal slurry system, thus allowing processing of high SC slurries with time delayed onset of slurry gelation. Such topic is explored in this chapters, where the impact of modified carbon black deagglomeration on slurry gelation is thoroughly examined. A refined mixing technique, referred to as Mixing 2^{ND}, is introduced as an alternative processing method to assess how improved CB deagglomeration influences slurry gelation behavior at elevated SCs. As described in the experimental section, this technique, performed at high SC, enhances CB deagglomeration by maximizing stress transfer in the denser medium, increasing collision frequency and friction due to reduced interparticle spacing and solvent usage[20,21]. With improved CB deagglomeration, this mixing method is combined with formulations that feature lower CB loadings, allowing investigation into how reduced conductive additive content influences the upper boundary of the SC processability window for electrode casting without rapid gelation. Additionally, the effects of enhanced CB deagglomeration and reduced CB loadings on electrical conductivity in uncalendered electrodes are explored, with a focus on determining the optimal calendering degree required to restore ideal conductivity. EIS after formation cycles is performed on the resulting cathodes as a mean to evaluate the impact of calendering on the resulting electrochemical performances. High-rate capability and the long-term cycling performances are explored in the reduced electrode porosity range from 27% to 15%.

4.3.1 Gelation behavior with PVdF type A and B and reduced CB

PVdF Type A and PVdF Type B are employed to formulate the 1wt.%$_{C65}$A and 1wt.%$_{C65}$B slurries, respectively, using Mixing 2^{ND}. This method enables the creation of formulations with exceptionally high solid contents (SCs), specifically 80.0 wt.% SC for both 1wt.%$_{C65}$A and 1wt.%$_{C65}$B slurries, as outlined in **Table 17** and delineated in **Table 2**. Despite the application of very high SCs, neither slurry undergoes significant gelation immediately after mixing, facilitating smooth processing during electrode manufacturing. Both mixtures maintain a predominantly fluid-like consistency throughout the casting process. When emulsion-polymerized PVdF Type A is utilized for the 1wt.%$_{C65}$A slurry, an initial low viscosity of 1.3 Pa*s is recorded immediately after mixing, as shown by the corresponding flow curves in **Figure 37** (depicted in blue). However, **Figure 37B** shows that, following a 3-day rest, the slurry's viscosity surges by 715% due to gelation, despite its initially low viscosity.

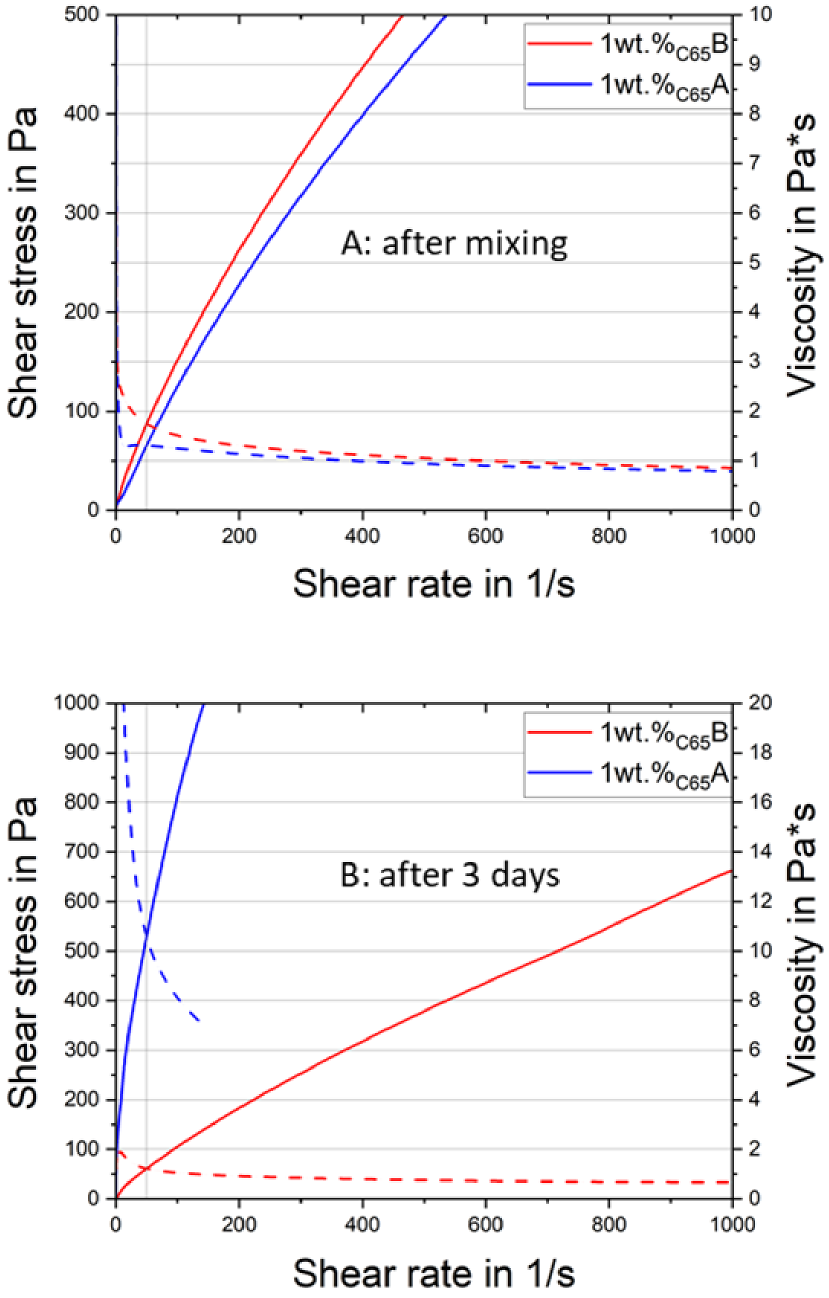

Figure 37. A: Flow (solid) and viscosity (dashed) profiles immediately after Mixing 2^{ND} of NMP slurries encompassing NMC622 powder, high-Mw PVdF, carbon black for the 1wt.%$_{C65}$A and the 1wt.%$_{C65}$B samples. The 1wt.%$_{C65}$A and the 1wt.%$_{C65}$B slurries have a SC of 80.0 wt.%. B: The same flow and viscosity measurements after three days' storage[1].

The amplitude sweeps for the 1wt.%$_{C65}$A formulation reveal that the slurry reaches a predominantly fluid state shortly after mixing. This observation is illustrated in **Figure 38A**, represented by the blue curves, where the loss modulus G" consistently exceeds the storage modulus G' across the entire shear strain range.

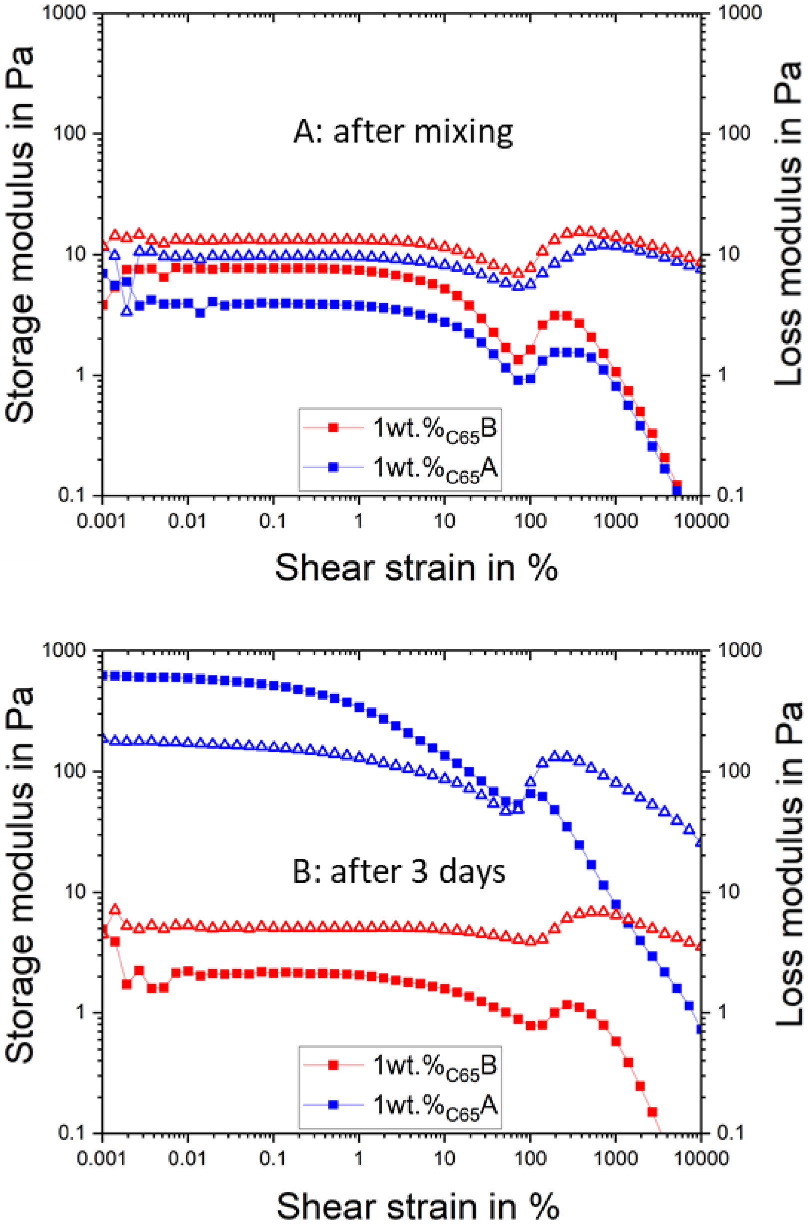

Figure 38. A: Amplitude sweeps (G′ ■, G′′ ▲) at $\omega=10s^{-1}$ immediately after Mixing 2^{ND} of NMP-based slurries encompassing NMC622 powder, high Mw PVdF, carbon black for the 1wt.%$_{C65}$A and the 1wt.%$_{C65}$B samples. The 1wt.%$_{C65}$A and the 1wt.%$_{C65}$B slurries have a SC of 80.0 wt.%. B: The same amplitude sweeps recorded after three days of storage[1].

After a three-day storage period, it becomes clear that the 1wt.%$_{C65}$A slurry sample has developed a strong gel network, as indicated by G´ dominating over G′′ in the low shear rate LVR region of the amplitude sweeps measurements (**Figure 38B**). By calculating the energy of the aggregated state using equation (1), a significant E_{coh} value of 2.5 mJ/m^3 vividly demonstrates the impact of gelation at the very high 80.0 wt.% SC. This characteristic suggests that the slurry may maintain stability during extended storage periods, and if the strength of its aggregated state is sufficiently high, the settling of active materials is improbable to follow. Conversely, under equal composition, Mixing 2 ND parameters (**Table 2**), and SC, the 1wt.%$_{C65}$B slurry incorporating suspension-polymerized PVdF Type B binder shows noticeable settling only after three days. Indeed, despite the slightly higher initial slurry viscosity of 1.7 Pa*s for the 1wt.%$_{C65}$B slurry compared to the 1wt.%$_{C65}$A sample, the former formulation exhibits a notable reversed chronological evolution, experiencing a significant -30% decrease in viscosity after three days of storage. This progression is testified by the flow curves measured after three days of storage, as depicted in **Figure 37B** and summarized in **Table 17**. In the amplitude sweeps measurements of the freshly mixed 1wt.%$_{C65}$B sample (**Figure 38A**), a predominantly liquid-like nature is evident. Even after allowing the slurry to rest for three days, the 1wt.%$_{C65}$B sample continues to show the absence of a gel network, as indicated by its prevailing liquid-like nature, still discernible in the corresponding amplitude sweeps measurement (shown in **Figure 38B**). Furthermore, in this measurement, both G′ and G" exhibit decreased magnitudes compared to the corresponding amplitude sweep performed just upon mixing. An insufficient gel network robustness fails to prevent the sedimentation of active material particles, thus correlating with the aforementioned viscosity decrease observed in the respective flow curves. These findings suggest that slurries formulated with PVdF Type B binder cannot sustain stability over extended storage periods.

Table 17. Rheological profiles of NMP slurries generated by Mixing 2ND with NMC622 powder, PVdF Type A or Type B binder and carbon black, recorded immediately after mixing and after three days' storage.

Slurry sample	η in Pa*s at 50s^{-1} - 0h	η in Pa*s at 50s^{-1} - 3days	E_{coh} in mJ/m^3 - 0h	E_{coh} in mJ/m^3 - 3days	Yield stress in Pa - 0h	Yield stress in Pa - 3days
1wt.%$_{C65}$A	1.3	10.6	-	2.5	-	16
1wt.%$_{C65}$B	1.7	1.2	-	-	-	-
1wt.%$_{C65}$B II	7.4	5.0	3.4	5.1	7	7
1wt.%$_{C65}$B III	33.1	35.0	20.9	23.0	116	217

Due to the lack of robust aggregated gel formation at 80.0 wt.% SC after mixing, higher SCs are required when using suspension-polymerized PVdF Type B binders in the slurry-making process, so that to allow the establishment of a formulation that may effectively prevent AM sedimentation. Thus, to investigate the impact of gelation on high SC slurries with PVdF Type B, three different samples are generated using the same composition and Mixing 2 ND (as delineated in **Table 2**), with incrementally higher SCs, namely 1wt.%$_{C65}$B at 80.0 wt.% S.C., 1wt.%$_{C65}$B II at 82.5 wt.% S.C. and 1wt.%$_{C65}$B III at 85.0 wt.% S.C. Immediately after mixing, the three samples demonstrate that the viscosity increases noticeably with increasing SC, following a progression from 1.7 Pa*s to 7.4 Pa*s and finally to 33.1 Pa*s, corresponding to 80.0 wt.%, 82.5 wt.%, and 85.0 wt.% SC, respectively. However, the viscosity recorded after three days of slurry storage demonstrates a strikingly different trend for the formulations at lower SCs (i.e., 80.0 wt.% and 82.5 wt.%) compared to the 1wt.%$_{C65}$B III sample at 85.0 wt.% SC. Specifically, the formulations at 80.0 wt.% and 82.5 wt.% SC exhibit a similar decrease in viscosity after three days of storage, amounting to approximately -30% and -32%, respectively. In contrast, the 1wt.%$_{C65}$B III sample at 85.0 wt.% SC demonstrates a notable increase in viscosity associated with gelation, registering a modest +6% (as depicted in **Figure 39** and detailed in **Table 17**).

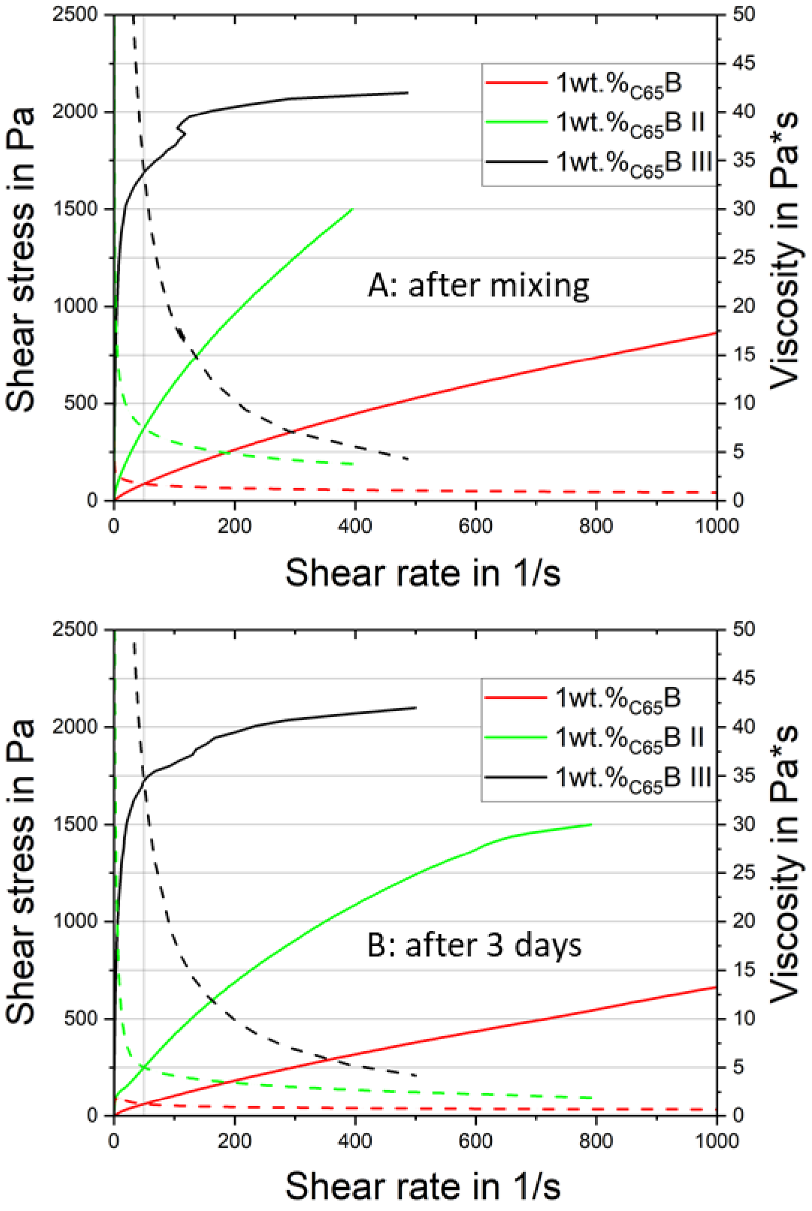

Figure 39. A: Flow (solid) and viscosity (dashed) profiles immediately after Mixing 2ND of NMP slurries encompassing NMC622 powder, high-Mw PVdF Type B, carbon black for samples at different SCs; i.e. 1wt.%$_{C65}$B at 80.0 wt.% S.C. (red), 1wt.%$_{C65}$B II at 82.5 wt.% S.C. (green) and 1wt.%$_{C65}$B III at 85.0 wt.% S.C. (black). B: The same flow and viscosity measurements after three days' storage[1].

Remarkably, despite the exceptionally high 85.0 wt.% SC applied and the surprisingly high initial viscosity reading of 33.1 Pa*s, only a minor viscosity increase related to gelation is observed after allowing the slurry to rest for three days. Kinks appearing between 100 and 200 s^{-1} in the 1wt.%$_{C65}$B III flow curve arise from wall slip, as excessive viscosity breaks contact with the rheometer plate. Amplitude sweep performed on the 80.0 wt.% sample right after slurry mixing (depicted by the red curve in **Figure 40A**) shows a predominantly liquid-like behavior, with the loss modulus G" dominating across the entire shear strain range.

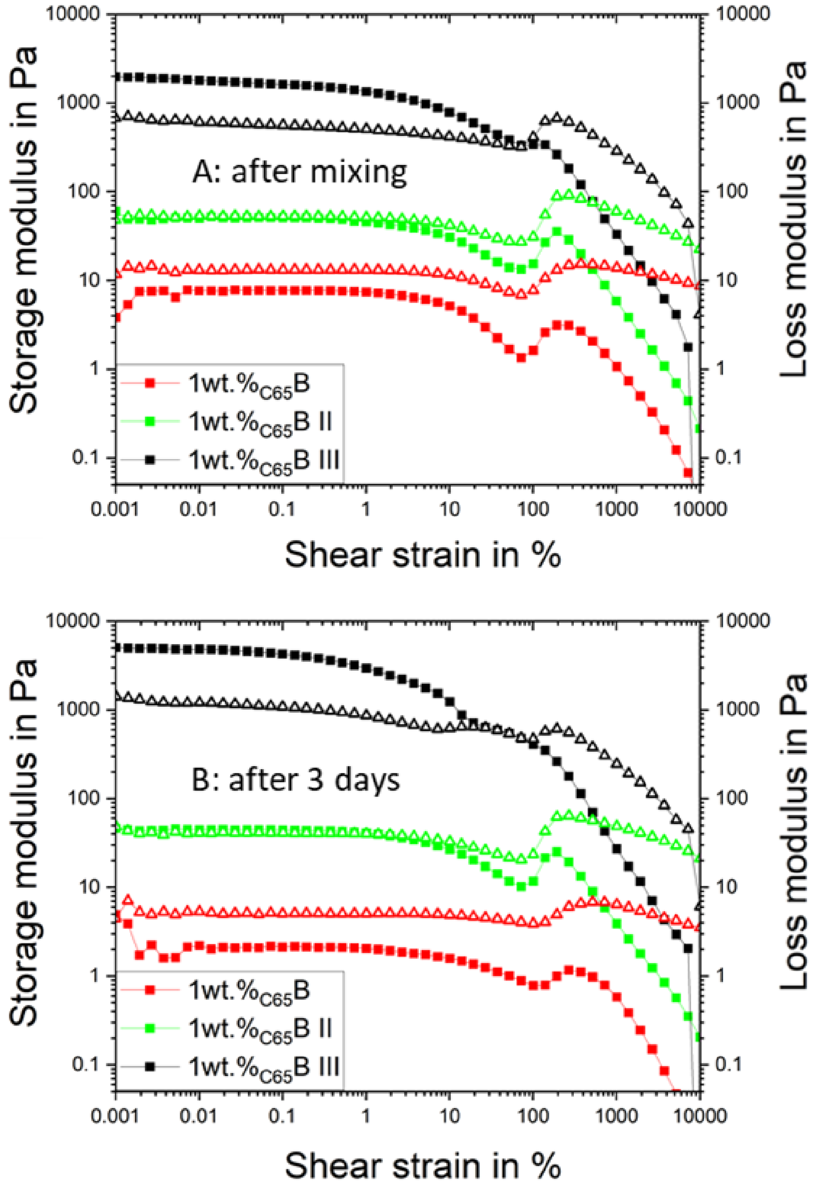

Figure 40. A: Amplitude sweeps (G' ■, G'' ▲) at ω=10s^{-1} immediately after Mixing 2ND of NMP-based slurries encompassing NMC622 powder, high Mw PVdF, carbon black for samples at different SCs; i.e. 1wt.%$_{C65}$B at 80.0 wt.% S.C. (red), 1wt.%$_{C65}$B II at 82.5 wt.% S.C. (green) and 1wt.%$_{C65}$B III at 85.0 wt.% S.C (black). B: The same amplitude sweeps recorded after three days of storage[1].

Even after three days of slurry storage, the 80.0 wt.% SC sample continues to exhibit a liquid-like behavior, characteristic of a slurry lacking a gel network. This absence of a stabilizing gel network contributes to the viscosity decrease observed in the previously analyzed flow curves, facilitating the sedimentation process of the active material (AM) particles. In contrast, upon chronological analysis of the amplitude sweeps at the significantly higher SC of 82.5 wt.%, mild gelation-driven effects become noticeable soon after mixing, wherein the slurry sample shows simultaneously both liquid and solid like behaviour. Notably, in the amplitude sweeps measurements of the freshly mixed 82.5 wt.% SC sample (**Figure 40A**), neither a predominant liquid nor solid like character can be distinguished, with the loss modulus G" almost overlapping the storage modulus G′ across the entire shear strain range. Interestingly, despite G" lying just upon G′, both moduli are closely matched and share nearly the same magnitude. Immediate post-mixing calculations yield an aggregated-state energy of 3.4 mJ/m^3, as detailed in **Table 17**. This progression is notably reflected in the flow curves observed after three days of storage, as depicted in **Figure 40B** and outlined in **Table 17**. Indeed, after three days of slurry storage the 82.5 wt.% SC sample still exhibits a weak gel network, with G´ lying just upon G′′ in the low shear rate LVR region of the amplitude sweeps measurements (**Figure 40B**). G´ and G′′ still remain closely aligned in values, with both moduli resembling those measured soon after mixing. Calculating the energy of the aggregated state after storage reveals a marginally higher value of E_{coh} =5.1 mJ/m^3, highlighting mild gelation-driven effects at the high SC of 82.5 wt.%. It is noteworthy that this slight increase in E_{coh} is attributed to the more extended LVR region compared to the amplitude sweeps measured immediately after mixing. The absence of a robust slurry gel network, coupled with reduced viscosity after allowing the formulation to rest for three days, suggests that the 82.5 wt.% SC sample containing the PVdF Type B binder is unlikely to maintain stability over prolonged storage periods, thus allowing AM sedimentation.

When examining the formulation at the exceptionally high solid content of 85.0 wt.%, gelation-driven effects become apparent immediately after mixing. This is evident in the predominant gel-like consistency of the slurry coupled with its high viscosity. Upon analyzing the amplitude sweeps of the 85.0 wt.% SC formulation, a robust slurry gel network is quickly established after the mixing process. This behavior is clearly demonstrated in **Figure 40A**, represented by the black curves, where the storage modulus G′ consistently dominates throughout the entire low shear strain region. By calculating the energy of the aggregated state immediately after mixing and after slurry storage, as reported in **Table 17**, the evolution over time of gelation-driven effects is followed. The energy of the aggregated state after mixing already exhibits a notable value of E_{coh}, precisely 20.9 mJ/m³. This highlights the significant impact of the rapid gelation of the slurry, occurring shortly after the mixing process. After a three-day storage period, the 85.0 wt.% slurry sample forms a stronger gel network, as indicated by G´ more dominantly surpassing G′′ in LVR region of the amplitude sweeps measurements (**Figure 40B**). A more noticeable distinction between the two moduli becomes apparent in the low shear strain region compared to the corresponding measurement immediately after the mixing process. Interestingly, upon computing the energy of the aggregated state, the E_{coh} value demonstrates a noteworthy increase of +10%, reaching 23.0 mJ/m³. This moderate rise in E_{coh} is a direct consequence of a less extended LVR region, which partly compensates for the substantial increase in the G´

modulus after allowing the slurry to rest for three days. The swift formation of a slurry gel, coupled with high viscosity, strongly indicates that the formulation is likely to retain stability over extended storage periods. This is attributed to its robust colloidal aggregated structure, which may prevent the segregation of slurry components and potentially mitigate AM sedimentation.

Comparing PVdF Type B and PVdF Type A at the same solid content reveals that emulsion-polymerized PVdF Type A induces rapid slurry gelation, whereas suspension-polymerized PVdF Type B binder fails to induce sufficient gelation, possibly resulting in sedimentation of the active material particles. The variation in rheological behavior observed between emulsion-polymerized PVdF-based slurries (PVdF Type A) and formulations utilizing suspension-polymerized binders (PVdF Type B) under identical conditions stems from a shift in the processability window's boundary. This shift is delineated by a distinct solid content threshold for each binder, at which the strong slurry gelation occurs, in consistency with conclusions drawn in earlier sections of this thesis. Therefore, as extensively discussed in the preceding chapter on the properties of additive-free slurries, also here, by application of Mixing 2^{ND} and the same solid content (SC), emulsion polymerized PVdF Type A induces rapid slurry gelation, while suspension polymerized PVdF Type B does not, leading to potential sedimentation of active material particles. This difference in rheological behavior at the same composition and SC for emulsion polymerized PVdF-based slurries (PVdF Type A) in comparison to slurries based on suspension polymerized binders (PVdF Type B) aligns with observations from previous literature[142]. The study also shows that at a higher 85.0 wt.% SC, PVdF Type B can trigger gelation after storage, although with different processability characteristics compared to PVdF Type A. Both binders face handling issues and compromised processability due to insufficient or excessive slurry gelation at certain SC levels. PVdF Type B stores less elastic energy, offering easier processing at higher SCs but potentially reducing segregation resistance and not hampering active material particle sedimentation. As previously discussed, the rapid gel-forming strength of PVdF Type A may be attributed to its macromolecular characteristics, which enhance structural strength but may limit the maximum SC for effective slurry processing.

When PVdF Type A is used in the production of the $1wt.\%_{C65}A$ slurry with Mixing 2^{ND}, the enhanced mixing produce results in a formulation with a remarkably high SC, specifically 80.0 wt.%, as detailed in **Table 17**. Following the aforementioned analysis of the amplitude sweeps for the $1wt.\%_{C65}A$ formulation, it becomes apparent that a prevailing liquid-like slurry is established soon after the mixing process, while a robust gel network develops only after a storage period of three days, as indicated by the calculated energy of the aggregated state of E_{coh} value of 2.5 mJ/m^3. Albeit a direct comparison is not possible owing to different compositions, the $1wt.\%_{C65}A$ slurry with 1wt.% of CB is qualitatively compared to the additive-free A slurry encompassing 1.5wt.% of CB, which was tested in the preceding chapters, in order to assess the influence of varying CB loadings on the slurry gelation behavior. To be noted that the additive-free A slurry has an increased binder content of 1.5wt.% PVdF Type A, in comparison to the 1wt.% PVdF Type A used for the $1wt.\%_{C65}A$ sample; both formulations sharing the same C65 to PVdF ratio, as detailed in **Table 1** and **Table 17**. Remarkably, when PVdF Type A is used to produce the additive-free A slurry sample at much lower 70 wt.% SC with Mixing 1^{ST}, gelation onset is so fast that a stiff gel is present already a few minutes after mixing. Even though a dissolver mixing step is applied to re-fluidize the additive-free A slurry just before casting, the sample returns to its gel-like state a few minutes after re-mixing. In fact, the gel network has an impressive cohesion energy of E_{coh}=25.0 mJ/m^3 just upon mixing and this value further increases to E_{coh}=97.6 mJ/m^3 whenever the formulation is left to rest for 3 days (**Table 17**). In conclusion it was shown in this chapter that enhancing CB deagglomeration by applying an improved mixing coupled with reduced CB contents in the formulation is a valuable strategy to increase the upper boundary of the SC processability window for electrode casting without rapid gelation for PVdF Type A at 80.0 wt.%. At the same time, this strategy also enables the application of exceedingly high 85.0 wt.% SC for PVdF Type B, so that to counteract the insufficient slurry gelation induced by this binder type.

For the sake of clarity, carbon black (secondary) aggregates will be often referred to as carbon black particles henceforth. In a study[77] involving polymer-carbon black composites, researchers have noted that, when considering a specific weight of carbon black, finer aggregates contribute to a more even distribution of particles within a given volume of plastic. While reduced distances between particles can enhance electron transfer efficiency, uniform dispersion alone may lead to identical particle spacing, breaking contact and thereby hindering conductivity. Therefore, optimal electron conductivity is achieved when carbon black particles are finely dispersed, yet maintaining close contact, ideally forming one-dimensional chains that preserve conductive pathways or fractal-like structures. In the context of a consistent mixing procedure that results in an identical distribution of carbon black aggregates within a polymer matrix, it has been observed that the viscosity of the medium emerges as the primary determinant governing the kinetics of carbon black flocculation. In a polymeric medium characterized by its low viscosity (≈0.5 Pa·s), carbon black aggregates readily diffuse and give rise to loosely structured agglomerates. As the carbon black loading increases, these agglomerates expand, eventually forming a conductive network. Conductivity experiences a rapid surge upon the formation of the CB network. Accordingly, a carbon black threshold loading can be delineated as the minimum quantity necessary to initiate percolation[77]. On the contrary, in a polymeric matrix marked by high viscosity (≈60 Pa·s), the diffusion of aggregates notably slows down, and the formation of structured agglomerates comes to a halt. Therefore, under the conditions of this study[77], achieving a conductive network hinges on the interconnection of individual carbon black aggregates so that, in polymeric matrices with high viscosity, higher carbon black loadings are usually required to attain the percolation threshold.

Another study explored the influence of carbon black on a styrene-butadiene rubber (SBR) matrix. It revealed that CB particles with slightly smaller diameter or higher surface roughness resulted in superior reinforcing properties[180]. The interfacial interaction mechanism of the CB/SBR nanocomposites was thoroughly examined. These nanocomposites feature a bound rubber layer with a dual-layer structure: a tightly bound rubber layer in direct connection to the CB surface and a loosely bound rubber layer. Within the tightly bound rubber layer, SBR molecules strongly adhere to the CB surface, and the polymer strands experience a significant reduction to their mobility. In this layer, the molecular chains are densely packed. Instead, in the loosely bound rubber layer, although not directly in contact with the CB surface, the polymer segments are intricately entangled with the tightly bound rubber layer[180]. As outlined in earlier studies[181–184] the configuration of surface adsorbed rubber chain comprises trains, loops and tails. The polymer portion in train conformation intimately adhere to the particle surface throughout their entire length and they are limited in mobility. Polymeric loops have both the extremities pinned to the particle surface and, depending on their extension, they normally possess enhanced mobility. Finally, the polymer strands called tails have only one extremity anchored to the particle surface, thus showing notably higher mobility, akin to free rubber chains. Together, these elements collectively shape the dynamic features of the adsorbed polymer chains. In the context of polymers with low adsorption tendencies, extended loops or tails tend to dominate, whereas for high adsorption energy, a larger portion of the polymer chains are in direct contact with the surface, in train conformation[104]. Employment of carbon blacks with increased surface roughness or with slightly diminished diameter fosters the creation of a greater number of loops. This occurrence can be primarily attributed to the augmented contact area between carbon blacks and rubber. Moreover, an increased surface roughness engenders additional grooves on the carbon black surface, thus promoting a better adsorption of the polymeric rubber chains. Consequently, an augmented density of loops emerges on the carbon black surface, owing to its expanded surface area[180]. In essence, the tightly bound rubber can be adsorbed in a more stretched configuration, forming a greater number of trains and an increased density of more compact loops, which protrude less into the surrounding solution. The thickness of the loosely bound rubber layer is chiefly governed by the properties of the tightly bound rubber layer, specifically by its chain density and by the abundance of its loops. A heightened density of loops translates into an increased overall rubber density in the loosely bound layer, particularly when carbon blacks with an expanded surface area are used. Consequently, the utilization of higher surface area carbon blacks result in CB/SBR composites featuring a greater proportion of immobilized rubber chains, owing to their enhanced ability to strongly restrict the interfacial chain mobility[180]. The same mechanism can be transferred to the C65-PVdF domains in the slurry system, as depicted in **Figure 41**.

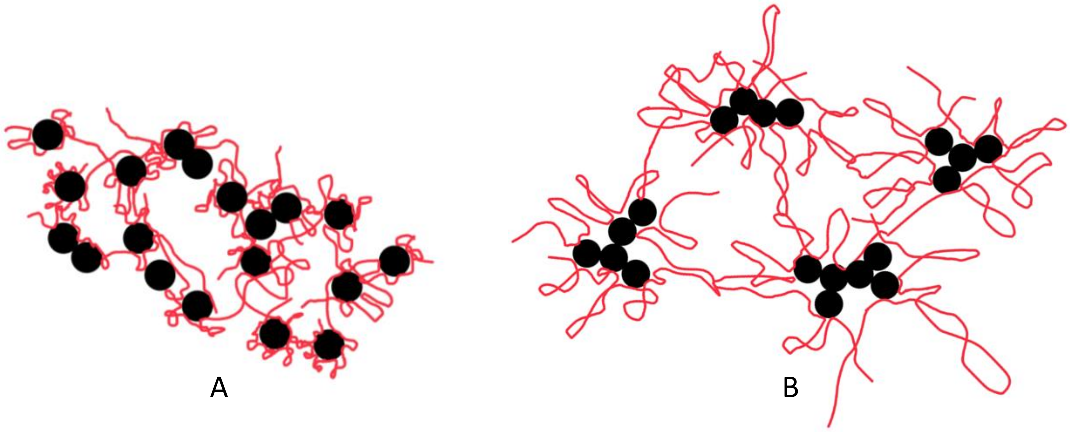

Figure 41. C65-PVdF colloidal domains in the slurry system. A: The CB particles are in an enhanced dispersed state, thus forming finer agglomerates with PVdF. In this case, the binder can better adsorb with a significantly higher portion of the polymer in train conformation and an increased number of 'compact' loops, which are in close proximity of the CB surface. The better entanglement of the polymer chains between adjacent CB particles can promote a more immobilized colloidal system with impaired carbon flocculation kinetics. B: The CB particles are in a worse dispersed state and they are present as flocculated agglomerates. The PVdF binder cannot be properly adsorbed onto the CB particles, thus forming less trains and a higher portion of tails and loops, which are protruding into the solution to a greater extent. The overall coiled PVdF cannot properly adsorb on different CB aggregates, thus resulting in a less immobilized system with unhindered carbon flocculation kinetics.

Indeed, the PVdF binder can be better adsorbed when CB particles are in an enhanced dispersed state, thus forming finer agglomerates. Consequently, the PVdF binder can adopt a more stretched conformation in the colloidal CB-PVdF domains, with more portions of the polymer in train conformation and an increased number of loops. An augmented number of loops in the close proximity of the CB surface can provide more pinning points for other polymer chains in the dispersion, thus providing an overall better and tighter entanglement of polymer chains between adjacent CB particles. Moreover, the overall better stretched conformation of the binder can allow the PVdF to adsorb on a higher number of different CB aggregates, therefore promoting a more immobilized colloidal system with impaired flocculation kinetics.

Previous findings[68] indicated that, within a carbon black-polymer NMP slurry, the interplay between attractive and repulsive forces among CB particles is largely regulated by the steric interactions between adsorbed polymer layers. These interactions are intricately tied to the molecular weight of the binder in use. When dealing with a low-molecular-weight polymer, the flocculation of CB particles happens swiftly, thus yielding low-density agglomerates, which are characterized by a more open structure. Conversely, as the molecular weight rises, the polymer's length increases, so that to foster the CB particles to coalesce into compact agglomerates, wherein the particles are more effectively immobilized and better packed. The morphology of the carbon black agglomerates plays a pivotal role in determining the final CB percolation network. Indeed, low-density agglomerates with a more open structures have a greater tendency to collide and intertwine in a network, when compared with compact agglomerates[185]. As a result, whenever low-molecular-weight PVdF (e.g. Mw=280.000 g/mol) is employed for carbon black dispersions, low-density agglomerates are formed, thus resulting in a better CB percolation network in the slurry state, when compared to high molecular weight grades of PVdF (e.g. Mw=1.000.000 g/mol)[185]. Interestingly, it is hypothesized that the enhanced Mixing 2ND, speculated to enable superior C65 deagglomeration, could promote a more stretched PVdF binder conformation. If true, this might mimic the effect of using higher Mw binders and thus yielding a weaker CB percolation network in the slurry state, when compared to Mixing 1ST. Hence, the enhanced Mixing 2ND procedure attains a superior state of carbon black dispersion, thereby postponing a rapid CB network formation in the slurry colloidal phase. Consequently, as demonstrated in the following chapter, a more intensive calendering process in the dry state, in comparison to Mixing 1ST, is necessary to generate an effective percolating network capable of connecting the better dispersed CB particles.

4.3.2 Electrochemistry of electrodes featuring improved CB deagglomeration and reduced CB loadings

The 1wt.%$_{C65}$B cathodes are manufactured using PVdF Type B and the enhanced Mixing 2ND, all exhibiting a modest AM loading of approximately 12 mg/cm². The composition details for the 1wt.%$_{C65}$B samples are outlined in **Table 2,** and pertinent data regarding the manufacturing process of the resulting coatings can be found in **Table 18**.

Table 18. Summary of mass loading, thickness, porosity, resistance, and adhesion for tested cathodes, evaluated before and after calendering and, if applicable, following heating treatment (FHT)[1].

Electrode sample	Mass loading in mg/cm^2	Thickness in µm	Porosity in %	Resistance in Ω - cal	Adhesion in N/m - uncal	Adhesion in N/m - cal	Adhesion in N/m - FHT
1wt.%$_{C65}$B	12.0	37.0	27	52	33.6	28.4	33.4
	11.8	33.6	21	49	33.6	27.1	29.8
	11.5	30.4	15	46	33.6	30.6	37.3
1wt.%$_{C65}$A	12.0	31.9	15	39	26.2	21.0	26.7

As discussed in the preceding section, the utilization of Mixing 2^{ND} generates a more efficient dispersion of CB particles both in the wet slurry state and in the final dry electrode. Consequently, a more intensive calendering process is applied to the resulting dry cathodes with the aim of establishing a more effective CB percolating network under the aforementioned manufacturing conditions (e.g. low CB loading), as demonstrated henceforth by EIS and cycling data analysis. However, it is imperative to exercise caution, as excessive calendering has the potential to clog the pores in the final electrodes or crack AM particles, eventually leading to sluggish and longer diffusion pathways for the charge transfer process. Hence, the 1wt.$\%_{C65}$B samples were subjected to porosity characterization to optimize the compromise between robust electrical pathways and unimpeded ion transport in the porous network.

Cycling experiments were executed on NMC-graphite full cells in a pouch-cell format, as detailed in the experimental section and illustrated in **Figure 42**, wherein all the reported curves and the following data are the average of two different cells for each sample. The electrochemical performance of 1wt.$\%_{C65}$B cathodes was assessed across a range of porosities, spanning from a relatively high value of 27% to an extremely reduced level of 15%, with 21% serving as the intermediary value. Throughout the formation cycles conducted at a low C-rate of C/20, the 1wt.$\%_{C65}$B 27% cells, which exhibit the highest porosity, achieved the most substantial mean discharge capacity, measuring 169.9 ± 0.5 mAh/g. Conversely, samples with lower porosities of 15% and 21% demonstrated a slightly reduced mean discharge capacity of 165.7 ± 2.9 mAh/g, displaying a wider variation among different samples. The superior mean discharge capacity observed in the 1wt.$\%_{C65}$B 27% cells, which feature the lowest calendering, is likely attributed to the increased active surface area and enhanced electrolyte penetration that result from higher porosity, promoting improved and more uniform lithium-ion diffusion. Reduced porosity increases the fraction of poorly wetted pores, impeding full electrolyte infiltration, whereas elevated porosity enlarges the electrode-electrolyte interface, promoting ion transport and enhancing charge/discharge efficiency. Consequently, the higher porosity in the 1wt.$\%_{C65}$B 27% cells combines a larger active surface area with reduced ion transport resistance, explaining the observed superior discharge capacity during the formation cycles. This hypothesis will be further supported by the upcoming EIS analysis, where the 1wt.$\%_{C65}$B 27% cells show significantly lower R_{el} values compared to samples calendered to lower porosities. Furthermore, it is plausible that the two samples with lower porosity may exhibit slight particle cracking due to the intense calendering process, leading to non-optimal contacting for certain AM fragments, that are not contributing to the overall capacity.

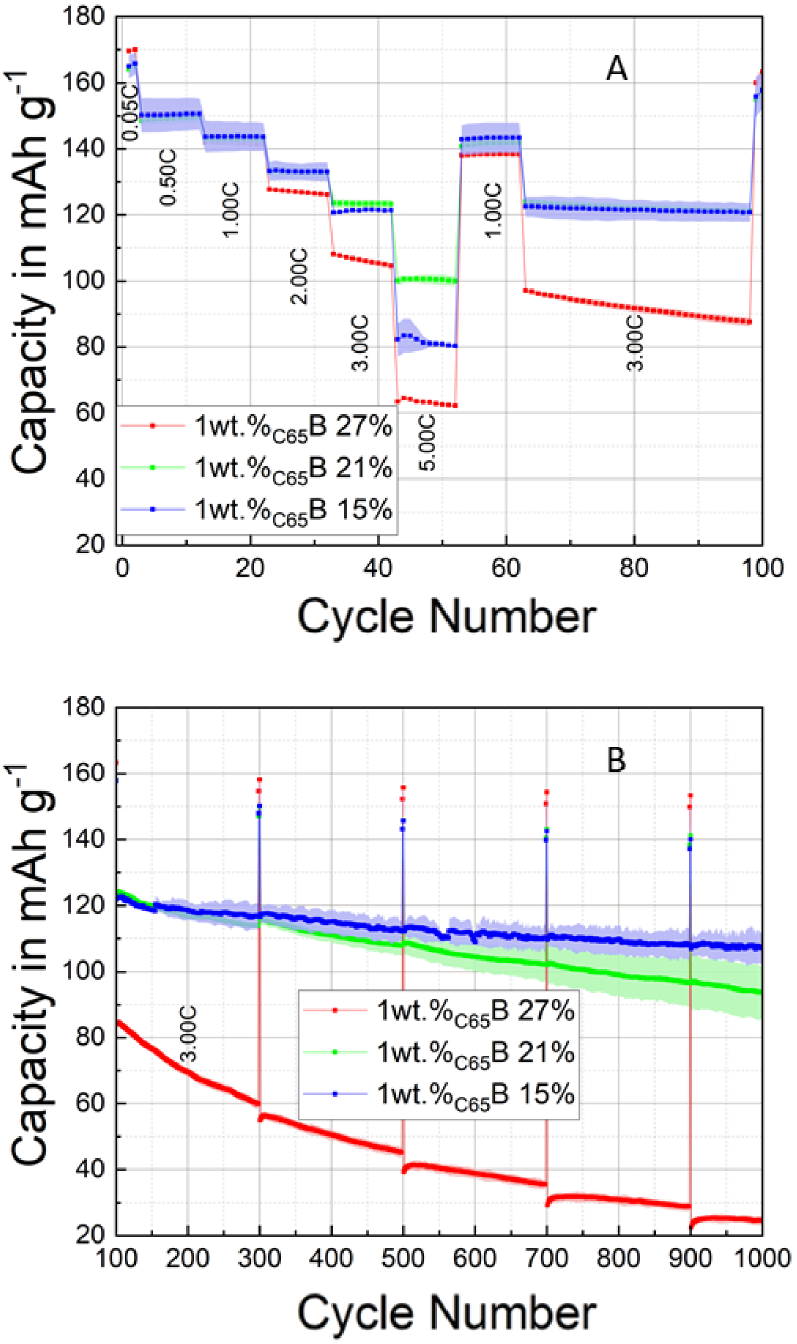

Figure 42. Rate capability (panel A) and prolonged cycling (panel B) metrics of graphite-NMC full cells for the 1wt.%$_{C65}$B cathodes at different porosities. The investigation covers three distinct porosity values: 27% (red), 21% (green) and 15% (blue). All the curves reported are the average of two different cells for each sample. The uncertainty for each sample is calculated as a standard deviation and it is highlighted by colored shading.

The rate-capability test (depicted in **Figure 42A**) conducted between C/2 and 1C, following 2 C/20 formation cycles, reveals comparable rate stability across all coatings, irrespective of their varied porosities. Interestingly, at higher C-rates, specifically from 2C to 5C, the 1wt.%$_{C65}$B 21% samples with intermediate porosity exhibit the highest capacity retention, followed by 1wt.%$_{C65}$B 15%, and by 1wt.%$_{C65}$B 27% with the lowest capacity. Notably, the 1wt.%$_{C65}$B 21% samples demonstrate enhanced electrical conductivity (refer to **Table 18**) compared to the 1wt.%$_{C65}$B 27% samples, and, presumably, a lower ion diffusion hindrance than the extensively calendered 1wt.%$_{C65}$B 15% cathodes. This condition enables an optimal balance in performance, especially at the highest 5C rate. Nevertheless, it's noteworthy that the two top performing samples, 1wt.%$_{C65}$B 21% and 1wt.%$_{C65}$B 15%, deliver, within the uncertainty of the measurement, the same capacity at the very high 3C rate. The long-term cycling, as illustrated in **Figure 42B**, reveals that electrodes with the lowest porosity, specifically the 1wt.%$_{C65}$B 15% samples, exhibit the minimal capacity loss after 1000 cycles at the high 3C discharge rate. Remarkably, the fatigued 1wt.%$_{C65}$B 15% electrodes maintain an average of 87.6% of the initial 3C discharge capacity upon long-term cycling. In contrast, the 1wt.%$_{C65}$B 21% samples with intermediate porosity, despite their superior performance in the initial high C-rate testing, exhibit performance close but not as commendable as the 1wt.%$_{C65}$B 15% samples in terms of long-term capacity retention. Indeed, the fatigued 1wt.%$_{C65}$B 21% electrodes maintain an average of 76.5% of the initial 3C discharge capacity over long-term cycling. Lastly, the 1wt.%$_{C65}$B 27% electrodes experience notably high capacity losses during extended cycling compared to the other samples, owing to their low concentration of carbon black per unit volume, which fails to establish an effective CB percolating network in the dry state. This hypothesis is further reinforced by the subsequent electrochemical impedance spectroscopy (EIS) analysis, which demonstrates that the 1wt.%$_{C65}$B 27% cells exhibit the highest overall impedance. This is particularly apparent in the Nyquist plot, where the 1wt.%$_{C65}$B 27% cells display the highest low-frequency intercept with the real axis. As highlighted by numerous studies[148], this characteristic strongly suggests that the 1wt.%$_{C65}$B 27% cells may possess inferior electronic conductivity compared to the other tested samples.

Examining the SEM images of ion-milled cross-sections of non-cycled, heavily calendered 1wt.%$_{C65}$B 15% cathodes, as illustrated in **Figure 43**, it's apparent how the intensive calendering employed to achieve low porosities can result in numerous cracked AM particles and indentation of the AM into the Al current collector.

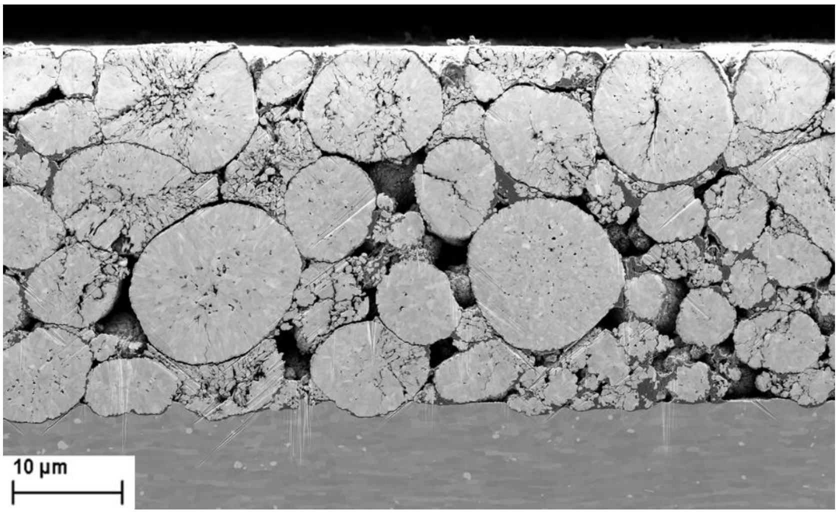

Figure 43. Ion-milled SEM cross-sections of pristine 1wt.%$_{C65}$B 15% electrodes after calendering displaying widespread AM particle fractures and AM penetration into the aluminum current collector due to intensive calendering.

For a more nuanced comprehension of potential variations in electrode processes, electrochemical impedance spectroscopy (EIS) is employed to evaluate the impact of calendering on electrochemical behavior at the electrode-electrolyte interface[1]. In **Figure 44**, the EIS data for all 1wt.%$_{C65}$B electrodes at 0.8 SOC are presented for the various studied porosities. The investigation encompasses three distinct porosity values: the higher porosity of 27% (red), the low porosity of 21% (green), and the extremely reduced porosity of 15% (blue). As elucidated elsewhere[1], the impedance at SOC=0.8 is selected and assessed since, at this charging state, the Nyquist plot accurately illustrates the electrochemical system for any SOC > 0.5. Due to the well-known reactivity of NMC622 with moisture or air during processing and storage[10], the SCRF equivalent circuit is selected and applied. The choice is grounded in the model[140] which explicitly addresses impedance components related to AM surface-film generation. The intricate physical origin of all elements employed in the equivalent SCRF[140] circuit model, inset of **Figure 44**, have been meticulously elucidated in prior discussions.

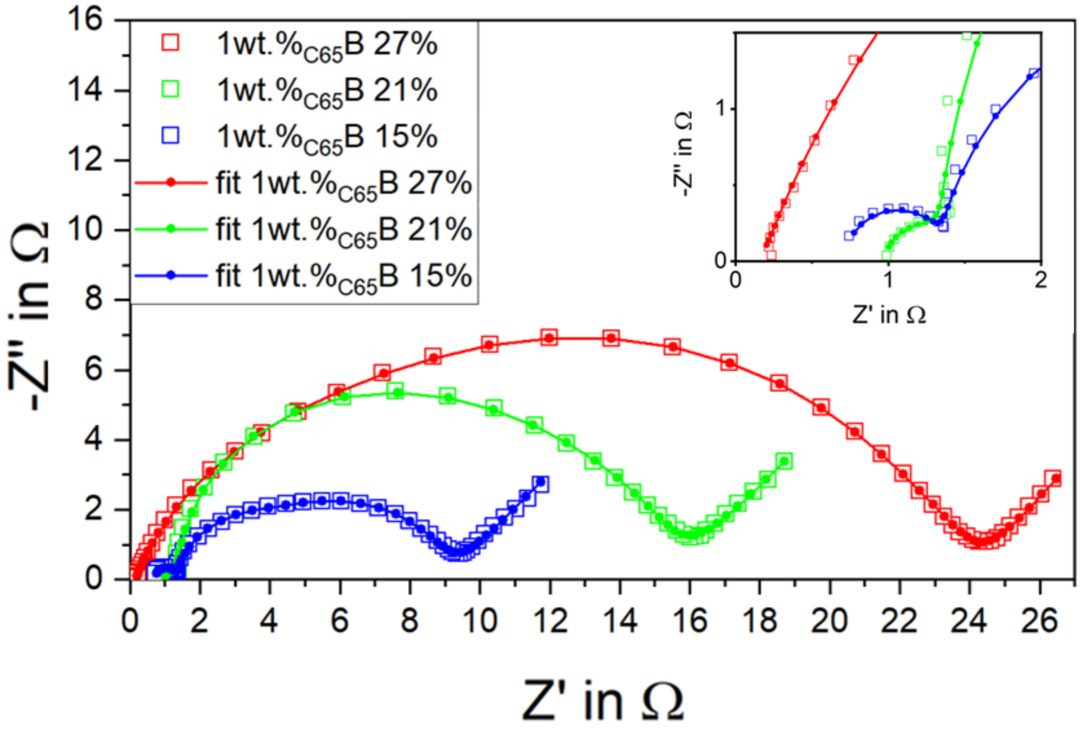

Figure 44. Nyquist plots (open squares) and fitted spectra (solid lines with markers) for fresh NMC622 electrodes at 0.8 SOC during the first cycle post-formation for 1wt.%$_{C65}$B cathodes at different porosities. The investigation covers three distinct porosity values: 27% (red), 21% (green) and 15% (blue). Data span 100 kHz to 50 mHz; the insert shows a magnified view of the high-frequency region. The matching Bode plots are presented in **Figure S-13**, **Figure S-14** and **Figure S-15**.

In **Figure 44**, the 1wt.%$_{C65}$B sample Nyquist spectra should exhibit a small high-frequency arc from contact impedance and a broad mid-to-low-frequency half-circle encompassing simultaneously surface-film and charge-transfer resistances. Calendering of 1wt.%$_{C65}$B electrodes reduces porosity and yields a corresponding impedance decrease, as shown by the shrinkage of both high- and mid-to-low-frequency arcs. In contrast, the highly porous 1wt.%$_{C65}$B 27% samples (red curve in **Figure 44**) exhibit pronounced expansion of these arcs. These expansions are linked, respectively, to a corresponding increase in interfacial and charge-transfer impedance when compared to the two samples with lower porosity.

Model variables obtained through equivalent-circuit fitting, as summarized in **Table 19**, bring attention to a significant impedance increase, notably concerning the contact resistance R_0, when comparing the 1wt.%$_{C65}$B 27% electrodes with those possessing lower porosities. Intriguingly, the lowest porosity 1wt.%$_{C65}$B 15% samples show a remarkably reduced R_0 over the 1wt.%$_{C65}$B 21% samples at intermediate porosity.

Table 19. Average EIS fitting variables, each based on two separate impedance runs, at 0.8 SOC for 1wt.%$_{C65}$B cathodes at various porosities. The investigation covers three distinct porosity values: 27%, 21% and 15%.

Sample	R_{el} in Ω	R_0 in Ω	Q_{CPE0} in $S*s^{\alpha}$	α_{CPE0}	R_0Q_{CPE0} in s^{α}	R_f in Ω	Q_{CPEf} in $S*s^{\alpha}$	α_{CPEf}	R_fQ_{CPEf} in s^{α}	R_1 in Ω	Q_{CPE1} in $S*s^{\alpha}$	α_{CPE1}	R_1Q_{CPE1} in s^{α}
1wt.%$_{C65}$B 27%	0.18	13	2.1E-04	0.80	2.7E-03	8.8	6.6E-04	0.85	5.8E-03	2.6	5.5E-02	0.75	1.4E-01
1wt.%$_{C65}$B 21%	0.68	2.7	2.9E-04	0.85	7.8E-04	6.2	2.1E-03	0.90	1.3E-02	3.3	2.9E-02	0.75	9.5E-02
1wt.%$_{C65}$B 15%	0.78	0.6	7.8E-06	0.98	4.8E-06	5.2	3.2E-04	0.89	1.7E-03	4.0	6.3E-03	0.75	2.5E-02

In this regard, the free Al refers to the regions of the current collector where electrode pores are present, while the remaining aluminum corresponds to the areas in direct contact with the composite electrode. In general, a coating with higher porosity, in direct contact with the native Al_2O_3 surface, enhances solvation with the $LiPF_6$-based electrolyte, facilitating improved wetting at the interface between the current collector and the composite electrode. This increased wetting is accompanied by a greater exposure of free aluminum, which is not directly connected to the composite electrode and is therefore more prone to passivation induced by $LiPF_6$[1]. Furthermore, the overall area of the current collector available for forming contact points with the composite electrode is reduced. As a consequence, the observed higher R_0 values in the 1wt.%$_{C65}$B 27% samples, characterized by the highest porosity, may be attributed to enhanced Al passivation, coupled with an overall reduction of contacting points. Conversely, the lower R_0 values for 1wt.%$_{C65}$B 21% and 1wt.%$_{C65}$B 15% at lower porosities might be linked to an improved contacting at the Al surface. Conversely, in examining the uncompensated resistance (R_{el}), the 1wt.%$_{C65}$B 27% samples with the highest porosity exhibited significantly lower R_{el} values in comparison to the 1wt.%$_{C65}$B 21% and 1wt.%$_{C65}$B 15% samples manufactured at lower porosities. This observation could be attributed to a larger volume of liquid electrolyte within the electrode pores at higher porosities, thereby locally enhancing ionic conductivity.

Electrochemical impedance spectroscopy (EIS) data unequivocally illustrate a consistent increase in interfacial impedance (R_f) as the porosity rises, progressing from the lowest R_f at 15% to the highest R_f at 27%. This behavior arises from enhanced electrolyte infiltration at higher porosities, which enlarges the wetted pore surface and, at elevated potentials, promotes more extensive surface-film formation[1] on carbon black and active material. Notably, the porosity of the coatings appears to have only a minor impact on the charge-transfer impedance (R_1), which remains almost unaltered across all the examined samples.

Fitting with 8 parameters may lead to an over-parametrization, especially when the relaxation frequencies of processes in the mid to low frequency range are similar[1]. The effect is especially clear in the relaxation frequencies, whose values apply exclusively when true capacitors are used, not Constant Phase Elements[1]. Nevertheless, for α-values exceeding 0.75, the product of R and Q should provide an estimate of the relaxation frequency[1], as per equation(7)[164]. **Table 19** reports the fitted relaxation frequencies for each RQ element in the equivalent circuit. In the 1wt.%$_{C65}$B 15% samples, these frequencies are well resolved, R_0 and R_f differ by three decades, and R_f and R_1 by one, whereas in the 1wt.%$_{C65}$B 27% samples R_0Q_{CPE0} and R_fQ_{CPEf} overlap, yielding a merged high- and mid-to-low-frequency semicircle. Conversely, **Figure 44** shows that for 1wt.%$_{C65}$B 21% (green) and 1wt.%$_{C65}$B 15% (blue), the Nyquist spectra present a well-defined high-frequency semicircle from contact resistance, followed by an expanded mid-to-low-frequency half-circle[1]. The 1wt.%$_{C65}$B 27% samples alone show distinctly separated mid-to-low-frequency relaxation frequencies (two decades apart), corresponding to a broadened impedance arc[1]. Overlap of these RQ elements in 1wt.%$_{C65}$B 21% and 1wt.%$_{C65}$B 15% makes individual contribution isolation difficult and elevates uncertainty in the derived parameters and their impact on cell behavior[1]. Although both R_f and R_1 lie between 2 and 10 Ω, masking clear patterns, a lower $R_f + R_1$ corresponds to higher capacity retention, which declines in the sequence 1wt.%$_{C65}$B 15% > 1wt.%$_{C65}$B 21% > 1wt.%$_{C65}$B 27%.

To assess the influence of different binders, namely PVdF Type B and PVdF Type A, on the final electrode characteristics, the electrochemical performance of 1wt.%$_{C65}$B and 1wt.%$_{C65}$A cathodes, sharing identical compositions, is comprehensively analyzed through cycling in graphite-NMC full cells. Specifically, the 1wt.%$_{C65}$B and 1wt.%$_{C65}$A cathodes are produced utilizing the enhanced Mixing 2ND, employing PVdF Type B and PVdF Type A, respectively. All coatings under investigation maintain a modest AM loading of around 12 mg/cm^2. Details regarding their compositions are presented in **Table 2**, and manufacturing-related data are available in **Table 18**. The exceptionally low porosity of 15% is selected as the benchmark for electrochemical comparison due to the minimized impedance observed in resulting electrodes in contrast to higher porosities (**Figure 44**). Additionally, the corresponding cathodes in graphite-NMC full cells exhibit superior long-term capacity retention (**Figure 42B**). Furthermore, as elucidated earlier, a harsh calendering process is imperative for the cathodes to establish an efficient CB percolating network in the dry state.

The rate-capability test for 1wt.%$_{C65}$B 15% and 1wt.%$_{C65}$A 15% cells is presented in **Figure 45A**, beginning with two slow formation cycles. At a formation rate of C/20, 1wt.%$_{C65}$B and 1wt.%$_{C65}$A cells exhibited comparable mean discharge capacities (166 ± 4 mAh/g), accompanied by appreciable inter-cell scatter. The subsequent rate-capability test (depicted in **Figure 45A**) was conducted after the 2 C/20 formation cycles and, within the measurement uncertainty, revealed comparable rate stability between the two cell types (1wt.%$_{C65}$B 15% and 1wt.%$_{C65}$A 15%) across the discharge rate range from C/2 to 5C. Hence, the rate capability performance of the cells appears comparable across various samples, irrespective of the binder type used in the cathode manufacturing process. Despite delivering a substantial capacity of 118 ± 5 mAh/g at 3C, both electrodes at 15% exhibited a significant drop in discharge capacity to 80 ± 10 mAh/g at the highest 5C discharge rate. Limited discharge capacity at 5C correlates with the preceding porosity study conducted on 1wt.%$_{C65}$B samples and it is attributed to the compromised ionic conductivity within the electrode pores resulting from the severe calendering employed to achieve low porosities. This is further supported by the highest R_{el} values measured for the 1wt.%$_{C65}$B 15% samples. The extended cycling, depicted in **Figure 45B**, demonstrates that 1wt.%$_{C65}$B 15% electrodes, characterized by reduced porosity, experience minimal capacity loss after 1000 cycles at the high 3C discharge rate. Notably, the fatigued 1wt.%$_{C65}$B 15% electrodes maintain an average of 87.6% of the initial 3C discharge capacity during prolonged cycling. The 1wt.%$_{C65}$A 15% cell samples, within the measurement uncertainty, exhibit comparable performance to the 1wt.%$_{C65}$B 15% electrodes concerning the long-term capacity retention.

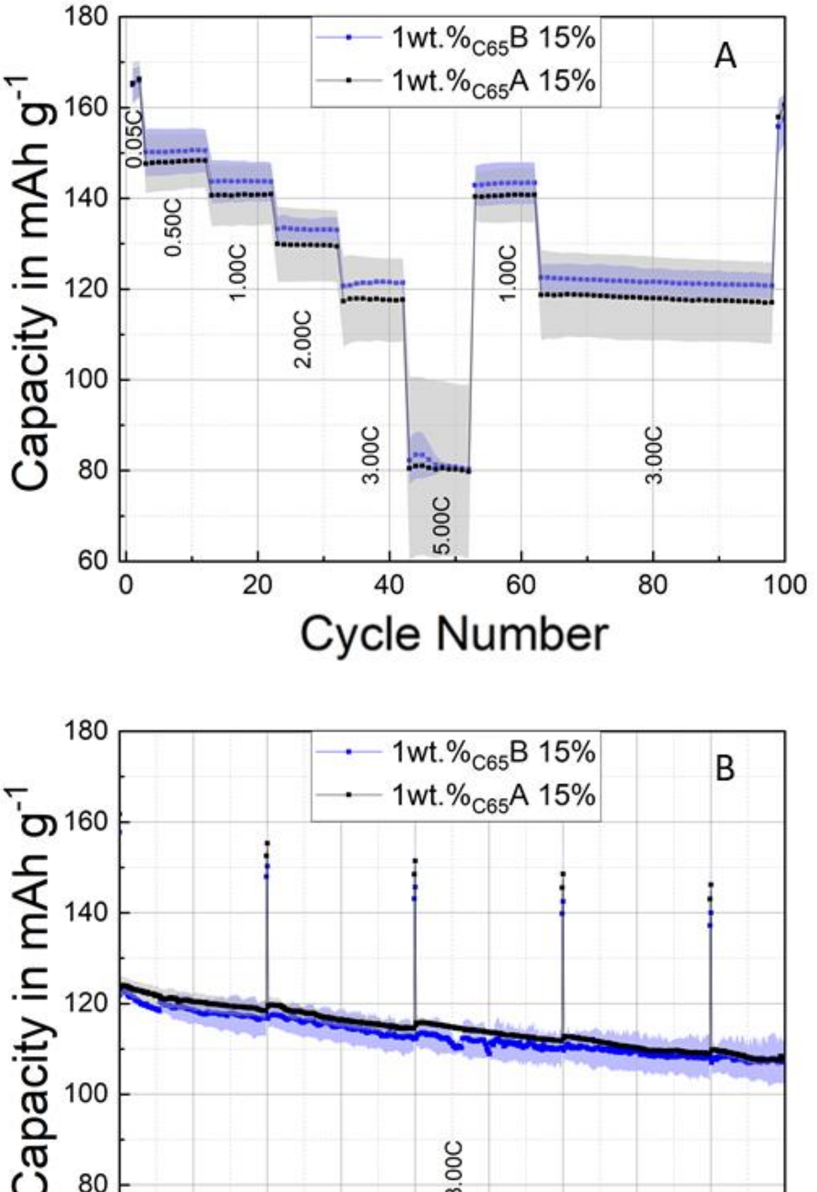

Figure 45. Rate capability (panel A) and prolonged cycling (panel B) metrics of graphite-NMC full cells for the 1wt.%$_{\mathrm{C65}}$B cathodes (blue) and the 1wt.%$_{\mathrm{C65}}$A cathodes (black). All the electrode samples are calendered to 15% porosity. All the curves reported are the average between at least two different cells for each sample. The uncertainty for each sample is calculated as a standard deviation and it is highlighted by colored shading.

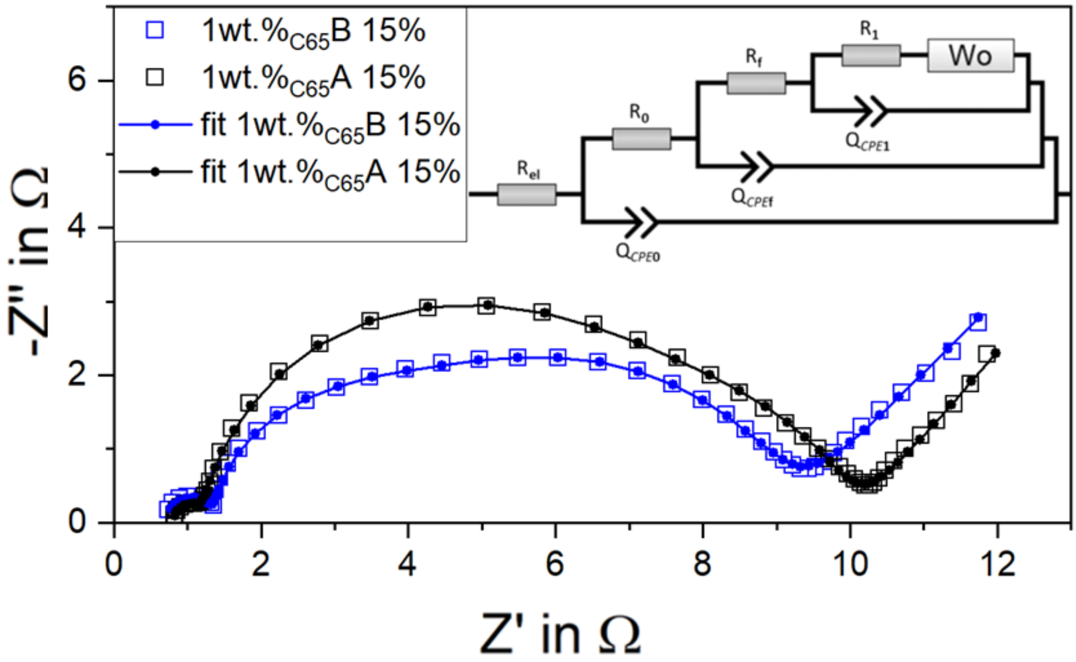

Figure 46. Nyquist plots (open squares) and fitted spectra (solid lines with markers) for fresh NMC622 electrodes at 0.8 SOC during the first cycle post-formation for 1wt.%$_{C65}$B 15% (blue curve) and 1wt.%$_{C65}$A (black curve). The investigation is performed at the same fixed porosity of 15% for both samples. Data span 100 kHz to 50 mHz; the model used for simulation is reported as insert[1]. The matching Bode plots are presented in **Figure S-15** and **Figure S-16**.

EIS was employed to determine the impact of binder selection at the electrode-electrolyte interface. In **Figure 46**, the EIS data for the 1wt.%$_{C65}$A 15% and the 1wt.%$_{C65}$B 15% electrodes at 0.8 SOC is displayed at the fixed porosity of 15%. As clarified in earlier sections, the impedance at the charging state of SOC=0.8 is chosen and evaluated to represent the electrochemical system for any SOC > 0.5. The curves are fitted using the SCRF[140] model, and the physical origins of all elements used in the equivalent circuit modelling have been extensively detailed previously. As illustrated in **Figure 46,** the Nyquist spectra of 1wt.%$_{C65}$B 21% and 1wt.%$_{C65}$B 15% feature a minor high-frequency arc and a wide mid-to-low-frequency semicircle, the physical genesis of which was covered in preceding chapters. When examining the contact resistance R_0, the 1wt.%$_{C65}$A 15% sample reveals a marginal yet noticeable increase in resistance compared to the 1wt.%$_{C65}$B 15% sample.

This increase directly correlates with the superior adhesion values of the latter, as outlined in **Table 18**. Specifically, cathodes produced with PVdF Type B exhibit an average 39.7% increase in adhesion compared to PVdF Type A under identical manufacturing conditions. It is hypothesized that a more extensive aerial coverage of the PVdF Type B binder on the current collector may offer enhanced protection against direct contact with the $LiPF_6$-based electrolyte.

Table 20. Average EIS fitting variables, each based on two separate impedance runs, at 0.8 SOC for 1wt.%$_{C65}$B 15% and 1wt.%$_{C65}$A 15% cathodes. The investigation is performed at the same fixed porosity of 15% for both samples.

Sample	R_{el} in Ω	R_0 in Ω	Q_{CPE0} in S*s$^{\alpha}$	α_{CPE0}	R_0Q_{CPE0} in s$^{\alpha}$	R_f in Ω	Q_{CPEf} in S*s$^{\alpha}$	α_{CPEf}	R_fQ_{CPEf} in s$^{\alpha}$	R_1 in Ω	Q_{CPE1} in S*s$^{\alpha}$	α_{CPE1}	R_1Q_{CPE1} in s$^{\alpha}$
1wt.%$_{C65}$ A 15%	0.81	1.4	2.1E-05	0.93	3.0E-05	6.3	1.0E-03	0.83	6.6E-03	2.0	1.3E-02	0.78	2.5E-02
1wt.%$_{C65}$ B 15%	0.78	0.6	7.8E-06	0.98	4.8E-06	5.2	3.2E-04	0.89	1.7E-03	4.0	6.3E-03	0.75	2.5E-02

This mechanism could potentially reduce the passivation of Al_2O_3 resulting from $LiPF_6$ degradation, while simultaneously increasing the available surface area of the current collector for establishing contact points with the composite electrode, thus lowering the contact resistance R_0. Furthermore, improved binder adhesion could help prevent electrode delamination from the current collector, a phenomenon that may arise due to the intense calendering used to achieve ultra-low porosities or during cell assembly. Electrode delamination may expose additional Al_2O_3 surfaces that are no longer capable of forming contact points with the composite electrode, thereby contributing to an increase in R_0, as highlighted in our previous study[1]. When analyzing the uncompensated resistance (R_{el}), both the 1wt.%$_{C65}$A 15% and 1wt.%$_{C65}$B 15% samples displayed nearly identical values within the margin of measurement uncertainty. This similarity can be attributed to the comparable volume of liquid electrolyte within the electrode pores at an extremely low porosity of 15%. In this scenario, the extremely reduced volume of liquid electrolyte may locally dampen the ionic conductivity into the electrode pores, in the same way for the same porosity value, and in an opposite direction compared to samples with higher porosities. Indeed, samples with higher porosities may show lower R_{el} values coupled with improved ionic conductivities, as demonstrated by the beforehand analyzed 1wt.%$_{C65}$B 27% samples.

Electrochemical impedance spectroscopy (EIS) data unmistakably reveal that the use of different binders in the 1wt.%$_{C65}$A 15% and the 1wt.%$_{C65}$B 15% samples results in only marginal changes in terms of interfacial impedance (R_f), with both electrodes demonstrating very similar values. Consequently, from a physical interpretation standpoint, this suggests the formation of a highly similar passive film on both the carbon black and active material particles at elevated potentials. Intriguingly, the choice of binder appears to significantly influence the charge-transfer impedance (R_1), which shows, on average, halved values when employing PVdF binders of Type

A. This, again, may be elucidated by a more favorable porosity assumed by the polymer in direct contact with the AM surface, that may lead, whenever PVdF binders of Type A binders are employed in place of Type B PVdF, to an enhanced ion-permeable interface coupled with an improved wetting with the electrolyte. Indeed, various factors associated with binder choice can influence charge transfer resistance. These include the polymer film's porosity and morphology, the degree and quality of crystallinity, and the specific interactions between the binder and the electrolyte. For example, higher crystallinity in certain PVdF types can reduce ion permeability and hinder effective wetting, leading to increased charge-transfer resistance. Conversely, a greater amorphous fraction, which promotes better electrolyte compatibility and more varied membrane porosity, can enhance ion transport and lower R_1. Model parameters obtained by fitting the impedance spectra to the equivalent circuit are presented in **Table 20**. In this context, the product R·Q serves as an estimate of the relaxation frequency, as per equation(7)[164], with α constrained to ≤0.75 to preserve the model's physical validity[1]. In the 1wt.%$_{C65}$B 15% samples, individual RQ element relaxation frequencies differ by three and one decades, and in the 1wt.%$_{C65}$A 15% samples by two and one, making separation of mid-to-low-frequency processes difficult. As shown in **Figure 46** (black = 1wt.%$_{C65}$A 15%; blue = 1wt.%$_{C65}$B 15%), both Nyquist plots feature a neat high-frequency semicircle due to contact resistance, followed by a widespread mid-to-low-frequency arc where component overlap obscures discrete contributions. Because the mid-to-low frequency RQ relaxation rates differ by just an order of magnitude, the surface-film and charge-transfer semicircles coalesce, leading to larger uncertainties in fitted values and their electrochemical significance[1]. With R_f and R_1 confined to the 2-6 Ω range, trend extraction is challenging. Nonetheless, it can be asserted that the combined resistance $R_0 + R_f + R_1$ is minimal and virtually the same for both the 1wt.%$_{C65}$A 15% and the 1wt.%$_{C65}$B 15% samples, which mirrors their unchanged long-term capacity performance.

4.4 Influence of conductive additives

In this final chapter, the concept of processability is framed by the maximum solid content (SC) that can be employed for electrode casting without disrupting roll-to-roll processing due to premature gelation. As outlined in the preceding chapter, improving carbon black (CB) deagglomeration through advanced mixing techniques, along with a reduction in CB content, offers a clear advantage in expanding the SC processability window for electrode casting, effectively delaying gelation in binders that are more prone to it. This strategy also enables the use of significantly higher SC levels, helping to counteract inadequate slurry gelation that may arise with certain PVdF binder types. Given the success of reducing CB content to optimize gelation and elevate SC thresholds for more efficient slurry processing, this chapter delves into further possibilities for manipulating the type and quantity of conductive additives to refine the process even further. Though this chapter serves as a focused case study, it highlights a broader potential for experimentation with various conductive additives—ranging from carbon nanotubes (CNT) and vapor-grown carbon fibers (VGCF) to graphite, graphene, and other advanced carbon materials. The experimental design builds on the alternative mixing method introduced in the previous chapter, using formulations with half the carbon black load compared to prior formulations. In a second experiment, graphite is incorporated as an additional conductive additive alongside CB. The primary focus of this study is to assess how reducing CB content and adding a second conductive additive affect the upper limit of the SC processability window, with particular attention to their influence on slurry gelation behavior. Beyond these rheological considerations, the electrochemical performance of the resulting electrodes is also meticulously evaluated.

4.4.1 Influence of graphite on the gelation behavior with PVdF type B

Two formulations with identical CB loadings, one further supplemented with graphite to double the total carbon content, were qualitatively compared to assess graphite's influence on rheology. Micrometer-scale graphite, dominated by hydrodynamic rather than van der Waals interactions and possessing a much lower specific surface area than CB, is expected to contribute minimally to slurry aggregation. PVdF Type B and KS6L graphite are employed in the formulation of 1wt.%$_{C65}$1wt.%$_{KS6L}$B slurries using Mixing 2ND, as outlined in **Table 2**. This mixing procedure enables the creation of a formulation with exceptionally high solid contents (SCs), specifically 85.0 wt.% SC for the 1wt.%$_{C65}$1wt.%$_{KS6L}$B slurry, as detailed in **Table 21**.

Table 21. Rheological profiles of NMP slurries generated by Mixing 2ND with NMC622 powder, PVdF Type B binder and carbon black, recorded immediately after mixing and after three days' storage.

Slurry sample	η in Pa*s at 50s^{-1} - 0h	η in Pa*s at 50s^{-1} - 3days	E_{coh} in mJ/m^3 - 0h	E_{coh} in mJ/m^3 - 3days	Yield stress in Pa - 0h	Yield stress in Pa - 3days
1wt.%$_{C65}$1wt.%$_{KS6L}$B	27.0	32.8	13.2	24.5	40	135
1wt.%$_{C65}$B III	33.1	35.0	20.9	23.0	116	217

To gauge the impact of graphite on the rheological behavior of the slurry, the 1wt.%$_{C65}$1wt.%$_{KS6L}$B sample is compared to the 1wt.%$_{C65}$B III formulation. The latter formulation is created using the same 85.0 wt.% solid content and it shares an identical composition with the 1wt.%$_{C65}$1wt.%$_{KS6L}$B sample, except for the non-utilization of graphite. The very high solid loading in the 1wt.%$_{C65}$1wt.%$_{KS6L}$B sample triggers swift gelation, producing a viscous, gel-like slurry that, despite its predominant gel-state, allows for uninterrupted electrode manufacturing. Notably, the flow curve measurement of the freshly mixed 1wt.%$_{C65}$1wt.%$_{KS6L}$B slurry sample reveals a surprisingly high initial viscosity reading of 27.0 Pa*s, as depicted in **Figure 47A** (in blue) and summarized in **Table 21**. Remarkably, beside the initially very high viscosity, only a minor increase in viscosity associated with gelation, totaling +21%, is observed in the flow curves after that the slurry is left to rest for 3 days (blue curves **Figure 47B**). Interestingly, the 1wt.%$_{C65}$B III sample displays, under the same SC, a significantly higher viscosity immediately after mixing, measuring 33.1 Pa*s and accounting to +22% in comparison to 1wt.%$_{C65}$1wt.%$_{KS6L}$B formulation. Nevertheless, despite the higher initial viscosity in comparison to the 1wt.%$_{C65}$1wt.%$_{KS6L}$B formulation, only a minor viscosity increase related to gelation is observed after that the 1wt.%$_{C65}$B III slurry is left to rest for three days, showing a modest rise of +6% (as illustrated in **Figure 47B** and detailed in in **Table 21**. For comparison, the formulation encompassing graphite demonstrated a higher viscosity increase of +21% after storage and, as a consequence, both the 1wt.%$_{C65}$B III and the 1wt.%$_{C65}$1wt.%$_{KS6L}$B formulations share roughly the same viscosity after 3 days of storage, as displayed in **Figure 47B**. Numerous kinks in both flow curves arise from wall slip, stemming from excessive viscosity which causes the loss of contact with the rheometer plate.

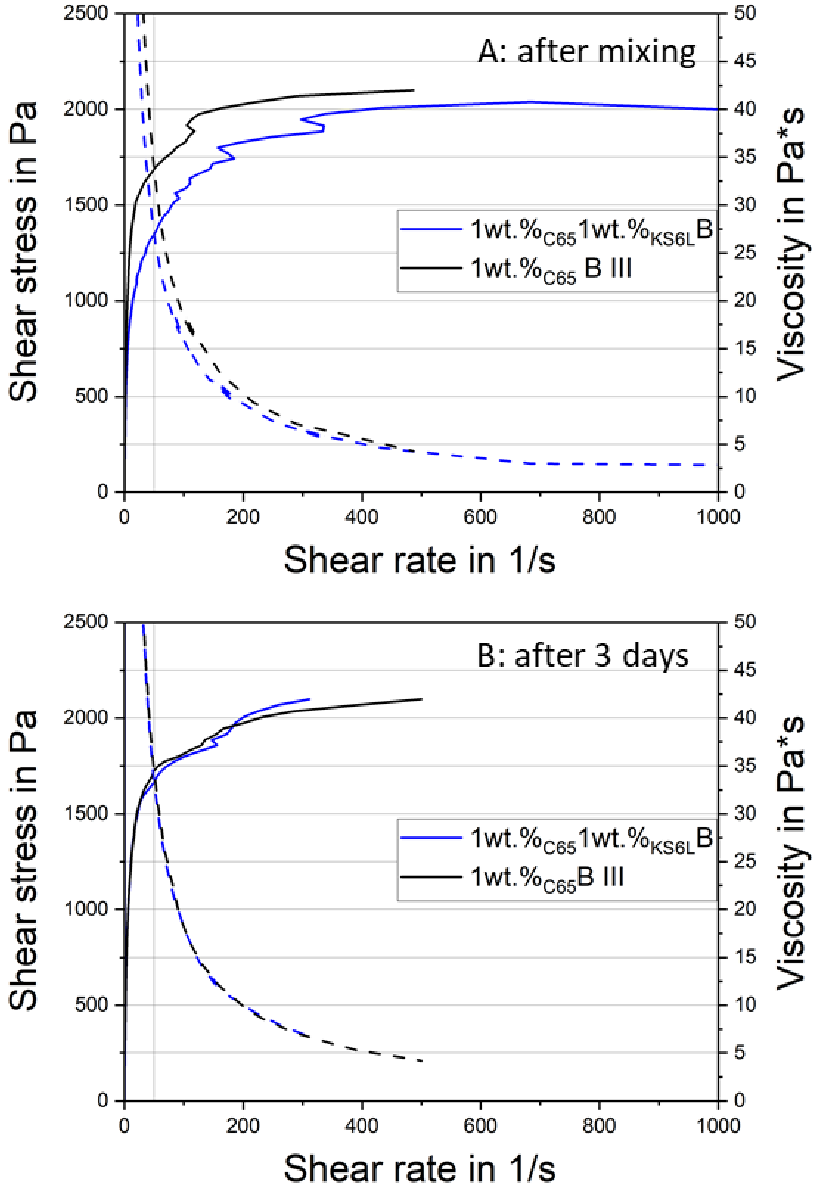

Figure 47. A: Flow (solid) and viscosity (dashed) profiles immediately after Mixing 2ND of NMP slurries encompassing NMC622 powder, high-Mw PVdF Type B, carbon black and graphite for the 1wt.%$_{C65}$1wt.%$_{KS6L}$B (blue) and the 1wt.%$_{C65}$B III (black) formulations. Both slurries have an identical SC of 85.0 wt.%. B: The same flow and viscosity measurements after three days' storage[1].

Analysis of the 1wt.%$_{C65}$1wt.%$_{KS6L}$B's amplitude-sweep data indicates that a durable slurry gel network is swiftly generated upon the mixing process, reflecting a highly aggregated colloidal structure. This is evident in **Figure 48A**, where the blue curves indicate that, in the low-shear-strain regime, G' consistently exceeds G''.

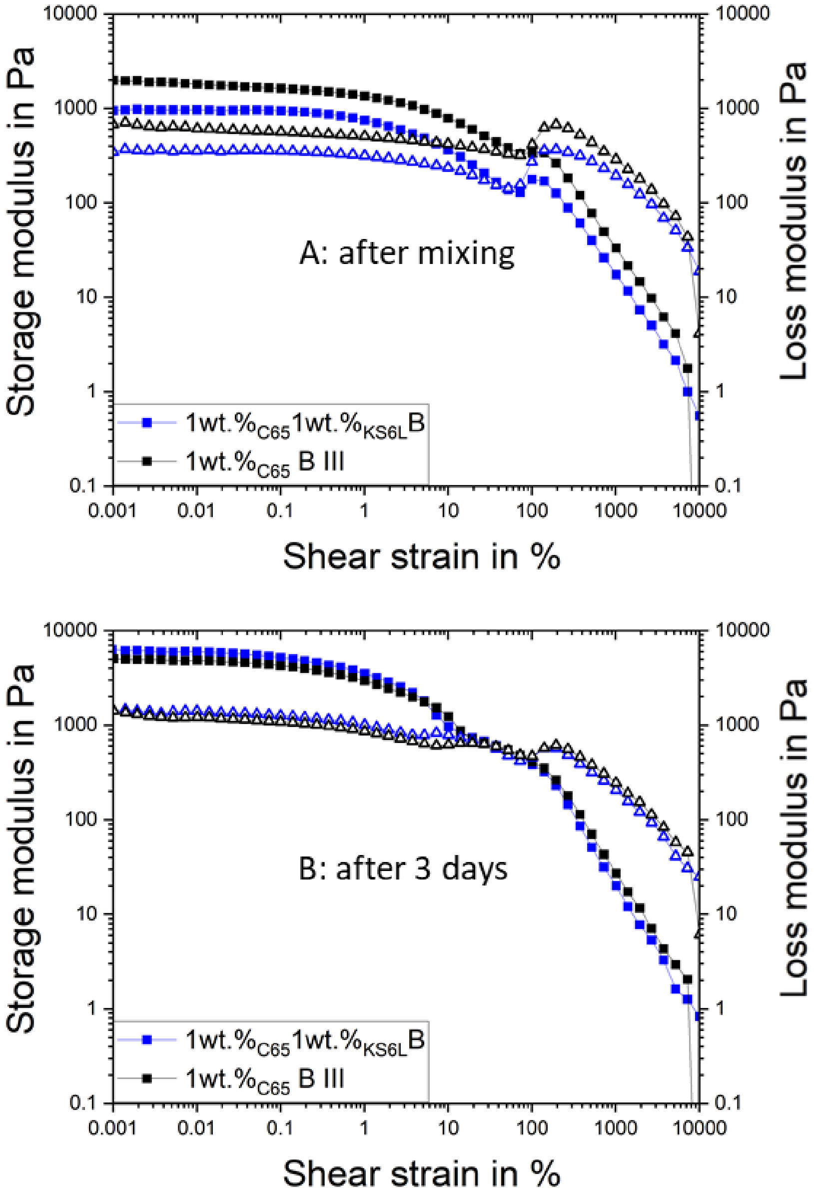

Figure 48. A: Amplitude sweeps (G' ■, G'' ▲) at $\omega=10s^{-1}$ immediately after Mixing 2^{ND} of NMP-based slurries encompassing NMC622 powder, high Mw PVdF, carbon black for the 1wt.%$_{C65}$1wt.%$_{KS6L}$B (blue, with graphite) and the 1wt.%$_{C65}$B III (black, graphite-free) formulations. Both slurries have an identical SC of 85.0 wt.%. B: The same amplitude sweeps recorded after three days of storage[1].

Accordingly, the aggregated-state energy immediately after mixing was calculated via equation (1), and is presented in **Table 21**. The energy of the aggregated state exhibits a notable value of E_{coh}, precisely 13.2 mJ/m^3, thereby clearly illustrating the impact of the rapid gelation of the slurry, which occurs shortly after the mixing process, whenever the substantial SC of 85.0 wt.% is applied.

Amplitude-sweep analysis of formulation 1wt.%$_{C65}$B III shows that mixing quickly yields a strong gel network within the slurry. The energy of the 1wt.%$_{C65}$B III aggregated state after mixing already exhibits a significant value of E_{coh}, specifically 20.9 mJ/m³, thus highlighting a substantially faster gelation shortly after the mixing process, when compared to the 1wt.%$_{C65}$1wt.%$_{KS6L}$B formulation. By calculating the energy of the aggregated state immediately after mixing and after slurry storage, as detailed in in **Table 21**, the progression of gelation-driven effects over time can be monitored. After three days' storage, the 1wt.%$_{C65}$1wt.%$_{KS6L}$B slurry exhibits a stronger gel network: its G′ in the LVR region of the amplitude sweep (**Figure 48B**) shifts to a higher modulus than immediately after mixing (**Figure 48A**). Interestingly, upon calculating the cohesion energy of the gel state after storage, E_{coh} exhibits a prominent increase of +85%, specifically reaching 24.5 mJ/m³. In a similar fashion, also the 1wt.%$_{C65}$B III slurry sample forms a stronger gel network after a three-day storage period, with G´ more prominently surpassing G'' in the low shear rate LVR region of the amplitude sweeps measurements (**Figure 48B**). Strikingly, upon determining the energy of the aggregated state upon storage, the E_{coh} value demonstrates a notably lesser increase when compared to the 1wt.%$_{C65}$1wt.%$_{KS6L}$B formulation, accounting to +10% and thus reaching 23.0 mJ/m³. This moderate increase in E_{coh} is a direct outcome of a less extended LVR region, which partially compensates for the substantial increase in the G´ modulus after that the slurry has been allowed to rest for 3 days. Consequently, the formulation encompassing graphite and the graphite-free sample share an almost identical E_{coh} after 3 days of storage, as illustrated in **Figure 48B** and outlined in in **Table 21**. It is hypothesized that incorporating graphite into the 1wt.%$_{C65}$1wt.%$_{KS6L}$B formulation may interpose graphite layers between neighboring particles within the complex slurry colloidal system, thus delaying the bridging flocculation process and, therefore, leading to a slurry with reduced viscosity and diminished gel strength immediately after mixing. Swift formation of the slurry gel post-mixing indicates both formulations might remain stable and prevent AM settling over extended storage periods. Indeed, if the strength of the colloidal aggregated state is adequately high, the possibility of active materials settling is expected to decrease considerably.

4.4.2 Electrochemical study of cathodes encompassing graphite

Building on previous experiments involving the same Mixing 2ND and the same CB and PVdF Type B content (e.g. 1wt.%$_{C65}$B), an investigation at significantly low porosity levels is also conducted on the 1wt.%$_{C65}$1wt.%$_{KS6L}$B samples. The aim is to strike an optimal balance between favorable electrical conductivity and minimal hindrance to ion diffusion into the electrode pores. To gauge the impact of graphite on electrochemical behavior, the cycling performance of the 1wt.%$_{C65}$1wt.%$_{KS6L}$B 21% sample is compared to its counterpart electrode, 1wt.%$_{C65}$B 21%. The 1wt.%$_{C65}$B 21% electrode is manufactured under identical conditions (e.g. same extremely reduced porosity, PVdF Type B, and enhanced Mixing 2ND) with the only difference being the absence of graphite. Both electrodes feature a modest AM loading of approximately 12 mg/cm². Comprehensive details regarding the compositions of the studied samples can be found in **Table**

2, and relevant manufacturing data are presented in **Table 22**. The rate-capability test comparing both samples is depicted in **Figure 49A**. From the initial formation cycles at a low C-rate of C/20, a distinct difference in the mean discharge capacity emerges between the 1wt.%$_{C65}$1wt.%$_{KS6L}$B 21% and 1wt.%$_{C65}$B 21% cells, with the 1wt.%$_{C65}$1wt.%$_{KS6L}$B 21% sample exhibiting, on average, a 4.5 mAh/g higher discharge capacity. This disparity reaches its peak at the C/2 discharge rate, expanding to 5.1 mAh/g, and gradually diminishes at higher C-rates (1C, 2C, and 3C), with averages of 4.7 mAh/g, 3.8 mAh/g, and 3.4 mAh/g, respectively. Intriguingly, at the highest 5C discharge rate, the mean discharge capacity gap between the two samples becomes negligible, within the uncertainty of the measurement.

Table 22. Summary of mass loading, thickness, porosity, resistance, and adhesion for tested cathodes, evaluated before and after calendering and, where performed, following heating treatment (FHT)[1].

Electrode sample	Mass loading in mg/cm^2	Thickness in µm	Porosity in %	Resistance in Ω - cal	Adhesion in N/m - uncal	Adhesion in N/m - cal	Adhesion in N/m - FHT
1wt.%$_{C65}$B	11.8	33.6	21	49	33.6	27.1	29.8
1wt.%$_{C65}$1wt.%$_{KS6L}$B	10.7	31.1	21	6	29.8	20.8	31.2
	12.1	32.6	15	7	29.8	24.9	31.2

As discussed earlier, the 1wt.%$_{C65}$B 21% cells exhibit compromised performance at lower C-rates due to the reduced amount of carbon additives and to the inadequately high calendering applied, leading to an inefficient carbon black (CB) percolating network in the dry state. This results in a fraction of the active material (AM) being electrically isolated and not contributing to the overall electrochemical process. At the highest 5C discharge rate, typically associated with impaired cycling performances when graphite is used[22], the 1wt.%$_{C65}$B 21% cells without graphite perform as well as the 1wt.%$_{C65}$1wt.%$_{KS6L}$B 21% cells. This intriguing outcome is speculated to be linked to lower ion diffusion hindrance into the electrode pores for the 1wt.%$_{C65}$B 21% cells, which lack the layered carbonaceous additive. The long-term cycling results, as depicted in **Figure 49B**, underscore that electrodes containing the carbonaceous additive, specifically the 1wt.%$_{C65}$1wt.%$_{KS6L}$B 21% samples, experience significantly minimal capacity loss after 1000 cycles at the high 3C discharge rate, at variance with the extremely high capacity losses measured for the 1wt.%$_{C65}$B 21% cells. This major outcome is attributed to the sluggish electrical conductivity of the 1wt.%$_{C65}$B 21% cells without graphite.

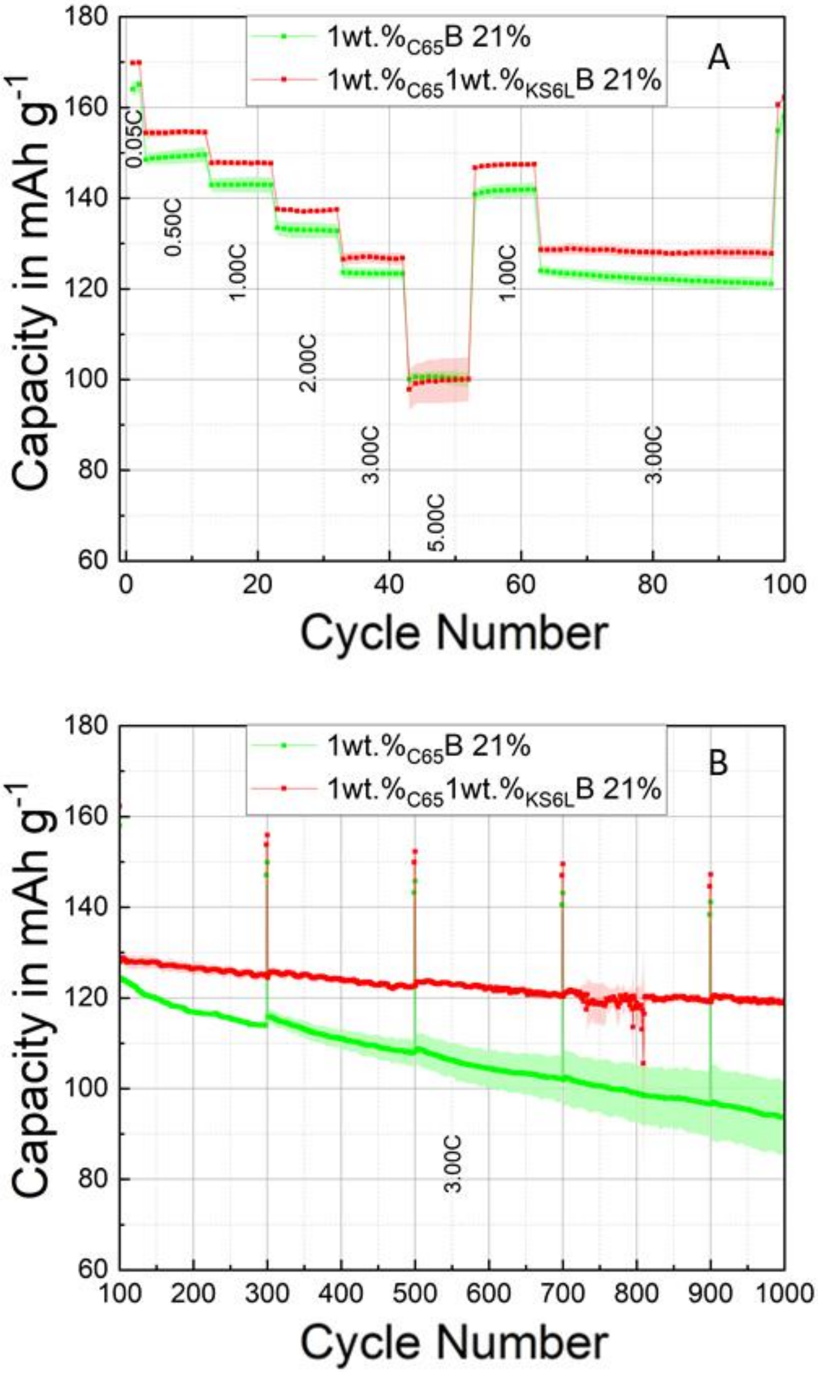

Figure 49. Rate capability (panel A) and prolonged cycling (panel B) metrics of graphite-NMC full cells for the 1wt.%$_{C65}$1wt.%$_{KS6L}$B 21% cathodes (red) and the 1wt.%$_{C65}$B 21% cathodes (green). All the curves reported are the average between at least two different cells for each sample. The uncertainty for each sample is calculated as a standard deviation and it is highlighted by colored shading.

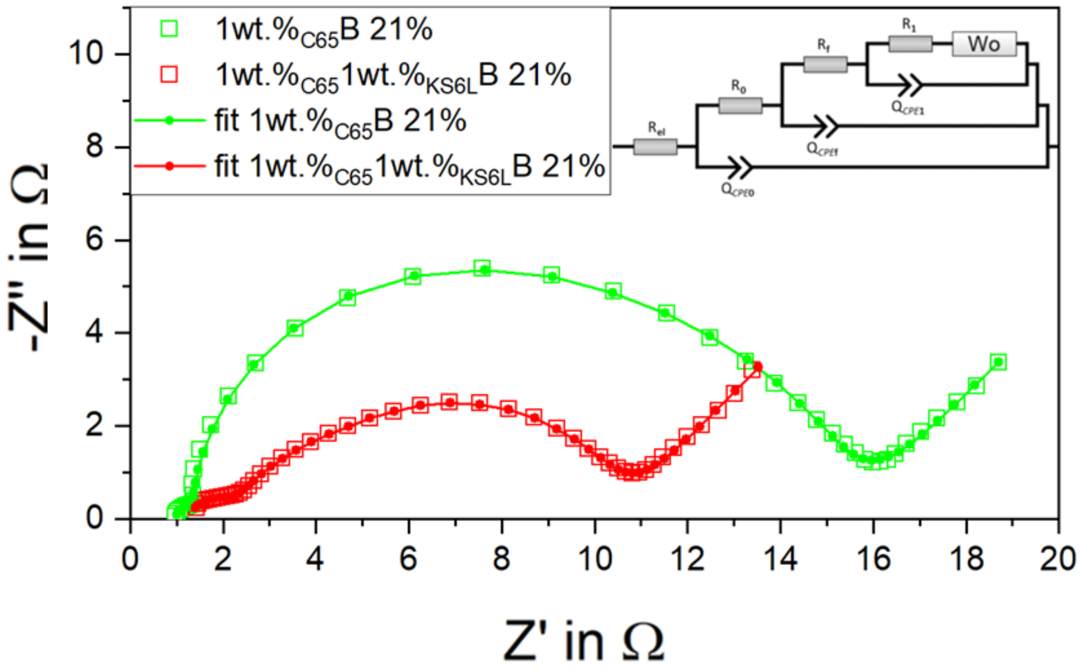

Figure 50. Nyquist plots (open squares) and fitted spectra (solid lines with markers) for fresh NMC622 electrodes at 0.8 SOC during the first cycle post-formation for 1wt.$\%_{C65}$1wt.$\%_{KS6L}$B (red curve) and 1wt.$\%_{C65}$B (green curve). The investigation is performed at the same fixed porosity of 21% for both samples. Data span 100 kHz to 50 mHz; the model used for simulation is reported as insert. The model used for simulation is reported as insert[1]. The matching Bode plots are presented in **Figure S-14** and **Figure S-17**.

EIS was applied to assess how graphite inclusion during electrode manufacturing alters the interfacial electrode-electrolyte response. To gauge this influence, the EIS results of the best-performing 1wt.$\%_{C65}$1wt.$\%_{KS6L}$B 21% samples are compared with its counterpart electrodes, 1wt.$\%_{C65}$B 21%. It is noteworthy that the 1wt.$\%_{C65}$B 21% electrode is fabricated under identical conditions as the 1wt.$\%_{C65}$1wt.$\%_{KS6L}$B 21% cathode, differing only in the absence of graphite. Both electrodes exhibit remarkably low porosity and are crafted with identical PVdF Type B and enhanced Mixing 2ND. In **Figure 50**, the EIS data for the 1wt.$\%_{C65}$1wt.$\%_{KS6L}$B 21% and 1wt.$\%_{C65}$B 21% electrodes are presented at a fixed porosity of 21%. The curves are fitted using the SCRF[140] model, and the detailed physical origins of all elements employed in modelling the equivalent circuit have been thoroughly discussed previously. In **Figure 50**, both 1wt.$\%_{C65}$1wt.$\%_{KS6L}$B 21% and 1wt.$\%_{C65}$B 21% exhibit a minor high-frequency semicircle attributable to contact resistance, succeeded by a wide mid-to-low-frequency arc that reflects the superimposed impedances of the surface film and charge transfer.

Table 23 provides the model parameters obtained from fitting the impedance data with the equivalent circuit.

Table 23. Average EIS fitting variables, each based on two separate impedance runs, at 0.8 SOC for 1wt.%$_{C65}$1wt.%$_{KS6L}$B 21% and 1wt.%$_{C65}$B 21% cathodes. The investigation is performed at the same fixed porosity of 21% for both samples.

Sample	R_{el} in Ω	R_0 in Ω	Q_{CPE0} in S*s$^{\alpha}$	α_{CPE0}	R_0Q_{CPE0} in s$^{\alpha}$	R_f in Ω	Q_{CPEf} in S*s$^{\alpha}$	α_{CPEf}	R_fQ_{CPEf} in s$^{\alpha}$	R_1 in Ω	Q_{CPE1} in S*s$^{\alpha}$	α_{CPE1}	R_1Q_{CPE1} in s$^{\alpha}$
1wt.%$_{C65}$ B 21%	0.68	2.7	2.9E-04	0.85	7.8E-04	6.2	2.1E-03	0.90	1.3E-02	3.3	2.9E-02	0.75	9.5E-02
1wt.%$_{C65}$ 1wt.%$_{KS6L}$ B 21%	1.03	1.0	1.2E-04	0.88	1.2E-04	4.1	2.0E-03	0.78	8.0E-03	3.4	1.2E-02	0.77	4.2E-02

Upon scrutinizing the contact resistance (R_0), it is evident that the 1wt.%$_{C65}$B 21% sample exhibits a noticeable increase in resistance compared to the 1wt.%$_{C65}$1wt.%$_{KS6L}$B 21% sample. This rise directly aligns with the significantly reduced electrical resistance of the latter, as detailed in **Table 22** and in **Table 18**. Certainly, an improved connection between the electrode composite and the current collector can lead to a notable reduction of the resistance for transferring electrons at the corresponding interface. Furthermore, it is postulated that an increased number of contact points at the current collector, or their enhanced physical extension facilitated by the introduction of graphite, may partially shield the Al_2O_3 surface from direct contact with the $LiPF_6$-based electrolyte. This mechanism could potentially mitigate Al_2O_3 passivation resulting from $LiPF_6$ degradation, a factor identified in our previous study[1] as a potential contributor to heightened contact resistance (R_0). When examining the uncompensated resistance (R_{el}), a marginal yet noticeable increase is observed in the 1wt.%$_{C65}$1wt.%$_{KS6L}$B 21% samples compared to the 1wt.%$_{C65}$B 21% samples. Interestingly, this finding aligns with the superior capacity retention of the 1wt.%$_{C65}$B 21% cells in the cyclability test at the highest 5C discharge rate, as opposed to the 1wt.%$_{C65}$1wt.%$_{KS6L}$B 21% cells. Assuming a similar volume of liquid electrolyte within the electrode pores at the identical low porosity of 21% for both samples, it is conjectured that the inclusion of graphite in the manufacturing of 1wt.%$_{C65}$1wt.%$_{KS6L}$B 21% electrodes may locally partially dampen ionic conductivity into the electrode pores.

Electrochemical impedance spectroscopy (EIS) data unequivocally demonstrate that the use of graphite in the electrode formulation of 1wt.%$_{C65}$1wt.%$_{KS6L}$B 21% cathodes leads to a slight decrease in interfacial impedance (R_f) compared to the 1wt.%$_{C65}$B 21% samples. Once again, this outcome correlates directly with the significantly reduced electrical resistance of the 1wt.%$_{C65}$1wt.%$_{KS6L}$B 21% cathodes relative to the 1wt.%$_{C65}$B 21% samples, as detailed in **Table 22** and **Table 18**. Improved contact between the AM particles and the CB-graphite-PVdF percolating network may actively contribute to a notable reduction in electron transfer resistance at the corresponding interface. Furthermore, it is posited, akin to the contact resistance (R_0), that better contact with the AM particles may partially shield the AM surface from direct contact with the $LiPF_6$-based electrolyte. This mechanism could potentially diminish the passive film on the AM surface resulting from $LiPF_6$ degradation at elevated potentials, owing to the increased physical extension of the CB-PVdF percolating network whenever graphite is introduced into the electrode formulation. Notably, the introduction of graphite into the electrode formulation does not seem to affect the charge-transfer impedance (R_1), which remains unchanged across all examined samples.

Table 23 illustrates the relaxation frequencies associated with individual RQ circuit pairs within the equivalent circuit. In this context, the product of R and Q is anticipated to yield an estimate of the relaxation frequency[1], as articulated equation(7)[164]. It is crucial to emphasize that the α-values were constrained to not exceed 0.75 to preserve the physical significance of the employed fitting model[1]. As represented in **Figure 50**, samples 1wt.%$_{C65}$1wt.%$_{KS6L}$B 21% and 1wt.%$_{C65}$B 21% (depicted as the red and green curves, respectively) exhibit a distinct high-frequency contact-impedance semicircle, then a wide mid-to-low-frequency semicircle whose overlapping features hinder discrete interpretation. Notably, because the mid-to-low-frequency RQ elements are separated by less than a decade, their surface-film and charge-transfer arcs coalesce, preventing clear resolution of the R_fQ_{CPEf} and R_1Q_{CPE1} contributions in 1wt.%$_{C65}$1wt.%$_{KS6L}$B 21% and 1wt.%$_{C65}$B 21%. Consequently, parameter values are subject to greater uncertainty when compared and interpreted. Indeed, since R_f and R_1 each fall within 3-6 Ω, extracting unequivocal patterns is challenging. Overall, the minimal R_0 + R_f + R_1 of the 1wt.%$_{C65}$1wt.%$_{KS6L}$B 21% sample corresponds to its best long-term capacity stability, in contrast to the 1wt.%$_{C65}$B 21% samples' higher impedance and lower retention.

The 1wt.%$_{C65}$1wt.%$_{KS6L}$B cathodes are created using PVdF Type B and the improved Mixing 2ND, featuring a modest active material (AM) loading of around 12 mg/cm^2. As discussed earlier, the application of Mixing 2ND results in a more effective dispersion of carbon black (CB) particles in both the wet slurry and the final dry electrode. Consequently, a rigorous calendering process is essential for these cathodes to establish an efficient CB percolating network in the dry state. However, it's crucial to exercise caution, as excessive calendering may lead to pore clogging in the final electrodes, resulting in sluggish ion diffusion pathways and diminished capacity retention at high discharging rates. Therefore, the electrochemical performance of the 1wt.%$_{C65}$1wt.%$_{KS6L}$B cathodes is evaluated by selecting 15% and 21% as two extremely reduced porosity values. The composition specifics for the cathode samples can be found in **Table 2,** and relevant manufacturing data are outlined in **Table 22**.

Cycling experiments are carried out on NMC-graphite full cells in a pouch-cell format, as detailed in the experimental section and depicted in **Figure 51**. Throughout the formation cycles at a low C-rate of C/20, all 1wt.%$_{C65}$1wt.%$_{KS6L}$B cells consistently demonstrate a very similar mean discharge capacity of 169.0 ± 1.3 mAh/g, regardless of porosity and within the measurement uncertainty. The rate-capability test (depicted in **Figure 51A**) conducted between C/2 and 1C, following 2 C/20 formation cycles, also reveals comparable rate stability across all coatings, irrespective of their varied porosities. Interestingly, at higher C-rates, specifically from 2C to 5C, the 1wt.%$_{C65}$1wt.%$_{KS6L}$B 21% samples with higher porosity exhibit the highest capacity retention compared to the extensively calendered 1wt.%$_{C65}$1wt.%$_{KS6L}$B 15% samples. It's noteworthy that the 1wt.%$_{C65}$1wt.%$_{KS6L}$B 21% samples demonstrate similar electrical resistance (see **Table 22**) and, presumably, lower ion diffusion hindrance than the extensively calendered 1wt.%$_{C65}$1wt.%$_{KS6L}$B 15% cathodes. This condition establishes an optimal performance balance, especially at the highest 5C rate, where the most significant difference in capacity retention between the two studied samples is observed, with the 1wt.%$_{C65}$1wt.%$_{KS6L}$B 21% cells outperforming the 1wt.%$_{C65}$1wt.%$_{KS6L}$B 15% samples. The long-term cycling, as illustrated in **Figure 51B**, reveals that electrodes with higher porosity, specifically the 1wt.%$_{C65}$1wt.%$_{KS6L}$B 21% samples, exhibit minimal capacity loss after 1000 cycles at the high 3C discharge rate. Notably, the fatigued 1wt.%$_{C65}$1wt.%$_{KS6L}$B 21% electrodes maintain an average of 93.2% of the initial 3C discharge capacity during long-term cycling. Similarly, the 1wt.%$_{C65}$1wt.%$_{KS6L}$B 15% samples, with even further reduced porosity, display nearly identical performance to the 1wt.%$_{C65}$1wt.%$_{KS6L}$B 21% samples in terms of long-term capacity retention. Indeed, the fatigued 1wt.%$_{C65}$1wt.%$_{KS6L}$B 15% electrodes sustain an average of 92.4% of the initial 3C discharge capacity over extended cycling.

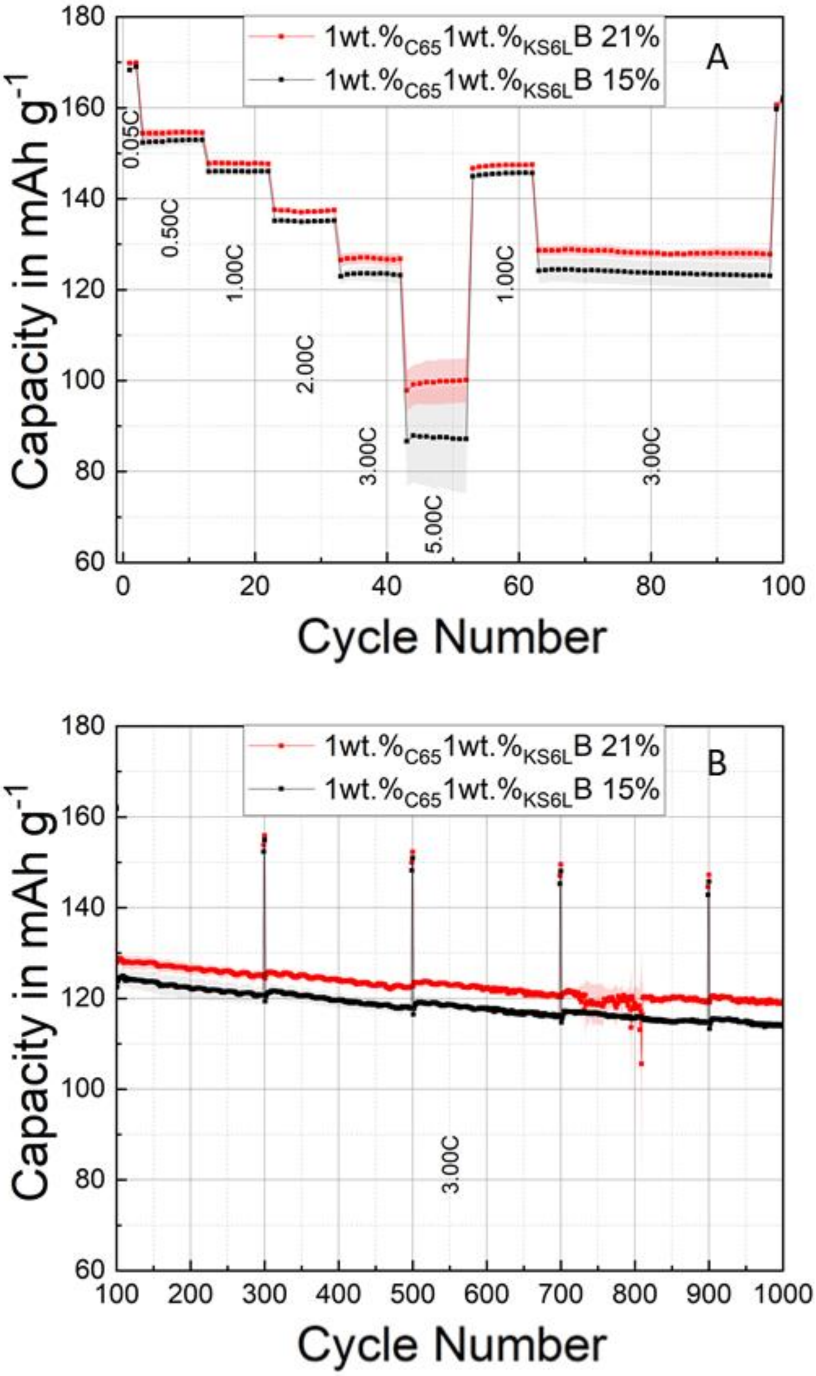

Figure 51. Rate capability (panel A) and prolonged cycling (panel B) metrics of graphite-NMC full cells for the 1wt.%$_{C65}$1wt.%$_{KS6L}$B 21% cathodes (red) and the 1wt.%$_{C65}$1wt.%$_{KS6L}$B 15% cathodes (black). All the curves reported are the average between three different cells for each sample. The uncertainty for each sample is calculated as a standard deviation and it is highlighted by colored shading.

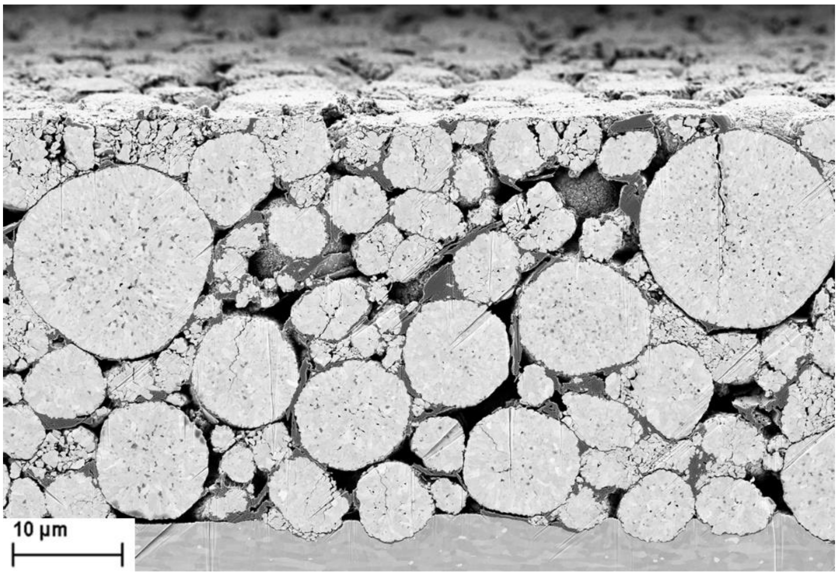

Figure 52. SEM images of ion-milled cross-sections of pristine, calendered electrodes of the 1wt.%$_{C65}$1wt.%$_{KS6L}$B sample. Compared to the graphite-free 1wt.%$_{C65}$B 15% electrode prepared under identical conditions and porosity (**Figure 43**), the 1wt.%$_{C65}$1wt.%$_{KS6L}$B electrode exhibits fewer AM particle cracks despite pronounced AM indentation into the Al current collector from intensive calendering. Surface particle cracks arise from calendering-induced stress, whereas particles in the bulk show minimal cracking as interparticle friction dissipates mechanical energy.

Upon examination of the SEM images of ion-milled cross-sections of non-cycled, heavily calendered 1wt.%$_{C65}$1wt.%$_{KS6L}$B 15% cathodes, as depicted in **Figure 52**, it becomes evident that the utilization of graphite, when intensive calendering is employed to achieve low porosities, results in a reduced number of cracked or completely destroyed active material (AM) particles compared to the 1wt.%$_{C65}$B 15% cathodes (shown in **Figure 43**). The 1wt.%$_{C65}$B 15% cathodes were produced under identical manufacturing conditions, at the same extremely reduced porosity, and with the same composition, except for the absence of graphite. The SEM images of ion-milled cross-sections of the 1wt.%$_{C65}$1wt.%$_{KS6L}$B 15% cathodes further highlight significant indentation of the active material into the Al current collector, consistent with the findings presented in the previous section for samples with the same porosity (depicted in **Figure 43**).

4.4.3 Influence of extremely reduced CB loadings on the gelation behavior with PVdF type B

Suspension-polymerized PVdF Type B is utilized in the production of the 0.5wt.%$_{C65}$B slurry with the improved Mixing 2ND, which enables the application of an exceptionally high solid content (SC) of 85.0 wt.%, as detailed in **Table 24**. Despite the application of exceptionally high SC, the slurry resists rapid gelation immediately after mixing, thereby ensuring a seamless manufacturing process, and maintaining an optimal fluid-to-solid ratio throughout the entire casting procedure.

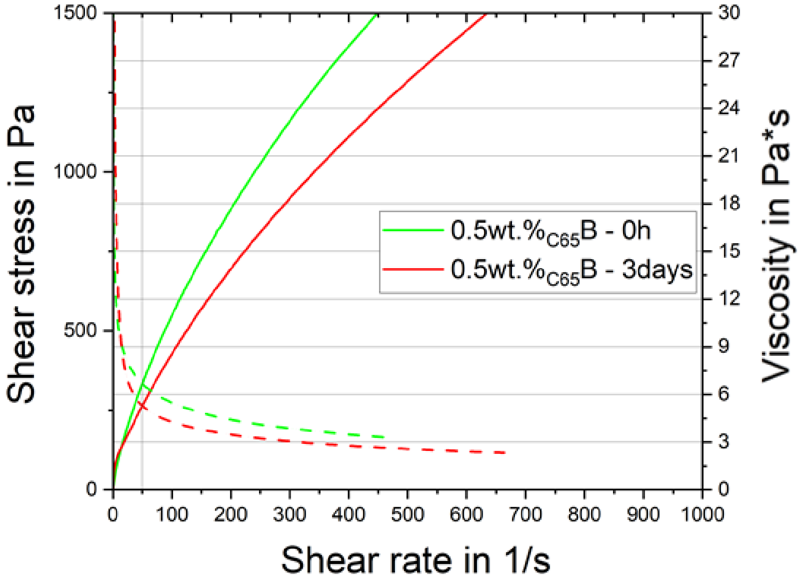

Figure 53. Flow (solid) and viscosity (dashed) profiles immediately after Mixing 2ND of NMP slurries encompassing NMC622 powder, high-Mw PVdF Type B, carbon black of the 0.5wt.%B NMP slurry sample. The 0.5wt.%B slurry has a SC of 85.0 wt.%. The same flow and viscosity measurements after three days' storage are colored in red[1].

Immediately after mixing, the 0.5wt.%$_{C65}$B slurry exhibits a notably high initial viscosity of 6.8 Pa*s, depicted by the green curve in **Figure 53**. Despite the significantly high initial slurry viscosity, the 0.5wt.%$_{C65}$B formulation exhibits a remarkable -20% reduction in viscosity after that the slurry has been allowed to rest for 3 days, as illustrated by the red curve in **Figure 53**.

Table 24. Rheological profiles of NMP slurries generated by Mixing 2ND with NMC622 powder, PVdF Type B binder and carbon black, recorded immediately after mixing and after three days' storage.

Slurry sample	η in Pa*s at 50s^{-1} - 0h	η in Pa*s at 50s^{-1} - 3days	E_{coh} in mJ/m^3 - 0h	E_{coh} in mJ/m^3 - 3days	Yield stress in Pa - 0h	Yield stress in Pa - 3days
0.5wt.%$_{C65}$B	6.8	5.4	0.1	-	4	7

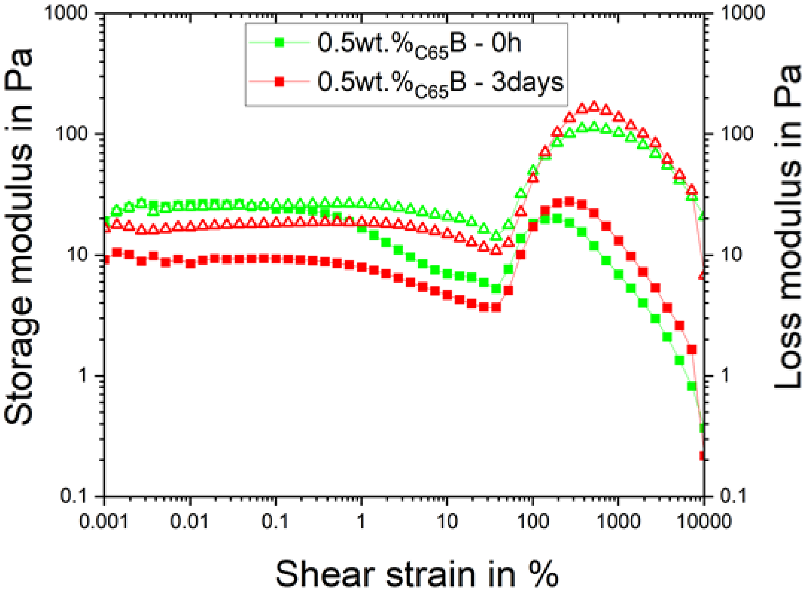

Figure 54. Amplitude sweeps (G′ ■, G″ ▲) at ω=10s^{-1} immediately after Mixing 2ND (green) of the 0.5wt.%B NMP slurry sample encompassing NMC622 powder, high Mw PVdF, carbon black. The 0.5wt.%B slurry has a SC of 85.0 wt.%. The same amplitude sweeps recorded after three days of storage are colored in red[1].

In amplitude sweeps of the freshly mixed 0.5wt.%$_{C65}$B sample (green curve in **Figure 54**), neither a predominant liquid nor gel-like character is discernible. This is indicated by the loss modulus G" remaining very closely aligned in value to the G′ modulus in the LVR region of the amplitude sweeps measurements (**Figure 54**). Despite this, both moduli are of substantial modulus in the low shear rate domain, thus making it meaningful to calculate the energy of the aggregated state right after mixing, yielding a value of 0.1 mJ/m^3, as reported in **Table 24**. After a storage period of three days, it is apparent that the 0.5wt.%$_{C65}$B slurry sample did not remain stable, as illustrated by G″ dominating over G´ in the LVR region of the amplitude sweeps measurements (**Figure 54**). This scenario is characteristic of the top portion of a slurry lacking a stabilizing gel network, which may therefore be prone to the sedimentation of the active materials at the bottom of the storage container. Indeed, the top portion of the 0.5wt.%$_{C65}$B formulation shows a predominant liquid-like character in the amplitude sweeps measurements upon 3 days of slurry storage, which is accompanied by a concurrent viscosity reduction. This data suggests that the slurry encompassing the PVdF Type B binder is unlikely to maintain stability against AM sedimentation over prolonged storage periods. Despite the presence of a weak aggregated state right after mixing, its strength is assumed to be inadequate in preventing settling of active materials. Therefore, when using suspension-polymerized PVdF Type B binders and 0.5wt.% of C65 loading, higher solid content should be applied in order to obtain a stable formulation.

At variance with previous results presented in this thesis, the 0.5wt.%$_{C65}$B slurry sample, detailed in **Table 2**, is formulated with 0.5wt.% of C65 and 0.75wt.% of PVdF Type B, thus deviating from the typical 1-to-1 ratio of C65 to PVdF. The increase in PVdF content was necessary to achieve a stable formulation. Attempts to create a slurry with 0.5wt.% of C65 and an equivalent amount of PVdF resulted in immediate sedimentation after mixing, with active material settling at the container bottom and a low viscosity NMP-rich supernatant. While direct comparison with other formulations is challenging due to diverse compositions, a qualitative comparison is made with the 1wt.%$_{C65}$B III slurry, serving as a pseudo reference to assess the impact of higher CB loadings on rheology at constant SC. The 1wt.%$_{C65}$B III slurry is formulated with higher additive quantities and a different C65 to PVdF ratio—specifically, 1 wt.% of C65 and 1 wt.% of PVdF Type B, as outlined in **Table 2**—while applying the same 85.0 wt.% SC as the 0.5wt.%$_{C65}$B formulation. A comparison of rheology from **Table 24** and **Table 17** reveals opposite behavior for the two formulations. Indeed, the 1wt.%$_{C65}$B III slurry exhibits rapid gel formation and increasing viscosity upon storage, while the 0.5wt.%$_{C65}$B slurry fails to induce sufficient gelation, resulting in active material particle sedimentation. This outcome demonstrates how reducing C65 in the slurry formulation may shift the processability window boundary, so that the threshold at which strong slurry gelation occurs is moved up to higher solid contents.

4.4.4 Electrochemistry of electrodes integrating extremely reduced CB loadings

The 0.5wt.%$_{C65}$B 15% cathodes are crafted using PVdF Type B and the enhanced Mixing 2ND, featuring a modest loading of active material (AM) at approximately 12 mg/cm^2. Specifics regarding the composition of 0.5wt.%$_{C65}$B 15% samples can be found **Table 2**, while pertinent manufacturing data are outlined in **Table 25**. As previously discussed, the utilization of Mixing 2ND leads to a more effective dispersion of carbon black (CB) particles in both the wet slurry and the final dry electrode.

Table 25. Summary of mass loading, thickness, porosity, resistance, and adhesion for tested cathodes, evaluated before and after calendering and, if applicable, following heating treatment^1.

Electrode sample	Mass loading in mg/cm^2	Thickness in µm	Porosity in %	Resistance in Ω - cal	Adhesion in N/m - uncal	Adhesion in N/m - cal
0.5wt.%$_{C65}$B	11.8	30.3	15	114	16.9	16.9

Consequently, a thorough calendering process is imperative for these cathodes to establish an efficient CB percolating network in the dry state. Building upon prior experiments with the same Mixing 2ND and reduced CB and PVdF Type B contents (e.g., 1wt.%$_{C65}$B), an investigation is undertaken on the 0.5wt.%$_{C65}$B samples at a notably low porosity level of 15%. The goal is to restore optimal electrical conductivity in the calendered electrodes. The electrochemical performance of the 0.5wt.%$_{C65}$B 15% cathode is evaluated and qualitatively compared to that of the 1wt.%$_{C65}$B 15%, which shares the same porosity level. While a direct comparison between the two electrodes is challenging due to their distinct compositions, the 1wt.%$_{C65}$B 15% electrode, despite being manufactured with a higher additives content as outlined in **Table 2** and **Table 18**, serves as a qualitative reference to assess the influence of varying additive amounts on electrochemical performance at the same reduced porosity level. Specifically, the 1wt.%$_{C65}$B 15% electrode encompasses 1wt.% of C65 and an equivalent amount of PVdF Type B, whereas the 0.5wt.%$_{C65}$B 15% sample includes 0.5wt.% of C65 and 0.75wt.% of PVdF Type B. Cycling experiments are conducted on NMC-graphite full cells in a pouch-cell format, as outlined in the experimental section and illustrated in **Figure 55**. Throughout the formation cycles at a low C-rate of C/20, all 0.5wt.%$_{C65}$B 15% cells consistently exhibit a mean discharge capacity of 164.9 ± 0.4 mAh/g. Comparing this value to the mean discharge capacity of 165.7 ± 2.9 mAh/g delivered by the 1wt.%$_{C65}$B 15% samples reveals that the further reduction of carbon additives does not result in any loss in capacity retention, provided the slow formation cycles are considered. However, when considering intermediate C-rates of C/2 and 1C, a noticeable difference in mean discharge capacity emerges between the 0.5wt.%$_{C65}$B 15% and 1wt.%$_{C65}$B 15% cells, with the latter sample showing, on average, a 6 mAh/g higher discharge capacity. The mean discharge capacity gap widens further to 8 mAh/g at the 2C discharge rate, once again showcasing the superior performance of the 1wt.%$_{C65}$B 15% cells. At the highest C-rates of 3C and 5C, the gap peaks at average values of 11 mAh/g and 18 mAh/g, respectively. It is conjectured that the diminished performance at C-rates beyond C/20 for the 0.5wt.%$_{C65}$B 15% cells may be attributed to an ineffective carbon black (CB) percolating network in the dry state, resulting from the significantly reduced C65 content employed. This inference finds support in the doubled electrical resistance value of the 0.5wt.%$_{C65}$B 15% electrodes (**Table 25**), compared to equivalent measurements on the 1wt.%$_{C65}$B 15% reference electrodes (**Table 18**). Consequently, a portion of the active material (AM) is loosely electrically connected within the 0.5wt.%$_{C65}$B 15% electrode composite structure, thereby not contributing to the overall electrochemical process at C-rates higher than the two slow formation cycles. The long-term cycling data, depicted in **Figure 55B**, reveals that electrodes with a higher C65 content, particularly the 1wt.%$_{C65}$B 15% samples, demonstrate minimal capacity loss after 1000 cycles at the demanding 3C discharge rate. Remarkably, the fatigued 1wt.%$_{C65}$B 15% electrodes maintain an average of 87.6% of the initial 3C discharge capacity over the prolonged cycling period. In contrast, the 0.5wt.%$_{C65}$B 15% electrodes incur significant capacity losses during prolonged cycling compared to the reference electrodes, attributed to their low concentration of carbon black per unit volume. This deficiency prevents the establishment of an effective carbon black percolating network in the dry state. Specifically, the fatigued 0.5wt.%$_{C65}$B 15% electrodes maintain an average of 70.1% of the initial 3C discharge capacity during long-term cycling. Notably, when examining long-cycling with slow C/20 cycles (initiating from cycle 100, where one C/20 charge-discharge cycle is repeated every 200 3C charge-discharge cycles), the electrodes with 0.5wt.%$_{C65}$B 15% exhibit a greater discharge capacity compared to the 1wt.%$_{C65}$B 15% samples. This observation leads to the hypothesis that the superior performance of the 0.5wt.%$_{C65}$B 15% sample may be attributed to the presence of loosely electrically connected active material. This material, not actively contributing to the overall electrochemical process at any C-rates higher than C/20, remains relatively unaffected by aging.

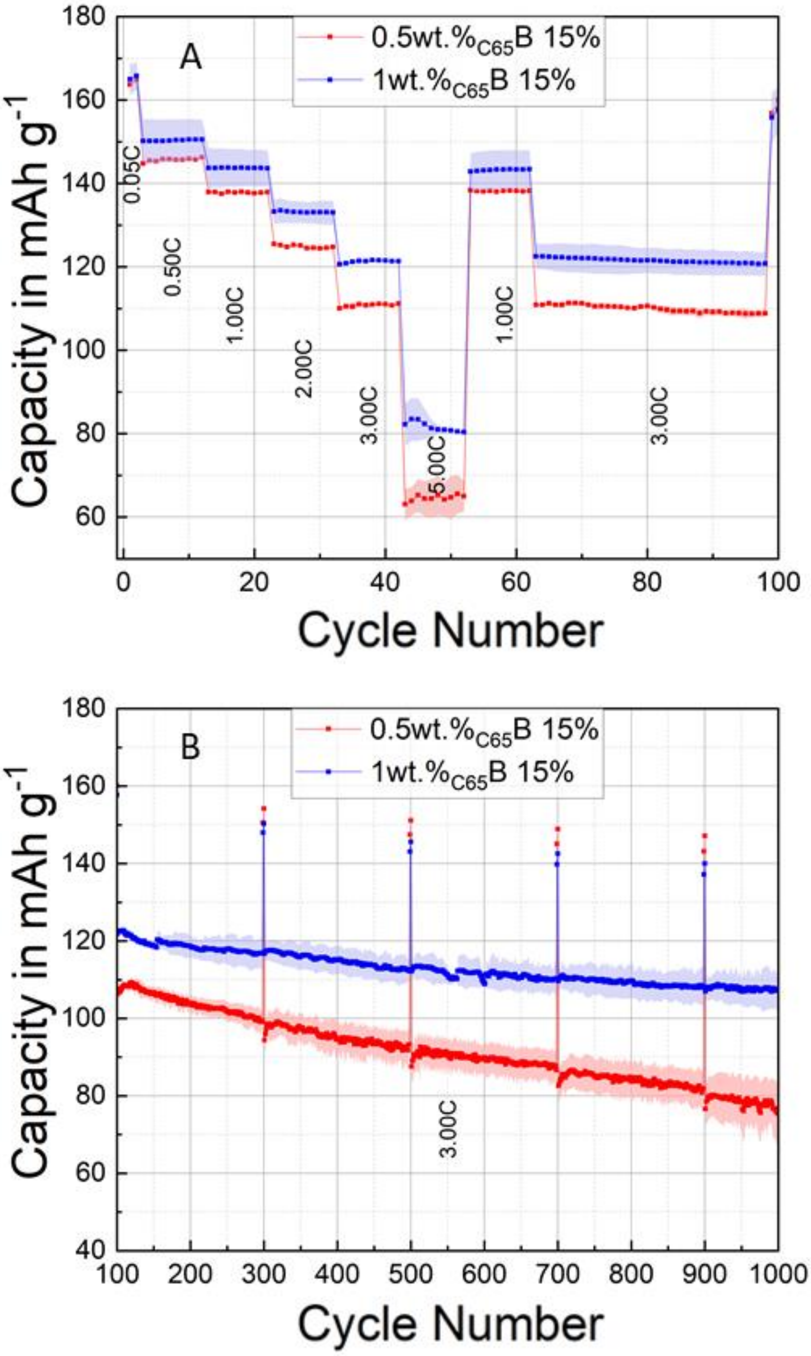

Figure 55. Rate capability (panel A) and prolonged cycling (panel B) metrics of graphite-NMC full cells for the 0.5wt.%$_{C65}$B 15% cathodes (red) and the 1wt.%$_{C65}$B 15% cathodes as a reference (blue). All the curves reported are the average between at least two different cells for the same electrode sample. The uncertainty for each sample is calculated as a standard deviation and it is highlighted by colored shading.

Upon thoroughly examining the scanning electron microscope (SEM) images portraying ion-milled cross-sections of non-cycled, heavily calendered 0.5wt.%$_{C65}$B 15% cathodes, as illustrated in **Figure 56**, it becomes evident that the remarkably diminished additives content, combined with an intensive calendering process, leads to a predominant occurrence of heavily cracked active material (AM) particles. The SEM image of the 0.5wt.%$_{C65}$B 15% cathode further accentuates a notable indentation of the active material into the aluminum current collector. Additionally, there is an apparent cohesion failure which is likely produced during the sample handling process in preparation for SEM imaging. This cohesion failure may be attributed to the deficient mechanical characteristics of the studied electrodes, stemming from their extremely low binder content (<1wt.%).

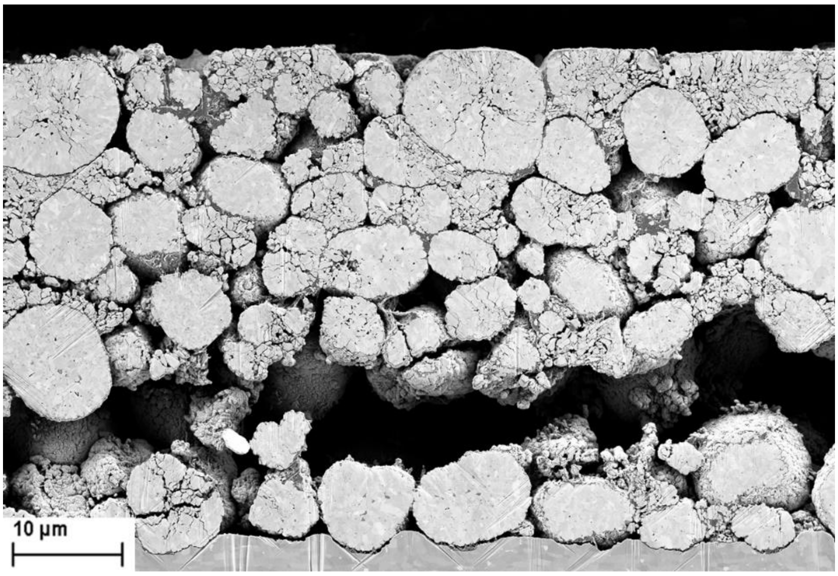

Figure 56. SEM images of ion-milled cross-sections of pristine calendered electrodes of the 0.5wt.%$_{C65}$B 15% sample showing severe AM particles cracking and AM indentation into the Al current collector owing to the intensive calendering applied. A cohesion failure is apparent along the longitudinal direction.

5 Conclusions

This thesis provides an in-depth analysis of optimizing slurry processability for electrode casting by addressing the behavior of slurry gelation in relation to various binder types, additives, and mixing methods.

The first chapter investigates the gelation properties of binder-free slurries, comparing PVdF binders with different molecular structures. This analysis emphasizes the role of ultra-high molecular weight binders in establishing the upper limit of the solid content (SC) processability window, i.e. the maximum SC suitable for electrode casting without hindering roll-to-roll process efficiency due to premature gelation. It was found that PVdF Type A (emulsion polymerized homopolymer) induced rapid gelation at 70 wt.% solid content, while PVdF Type B (suspension polymerized homopolymer with polar functional groups along the polymer backbone) allowed processing at higher solid contents (up to 75.5 wt.%) with reduced gelation. Both binders eventually reached a gelation point, but at different solid content thresholds, thus influencing their processability. Notably, when comparing PVdF Type B with PVdF Type A at the same SC, the former did not induce sufficient gelation, risking sedimentation of active material particles, while the latter caused rapid slurry gelation.

The second chapter explores the impact of slurry additives, specifically lithium salts (LiTFA, LiTFSI, LiODFB) and H_3PO_4, on modifying gelation behavior and enhancing rheological properties when processing high SC NMC662 slurries with PVdF Type A and Mixing 1ST. These additives effectively delayed gelation at 75.5 wt.% solid content, allowing continuous roll-to-roll processing without compromising electrode quality. The mechanisms behind rheology modification are explained, with lithium and proton-based additives preventing chemical and physical slurry gelation by neutralizing and complexing surface charges on the NMC622. While these additives improved slurry processability, the electrochemical performance of the resulting electrodes showed varied outcomes. Li-salt additives enhanced high-rate performance, whereas H_3PO_4-treated electrodes exhibited accelerated degradation during long-term cycling due to acerbated SEI formation. Electrochemical impedance spectroscopy (EIS) analysis of fresh electrodes revealed that H_3PO_4-treated samples exhibited the largest increase in contact resistance, attributed to enhanced Al surface passivation. Instead, in Li-salt-enhanced cathodes, post-mortem EIS reveals that contact resistance at the Al current collector drives most of the impedance rise after 1000 cycles, far more so than in the additive-free sample, and may only cause delamination under extended cycling.

The third chapter investigates the effect of advanced mixing techniques on slurry gelation, particularly in improving carbon black (CB) deagglomeration. By enhancing binder conformation and promoting PVdF adsorption onto a greater number of CB aggregates, the refined mixing process (Mixing 2ND), combined with reduced 1wt.% CB contents in the formulation, facilitated the creation of slurries with significantly higher solid content (up to 85 wt.% for PVdF Type B) without premature gelation. This led to improved slurry processability and delayed gelation onset, extending the SC processability window while ensuring uniform coatings. The electrochemical effects of optimized CB dispersion and reduced CB content were also explored. EIS analysis demonstrated that achieving optimal calendering degrees was essential for creating an effective percolating network, thus ensuring good electrical conductivity. Electrodes subjected to intensive calendering showed minimal capacity loss after 1000 cycles at a high 3C discharge rate, owing to improved connection with the current collector and greatly reduced contact impedance at 15% porosity.

Building on the findings of reduced CB content and enhanced mixing, the final chapter investigates further adjustments to conductive additives to refine slurry processability. By minimizing CB content to 0.5wt.% or adding a second conductive additive, the influence on slurry gelation behavior was assessed. Reducing CB content improved processability and almost completely suppressed gelation at 85 wt.% solid content, but at the cost of electrochemical performance, particularly at high C-rates and during long-term cycling, due to insufficient conductivity. The addition of graphite to formulations with reduced 1wt.% CB content provided a significant improvement, delaying gelation at 85 wt.% solid content by intercalating graphite layers between slurry particles, thereby reducing viscosity and slowing the flocculation process. Electrochemical analysis revealed that graphite-containing electrodes outperformed the graphite-free counterparts in terms of high-rate performance up to 3C and demonstrated significantly better long-term capacity retention owing to reduced electrode impedance at the reduced porosity of 21%. However, at the highest 5C discharge rate, the graphite-containing electrodes exhibited diminished performance, likely due to hindered ion diffusion caused by the layered carbonaceous additive.

These findings highlight the delicate balance required between binder formulation, mixing techniques, and conductive additive content to optimize both slurry processability and electrochemical performance. Overall, this thesis demonstrates that a combination of binder selection, slurry additives, advanced mixing methods, and conductive additive optimization can significantly enhance slurry processability and performance, which is essential for efficient electrode manufacturing in roll-to-roll processes. Nonetheless, careful consideration of the interactions between these variables is crucial to ensure that improvements in slurry processability do not undermine optimal electrochemical efficiency.

Appendix

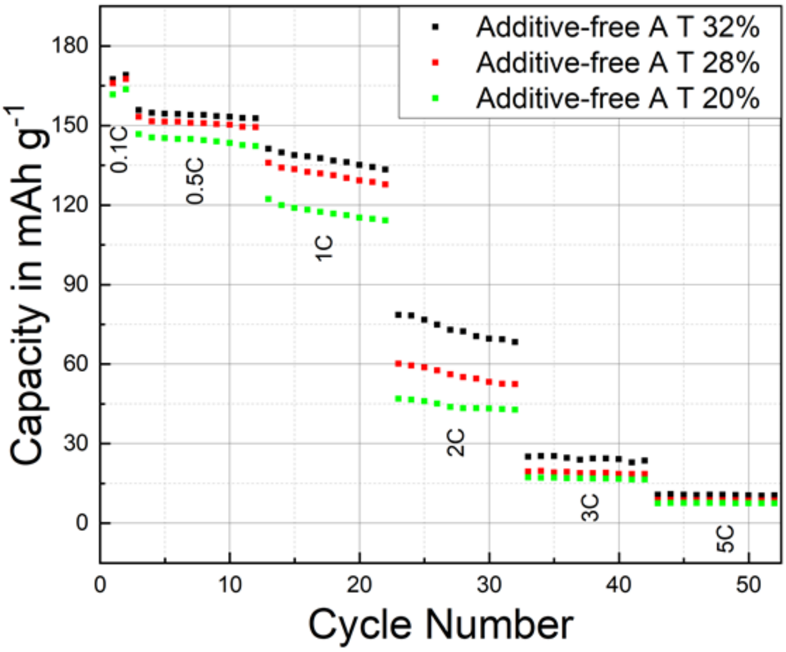

Figure S-1. Control experiment. C-rate performance of Li-NMC half cells for the additive-free A T cathode at different porosities.

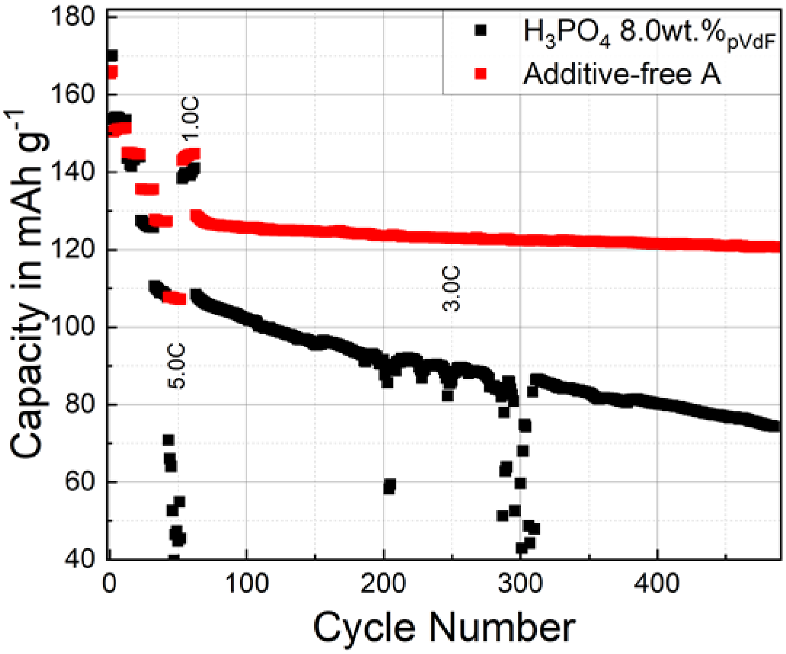

Figure S-2. Control experiment. Rate capability and extended cycling of graphite-NMC full cells using the H_3PO_4 8.0 wt.%$_{PVdF}$ (black) and the additive-free A (red) cathodes; black markers indicate brief potentiostat malfunctions.

Table S-1. Voltage difference between the main upper and lower anodic/cathodic redox peaks extracted from dQ/dV curves during cycling for additive-free A and 2 mass%$_{PVdF}$ LiTFA, 2 mass%$_{PVdF}$ LiODFB and 2 mass%$_{PVdF}$ LiTFSI.

Cycle n. - Charge/Disch. C-rate	ΔV in mV main RedOx peaks - additive-free A	ΔV in mV main RedOx peaks - LiTFA	ΔV in mV main RedOx peaks - LiTFSI	ΔV in mV main RedOx peaks - LiODFB
1 - 0.05C/0.05C	23	24	28	30
40 - 1C/3C	261	289	257	268
70 - 1C/3C	270	302	265	284
100 - 1C/3C	283	313	277	296
200 - 1C/3C	297	343	298	330
400 - 1C/3C	318	401	347	394
600 - 1C/3C	329	450	381	443
800 - 1C/3C	347	516	409	515
1000 - 1C/3C	378	608	465	605

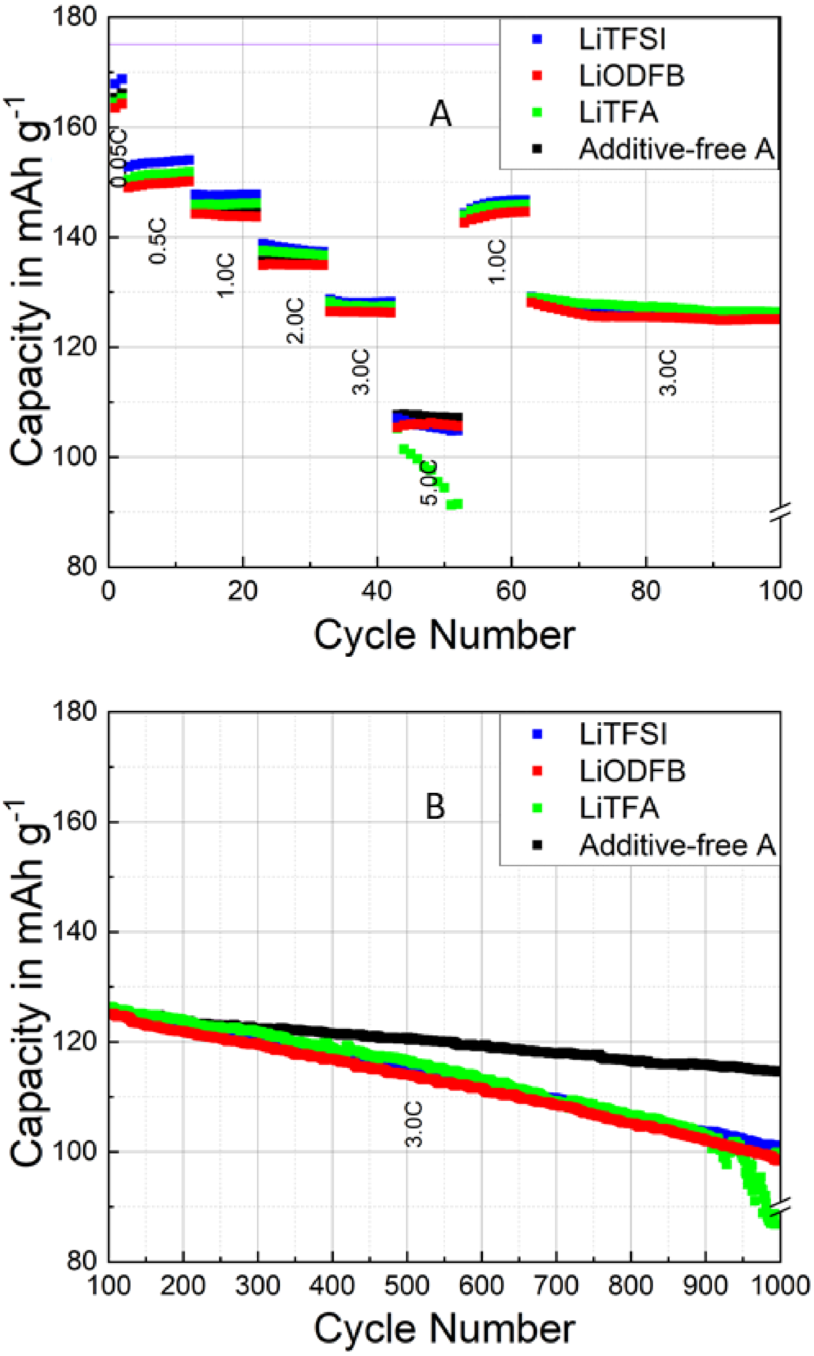

Figure S-3. Control experiment. Rate capability and extended cycling of graphite-NMC full cells using additive-free A (black), 2 wt.%$_{PVdF}$ LiTFA (green), 2 wt.%$_{PVdF}$ LiODFB (red) and 2 wt.%$_{PVdF}$ LiTFSI (blue) cathodes.

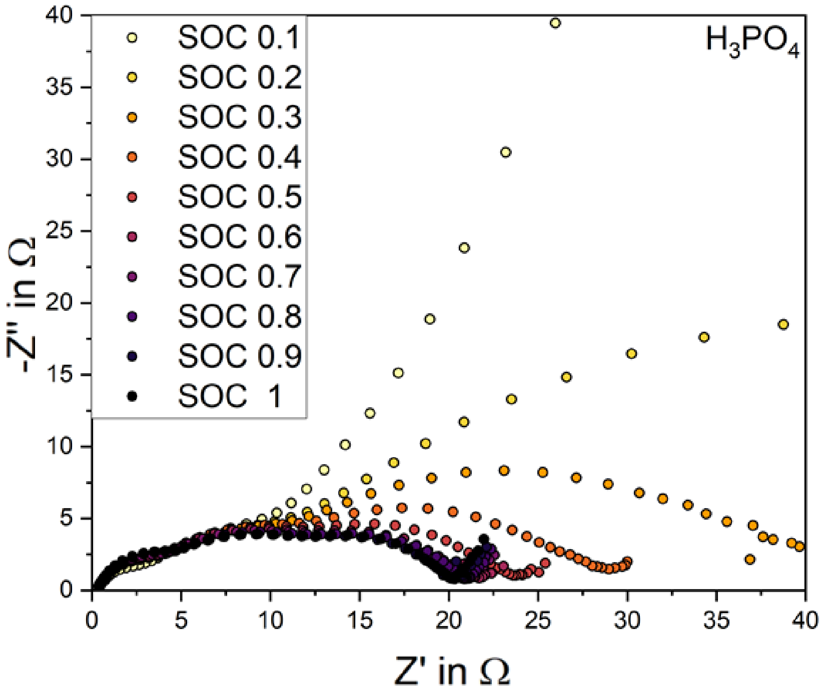

Figure S-4. Measured impedance Nyquist plot of NMC622 electrode from fully discharged SOC=0.1 up to fully charged SOC=1 for the H_3PO_4 8.0 wt.$\%_{PVdF}$ cathode.

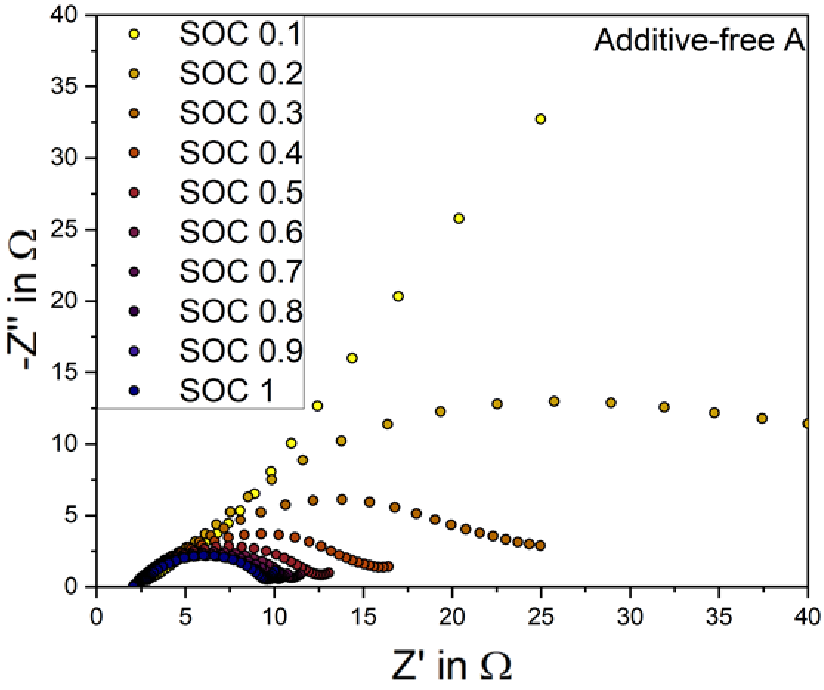

Figure S-5. Measured impedance Nyquist plot of NMC622 electrode from fully discharged SOC=0.1 up to fully charged SOC=1 for the additive-free A cathode.

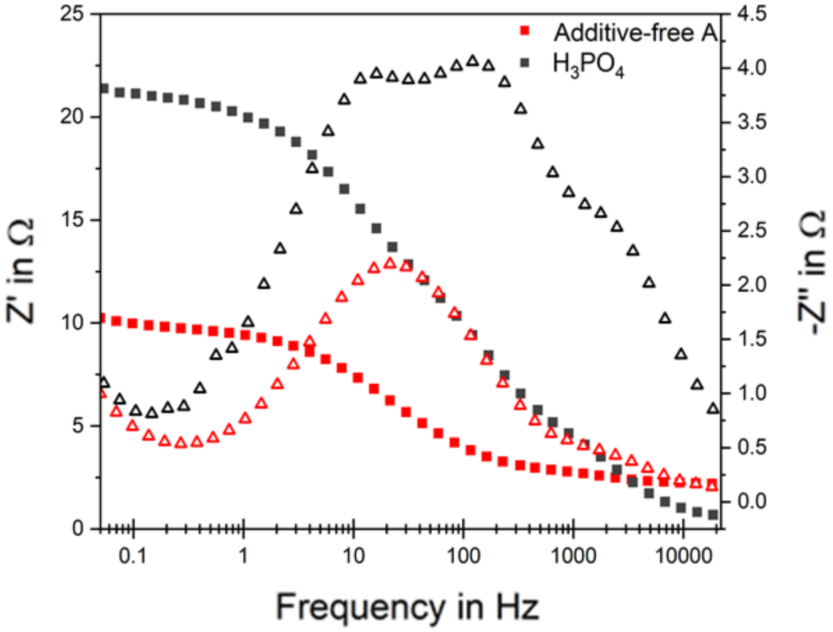

Figure S-6. Electrochemical Impedance Spectroscopy (EIS) measurement of additive-free A (red) and H_3PO_4 8.0 wt.%$_{PVdF}$ (black) cathodes at 0.8 SOC. The Bode representations are shown for the real (squares) and the imaginary part (triangles). The corresponding Nyquist plots are shown in **Figure 29**.

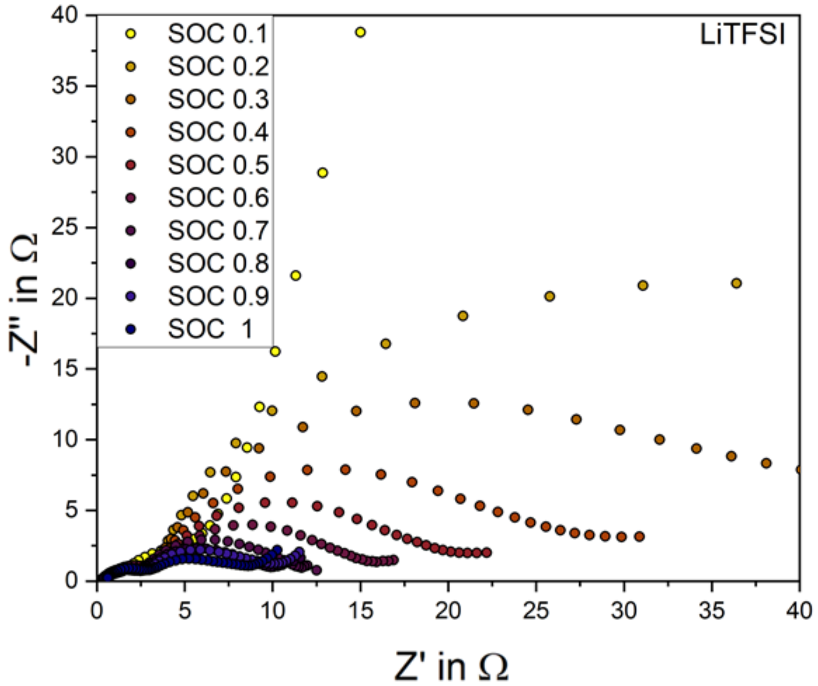

Figure S-7. Measured impedance Nyquist plot of NMC622 electrode from fully discharged SOC=0.1 up to fully charged SOC=1 for 2 mass%PVdF LiTFSI cathode.

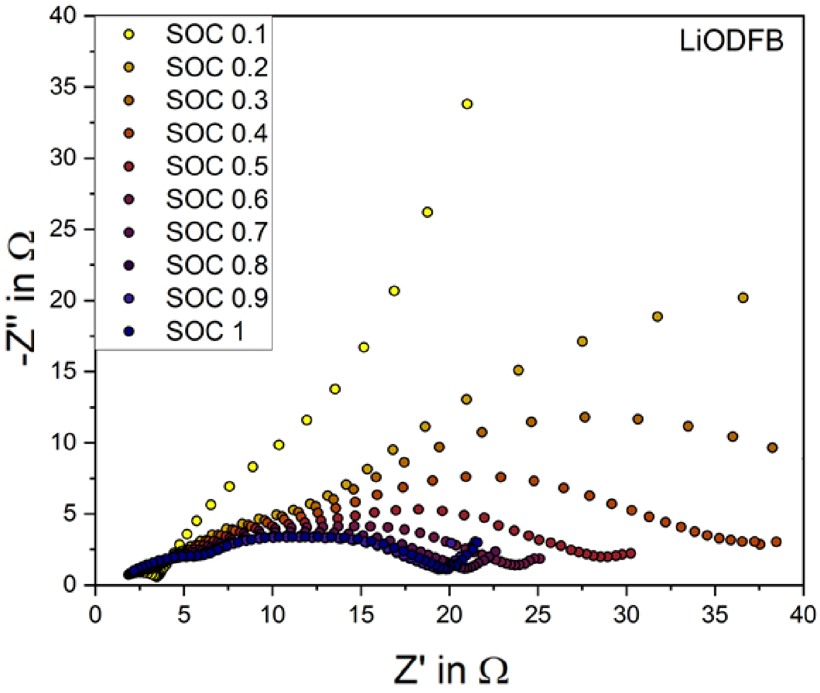

Figure S-8. Measured impedance Nyquist plot of NMC622 electrode from fully discharged SOC=0.1 up to fully charged SOC=1 for 2 mass%PVdF LiODFB cathode.

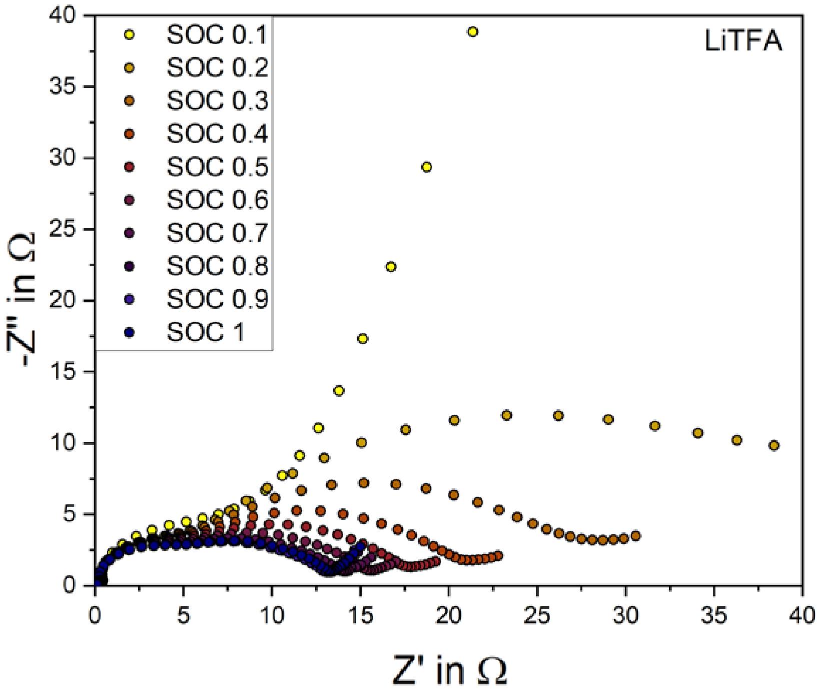

Figure S-9. Measured impedance Nyquist plot of NMC622 electrode from fully discharged SOC=0.1 up to fully charged SOC=1 for 2 mass%PVdF LiTFA cathode.

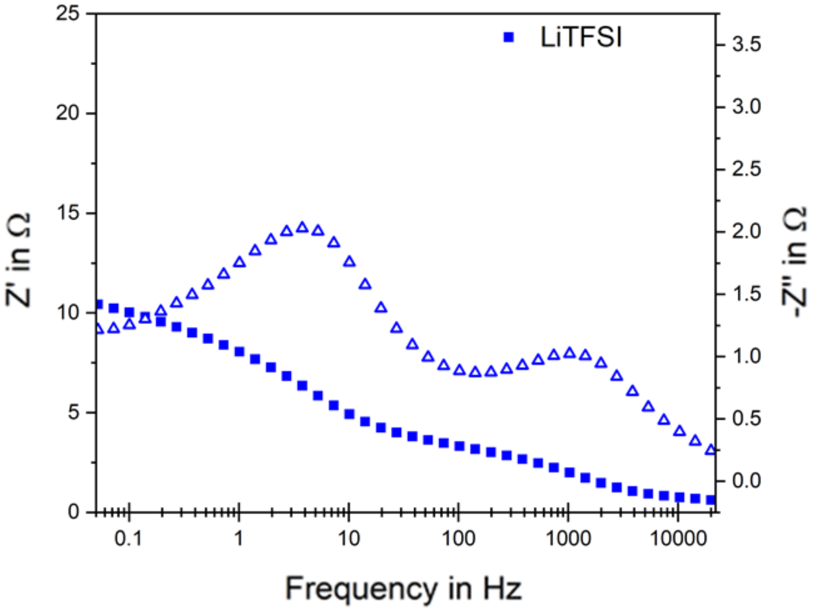

Figure S-10. Electrochemical Impedance Spectroscopy (EIS) measurement of 2 wt.%$_{\mathrm{PVdF}}$ LiTFSI cathode at 0.8 SOC. The Bode representation is shown for the real (squares) and the imaginary part (triangles). The corresponding Nyquist plots are shown in **Figure 35.**

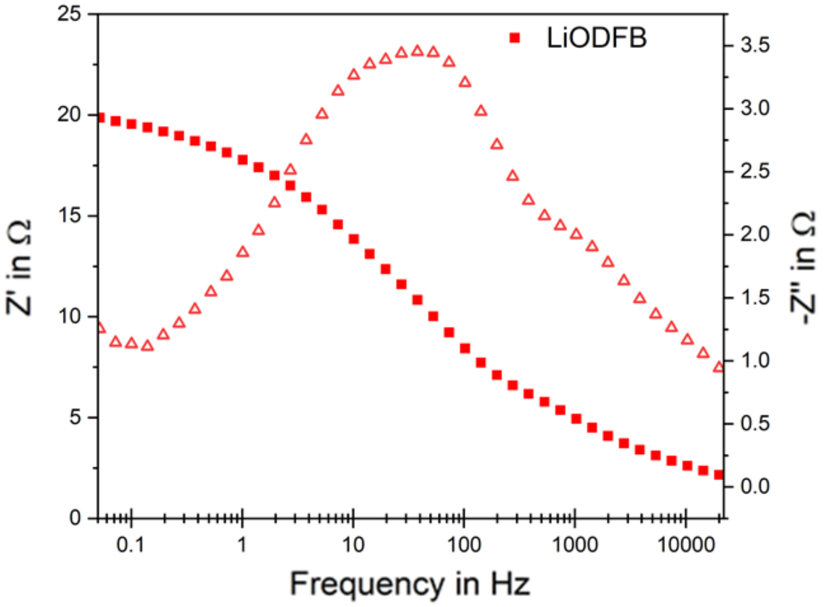

Figure S-11. Electrochemical Impedance Spectroscopy (EIS) measurement of 2 wt.%$_{\mathrm{PVdF}}$ LiODFB cathode at 0.8 SOC. The Bode representation is shown for the real (squares) and the imaginary part (triangles). The corresponding Nyquist plots are shown in **Figure 35**.

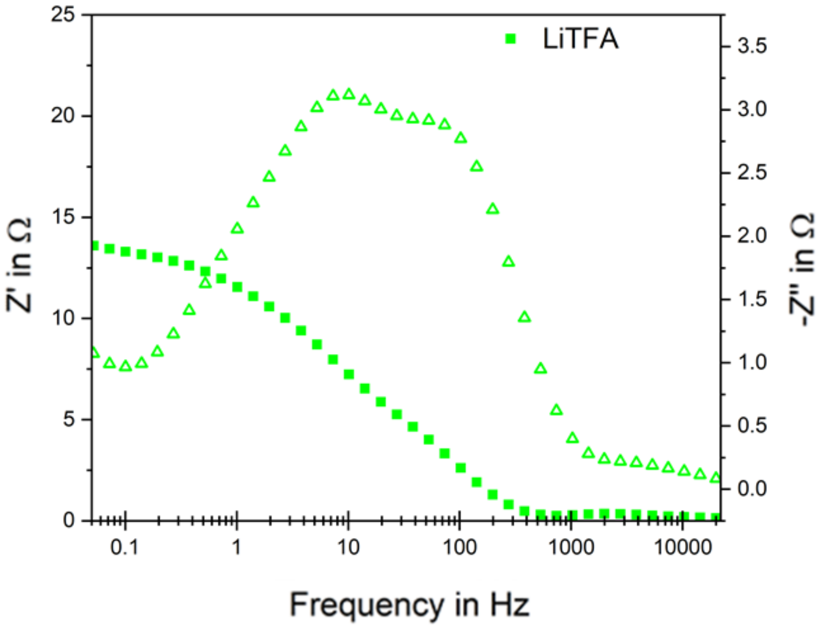

Figure S-12. Electrochemical Impedance Spectroscopy (EIS) measurement of 2 wt.%$_{PVdF}$ LiTFA cathode at 0.8 SOC. The Bode representation is shown for the real (squares) and the imaginary part (triangles). The corresponding Nyquist plots are shown in **Figure 35**.

Table S-2. Fitting parameters for the equivalent circuits of the impedance spectra for additive-free A, 2 wt.%$_{PVdF}$ LiTFA, 2 wt.%$_{PVdF}$ LiODFB and 2 wt.%$_{PVdF}$ LiTFSI cathodes; all values being the average of 2 different impedance measurement. Data fitting was carried out in RelaxIS (Version 3.0.20) using the equivalent circuit in **Figure 35**. Note that parameters representing resistances have not been corrected for the (geometric) surface area (A = 2.010 cm^2) yet and that Wo is affected by large errors due to missing low frequency points.

Sample	R_{el} in Ω	R_0 in Ω	Q_{CPE0} in mS*s^α	$α_{CPE0}$	R_f in Ω	Q_{CPEf} in mS*s^α	$α_{CPEf}$	R_1 in Ω	Q_{CPE1} in mS*s^α	$α_{CPE1}$	Z_{Wo} in Ω	$τ_{Wo}$ in s	$α_{Wo}$
additive-free A	1.3	0.5	0.1	1	3.9	2.4	0.84	2.1	27.1	0.75	2.8	17.0	0.54
LiTFA	0.3	5.7	0.2	0.89	6.2	4.3	0.78	3.3	48.6	0.86	7.7	80.0	0.50
LiODFB	0.4	3.2	0.4	0.75	10	2.6	0.75	4.7	41.7	0.75	0.0	0.0	0.35
LiTFSI	0.5	2	0.5	0.78	4.6	8	0.75	3.6	115.7	0.75	236	1.3E+05	0.50

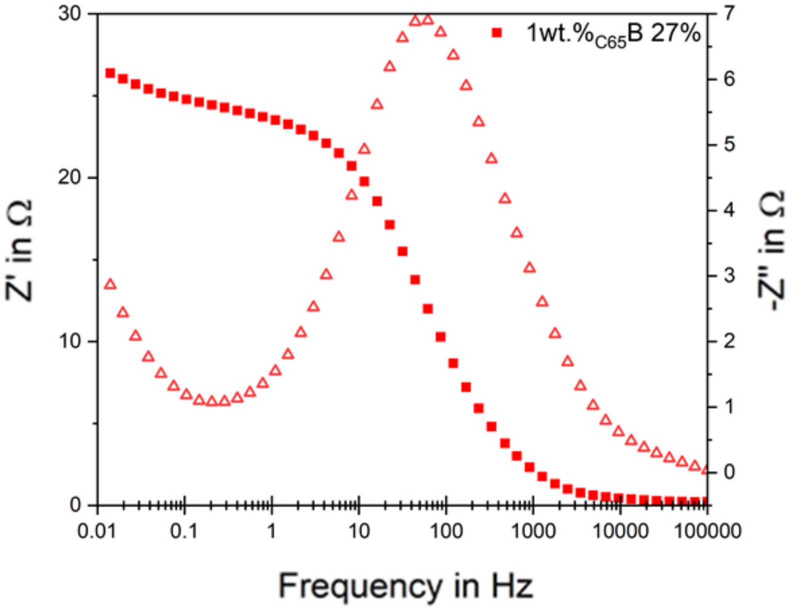

Figure S-13. Electrochemical Impedance Spectroscopy (EIS) measurement of 1wt.%$_{C65}$B 27% cathode at 0.8 SOC. The Bode representation is shown for the real (squares) and the imaginary part (triangles). The corresponding Nyquist plots are shown in **Figure 44.**

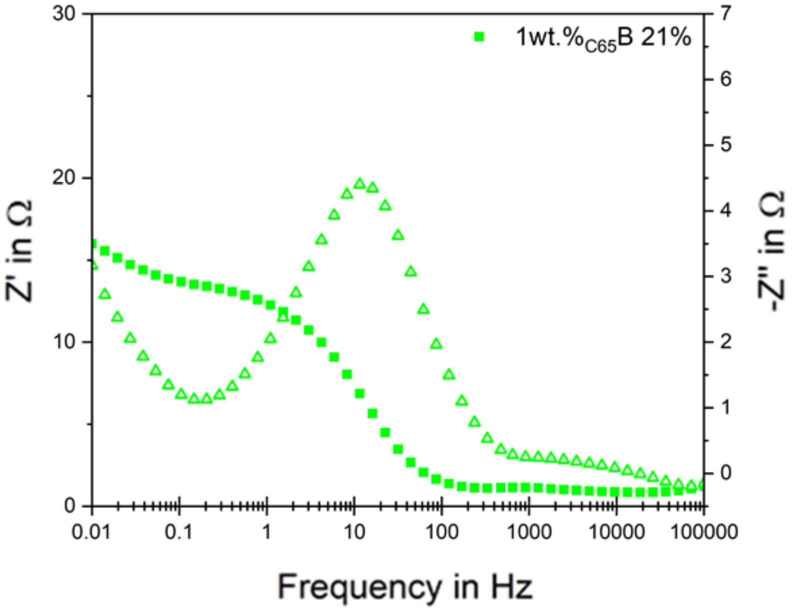

Figure S-14. Electrochemical Impedance Spectroscopy (EIS) measurement of 1wt.%$_{C65}$B 21% cathode at 0.8 SOC. The Bode representation is shown for the real (squares) and the imaginary part (triangles). The corresponding Nyquist plots are shown in **Figure 44.**

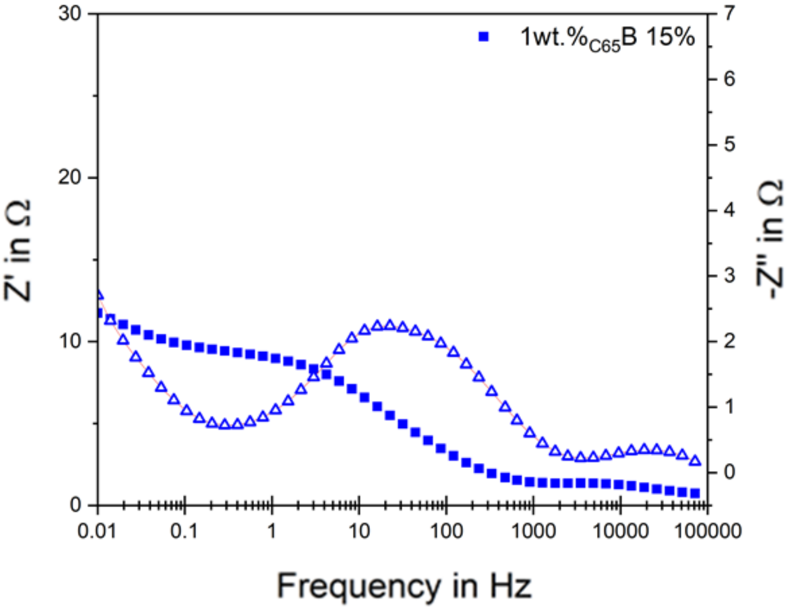

Figure S-15. Electrochemical Impedance Spectroscopy (EIS) measurement of 1wt.%$_{C65}$B 15% cathode at 0.8 SOC. The Bode representation is shown for the real (squares) and the imaginary part (triangles). The corresponding Nyquist plots are shown in **Figure 44.**

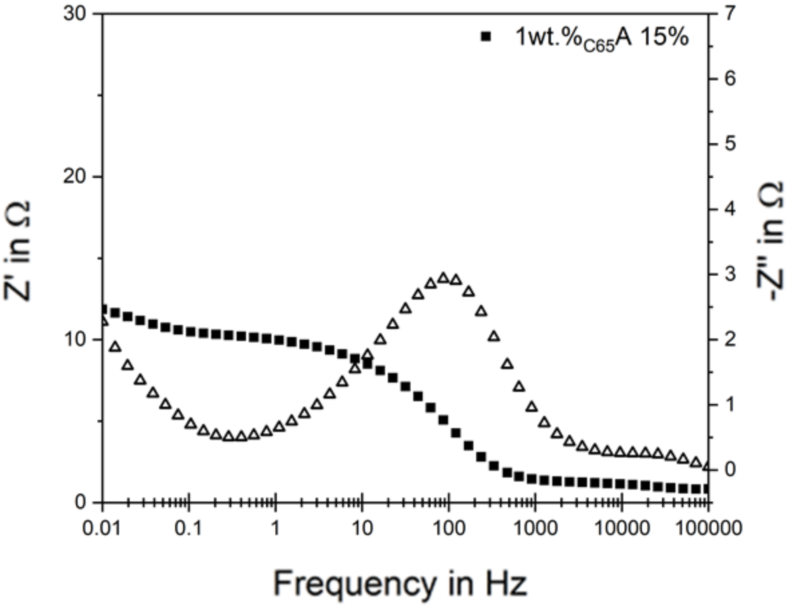

Figure S-16. Electrochemical Impedance Spectroscopy (EIS) measurement of 1wt.%$_{C65}$A 15% cathode at 0.8 SOC. The Bode representation is shown for the real (squares) and the imaginary part (triangles). The corresponding Nyquist plots are shown in **Figure 46**.

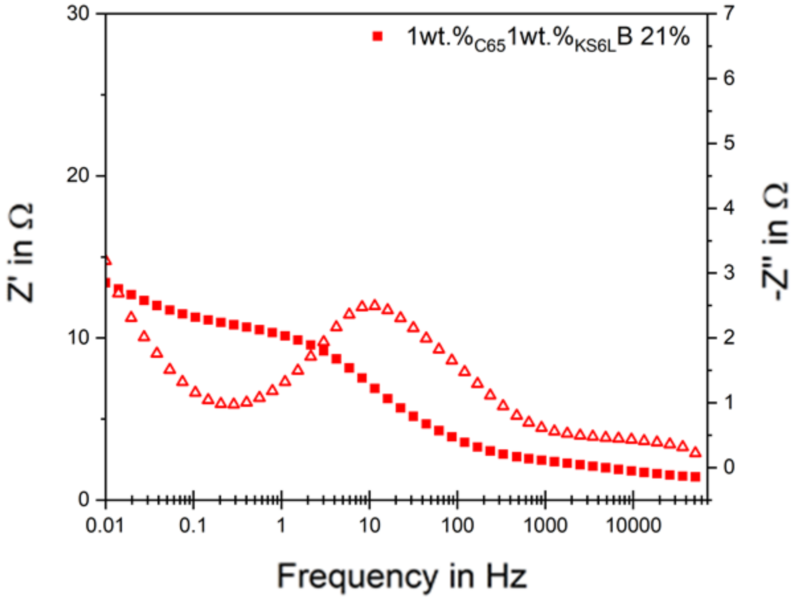

Figure S-17. Electrochemical Impedance Spectroscopy (EIS) measurement of 1wt.%$_{C65}$1wt.%$_{KS6L}$B 21% cathode at 0.8 SOC. The Bode representation is shown for the real (squares) and the imaginary part (triangles). The corresponding Nyquist plots are shown in **Figure 50**.

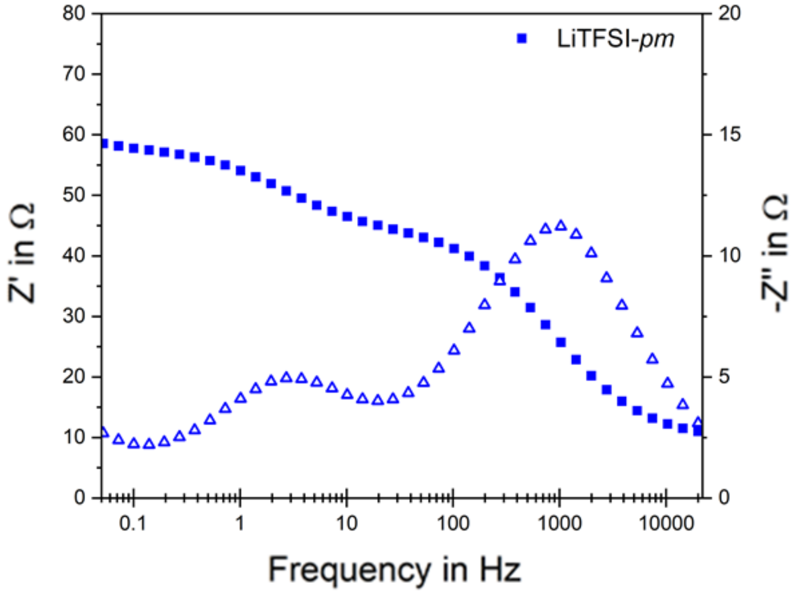

Figure S-18. Electrochemical Impedance Spectroscopy (EIS) measurement of fatigued 2 wt.%$_{PVdF}$ LiTFSI cathode at 0.8 SOC. The Bode representation is shown with the real (squares) and the imaginary part (triangles) for the lowest impedance electrode (one of the two different measured cells) reported in the corresponding Nyquist plots of **Figure 36**.

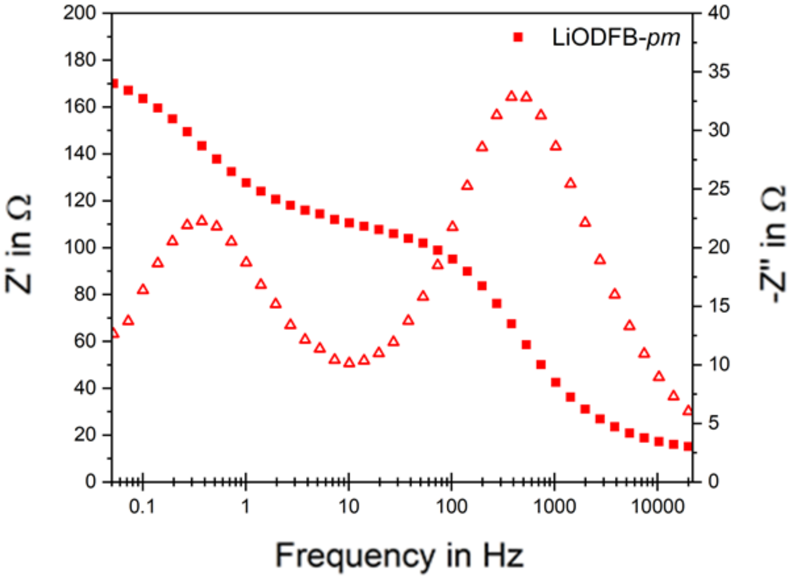

Figure S-19. Electrochemical Impedance Spectroscopy (EIS) measurement of fatigued 2 wt.%$_{\text{PVdF}}$ LiODFB cathode at 0.8 SOC. The Bode representation is shown with the real (squares) and the imaginary part (triangles) for the lowest impedance electrode (one of the two different measured cells) reported in the corresponding Nyquist plots of **Figure 36**.

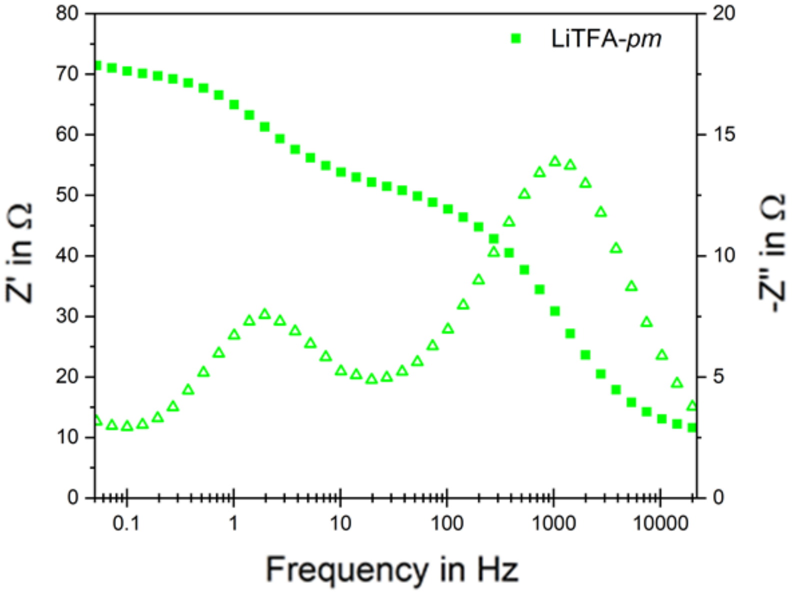

Figure S-20. Electrochemical Impedance Spectroscopy (EIS) measurement of fatigued 2 wt.%$_{\text{PVdF}}$ LiTFA cathode at 0.8 SOC. The Bode representation is shown with the real (squares) and the imaginary part (triangles) for the lowest impedance electrode (one of the two different measured cells) reported in the corresponding Nyquist plots of **Figure 36**.

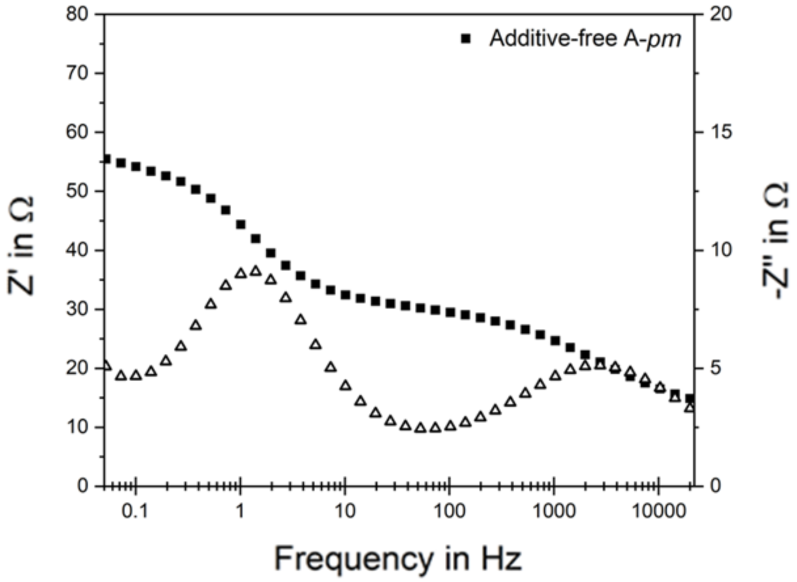

Figure S-21. Electrochemical Impedance Spectroscopy (EIS) measurement of fatigued additive-free A cathode at 0.8 SOC. The Bode representation is shown with the real (squares) and the imaginary part (triangles) for the lowest impedance electrode (one of the two different measured cells) reported in the corresponding Nyquist plots of **Figure 36**.

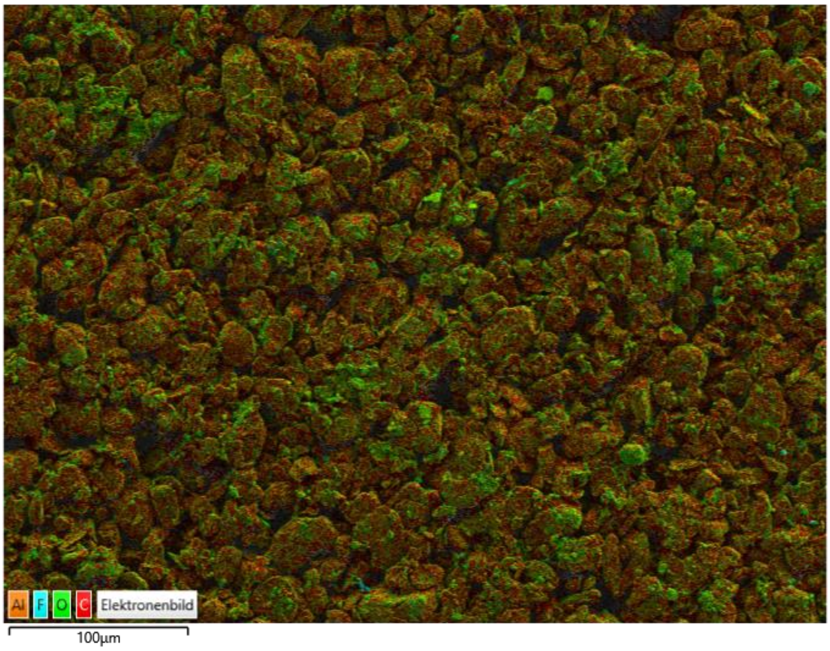

Figure S-22.SEM post mortem image of Anode coupled to the additive-free A cathode.

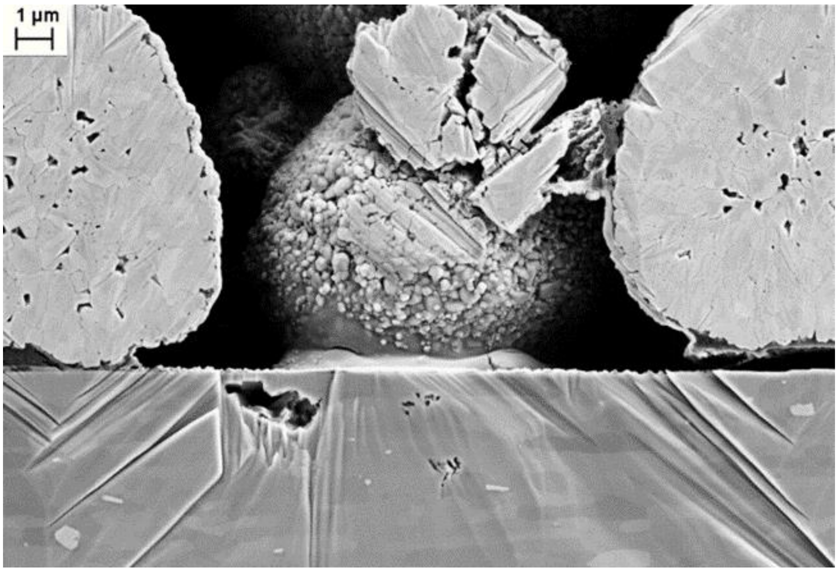

Figure S-23. Post mortem SEM cross section of 2 mass%$_{\text{PVdF}}$ LiTFA cathode with Al foil corrosion.

References

1 F. Colombo, M. Müller, A. Weber, N. Keim, F. Jeschull, W. Bauer and H. Ehrenberg, Electrochemical investigation of fluorine-containing Li-salts as slurry cathode additives for tunable rheology in super high solid content NMP slurries, *RSC Energy Adv.*, 2023, **2**, 2093–2108.

2 B. Ameduri and B. Améduri, The Promising Future of Fluoropolymers Promising Future of Fluoropolymers, *Macromol. Chem. Phys.*, 2020, 221.

3 W. Bauer and D. Nötzel, Rheological properties and stability of NMP based cathode slurries for lithium ion batteries, *Ceram. Int.*, 2014, **40**, 4591–4598.

4 J. A. Lewis, Colloidal Processing of Ceramics, *J. Am. Ceram. Soc.*, 2000, **83**, 2341–2359.

5 W. Bauer and D. Nötzel, Rheological properties and stability of NMP based cathode slurries for lithium ion batteries, *Ceram. Int.*, 2014, **40**, 4591–4598.

6 L. Ouyang, Z. Wu, J. Wang, X. Qi, Q. Li, J. Wang and S. Lu, The effect of solid content on the rheological properties and microstructures of a Li-ion battery cathode slurryOuyang, Lixia Wu, Zhaohui Wang, Jun Qi, Xiaopeng Li, Qiang, *RSC Adv.*, 2020, **10**, 19360–19370.

7 F. Jeschull, D. Brandell, M. Wohlfahrt-Mehrens and M. Memm, Water-Soluble Binders for Lithium-Ion Battery Graphite Electrodes: Slurry Rheology, Coating Adhesion, and Electrochemical Performance, *Energy Technol.*, 2017, **5**, 2108–2118.

8 J. Lee, S. J. Lee, K. H. Ahn and S. J. Lee, Nanoparticle-Induced Gelation of Bimodal Slurries with Highly Size-Asymmetric Particles: Effect of Surface Chemistry and Concentration, *Langmuir*, 2015, **31**, 13639–13646.

9 S. S. Zhang, X. Fan and C. Wang, Enhanced Electrochemical Performance of Ni-Rich Layered Cathode Materials by using LiPF6 as a Cathode Additive, *ChemElectroChem*, 2019, **6**, 1536–1541.

10 S. S. Zhang, Problems and their origins of Ni-rich layered oxide cathode materials, *Energy Storage Mater.*, 2020, **24**, 247–254.

11 H. Arai, S. Okada, H. Ohtsuka, M. Ichimura and J. Yamaki, Characterization and cathode performance of Li1 − xNi1 + xO2 prepared with the excess lithium method, *Solid State Ionics*, 1995, **80**, 261–269.

12 K. Park, J. H. Park, S. G. Hong, B. Choi, S. Heo, S. W. Seo, K. Min and J. H. Park, Re-construction layer effect of LiNi0.8Co0.15Mn0.05O2 with solvent evaporation process, *Sci. Reports 2017 71*, 2017, **7**, 1–10.

13 X. Xiong, Z. Wang, P. Yue, H. Guo, F. Wu, J. Wang and X. Li, Washing effects on electrochemical performance and storage characteristics of LiNi0.8Co0.1Mn0.1O2 as cathode material for lithium-ion batteries, *J. Power Sources*, 2013, **222**, 318–325.

14 H. G. Song, J. Y. Kim, K. T. Kim and Y. J. Park, Enhanced electrochemical properties of Li(Ni0.4Co0.3Mn0.3)O2 cathode by surface modification using Li3PO4-based materials,

J. Power Sources, 2011, **196**, 6847–6855.

15 C. H. Jo, D. H. Cho, H. J. Noh, H. Yashiro, Y. K. Sun and S. T. Myung, An effective method to reduce residual lithium compounds on Ni-rich Li[Ni0.6Co0.2Mn0.2]O2 active material using a phosphoric acid derived Li3PO4 nanolayer, *Nano Res. 2014 85*, 2014, **8**, 1464–1479.

16 V. Aravindan, J. Gnanaraj, S. Madhavi and H. K. Liu, Lithium-ion conducting electrolyte salts for lithium batteries, *Chem. - A Eur. J.*, 2011, **17**, 14326–14346.

17 A. Abend, V. Illich and J. Rétey, Further insights into the mechanism of action of methylmalonyl-CoA mutase by electron paramagnetic resonance studies, *Eur. J. Biochem.*, 1997, **249**, 180–186.

18 K. Oka, C. Strietzel, R. Emanuelsson, H. Nishide, K. Oyaizu, M. Strømme and M. Sjödin, Characterization of PEDOT-Quinone conducting redox polymers in water-in-salt electrolytes for safe and high-energy Li-ion batteries, *Electrochem. commun.*, 2019, **105**, 106489.

19 W. Bauer, F. A. Çetinel, M. Müller and U. Kaufmann, Effects of pH control by acid addition at the aqueous processing of cathodes for lithium ion batteries, *Electrochim. Acta*, 2019, **317**, 112–119.

20 H. Rumpf, Beanspruchungstheorie der Prallzerkleinerung, *Chemie Ing. Tech.*, 1959, **31**, 323–337.

21 D. Grießl, K. Huber, R. Scherbauer and A. Kwade, Dispersion kinetics of carbon black for the application in lithium-ion batteries, *Adv. Powder Technol.*, 2021, **32**, 2280–2288.

22 M. Haarmann, W. Haselrieder and A. Kwade, Extrusion-Based Processing of Cathodes: Influence of Solid Content on Suspension and Electrode Properties, *Energy Technol.*, 2020, **8**, 1–9.

23 J. Li, J. Fleetwood, W. B. Hawley and W. Kays, From Materials to Cell: State-of-the-Art and Prospective Technologies for Lithium-Ion Battery Electrode Processing, *Chem. Rev.*, 2022, **122**, 903–956.

24 D. W. Brown and L. A. Wall, High-temperature aging of fluoropolymers, *J. Polym. Sci. Part A-1 Polym. Chem.*, 1972, **10**, 2967–2982.

25 J. Nieratschker, Fluoroplastics, *Kunststoffe Plast Eur.*, 1994, **86**, 339–372.

26 P. R. Resnick and W. H. Buck, *Teflon® AF: A Family of Amorphous Fluoropolymers with Extraordinary Properties*, Springer, Boston, MA, USA, 2002.

27 B. Ameduri and B. Boutevin, *Well-Architectured Fluoropolymers: Synthesis, Properties and Applications*, Elsevier Ltd, Oxford, UK, 2004.

28 A. L. Moore, *Fluoroelastomers Handbook: The Definitive User's Guide and Databook*, William Andrew Inc., Wilmington, DE, USA, 2005.

29 M. Wehbi, *Fluoropolymers functionalized by phosphorous and silicon groups : syntheses, characterization and applications*, doctoral dissertation, École doctorale Sciences Chimiques Balard, Université de Montpellier, Montpellier, France, 2018.

30 B. Ameduri, From vinylidene fluoride (VDF) to the applications of VDF-Containing polymers and copolymers: Recent developments and future trends, *Chem. Rev.*, 2009, **109**, 6632–6686.

31 B. Améduri, B. Boutevin and G. Kostov, Fluoroelastomers: synthesis, properties and applications, *Prog. Polym. Sci.*, 2001, **26**, 105–187.

32 S. B. Lang, Guide to the literature of piezoelectricity and pyroelectricity. 3, *Ferroelectrics*, 2011, **123**, 69–232.

33 F. Colombo, S. Bonizzoni, C. Ferrara, R. Simonutti, M. Mauri, M. Falco, C. Gerbaldi, P. Mustarelli and R. Ruffo, Polymer-in-Ceramic Nanocomposite Solid Electrolyte for Lithium Metal Batteries Encompassing PEO-Grafted TiO2 Nanocrystals, *J. Electrochem. Soc.*, 2020, **167**, 070535.

34 N. Ahbab, S. Naz, T.-B. Xu and S. Zhang, A Comprehensive Review of Piezoelectric PVDF Polymer Fabrications and Characteristics, *Micromachines*, 2025, **16**, 386.

35 B. Ameduri, Fluoropolymers: The Right Material for the Right Applications, *Chem. - A Eur. J.*, 2018, **24**, 18830–18841.

36 A. Taguet, B. Ameduri and B. Boutevin, Crosslinking of Vinylidene Fluoride-Containing Fluoropolymers, *Adv. Polym. Sci.*, 2005, **184**, 127–211.

37 G. Kutringer and G. Weill, Solution properties of poly(vinylidene fluoride): 1. Macromolecular characterization of soluble samples, *Polymer (Guildf).*, 1991, **32**, 877–883.

38 B. Soegijono, J. Chanra, Z. Zhongwu and P. Mi, Synthesis Polymer Styrene Butadiene Hybrid Latex with Laponite Organoclay as Filler via Emulsion Polymerization Technique for Application in Paper Coating, *ARPN J. Eng. Appl. Sci.*, 2020, **15**, 2673–2687.

39 B. Ameduri and A. Bruno, Copolymers: Recent Developments and Future Trends, *Chem. Rev.*, 2009, **109**, 6632–6686.

40 J. Yang, *Phosphonium ionic liquids : Versatile nanostructuration and interfacial agents for poly(vinylidene fluoride-chlorotrifluoroethylene)*, doctoral dissertation, Université de Lyon, Lyon, France, 2016.

41 J. Guiot, B. Ameduri and B. Boutevin, Radical homopolymerization of vinylidene fluoride initiated by tert-butyl peroxypivalate. Investigation of the microstructure by 19F and 1H NMR spectroscopies and mechanisms, *Macromolecules*, 2002, **35**, 8694–8707.

42 R. Timmerman and W. Greyson, The predominant reaction of some fluorinated polymers to ionizing radiation, *J. Appl. Polym. Sci.*, 1962, **6**, 456–460.

43 N. Anousheh, *Atomistic simulation of fluoropolymers : impact of regiodefects on characterization of polyvinylidene fluoride*, doctoral dissertation, Université de Sherbrooke, Quebec, Canada, 2017.

44 G. A. Otradina, L. Y. Madorskaya, V. M. Belyayev, K. A. Vylegzhanina, O. K. Belomutskaya and T. V. Kornilova, Effect of conditions of synthesis on molecular mass distribution and molecular structure of poly(vinylidene fluoride), *Polym. Sci. U.S.S.R.*, 1990, **32**, 812–817.

45 S. Das Mahapatra, P. C. Mohapatra, A. I. Aria, G. Christie, Y. K. Mishra, S. Hofmann and V.

K. Thakur, Piezoelectric Materials for Energy Harvesting and Sensing Applications: Roadmap for Future Smart Materials, *Adv.Sci., 2021, 8*.

46 D. R. Dillon, K. K. Tenneti, C. Y. Li, F. K. Ko, I. Sics and B. S. Hsiao, On the structure and morphology of polyvinylidene fluoride–nanoclay nanocomposites, *Polymer (Guildf).*, 2006, **47**, 1678–1688.

47 R. Hasegawa, Y. Takahashi, Y. Chatani and H. T. Adokoro, Crystal Structures of Three Crystalline Forms of Poly(vinylidene fluoride), *Polym. J. 1972 35*, 1972, **3**, 600–610.

48 M. Kobayashi, K. Tashiro and H. Tadokoro, Molecular Vibrations of Three Crystal Forms of Poly(vinylidene fluoride), *Macromolecules*, 1975, **8**, 158–171.

49 A. Bachmann and J. B. Lando, A Reexamination of the Crystal Structure of Phase II of Poly(vinylidene fluoride), *Macromolecules*, 1981, **14**, 40–46.

50 M. M. Nasef, H. Saidi and K. Z. M. Dahlan, Investigation of electron irradiation induced-changes in poly(vinylidene fluoride) films, *Polym. Degrad. Stab.*, 2002, **75**, 85–92.

51 J. S. Humphrey and R. Amin-Sanayei, *Vinylidene Fluoride Polymers*, John Wiley & Sons, Inc., Hoboken, New Jersey, USA, 2002.

52 F. Bovey, *Chain Structure and Conformation of Macromolecules*, Academic Press, Cambridge, MA, USA, 2012.

53 A. K. Koech, G. Mwandila, F. Mulolani and P. Mwaanga, Lithium-ion battery fundamentals and exploration of cathode materials: A review, *South African J. Chem. Eng.*, 2024, **50**, 321–339.

54 Y. Ruan, X. Song, Y. Fu, C. Song and V. Battaglia, Structural evolution and capacity degradation mechanism of LiNi0.6Mn0.2Co0.2O2 cathode materials, *J. Power Sources*, 2018, **400**, 539–548.

55 T. Le Thi, T. Phan Van, B. Nguyen Van, N. To Van, T. Nguyen Van, T. P. Doan, T. L. Ngo, N. H. Vu, T. T. Nguyen, H. N. Nguyen, N. V. Anh Duy and M. T. Dang, Modified Coprecipitation Synthesis of Nickel-Rich NMC (Li1.0Ni0.6Mn0.2Co0.2O2) for Lithium-Ion Batteries: A Simple, Cost-Effective, Environmentally Friendly Method, *ACS Omega*, 2023, **8**, 45414–45427.

56 T. Wang, K. Ren, M. He, W. Dong, W. Xiao, H. Pan, J. Yang, Y. Yang, P. Liu, Z. Cao, X. Ma and H. Wang, Synthesis and Manipulation of Single-Crystalline Lithium Nickel Manganese Cobalt Oxide Cathodes: A Review of Growth Mechanism, *Front. Chem.*, 2020, **8**, 575356.

57 M. Malik, K. H. Chan and G. Azimi, Review on the synthesis of LiNixMnyCo1-x-yO2 (NMC) cathodes for lithium-ion batteries, *Mater. Today Energy*, 2022, **28**, 101066.

58 J. Tan and J. Keiding, *The cobalt and lithium global supply chains: status, risks and recommendations*, Report, Center for Minerals and Materials, Geological Survey of Denmark and Greenland, GEUS, Copenhagen, Denmark, 2023.

59 K. R. Tallman, G. P. Wheeler, C. J. Kern, E. Stavitski, X. Tong, K. J. Takeuchi, A. C. Marschilok, D. C. Bock and E. S. Takeuchi, Nickel-rich Nickel Manganese Cobalt (NMC622) Cathode Lithiation Mechanism and Extended Cycling Effects Using Operando X-ray Absorption Spectroscopy, *J. Phys. Chem. C*, 2021, **125**, 58–73.

60 W. Liu, P. Oh, X. Liu, M. J. Lee, W. Cho, S. Chae, Y. Kim and J. Cho, Nickel-Rich Layered Lithium Transition-Metal Oxide for High-Energy Lithium-Ion Batteries, *Angew. Chemie - Int. Ed.*, 2015, **54**, 4440–4457.

61 Y. Duan, L. Yang, M. J. Zhang, Z. Chen, J. Bai, K. Amine, F. Pan and F. Wang, Insights into Li/Ni ordering and surface reconstruction during synthesis of Ni-rich layered oxides, *J. Mater. Chem. A*, 2019, **7**, 513–519.

62 F. Lin, I. M. Markus, D. Nordlund, T. C. Weng, M. D. Asta, H. L. Xin and M. M. Doeff, Surface reconstruction and chemical evolution of stoichiometric layered cathode materials for lithium-ion batteries, *Nat. Commun. 2014 51*, 2014, **5**, 1–9.

63 K. G. Gallagher, S. E. Trask, C. Bauer, T. Woehrle, S. F. Lux, M. Tschech, P. Lamp, B. J. Polzin, S. Ha, B. Long, Q. Wu, W. Lu, D. W. Dees and A. N. Jansen, Optimizing Areal Capacities through Understanding the Limitations of Lithium-Ion Electrodes, *J. Electrochem. Soc.*, 2016, **163**, A138–A149.

64 L. Wang, J. Li, X. He, W. Pu, C. Wan and C. Jiang, Recent advances in layered LiNi x Co yMn 1-x-y O 2 cathode materials for lithium ion batteries, *J. Solid State Electrochem.*, 2009, **13**, 1157–1164.

65 F. De Giorgio, *High-Voltage Lithium-Ion Batteries for a Sustainable Transport*, doctoral dissertation, Alma Mater Studiorum Università di Bologna, Università di Bologna, Bologna, Italy, 2016.

66 S. Wang, M. Yan, Y. Li, C. Vinado and J. Yang, Separating electronic and ionic conductivity in mix-conducting layered lithium transition-metal oxides, *J. Power Sources*, 2018, **393**, 75–82.

67 S. J. Rajoba, L. D. Jadhav, P. S. Patil, D. K. Tyagi, S. Varma and B. N. Wani, Enhancement of Electrical Conductivity of LiFePO4 by Controlled Solution Combustion Synthesis, *J. Electron. Mater.*, 2017, **46**, 1683–1691.

68 F. Ma, Y. Fu, V. Battaglia and R. Prasher, Microrheological modeling of lithium ion battery anode slurry, *J. Power Sources*, 2019, **438**, 226994.

69 M. Weber, J. K. Mayer and A. Kwade, The Carbon Black Dispersion Index DICB: A Novel Approach Describing the Dispersion Progress of Carbon Black Containing Battery Slurries, *Energy Technol.*, 2023, **2201299**, 1–7.

70 A. A. Potanin and W. B. Russel, Fractal model of consolidation of weakly aggregated colloidal dispersions, *Phys. Rev. E - Stat. Physics, Plasmas, Fluids, Relat. Interdiscip. Top.*, 1996, **53**, 3702–3709.

71 A. A. Potanin, R. De Rooij, D. Van Den Ende and J. Mellema, Microrheological modeling of weakly aggregated dispersions, *J. Chem. Phys.*, 1995, **102**, 5845–5853.

72 A. Narayanan, F. Mugele and M. H. G. Duits, Mechanical History Dependence in Carbon Black Suspensions for Flow Batteries: A Rheo-Impedance Study, *Langmuir*, 2017, **33**, 1629–1638.

73 V. Wenzel, H. Nirschl and D. Nötzel, Challenges in Lithium-Ion-Battery Slurry Preparation and Potential of Modifying Electrode Structures by Different Mixing Processes, *Energy Technol.*, 2015, **3**, 692–698.

74 L. H. Hanus, R. U. Hartzler and N. J. Wagner, Electrolyte-induced aggregation of acrylic latex. 1: Dilute particle concentrations, *Langmuir*, 2001, **17**, 3136–3147.

75 A. Basch, R. Horn and J. O. Besenhard, Substrate induced coagulation (SIC) of nano-disperse carbon black in non-aqueous media: The dispersibility and stability of carbon black in N-methyl-2-pyrrolidinone, *Colloids Surfaces A Physicochem. Eng. Asp.*, 2005, **253**, 155–161.

76 M. A. C. Stuart, Adsorbed polymers in colloidal systems: From statics to dynamics, *Polym. J.*, 1991, **23**, 669–682.

77 S. P. Rwei, F. H. Ku and K. C. Cheng, Dispersion of carbon black in a continuous phase: Electrical, rheological, and morphological studies, *Colloid Polym. Sci.*, 2002, **280**, 1110–1115.

78 W. K. Goertzen and M. R. Kessler, Dynamic mechanical analysis of fumed silica/cyanate ester nanocomposites, *Compos. Part A Appl. Sci. Manuf.*, 2008, **39**, 761–768.

79 M. Kuenzel, D. Bresser, T. Diemant, D. V. Carvalho, G. Kim, R. J. Behm and S. Passerini, Complementary Strategies Toward the Aqueous Processing of High-Voltage $LiNi_{0.5}Mn_{1.5}O_4$ Lithium-Ion Cathodes, *ChemSusChem*, 2018, **11**, 562–573.

80 M. Memm, A. Hoffmann and M. Wohlfahrt-Mehrens, Water-based LiNi1/3Mn1/3Co1/3O2-cathodes with good electrochemical performance by use of additives, *Electrochim. Acta*, 2018, **260**, 664–673.

81 N. Loeffler, J. Von Zamory, N. Laszczynski, I. Doberdo, G. T. Kim and S. Passerini, Performance of LiNi1/3Mn1/3Co1/3O 2/graphite batteries based on aqueous binder, *J. Power Sources*, 2014, **248**, 915–922.

82 N. Loeffler, G.-T. Kim, F. Mueller, T. Diemant, J.-K. Kim, R. J. Behm and S. Passerini, In Situ Coating of $Li[Ni_{0.33}Mn_{0.33}Co_{0.33}]O_2$ Particles to Enable Aqueous Electrode Processing, *ChemSusChem*, 2016, **9**, 1112–1117.

83 Z. Wang, N. Dupré, A. C. Gaillot, B. Lestriez, J. F. Martin, L. Daniel, S. Patoux and D. Guyomard, CMC as a binder in LiNi 0.4Mn 1.6O 4 5 v cathodes and their electrochemical performance for Li-ion batteries, *Electrochim. Acta*, 2012, **62**, 77–83.

84 R. Jung, F. Linsenmann, R. Thomas, J. Wandt, S. Solchenbach, F. Maglia, C. Stinner, M. Tromp and H. A. Gasteiger, Nickel, Manganese, and Cobalt Dissolution from Ni-Rich NMC and Their Effects on NMC622-Graphite Cells, *J. Electrochem. Soc.*, 2019, **166**, A378–A389.

85 Y. Xu, S. Fang, M. Zarrabeitia, M. Kuenzel, D. Geiger, U. Kaiser, S. Passerini and D. Bresser, Important Impact of the Slurry Mixing Speed on Water-Processed Li4Ti5O12Lithium-Ion Anodes in the Presence of H3PO4as the Processing Additive, *ACS Appl. Mater. Interfaces*, 2022, **14**, 43237–43245.

86 D. Aurbach, B. Markovsky, M. D. Levi, E. Levi, A. Schechter, M. Moshkovich and Y. Cohen, New insights into the interactions between electrode materials and electrolyte solutions for advanced nonaqueous batteries, *J. Power Sources*, 1999, **81**–**82**, 95–111.

87 A. Webber, Conductivity and Viscosity of Solutions of LiCF3 SO 3, Li (CF 3 SO 2) 2 N , and Their Mixtures, *J. Electrochem. Soc.*, 1991, **138**, 2586–2590.

88 J. Foropoulos and D. D. Desmarteau, Contribution from the Synthesis, Properties, and Reactions of Bis((trifluoromethyl)sulfonyl) Imide, (CF3S02)2NH1, *Inorg. Chem*, 1984, **23**, 3720–3723.

89 H. Zhou, Z. Fang and J. Li, LiPF6 and lithium difluoro(oxalato)borate/ethylene carbonate + dimethyl carbonate + ethyl(methyl)carbonate electrolyte for Li4Ti5O12 anode, *J. Power Sources*, 2013, **230**, 148–154.

90 S. S. Zhang, Lithium Oxalyldifluoroborate as a Salt for the Improved Electrolytes of Li-Ion Batteries, *ECS Trans.*, 2007, **3**, 59–68.

91 J. Huang, L. Z. Fan, B. Yu, T. Xing and W. Qiu, Density functional theory studies on the B-containing lithium salts, *Ionics (Kiel).*, 2010, **16**, 509–513.

92 H. Zhou, F. Liu and J. Li, Preparation, Thermal Stability and Electrochemical Properties of LiODFB, *J. Mater. Sci. Technol.*, 2012, **28**, 723–727.

93 N. Ehteshami, L. Ibing, L. Stolz, M. Winter and E. Paillard, Ethylene carbonate-free electrolytes for Li-ion battery: Study of the solid electrolyte interphases formed on graphite anodes, *J. Power Sources*, 2020, **451**, 227804.

94 H. Zhou, D. Xiao, C. Yin, Z. Yang, K. Xiao and J. Li, Enhanced performance of the electrolytes based on sulfolane and lithium difluoro(oxalate)borate with enhanced interfacial stability for LiNi0.5Mn1.5O4 cathode, *J. Electroanal. Chem.*, 2018, **808**, 293–302.

95 S. Li, Y. Liang, J. Xie, L. Ai, Y. Xie, C. Li, C. Wang and X. Cui, Compatibility between lithium difluoro (oxalate) borate-based electrolytes and Li1.2Mn0.54Ni0.13Co0.13O2 cathode for lithium-ion batteries, *J. Electroanal. Chem.*, 2018, **823**, 688–696.

96 A. Hofmann, A. Höweling, N. Bohn, M. Müller, J. R. Binder and T. Hanemann, Additives for Cycle Life Improvement of High-Voltage LNMO-Based Li-Ion Cells, *ChemElectroChem*, 2019, **6**, 5255–5263.

97 Z. Wang, F. Qi, L. Yin, Y. Shi, C. Sun, B. An, H. M. Cheng and F. Li, An Anion-Tuned Solid Electrolyte Interphase with Fast Ion Transfer Kinetics for Stable Lithium Anodes, *Adv. Energy Mater.*, 2020, **10**, 1903843.

98 G. Park, J. S. Park, H. S. Kim and K. J. Lee, Preparation of cathode slurry for lithium-ion battery by three-roll mill process, *Carbon Lett.*, 2022, **32**, 265–272.

99 H. A. Barnes, J. F. (John F. Hutton and K. Walters, *An introduction to rheology*, Elsevier Science, Amsterdam, Netherlands, 1989.

100 S. H. Sung, S. Kim, J. H. Park, J. D. Park and K. H. Ahn, Role of PVDF in rheology and microstructure of NCM cathode slurries for lithium-ion battery, *Materials (Basel).*, 2020, **13**, 4544.

101 J. J. Lee and G. G. Fuller, Adsorption and desorption of flexible polymer chains in flowing systems, *J. Colloid Interface Sci.*, 1985, **103**, 569–577.

102 G. J. Fleer, M. A. Cohen Stuart, J. M. H. M. Scheutjens, T. Cosgrove, B. V. Chapman and H. London, Polymers at interfaces, *Polym. Int.*, 1995, **36**, 102–102.

103 Y. Adachi, Polyelectrolyte Dynamics, *Encycl. Colloid Interface Sci.*, 2013, 931–944.

104 E. Dickinson and S. R. Euston, Computer simulation of bridging flocculation, *J. Chem. Soc. Faraday Trans.*, 1991, **87**, 2193–2199.

105 M. G. Rasteiro, F. A. P. Garcia, P. Ferreira, A. Blanco, C. Negro and E. Antunes, The use of LDS as a tool to evaluate flocculation mechanisms, *Chem. Eng. Process. Process Intensif.*, 2008, **47**, 1323–1332.

106 L. Ouyang, Z. Wu, J. J. Wang, X. Qi, Q. Li, J. J. Wang and S. Lu, The effect of solid content on the rheological properties and microstructures of a Li-ion battery cathode slurry, *RSC Adv.*, 2020, **10**, 19360–19370.

107 K. Matsumoto, R. Kuzuo, K. Takeya and A. Yamanaka, Effects of CO2 in air on Li deintercalation from LiNi1-x-yCoxAlyO2, *J. Power Sources*, 1999, **81**–**82**, 558–561.

108 Y. Kim, Investigation of the gas evolution in lithium ion batteries: Effect of free lithium compounds in cathode materials, *J. Solid State Electrochem.*, 2013, **17**, 1961–1965.

109 A. A. Henry A. Sodano, *US10584189B2 -Ferroelectric polymers from dehydrofluorinated PVDF - Google Patents*, 2020.

110 C. Van Goethem, M. M. Magboo, M. Mertens, M. Thijs, G. Koeckelberghs and I. F. J. Vankelecom, A scalable crosslinking method for PVDF-based nanofiltration membranes for use under extreme pH conditions, *J. Memb. Sci.*, 2020, **611**, 118274.

111 C. Van Goethem, M. Mertens and I. F. J. Vankelecom, Crosslinked PVDF membranes for aqueous and extreme pH nanofiltration, *J. Memb. Sci.*, 2019, **572**, 489–495.

112 L. Pagliaro and D. A. Lowy, Interaction of polyvinylidene fluoride (PVDF)-based binders with strongly alkaline solutions, *Granja*, 2019, **29**, 18–32.

113 R. Patidar, D. Burkitt, K. Hooper, D. Richards and T. Watson, Slot-die coating of perovskite solar cells: An overview, *Mater. Today Commun.*, 2020, **22**, 100808.

114 S. N. Bryntesen, A. H. Strømman, I. Tolstorebrov, P. R. Shearing, J. J. Lamb and O. Stokke Burheim, Opportunities for the state-of-the-art production of lib electrodes—a review, *MDPI AG*, 2021.

115 W. B. Hawley and J. Li, Beneficial Rheological Properties of Lithium-Ion Battery Cathode Slurries 1 from Elevated Mixing and Coating Temperatures 2 3, *J. Energy Storage*, 2019, **26**, 574–4978.

116 M. Nikpour, B. Liu, P. Minson, Z. Hillman, B. A. Mazzeo and D. R. Wheeler, Li-ion Electrode Microstructure Evolution during Drying and Calendering, *Batter. 2022, Vol. 8, Page 107*, 2022, **8**, 107.

117 D. Leanza, C. A. F. Vaz, G. Melinte, X. Mu, P. Novák and M. El Kazzi, Revealing the Dual Surface Reactions on a HE-NCM Li-Ion Battery Cathode and Their Impact on the Surface Chemistry of the Counter Electrode, *ACS Appl. Mater. Interfaces*, 2019, **11**, 6054–6065.

118 F. Font, B. Protas, G. Richardson and J. M. Foster, Binder migration during drying of lithium-ion battery electrodes: Modelling and comparison to experiment, *J. Power Sources*, 2018, **393**, 177–185.

119 S. Jaiser, M. Müller, M. Baunach, W. Bauer, P. Scharfer and W. Schabel, Investigation of film solidification and binder migration during drying of Li-Ion battery anodes, *J. Power*

Sources, 2016, **318**, 210–219.

120 J. Klemens, L. Schneider, E. C. Herbst, N. Bohn, M. Müller, W. Bauer, P. Scharfer and W. Schabel, Drying of NCM Cathode Electrodes with Porous, Nanostructured Particles Versus Compact Solid Particles: Comparative Study of Binder Migration as a Function of Drying Conditions, *Energy Technol.*, 2022, **10**, 2100985.

121 M. Müller, L. Pfaffmann, S. Jaiser, M. Baunach, V. Trouillet, F. Scheiba, P. Scharfer, W. Schabel and W. Bauer, Investigation of binder distribution in graphite anodes for lithium-ion batteries, *J. Power Sources*, 2017, **340**, 1–5.

122 M. Armand, P. Axmann, D. Bresser, M. Copley, K. Edström, C. Ekberg, D. Guyomard, B. Lestriez, P. Novák, M. Petranikova, W. Porcher, S. Trabesinger, M. Wohlfahrt-Mehrens and H. Zhang, Lithium-ion batteries – Current state of the art and anticipated developments, *J. Power Sources, 2020.*

123 D. L. Wood, M. Wood, J. Li, Z. Du, R. E. Ruther, K. A. Hays, N. Muralidharan, L. Geng, C. Mao and I. Belharouak, Perspectives on the relationship between materials chemistry and roll-to-roll electrode manufacturing for high-energy lithium-ion batteries, *Energy Storage Mater.*, 2020, **29**, 254–265.

124 D. Parikh, T. Christensen and J. Li, Correlating the influence of porosity, tortuosity, and mass loading on the energy density of LiNi0.6Mn0.2Co0.2O2 cathodes under extreme fast charging (XFC) conditions, *J. Power Sources*, 2020, **474**, 228601.

125 Z. Du, D. L. Wood, C. Daniel, S. Kalnaus and J. Li, Understanding limiting factors in thick electrode performance as applied to high energy density Li-ion batteries, *J. Appl. Electrochem.*, 2017, **47**, 405–415.

126 Y. Qi, T. Jang, V. Ramadesigan, D. T. Schwartz and V. R. Subramanian, Is There a Benefit in Employing Graded Electrodes for Lithium-Ion Batteries?, *J. Electrochem. Soc.*, 2017, **164**, A3196–A3207.

127 W. Bauer, D. Nötzel, V. Wenzel and H. Nirschl, Influence of dry mixing and distribution of conductive additives in cathodes for lithium ion batteries, *J. Power Sources*, 2015, **288**, 359–367.

128 M. Muller, L. Schneider, N. Bohn, J. R. Binder and W. Bauer, Effect of Nanostructured and Open-Porous Particle Morphology on Electrode Processing and Electrochemical Performance of Li-Ion Batteries, *ACS Appl. Energy Mater.*, 2021, **4**, 1993–2003.

129 L. Zhang, E. A. Müller Gubler, C. W. Tai, Ł. Kondracki, H. Sommer, P. Novák, M. El Kazzi and S. Trabesinger, Elucidating the Humidity-Induced Degradation of Ni-Rich Layered Cathodes for Li-Ion Batteries, *ACS Appl. Mater. Interfaces*, 2022, **14**, 13240–13249.

130 L. Schneider, J. Klemens, E. C. Herbst, M. Müller, P. Scharfer, W. Schabel, W. Bauer and H. Ehrenberg, Transport Properties in Electrodes for Lithium-Ion Batteries: Comparison of Compact versus Porous NCM Particles, *J. Electrochem. Soc.*, 2022, **169**, 100553.

131 A. Davoodabadi, J. Li, Y. Liang, R. Wang, H. Zhou, D. L. Wood, T. J. Singler and C. Jin, Characterization of Surface Free Energy of Composite Electrodes for Lithium-Ion Batteries, *J. Electrochem. Soc.*, 2018, **165**, A2493–A2501.

132 W. B. Hawley, *Understanding Colloidal and Surface Phenomena to Manufacture Energy-*

Dense Lithium-Ion and Solid-State Battery Cathodes, doctoral dissertation, University of Tennessee, Knoxville, USA, 2021.

133 C. Meyer, M. Weyhe, W. Haselrieder and A. Kwade, Heated Calendering of Cathodes for Lithium-Ion Batteries with Varied Carbon Black and Binder Contents, *Energy Technol.*, 2020, **8**, 1900175.

134 Y. Ma, J. Ma and G. Cui, Small things make big deal: Powerful binders of lithium batteries and post-lithium batteries, *Energy Storage Mater.*, 2019, **20**, 146–175.

135 A. Figoli, S. Simone, A. Criscuoli, S. A. Al-Jlil, F. S. Al Shabouna, H. S. Al-Romaih, E. Di Nicolò, O. A. Al-Harbi and E. Drioli, Hollow fibers for seawater desalination from blends of PVDF with different molecular weights: Morphology, properties and VMD performance, *Polymer (Guildf).*, 2014, **55**, 1296–1306.

136 D. Megías-Alguacil, Characterization of the Linear Viscoelastic Region in Suspensions of Zirconium Oxide: Cohesive Energy Obtained From the Critical Parameters, *Appl. Rheol.*, 2004, **14**, 57–126.

137 F. Matsumoto and T. Gunji, *Water in Lithium-Ion Batteries*, Springer Nature Singapore, Singapore, 2022.

138 A. Purwanto, S. Nisa, I. P. Lestari, M. N. Ikhsanudin, C. S. Yudha and H. Widiyandari, High Performance Nickel Based Electrodes in State-of-the-Art Lithium-Ion Batteries: Morphological Perspectives, *KONA Powder Part. J.*, 2022, **39**, 130–149.

139 Y. Li, M. Abdel-Monem, R. Gopalakrishnan, M. Berecibar, E. Nanini-Maury, N. Omar, P. van den Bossche and J. Van Mierlo, A quick on-line state of health estimation method for Li-ion battery with incremental capacity curves processed by Gaussian filter, *J. Power Sources*, 2018, **373**, 40–53.

140 J.-M. Atebamba, J. Moskon, S. Pejovnik and M. Gaberscek, On the Interpretation of Measured Impedance Spectra of Insertion Cathodes for Lithium-Ion Batteries, *J. Electrochem. Soc.*, 2010, **157**, A1218.

141 S. M. Iveson, J. D. Litster, K. Hapgood and B. J. Ennis, Nucleation, growth and breakage phenomena in agitated wet granulation processes: a review, *Powder Technol.*, 2001, **117**, 3–39.

142 M. Biso, R. Colombo, M. J. Uddin, M. Stanga and S. J. Cho, A rheological behavior of various polyvinylidene difluoride binders for high capacity LiNi0.6Mn0.2Co0.2O2, *Polym. Eng. Sci.*, 2016, **56**, 760–764.

143 C. Friedrich, W. Gleinser, E. Korat, D. Maier and J. Weese, Comparison of sphere-size distributions obtained from rheology and transmission electron microscopy in PMMA/PS blends, *J. Rheol. (N. Y. N. Y).*, 1995, **39**, 1411–1425.

144 M. A. Kohudic and K. M. Finlayson, *Advances in Polymer Blends and Alloys Technology*, CRC Press, Boca Raton, FL, USA, 1988, vol. 1–2.

145 N. Lawrence, *Mechanical properties of polymers and composites*, M. Dekker, New York, USA, 1974, vol. 1.

146 X. Lu, X. Zhang, C. Tan, T. M. M. Heenan, M. Lagnoni, K. O'Regan, S. Daemi, A. Bertei, H.

G. Jones, G. Hinds, J. Park, E. Kendrick, D. J. L. Brett and P. R. Shearing, Multi-length scale microstructural design of lithium-ion battery electrodes for improved discharge rate performance, *Energy Environ. Sci.*, 2021, **14**, 5929–5946.

147 J. Zheng, G. Xing, L. Jin, Y. Lu, N. Qin, S. Gao and J. P. Zheng, Strategies and Challenge of Thick Electrodes for Energy Storage: A Review, *Batter. 2023, Vol. 9, Page 151*, 2023, **9**, 151.

148 E. Barsoukov and J. R. (James R. Macdonald, *Impedance spectroscopy : theory, experiment, and applications.*, John Wiley & Sons, Inc., Hoboken, NJ, USA, Second edi., 2005.

149 L. Zhang, C. Zhao, X. Qin, S. Wang, L. He, K. Qian, T. Han, Z. Yang, F. Kang and B. Li, Heterogeneous Degradation in Thick Nickel-Rich Cathodes During High-Temperature Storage and Mitigation of Thermal Instability by Regulating Cationic Disordering, *Small*, 2021, **17**, 1–8.

150 J. E. Vogel, M. M. Forouzan, E. E. Hardy, S. T. Crawford, D. R. Wheeler and B. A. Mazzeo, Electrode microstructure controls localized electronic impedance in Li-ion batteries, *Electrochim. Acta*, 2019, **297**, 820–825.

151 S. Lopez, J. Petit, G. Tourillon, H. M. Dunlop and J. Butruille, Acid-Base Properties of Passive Films on Aluminum: II. An X-Ray Photoelectron Spectroscopy and X-Ray Absorption Near Edge Structure Study, *J. Electrochem. Soc.*, 1998, **145**, 829–834.

152 A. Schulze, M. F. Maitz, R. Zimmermann, B. Marquardt, M. Fischer, C. Werner, M. Went and I. Thomas, Permanent surface modification by electron-beam-induced grafting of hydrophilic polymers to PVDF membranes, *RSC Adv.*, 2013, **3**, 22518–22526.

153 E. McCafferty, Lewis Acid/Lewis Base Effects in Corrosion and Polymer Adhesion at Aluminum Surfaces, *J. Electrochem. Soc.*, 2003, **150**, B342.

154 P. Melnikov, S. B. Santagnelli, F. J. Dos Santos, A. A. S. T. Delben, J. R. J. Delben and A. L. R. Teixeira, Phosphate functionalization of spongiolite surface, *Mater. Chem. Phys.*, 2003, **82**, 980–983.

155 P. H. Given and L. W. Hill, Analysis of surface groups on carbon blacks, *Carbon N. Y.*, 1969, **7**, 649–658.

156 B. Strzemiecka, A. Voelkel, J. Donate-Robles and J. M. Martín-Martínez, Assessment of the surface chemistry of carbon blacks by TGA-MS, XPS and inverse gas chromatography using statistical chemometric analysis, *Appl. Surf. Sci.*, 2014, **316**, 315–323.

157 X. Li and K. Horita, Electrochemical characterization of carbon black subjected to RF oxygen plasma, *Carbon N. Y.*, 2000, **38**, 133–138.

158 T. Takada, M. Nakahara, H. Kumagai and Y. Sanada, Surface modification and characterization of carbon black with oxygen plasma, *Carbon N. Y.*, 1996, **34**, 1087–1091.

159 S. Hagiwara, K. Tsutsumi and H. Takahashi, Change of Polarity on Carbon Black Surface by Oxidation with Various Oxidizing Agents, *TANSO*, 1981, **1981**, 139–143.

160 A. J. Groszek, Graphitic and polar surface sites in carbonaceous solids, *Carbon N. Y.*, 1987, **25**, 717–722.

161 N. Tsubokawa, Functionalization of carbon material by surface grafting of polymers, *Bull. Chem. Soc. Jpn.*, 2002, **75**, 2115–2136.

162 T. Goto, Y. Amano, M. Machida and F. Imazeki, Effect of polarity of activated carbon surface, solvent and adsorbate on adsorption of aromatic compounds from liquid phase, *Chem. Pharm. Bull.*, 2015, **63**, 726–730.

163 D. Leistenschneider, K. Zürbes, C. Schneidermann, S. Grätz, S. Oswald, K. Wegner, B. Klemmed, L. Giebeler, A. Eychmüller and L. Borchardt, Mechanochemical Functionalization of Carbon Black at Room Temperature, *C*, 2018, **4**, 14.

164 M. E. Orazem and B. Tribollet, *Electrochemical Impedance Spectroscopy*, John Wiley and Sons, Hoboken, New Jersey, USA, 2008.

165 J. Zhu, M. S. Dewi Darma, M. Knapp, D. R. Sørensen, M. Heere, Q. Fang, X. Wang, H. Dai, L. Mereacre, A. Senyshyn, X. Wei and H. Ehrenberg, Investigation of lithium-ion battery degradation mechanisms by combining differential voltage analysis and alternating current impedance, *J. Power Sources*, 2020, **448**, 227575.

166 J. P. Meyers, M. Doyle, R. M. Darling and J. Newman, The Impedance Response of a Porous Electrode Composed of Intercalation Particles, *J. Electrochem. Soc.*, 2000, **147**, 2930.

167 M. Doyle, J. P. Meyers and J. Newman, Computer Simulations of the Impedance Response of Lithium Rechargeable Batteries, *J. Electrochem. Soc.*, 2000, **147**, 99.

168 B. C. Han, A. Van Der Ven, D. Morgan and G. Ceder, Electrochemical modeling of intercalation processes with phase field models, *Electrochim. Acta*, 2004, **49**, 4691–4699.

169 L. Zhang, J. Jiang and W. Zhang, Capacity Decay Mechanism of the LCO + NMC532/Graphite Cells Combined with Post-Mortem Technique, *Energies*, 2017, **10**, 1147.

170 T. Ohzuku, Y. Iwakoshi and K. Sawai, Formation of Lithium-Graphite Intercalation Compounds in Nonaqueous Electrolytes and Their Application as a Negative Electrode for a Lithium Ion (Shuttlecock) Cell, *J. Electrochem. Soc.*, 1993, **140**, 2490–2498.

171 S. S. Zhang, Is Li/Graphite Half-Cell Suitable for Evaluating Lithiation Rate Capability of Graphite Electrode?, *J. Electrochem. Soc.*, 2020, **167**, 100510.

172 M. Müller, L. Schneider, N. Bohn, J. R. Binder and W. Bauer, Effect of Nanostructured and Open-Porous Particle Morphology on Electrode Processing and Electrochemical Performance of Li-Ion Batteries, *ACS Appl. Energy Mater.*, 2021, **4**, 1993–2003.

173 R. Jung, M. Metzger, F. Maglia, C. Stinner and H. A. Gasteiger, Oxygen Release and Its Effect on the Cycling Stability of LiNi x Mn y Co z O 2 (NMC) Cathode Materials for Li-Ion Batteries , *J. Electrochem. Soc.*, 2017, **164**, A1361–A1377.

174 R. Jung, F. Linsenmann, R. Thomas, J. Wandt, S. Solchenbach, F. Maglia, C. Stinner, M. Tromp and H. A. Gasteiger, Nickel, Manganese, and Cobalt Dissolution from Ni-Rich NMC and Their Effects on NMC622-Graphite Cells, *J. Electrochem. Soc.*, 2019, **166**, A378–A389.

175 H. Tsunekawa, S. Tanimoto,a, R. Marubayashi, M. Fujita, K. Kifune and M. Sano, Capacity Fading of Graphite Electrodes Due to the Deposition of Manganese Ions on Them in Li-

Ion Batteries, *J. Electrochem. Soc.*, 2002, **149**, A1326.

176 X. Xiao, Z. Liu, L. Baggetto, G. M. Veith, K. L. More and R. R. Unocic, Unraveling manganese dissolution/deposition mechanisms on the negative electrode in lithium ion batteries, *Phys. Chem. Chem. Phys.*, 2014, **16**, 10398–10402.

177 C. Delacourt, A. Kwong, X. Liu, R. Qiao, W. L. Yang, P. Lu, S. J. Harris and V. Srinivasan, Effect of Manganese Contamination on the Solid-Electrolyte-Interphase Properties in Li-Ion Batteries, *J. Electrochem. Soc.*, 2013, **160**, A1099–A1107.

178 J. A. Gilbert, I. A. Shkrob and D. P. Abraham, Transition Metal Dissolution, Ion Migration, Electrocatalytic Reduction and Capacity Loss in Lithium-Ion Full Cells, *J. Electrochem. Soc.*, 2017, **164**, A389–A399.

179 T. Placke, S. Rothermel, O. Fromm, P. Meister, S. F. Lux, J. Huesker, H.-W. Meyer and M. Winter, Influence of Graphite Characteristics on the Electrochemical Intercalation of Bis(trifluoromethanesulfonyl) imide Anions into a Graphite-Based Cathode, *J. Electrochem. Soc.*, 2013, **160**, A1979–A1991.

180 C. Tian, J. Cui, N. Ning, L. Zhang and M. Tian, Quantitative characterization of interfacial properties of carbon black/elastomer nanocomposites and mechanism exploration on their interfacial interaction, *Compos. Sci. Technol.*, 2022, **222**, 109367.

181 P. Klonos, K. Kulyk, M. V. Borysenko, V. M. Gun’ko, A. Kyritsis and P. Pissis, Effects of Molecular Weight below the Entanglement Threshold on Interfacial Nanoparticles/Polymer Dynamics, *Macromolecules*, 2016, **49**, 9457–9473.

182 A. P. Holt, P. J. Griffin, V. Bocharova, A. L. Agapov, A. E. Imel, M. D. Dadmun, J. R. Sangoro and A. P. Sokolov, Dynamics at the polymer/nanoparticle interface in poly(2-vinylpyridine)/ silica nanocomposites, *Macromolecules*, 2014, **47**, 1837–1843.

183 D. Wang and T. P. Russell, Advances in Atomic Force Microscopy for Probing Polymer Structure and Properties, *Macromolecules*, 2018, **51**, 3–24.

184 D. Welch, M. P. Lettinga, M. Ripoll, Z. Dogic and G. A. Vliegenthart, Trains, tails and loops of partially adsorbed semi-flexible filaments, *Soft Matter*, 2015, **11**, 7507–7514.

185 N. C. Crawford, S. K. R. Williams, D. Boldridge and M. W. Liberatore, Shear-induced structures and thickening in fumed silica slurries, *Langmuir*, 2013, **29**, 12915–12923.

Publications by the author

Publications related to this thesis

1. **F. Colombo**, M. Müller, A. Weber, N. Keim, F. Jeschull, W. Bauer and H. Ehrenberg, Electrochemical investigation of fluorine-containing Li-salts as slurry cathode additives for tunable rheology in super high solid content NMP slurries, *RSC Energy Adv.*, 2023, **2**, 2093–2108.
2. A. Weber, N. Keim, A. Gyulai, M. Müller, **F. Colombo**, W. Bauer and H. Ehrenberg, The Role of Surface Free Energy in Binder Distribution and Adhesion Strength of Aqueously Processed LiNi 0.5 Mn 1.5 O 4 Cathodes, *J. Electrochem. Soc.*, 2024, **171**, 040523.

Other relevant publications

3. **F. Colombo**, S. Bonizzoni, C. Ferrara, R. Simonutti, M. Mauri, M. Falco, C. Gerbaldi, P. Mustarelli and R. Ruffo, Polymer-in-Ceramic Nanocomposite Solid Electrolyte for Lithium Metal Batteries Encompassing PEO-Grafted TiO2 Nanocrystals, *J. Electrochem. Soc.*, 2020, **167**, 070535.